

**EXPERIMENTAL INVESTIGATION OF  
ROTOR-STATOR INTERACTION  
IN DIFFUSER PUMPS**

**Thesis by**  
**Norbert Karl Erhard Arndt**  
**Division of Engineering and Applied Science**

**In Partial Fulfillment  
of the Requirements for the Degree of  
Doctor of Philosophy**

**California Institute of Technology  
Pasadena, California  
1988  
(Submitted April 13, 1988)**

-ia-

**EXPERIMENTAL INVESTIGATION OF  
ROTOR-STATOR INTERACTION  
IN DIFFUSER PUMPS**

**Norbert Karl Erhard Arndt**

**Division of Engineering and Applied Science**

**1988**

**Report No. 249.7**

**on**

**Contract NAS 8-33108**

©1988

**Norbert Karl Erhard Arndt**  
**All rights reserved**

## ACKNOWLEDGEMENTS

I would like to express my most sincere gratitude to my advisor, Professor A.J. Acosta, whose guidance and advice were irreplaceable during this work. I would also like to thank Professors C.E. Brennen and T.K. Caughey for their continued interest in this research.

Special thanks to Mike Gerfen who machined the measurement devices and most of the other parts required for this experimental investigation. I am also thankful to George Lundgren and his team for the machining done during the initial part of this work.

The help of fellow graduate student Ron Franz in the course of the experiment was much appreciated. Furthermore, I want to acknowledge the assistance provided by Scott Miskovich. I also want to express my gratefulness to many other people, even if they are not mentioned here, who contributed in different ways to this research.

I very much appreciated the financial support of the Rotary Foundation of Rotary International during my first year as a graduate student at Caltech. I would also like to give grateful acknowledgements for the financial support for me and for this research to NASA's George C. Marshall Space Flight Center. In addition, I want to express my thanks to the George C. Marshall Space Flight Center and to the Rocketdyne Division of Rockwell International for providing one half of the double suction pump impeller of the High Pressure Oxygen Turbopump of the Space Shuttle Main Engine for testing during the experiment.

Last, but not least, I thank my parents and my sister for the support, the understanding and the encouragement they have given to me.

## ABSTRACT

The interaction between impeller blades and diffuser vanes in diffuser pumps was investigated. Steady and unsteady pressure measurements were made on the diffuser vanes and on the front shroud wall of a vaned and a vaneless diffuser. Two different impellers were used, one half of the impeller of the double suction pump of the HPOTP (High Pressure Oxygen Turbopump) of the SSME (Space Shuttle Main Engine), and a two-dimensional impeller. The measurements were made for different flow coefficients, shaft speeds, and radial gaps between the impeller blades and the diffuser vanes (1.5% and 4.5% of the impeller discharge radius for the impeller of the HPOTP, and 5% and 8% for the two-dimensional impeller). The vane pressure fluctuations were larger on the vane suction than on the vane pressure side attaining their maximum value, of the same order of magnitude as the total pressure rise across the pump, near the leading edge. The resulting lift on the vane, both steady and unsteady, was computed from the pressure measurements at mid vane height. The magnitude of the fluctuating lift was found to be larger than the steady lift. For the impeller of the HPOTP, pressure measurements on the front shroud of a vaned and a vaneless diffuser showed that the front shroud pressure fluctuations increased with the presence of the diffuser vanes.

For the two-dimensional impeller, also unsteady impeller blade pressure measurements were made. The largest blade pressure fluctuations, of the same magnitude as the large pressure fluctuations on the vane suction side, occurred at the blade trailing edge. However, the dependence of those pressure fluctuations on the flow coefficient was found to be different; on the vane suction side, the fluctuations were largest for maximum flow and decreased with decreasing flow coefficient, whereas at the blade trailing edge, the fluctuations were smallest for maximum flow and increased with decreasing flow coefficient. Increasing the vane number resulted in a significant decrease of the blade pressure fluctuations.

Lift, vane and blade pressure, and front shroud pressure fluctuations decreased strongly with increasing radial gap.

## TABLE OF CONTENTS

	Page
Acknowledgements	iii
Abstract	iv
Table of Contents	v
Nomenclature	viii
List of Figures	xii
List of Tables	xxiv
<b>1. Introduction</b>	<b>1</b>
1.1. Description of the Problem	1
1.2. Survey of Current Knowledge	2
1.3. Outline of the Experimental Investigation	6
<b>2. Test Facility, Instrumentation and Data Acquisition</b>	<b>11</b>
2.1. Description of the Test Facility	11
2.2. Description of the Impellers and Diffusers Used in the Experiment	13
2.3. Pressure Measurement Techniques	17
2.4. Instrumentation	18
2.5. Data Acquisition and Data Reduction	20
<b>3. Three-Hole Tube Measurements</b>	<b>45</b>
3.1. Three-Hole Tube Calibration	45
3.2. Steady Three-Hole Tube Measurements	49
3.3. Unsteady Three-Hole Tube Measurements	53
3.3.1. Data Reduction	53
3.3.2. Spectra of Unsteady Pressure Measurements	55
3.3.3. Comparing the Total Pressure Measurements Obtained by the Total Pressure Probe and the Three-Hole Tube	55
3.3.4. Ensemble Averaged Unsteady Three-Hole Tube Measurements	58

3.4.	Summary	63
4.	<b>Total Pressure Measurements</b>	86
4.1.	Introduction	86
4.2.	Measurements for Impeller R and Volute D	87
4.2.1.	Steady Total Pressure Measurements	87
4.2.2.	Ensemble Averaged Unsteady Total Pressure Measurements	88
4.3.	Measurements for Impeller Z1 and Volute D	91
4.3.1.	Steady Total Pressure Measurements	91
4.3.2.	Ensemble Averaged Unsteady Total Pressure Measurements	91
4.4.	Ensemble Averaged Unsteady Total Pressure Measurements for Impeller Z1 and Diffuser S	93
4.5.	Summary	94
5.	<b>Diffuser Vane Pressure Measurements for the Pump Impeller of the HPOTP of the SSME</b>	106
5.1.	Introduction	106
5.2.	Overall Performance	107
5.3.	Steady Vane Pressure Measurements and Steady Vane Lift Computations	107
5.4.	Unsteady Vane Pressure Measurements	109
5.5.	Magnitude and Phase of Fourier Coefficients of Ensemble Averaged Vane Pressure Fluctuations	113
5.6.	Magnitude of Ensemble Averaged Vane Pressure Fluctuations	114
5.7.	Ensemble Averaged Lift and Moment Computations	117
5.8.	Magnitude of Ensemble Averaged Front Shroud Pressure Fluctuations	121
5.9.	Summary	122
6.	<b>Impeller Blade and Diffuser Vane Pressure Measurements in a Radial Pump</b>	148
6.1.	Introduction	148
6.2.	Overall Performance	149

6.3.	Diffuser Vane Pressure Measurements	149
6.3.1.	Steady Vane Pressure Measurements and Steady Vane Lift Computations	149
6.3.2.	Ensemble Averaged Unsteady Vane Pressure Measurements and Spectra of Unsteady Vane Pressure Measurements	151
6.3.3.	Magnitude of Ensemble Averaged Diffuser Vane Pressure Fluctuations	153
6.3.4.	Magnitude and Phase of Fourier Coefficients of Ensemble Averaged Vane Pressure Fluctuations	155
6.3.5.	Ensemble Averaged Lift Computations	156
6.3.6.	Comparing the Vane Pressure Measurements for Impeller R and Impeller Z1	157
6.4.	Unsteady Impeller Blade Pressure Measurements Using Diffuser S	158
6.4.1.	Ensemble Averaged Unsteady Blade Pressure Measurements and Spectra of Unsteady Blade Pressure Measurements	159
6.4.2.	Magnitude of Ensemble Averaged Blade Pressure Fluctuations	163
6.5.	Unsteady Impeller Blade Pressure Measurements Using Different Diffusers	164
6.5.1.	Ensemble Averaged Unsteady Blade Pressure Measurements and Spectra of Unsteady Blade Pressure Measurements	165
6.5.2.	Magnitude of Ensemble Averaged Blade Pressure Fluctuations	168
6.6.	Summary	172
7.	<b>Conclusion</b>	198
	List of References	205
	Appendix	209

## NOMENCLATURE

$a_i$	coefficient of the $i$ th $\cos$ term in a Fourier series, normalized by $(1/2)\rho u_2^2$
$A_2$	impeller discharge area
$b_2$	impeller discharge width
$b_3$	diffuser inlet width
$b_i$	coefficient of the $i$ th $\sin$ term in a Fourier series, normalized by $(1/2)\rho u_2^2$
$c$	vane chord
$c_b$	blade pressure coefficient, $c_b = p_b/(1/2)\rho u_2^2$
$c_f$	front shroud pressure coefficient, $c_f = p_f/(1/2)\rho u_2^2$
$c_i$	magnitude of $i$ th Fourier coefficient, $c_i = \sqrt{a_i^2 + b_i^2}$
$c_L$	lift coefficient, $c_L = L/(1/2)\rho u_2^2 c$
$c_M$	moment coefficient, $c_M = M_z/(1/4)\rho u_2^2 c^2$
$\bar{c}_p$	steady vane pressure coefficient, $\bar{c}_p = (\bar{p}_v - \bar{p}_{up})/(1/2)\rho u_2^2$
$\tilde{c}_p$	unsteady vane pressure coefficient, $\tilde{c}_p = \tilde{p}_v/(1/2)\rho u_2^2$
$\tilde{c}_{p,av}$	ensemble averaged unsteady vane pressure coefficient, $\tilde{c}_{p,av} = \tilde{p}_{v,av}/(1/2)\rho u_2^2$
$c_{p,av}$	ensemble averaged vane pressure coefficient, $c_{p,av} = \bar{c}_p + \tilde{c}_{p,av}$
$c_r, c_u$	absolute radial and circumferential velocity component
$d_{th}$	three-hole tube width
$\mathbf{F}$	force vector on diffuser vane
$f$	frequency
$f_b$	impeller blade passage frequency, $f_b = z_b(rpm/60)$
$f_s$	shaft frequency, $f_s = (rpm/60)$
$f_v$	impeller blade passage frequency, $f_v = z_v(rpm/60)$
$K_\theta$	three-hole tube calibration coefficient (for flow angle)
$K_q$	three-hole tube calibration coefficient (for dynamic pressure)
$K_T$	three-hole tube calibration coefficient (for total pressure)

$L$	lift (= component of the force vector on the vane normal to the chord joining the vane leading edge and the vane trailing edge)
$Ma$	Mach number
$M_z$	moment about the leading edge of the diffuser vane
$\mathbf{n}$	outward normal vector on diffuser vane
$p$	pressure
$p_t$	absolute total pressure
$P_t$	relative total pressure
$q$	(absolute) dynamic pressure
$Q$	flow rate
$r_3$	distance from impact probe (three-hole tube) to the center of the impeller rotation
$R$	radius
$R_2$	impeller discharge radius
$R_3$	diffuser inlet radius
$Re$	Reynolds number
$R_{mean}$	mean line radius of the circular arc vanes
$rpm$	revolutions per minute
$s$	nondimensionalized arclength on vane suction side
$t_b, t_v$	impeller blade thickness, diffuser vane thickness
$t_b^*, t_v^*$	impeller blade thickness, normalized by $(1/z_b)2\pi R_2$ , diffuser vane thickness, normalized by $(1/z_v)2\pi R_3$
$u_2$	impeller tip speed, $u_2 = 2\pi R_2 (rpm/60)$
$w_r, w_u$	relative radial, circumferential velocity
$x, y$	diffuser vane coordinates
$z_b, z_v$	number of impeller blades, number of diffuser vanes
$z_{fb}, z_{pb}$	number of full impeller blades, number of partial impeller blades
$\alpha$	absolute flow angle
$\alpha^*$	impeller blade trailing edge angle (= impeller blade angle)
$\beta$	relative flow angle

$\beta^*$	diffuser vane leading edge mean line angle (= diffuser vane angle)
$\gamma$	three-hole tube/total pressure probe alignment angle
$\theta$	flow angle relative to the three-hole tube
$\nu$	kinematic viscosity
$\xi$	parametric diffuser vane coordinate
$\rho$	density
$\varphi_i$	phase of $i$ th Fourier coefficient, $\varphi_i = \tan^{-1}(a_i/b_i)$
$\phi$	flow coefficient, $\phi = Q/u_2 A_2$
$\psi$	total head coefficient, $\psi = (p_{down} - p_{up})/\rho u_2^2$

### Subscripts

$av$	ensemble averaged
$b$	impeller blade
$c$	center
$down$	downstream
$f$	front shroud
$fb, pb$	full impeller blade, partial impeller blade
$l$	left
$max$	maximum
$r$	right
$s$	shaft
$up$	upstream
$v$	diffuser vane

### Superscripts

-	steady, time mean
$\sim$	unsteady
*	normalized

## Abbreviations

FB	full impeller blade
FP	pressure side of full impeller blade
FS	suction side of full impeller blade
HPOTP	High Pressure Oxygen Turbopump
LE	diffuser vane leading edge
PCB	PCB Piezoelectronics, INC. Depew, NY 14043
PB	partial impeller blade
PP	pressure side of partial impeller blade
PS	suction side of partial impeller blade
PS	diffuser vane pressure side
SS	diffuser vane suction side
SSME	Space Shuttle Main Engine
TE	diffuser vane trailing edge

## LIST OF FIGURES

	Page
<b>Fig. 1.1.</b> Cavitation damage at the trailing edge of the impeller of the double suction pump of the HPOTP of the SSME.	10
<b>Fig. 2.1.</b> Head view of the Rotor Force Test Facility.	23
<b>Fig. 2.2.</b> Photograph of Rotor Force Test Facility.	24
<b>Fig. 2.3.</b> Assembly drawing of the eccentric drive system and the test section with Impeller Z2 installed.	25
<b>Fig. 2.4.</b> Photograph of the test section of the RFTF.	26
<b>Fig. 2.5.</b> Photograph showing the drive shaft, the slip ring assembly, and the drive shaft gear box.	27
<b>Fig. 2.6.</b> Photograph of Impeller R.	28
<b>Fig. 2.7.</b> Schematic assembly drawing of the test section with Impeller R installed.	29
<b>Fig. 2.8.</b> Photograph of Impeller Z2 (the front shroud of the impeller was removed to show the impeller blade shapes).	30
<b>Fig. 2.9.</b> Diffuser vane with pressure taps at mid vane height.	31
<b>Fig. 2.10.</b> Photograph of Diffuser S with the total pressure probe installed.	32
<b>Fig. 2.11.</b> Photograph of Impeller R and Diffuser S installed in the test section.	33
<b>Fig. 2.12.</b> Assembly drawing of Impeller R and Diffuser S installed in the test section.	34
<b>Fig. 2.13.</b> Photograph of Impeller Z2 and Diffuser G installed in the test section (the front shroud of the impeller was removed to show the impeller blade shapes).	35

<b>Fig. 2.14.</b> Photograph of Impeller Z2 and Diffuser F (left upper corner), Impeller Z2 and Diffuser G (right upper corner), and Impeller Z2 and Dif- fuser H (left lower corner) (the front shroud of the impeller was removed to show the impeller blade shapes).	36
<b>Fig. 2.15.</b> Installation of the total pressure probe in Volute D.	37
<b>Fig. 2.16.</b> Machine drawing of the total pressure probes.	38
<b>Fig. 2.17.</b> Machine drawing of the total pressure probe holding device.	39
<b>Fig. 2.18.</b> Photograph showing the total pressure probe mounted on the total pressure probe holding device.	40
<b>Fig. 2.19.</b> Geometry of the vane (and blade) pressure tap.	41
<b>Fig. 2.20.</b> Static calibration curve for the total pressure probe.	42
<b>Fig. 2.21.</b> Spectrum of unsteady total pressure measurements for Impeller R ( $\phi = 0.135$ , $r_3/R_2 = 1.02$ , rpm = 1200).	43
<b>Fig. 2.22.</b> Spectrum of unsteady diffuser vane pressure measurements for Impeller R and Diffuser S at pressure tap S2C ( $\phi = 0.12$ , $R_3/R_2 =$ 1.015, rpm = 1800).	43
<b>Fig. 2.23.</b> Ensemble average total pressure measurements for Impeller R with total pressure probes of different orifices, 0.025 and 0.050 inch. ( $\phi =$ $0.135$ , $r_3/R_2 = 1.02$ , rpm = 1200).	44
<b>Fig. 3.1.</b> Schematic three-hole tube drawing.	65
<b>Fig. 3.2.</b> Schematic three-hole tube drawing.	66
<b>Fig. 3.3a.</b> Photograph of the three-hole tube with the pressure transducers installed.	67
<b>Fig. 3.3b.</b> Photograph of the three-hole tube installed in Diffuser T.	68
<b>Fig. 3.4.</b> Three-hole tube calibration facility.	69

<b>Fig. 3.5.</b> Three-hole tube calibration measurements ( $(p_r - p_{res})$ vs. $\theta$ ).	70
<b>Fig. 3.6.</b> Three-hole tube calibration measurements, ( $(p_c - p_{res})$ vs. $\theta$ ).	70
<b>Fig. 3.7.</b> Three-hole tube calibration measurements, ( $(p_l - p_{res})$ vs. $\theta$ ).	71
<b>Fig. 3.8.</b> Three-hole tube calibration curve ( $\theta$ vs. $K_\theta$ ).	71
<b>Fig. 3.9.</b> Three-hole tube calibration curve ( $K_q$ vs. $K_\theta$ ).	72
<b>Fig. 3.10</b> Three-hole tube calibration curve ( $K_T$ vs. $K_\theta$ ).	72
<b>Fig. 3.11.</b> Velocity triangle.	73
<b>Fig. 3.12.</b> Spectrum of unsteady three-hole tube measurements and ensemble averaged unsteady three-hole tube measurements (left pressure tap) for Impeller Z1 ( $\phi = 0.135, r_3/R_2 = 1.08$ , rpm = 1200).	73
<b>Fig. 3.13.</b> Ensemble averaged unsteady total pressure measurements for Impeller R for $\phi = 0.145, r_3/R_2 = 1.05$ (comparing the three-hole tube to the total pressure probe).	74
<b>Fig. 3.14.</b> Ensemble averaged unsteady total pressure measurements for Impeller R for $\phi = 0.12, r_3/R_2 = 1.05$ (comparing the three-hole tube to the total pressure probe).	74
<b>Fig. 3.15.</b> Ensemble averaged unsteady total pressure measurements for Impeller Z1 for $\phi = 0.135, r_3/R_2 = 1.08$ (comparing the three-hole tube to the total pressure probe).	75
<b>Fig. 3.16.</b> Ensemble averaged unsteady total pressure measurements for Impeller Z1 for $\phi = 0.135, r_3/R_2 = 1.11$ (comparing the three-hole tube to the total pressure probe).	75
<b>Fig. 3.17.</b> Ensemble averaged unsteady total pressure measurements for Impeller Z1 for $\phi = 0.10, r_3/R_2 = 1.08$ (comparing the three-hole tube to the total pressure probe).	76

<b>Fig. 3.18.</b> Ensemble averaged unsteady total pressure measurements for Impeller Z1 for $\phi = 0.10, r_3/R_2 = 1.11$ (comparing the three-hole tube to the total pressure probe).	76
<b>Fig. 3.19.</b> Ensemble averaged unsteady pressure measurements of the right, center, and the left three-hole tube pressure tab for Impeller Z1 ( $\phi = 0.135, r_3/R_2 = 1.08$ , rpm = 1200).	77
<b>Fig. 3.20.</b> Presenting the results from the three-hole tube measurements for Impeller Z1 ( $\phi = 0.135, r_3/R_2 = 1.08$ , rpm = 1200).	78,79
<b>Fig. 3.21.</b> Presenting the results from the three-hole tube measurements for Impeller Z1 ( $\phi = 0.135, r_3/R_2 = 1.11$ , rpm = 1200).	80,81
<b>Fig. 3.22.</b> Presenting the results from the three-hole tube measurements for Impeller Z1 ( $\phi = 0.10, r_3/R_2 = 1.08$ , rpm = 1200).	82,83
<b>Fig. 3.23.</b> Presenting the results from the three-hole tube measurements for Impeller Z1 ( $\phi = 0.10, r_3/R_2 = 1.11$ , rpm = 1200).	84,85
<b>Fig. 4.1.</b> Machine drawing of the total pressure probe.	96
<b>Fig. 4.2.</b> Installation of the total pressure probe in Volute D.	97
<b>Fig. 4.3.</b> Steady total pressure measurements for Impeller R and Volute D between the volute shroud and the volute hub ( $\phi = 0.14, 0.12, 0.09$ and $0.06, r_3/R_2 = 1.05$ , rpm = 1200).	98
<b>Fig. 4.4.</b> Magnitude of ensemble averaged unsteady total pressure fluctuations for Impeller R and Volute D at $z/b = 0.47$ ( $\phi = 0.14, 0.12$ , and $0.09, r_3/R_2 = 1.02$ and $1.05$ , rpm = 1200).	98
<b>Fig. 4.5.</b> Ensemble averaged unsteady total pressure measurements for Impeller R and Volute D at $z/b = 0.47$ ( $\phi = 0.12, r_3/R_2 = 1.02$ and $1.05$ , rpm = 1200).	99
<b>Fig. 4.6.</b> Magnitude of ensemble averaged unsteady total pressure fluctuations for Impeller R and Volute D between the volute shroud and the volute hub ( $\phi = 0.14, 0.12$ , and $0.09, r_3/R_2 = 1.05$ , rpm = 1200).	99

<b>Fig. 4.7.</b> Ensemble averaged unsteady total pressure measurements for Impeller R and Volute D between the volute shroud and the volute hub ( $\phi = 0.14, r_3/R_2 = 1.05$ , rpm = 1200).	100
<b>Fig. 4.8.</b> Ensemble averaged unsteady total pressure measurements for Impeller R and Volute D between the volute shroud and the volute hub ( $\phi = 0.12, r_3/R_2 = 1.05$ , rpm = 1200).	100
<b>Fig. 4.9.</b> Ensemble averaged unsteady total pressure measurements for Impeller R and Volute D between the volute shroud and the volute hub ( $\phi = 0.09, r_3/R_2 = 1.05$ , rpm = 1200).	101
<b>Fig. 4.10.</b> Steady total pressure measurements for Impeller Z1 and Volute D between the volute shroud and the volute hub ( $\phi = 0.133, 0.10$ , and $0.06, r_3/R_2 = 1.055$ , rpm = 1200).	102
<b>Fig. 4.11.</b> Magnitude of ensemble averaged unsteady total pressure fluctuations for Impeller Z1 and Volute D between the volute shroud and the volute hub ( $\phi = 0.133$ and $0.10, r_3/R_2 = 1.055$ and $1.085$ , rpm = 1200).	102
<b>Fig. 4.12.</b> Ensemble averaged unsteady total pressure measurements for Impeller Z1 and Volute D between the volute shroud and the volute hub ( $\phi = 0.133, r_3/R_2 = 1.055$ , rpm = 1200).	103
<b>Fig. 4.13.</b> Ensemble averaged unsteady total pressure measurements for Impeller Z1 and Volute D between the volute shroud and the volute hub ( $\phi = 0.10, r_3/R_2 = 1.055$ , rpm = 1200).	103
<b>Fig. 4.14.</b> Ensemble averaged unsteady total pressure measurements for Impeller Z1 and Diffusers S and T at the mid height of the diffuser channel ( $\phi = 0.10, r_3/R_2 = 1.07, R_3/R_2 = 1.05$ , rpm = 1200).	104
<b>Fig. 4.15.</b> Ensemble averaged unsteady total pressure measurements for Impeller Z1 and Diffusers S and T at the mid height of the diffuser channel ( $\phi = 0.10, r_3/R_2 = 1.10, R_3/R_2 = 1.08$ , rpm = 1200).	105
<b>Fig. 5.1.</b> Performance curves for Diffuser S and Diffuser T.	124

<b>Fig. 5.2.</b> Steady pressure measurements at mid vane height for Impeller R and Diffuser S ( $\phi = 0.12, R_3/R_2 = 1.015$ and $1.045$ , rpm $1800$ ).	125
<b>Fig. 5.3.</b> Steady pressure measurements at mid vane height for Impeller R and Diffuser S ( $\phi = 0.09, R_3/R_2 = 1.015$ and $1.045$ , rpm $1800$ ).	125
<b>Fig. 5.4.</b> Steady pressure measurements across the span of the vane for Impeller R and Diffuser S ( $\phi = 0.15, 0.12, 0.09$ and $0.06, s = 0.10, R_3/R_2 = 1.015$ , rpm $= 1800$ ).	126
<b>Fig. 5.5.</b> Steady pressure measurements across the span of the vane for Impeller R and Diffuser S ( $\phi = 0.15, 0.12, 0.09$ and $0.06, s = 0.37, R_3/R_2 = 1.015$ , rpm $= 1800$ ).	126
<b>Fig. 5.6.</b> Diffuser vane with pressure taps at mid vane height.	127
<b>Fig. 5.7.</b> Steady lift and steady moment versus flow coefficient for Impeller R and Diffuser S ( $R_3/R_2 = 1.015$ and $1.045$ , rpm $= 1800$ ).	128
<b>Fig. 5.8.</b> Unsteady diffuser vane pressure measurements at pressure tap S2C for Impeller R and Diffuser S ( $\phi = 0.15, 0.12, 0.09$ and $0.06, R_3/R_2 = 1.015$ , rpm $= 1800$ ).	129
<b>Fig. 5.9.</b> Unsteady diffuser vane pressure measurements at pressure tap S2C for Impeller R and Diffuser S ( $\phi = 0.15, 0.12, 0.09$ and $0.06, R_3/R_2 = 1.045$ , rpm $= 1800$ ).	130
<b>Fig. 5.10.</b> Spectra of unsteady diffuser vane pressure measurements at pressure tap S2C for Impeller R and Diffuser S ( $\phi = 0.15, 0.12, 0.09$ and $0.06, R_3/R_2 = 1.015$ , rpm $= 1800$ ).	131
<b>Fig. 5.11.</b> Spectra of unsteady diffuser vane pressure measurements at pressure tap S2C for Impeller R and Diffuser S ( $\phi = 0.15, 0.12, 0.09$ and $0.06, R_3/R_2 = 1.045$ , rpm $= 1800$ ).	132
<b>Fig. 5.12.</b> Spectrum of unsteady vane pressure measurements at pressure tap S6C for Impeller R and Diffuser S ( $\phi = 0.12, R_3/R_2 = 1.015$ , rpm $= 1800, c_{i,max} = 0.070$ ).	133

<b>Fig. 5.13.</b> Spectra of unsteady vane pressure measurements at pressure tap P1C for Impeller R and Diffuser S ( $\phi = 0.12$ and $0.08$ , $R_3/R_2 = 1.015$ , rpm = 1800, $c_{i,max} = 0.060$ and $0.071$ ).	134
<b>Fig. 5.14.</b> Geometric reference configuration for the phase computation.	135
<b>Fig. 5.15.</b> Magnitude of Fourier coefficients of impeller blade passage harmonics for Impeller R and Diffuser S ( $\phi = 0.12$ , $R_3/R_2 = 1.015$ , rpm = 1800).	136
<b>Fig. 5.16.</b> Phase of Fourier coefficients of impeller blade passage harmonics for Impeller R and Diffuser S ( $\phi = 0.12$ , $R_3/R_2 = 1.015$ , rpm = 1800).	137
<b>Fig. 5.17.</b> Magnitude of ensemble averaged pressure fluctuations at mid vane height for Impeller R and Diffuser S ( $\phi = 0.12$ , $R_3/R_2 = 1.015$ and $1.045$ , rpm = 1800).	138
<b>Fig. 5.18.</b> Magnitude of ensemble averaged pressure fluctuations at mid vane height for Impeller R and Diffuser S ( $\phi = 0.12$ , $R_3/R_2 = 1.015$ , rpm = 1200, 1800 and 2400).	138
<b>Fig. 5.19.</b> Magnitude of ensemble averaged pressure fluctuations at mid vane height for Impeller R and Diffuser S ( $\phi = 0.15, 0.12, 0.09$ and $0.06$ , $R_3/R_2 = 1.045$ , rpm = 1800).	139
<b>Fig. 5.20.</b> Magnitude of ensemble averaged pressure fluctuations at pressure tap P1C for Impeller R and Diffuser S ( $\phi = 0.05 - 0.15$ , $R_3/R_2 = 1.015$ and $1.045$ , rpm = 1800). Best efficiency flow coefficient: $\phi = 0.12$ .	140
<b>Fig. 5.21.</b> Magnitude of ensemble averaged pressure fluctuations at pressure tap S2C for Impeller R and Diffuser S ( $\phi = 0.05 - 0.15$ , $R_3/R_2 = 1.015$ and $1.045$ , rpm = 1800). Best efficiency flow coefficient: $\phi = 0.12$ .	140
<b>Fig. 5.22.</b> Magnitude of ensemble averaged pressure fluctuations across the span of the vane for Impeller R and Diffuser S ( $\phi = 0.15, 0.12, 0.09$ and $0.06$ , $R_3/R_2 = 1.015$ , rpm = 1800).	141

<b>Fig. 5.23.</b> Magnitude of ensemble averaged pressure fluctuations across the span of the vane for Impeller R and Diffuser S ( $\phi = 0.15, 0.12, 0.09$ and $0.06, R_3/R_2 = 1.045$ , rpm = 1800).	141
<b>Fig. 5.24.</b> Ensemble averaged pressured distribution at mid vane height for Impeller R and Diffuser S ( $\phi = 0.12, R_3/R_2 = 1.015$ , rpm = 1800).	142
<b>Fig. 5.25.</b> Ensemble averaged lift on diffuser vane at mid vane height for Impeller R and Diffuser S ( $\phi = 0.12, R_3/R_2 = 1.015$ and $1.045$ , rpm = 1800).	143
<b>Fig. 5.26.</b> Ratio of ensemble averaged lift to steady lift at mid vane height for Impeller R and Diffuser S ( $\phi = 0.12, R_3/R_2 = 1.015$ and $1.045$ , rpm = 1800).	143
<b>Fig. 5.27.</b> Ensemble averaged lift on diffuser vane at mid vane height for Impeller R and Diffuser S ( $\phi = 0.15$ and $0.12, R_3/R_2 = 1.045$ , rpm = 1800).	144
<b>Fig. 5.28.</b> Ensemble averaged lift on diffuser vane at mid vane height for Impeller R and Diffuser S ( $\phi = 0.09$ and $0.06, R_3/R_2 = 1.045$ , rpm = 1800).	144
<b>Fig. 5.29.</b> Ratio of ensemble averaged lift to steady lift at mid vane height for Impeller R and Diffuser S ( $\phi = 0.15$ and $0.12, R_3/R_2 = 1.045$ , rpm = 1800).	145
<b>Fig. 5.30.</b> Ratio of ensemble averaged lift to steady lift at mid vane height for Impeller R and Diffuser S ( $\phi = 0.09$ and $0.06, R_3/R_2 = 1.045$ , rpm = 1800).	145
<b>Fig. 5.31.</b> Ensemble averaged moment about the diffuser vane leading edge for Impeller R and Diffuser S ( $\phi = 0.12, R_3/R_2 = 1.015$ and $1.045$ , rpm = 1800).	146
<b>Fig. 5.32.</b> Ratio of ensemble averaged moment to steady moment (about the diffuser vane leading edge) for Impeller R and Diffuser S ( $\phi = 0.12, R_3/R_2 = 1.015$ and $1.045$ , rpm = 1800).	146
<b>Fig. 5.33.</b> Magnitude of ensemble averaged front shroud pressure fluctuations on Diffuser S and Diffuser T using Impeller R ( $\phi = 0.12, R_3/R_2$ , rpm = 1800).	147
<b>Fig. 6.1.</b> Performance curves for Diffusers F,G,H and S.	174

<b>Fig. 6.2.</b> Steady pressure measurements at mid vane height for Impeller Z1 and Diffuser S ( $\phi = 0.10, R_3/R_2 = 1.05$ and $1.08$ , rpm = 1200).	175
<b>Fig. 6.3.</b> Steady pressure measurements across the span of the vane for Impeller Z1 and Diffuser S ( $\phi = 0.10$ and $0.135, s = 0.10, R_3/R_2 = 1.05$ , rpm = 1200).	176
<b>Fig. 6.4.</b> Steady pressure measurements across the span of the vane for Impeller Z1 and Diffuser S ( $\phi = 0.10$ and $0.135, s = 0.37, R_3/R_2 = 1.05$ , rpm = 1200).	176
<b>Fig. 6.5</b> Diffuser vane with pressure taps at mid vane height.	177
<b>Fig. 6.6.</b> Spectrum of unsteady vane pressure measurements and ensemble averaged unsteady vane pressure measurements at pressure tap S2C for Impeller Z1 and Diffuser S ( $\phi = 0.10, R_3/R_2 = 1.05$ , rpm = 3000).	178
<b>Fig. 6.7.</b> Spectrum of unsteady vane pressure measurements and ensemble averaged unsteady vane pressure measurements at pressure tap P2C for Impeller Z1 and Diffuser S ( $\phi = 0.10, R_3/R_2 = 1.05$ , rpm = 3000).	178
<b>Fig. 6.8.</b> Magnitude of ensemble averaged vane pressure fluctuations at mid vane height for Impeller Z1 and Diffuser S ( $\phi = 0.10, R_3/R_2 = 1.05$ and $1.08$ , rpm = 3000).	179
<b>Fig. 6.9.</b> Magnitude of ensemble averaged vane pressure fluctuations at mid vane height for Impeller Z1 and Diffuser S ( $\phi = 0.135$ and $0.10, R_3/R_2 = 1.05$ , rpm = 3000).	179
<b>Fig. 6.10.</b> Magnitude of ensemble averaged vane pressure fluctuations at mid vane height for Impeller Z1 and Diffuser S ( $\phi = 0.135, R_3/R_2 = 1.05$ , rpm = 3000 and 1200).	180
<b>Fig. 6.11.</b> Magnitude of ensemble averaged vane pressure fluctuations at pressure tap S2C for Impeller Z1 and Diffuser S ( $\phi = 0.06 - 0.135, R_3/R_2 = 1.05$ and $1.08$ , rpm = 1500).	180

<b>Fig. 6.12.</b> Magnitude of ensemble averaged pressure fluctuations across the span of the vane for Impeller Z1 and Diffuser S ( $\phi = 0.135$ and $0.10$ , $R_3/R_2 = 1.05$ , $s = 0.10$ and $0.37$ , rpm = 1200).	181
<b>Fig. 6.13.</b> Geometric reference configuration for phase computation.	182
<b>Fig. 6.14.</b> Magnitude of Fourier coefficients of impeller blade passage harmonics for Impeller Z1 and Diffuser S ( $\phi = 0.10$ , $R_3/R_2 = 1.05$ , rpm = 1200).	183
<b>Fig. 6.15.</b> Phase of Fourier coefficients of impeller blade passage harmonics for Impeller Z1 and Diffuser S ( $\phi = 0.10$ , $R_3/R_2 = 1.05$ , rpm = 1200).	184
<b>Fig. 6.16.</b> Ensemble averaged lift on the diffuser vane at vane mid height for Impeller Z1 and Diffuser S ( $\phi = 0.10$ , $R_3/R_2 = 1.05$ and $1.08$ , rpm = 1200).	185
<b>Fig. 6.17.</b> Ratio of ensemble averaged lift to steady lift on the diffuser vane at vane mid height for Impeller Z1 and Diffuser S ( $\phi = 0.10$ , $R_3/R_2 = 1.05$ and $1.08$ , rpm = 1200).	185
<b>Fig. 6.18.</b> Magnitude of ensemble averaged pressure fluctuations at mid vane height for Impeller R and Diffuser S ( $\phi = 0.12$ , $R_3/R_2 = 1.045$ , rpm = 1800), and Impeller Z1 and Diffuser S ( $\phi = 0.10$ , $R_3/R_2 = 1.05$ , rpm = 3000).	186
<b>Fig. 6.19.</b> Spectrum of unsteady blade pressure measurements and ensemble averaged unsteady blade pressure measurements at the trailing edge pressure tap for Impeller Z2 and Diffuser S ( $\phi = 0.10$ , rpm = 1500).	187
<b>Fig. 6.20.</b> Spectrum of unsteady blade pressure measurements and ensemble averaged unsteady blade pressure measurements at the trailing edge pressure tap for Impeller Z2 and Diffuser S ( $\phi = 0.135$ , rpm = 1500).	187
<b>Fig. 6.21.</b> Spectrum of unsteady blade pressure measurements and ensemble averaged unsteady blade pressure measurements at the trailing edge pressure tap for Impeller Z2 and Diffuser S ( $\phi = 0.06$ , rpm = 1500).	188

<b>Fig. 6.22.</b> Spectrum of unsteady blade pressure measurements and ensemble averaged unsteady blade pressure measurements at the pressure side pressure tap for Impeller Z2 and Diffuser S ( $\phi = 0.10$ , rpm = 1500).	188
<b>Fig. 6.23.</b> Spectrum of unsteady blade pressure measurements and ensemble averaged unsteady blade pressure measurements at the suction side pressure tap for Impeller Z2 and Diffuser S ( $\phi = 0.10$ , rpm = 1500).	189
<b>Fig. 6.24.</b> Magnitude of ensemble averaged pressure fluctuations at the three impeller blade pressure taps during one shaft revolution for Impeller Z2 and Diffuser S ( $\phi = 0.10$ , rpm = 1500)	190
<b>Fig. 6.25.</b> Magnitude of ensemble averaged pressure fluctuations at the three impeller blade pressure taps for Impeller Z2 and Diffuser S ( $\phi = 0.06 - 0.135$ , $R_3/R_2 = 1.05$ , rpm = 1500)	191
<b>Fig. 6.26.</b> Magnitude of ensemble averaged pressure fluctuations at the pressure tap on the blade pressure side for Impeller Z2 and Diffuser S ( $\phi = 0.06 - 0.135$ , $R_3/R_2 = 1.05$ , rpm = 1500 and 2100)	191
<b>Fig. 6.27</b> Spectrum of unsteady blade pressure measurements and ensemble averaged unsteady blade pressure measurements at the trailing edge pressure tap for Impeller Z2 and Diffuser G ( $\phi = 0.06$ , rpm = 1500).	192
<b>Fig. 6.28.</b> Spectrum of unsteady blade pressure measurements and ensemble averaged unsteady blade pressure measurements at the trailing edge pressure tap for Impeller Z2 and Diffuser F ( $\phi = 0.06$ , rpm = 1500).	192
<b>Fig. 6.29.</b> Spectrum of unsteady blade pressure measurements and ensemble averaged unsteady blade pressure measurements at the trailing edge pressure tap for Impeller Z2 and Diffuser F ( $\phi = 0.08$ , rpm = 1500).	193
<b>Fig. 6.30.</b> Spectrum of unsteady blade pressure measurements and ensemble averaged unsteady blade pressure measurements at the pressure side pressure tap for Impeller Z2 and Diffuser G ( $\phi = 0.10$ , rpm = 1500).	193
<b>Fig. 6.31.</b> Spectrum of unsteady blade pressure measurements and ensemble averaged unsteady blade pressure measurements at the suction side pressure tap for Impeller Z2 and Diffuser H ( $\phi = 0.10$ , rpm = 1500).	194

**Fig. 6.32.** Magnitude of ensemble averaged pressure fluctuations at the pressure tap at the impeller blade trailing edge for Impeller Z2 and Diffusers F, G and H ( $\phi = 0.06 - 0.135$ ,  $R_3/R_2 = 1.05$ , rpm = 1500). 194

**Fig. 6.33.** Magnitude of ensemble averaged pressure fluctuations at the pressure tap at the impeller blade pressure side for Impeller Z2 and Diffusers F, G and H ( $\phi = 0.06 - 0.135$ ,  $R_3/R_2 = 1.5$ , rpm = 1500). 195

**Fig. 6.34.** Magnitude of ensemble averaged pressure fluctuations at the pressure tap at the impeller blade suction side for Impeller Z2 and Diffusers F, G and H ( $\phi = 0.06 - 0.135$ ,  $R_3/R_2 = 1.05$ , rpm = 1500). 195

**Fig. 6.35.** Magnitude of ensemble averaged pressure fluctuations at the three impeller blade pressure taps for Impeller Z2 and Diffusers F ( $\phi = 0.06 - 0.135$ ,  $R_3/R_2 = 1.05$ , rpm = 1500). 196

**Fig. 6.36.** Magnitude of ensemble averaged pressure fluctuations at the three impeller blade pressure taps for Impeller Z2 and Diffusers G ( $\phi = 0.06 - 0.135$ ,  $R_3/R_2 = 1.05$ , rpm = 1500). 196

**Fig. 6.37.** Magnitude of ensemble averaged pressure fluctuations at the three impeller blade pressure taps for Impeller Z2 and Diffusers H ( $\phi = 0.06 - 0.135$ ,  $R_3/R_2 = 1.05$ , rpm = 1500). 197

## LIST OF TABLES

	Page
<b>Table 2.1. Impellers.</b>	13
<b>Table 2.2. Geometry of the Circular Arc Vanes.</b>	16
<b>Table 2.3. Diffusers.</b>	16
<b>Table 2.4. Number of Sampling Periods for Ensemble Averaging.</b>	21
<b>Table 3.1. Steady Three-Hole Tube Measurements.</b> (for Impeller R and Impeller Z1)	51
<b>Table 3.2. Steady and Time Mean Flow Measurements.</b> (Impeller Z1, $r_3/R_2 = 1.08$ , $\phi = 0.135$ )	55
<b>Table 3.3. Time Mean and Fluctuating Flow Measurements.</b> (Impeller Z1, $r_3/R_2 = 1.08$ , $\phi = 0.135$ )	79
<b>Table 3.4. Time Mean and Fluctuating Flow Measurements.</b> (Impeller Z1, $r_3/R_2 = 1.11$ , $\phi = 0.135$ )	81
<b>Table 3.5. Time Mean and Fluctuating Flow Measurements.</b> (Impeller Z1, $r_3/R_2 = 1.08$ , $\phi = 0.10$ )	83
<b>Table 3.6. Time Mean and Fluctuating Flow Measurements.</b> (Impeller Z1, $r_3/R_2 = 1.11$ , $\phi = 0.10$ )	85
<b>Table 5.1. Steady Lift and Moment on a Vane of Diffuser S.</b> (Impeller R and Diffuser S)	109
<b>Table 5.2. Magnitude of the Vane Pressure Fluctuations at Vane Pressure Tap S2C. (Impeller R and Diffuser S)</b>	111
<b>Table 6.1. Steady Lift and Moment on a Vane of Diffuser S.</b> (Impeller Z1 and Diffuser S)	151

## CHAPTER 1

### 1. Introduction

#### 1.1. Description of the Problem

Blade and vane design in diffuser pumps is currently based upon the assumption that the flow in both the impeller and the diffuser is steady. This, however, implies that the radial gap between the impeller discharge and the diffuser inlet is large so that no flow unsteadiness of any kind due to rotor-stator interaction may occur. If, however, the radial gap between impeller blades and diffuser vanes is small, i.e., of the order of a small percentage of the impeller discharge radius, as it actually is for many diffuser pumps, there may be a strong interaction that may influence both the aerodynamic and the structural performance of the impeller blades and the diffuser vanes. About fifty years ago, Lalive (1936) reported fluctuating diffuser wall pressures at the inlet of the diffuser of a diffuser pump, which were of the same order of magnitude as the pressure rise across the pump. When the pump was operated under heavy cavitation, cavitation erosion due to rotor-stator interaction was observed within several hours.

The drive to higher and higher power densities in diffuser pumps, especially in the liquid propellant pumps for rocket engines, where demands of small size and high power output require very high impeller speeds, has led to problems due to rotor-stator interaction even during normal pump operation. For a pump with an extremely high power density, for example, the High Pressure Oxygen Turbopump (HPOTP) of the Space Shuttle Main Engine (SSME) erosion due to rotor-stator interaction during normal operation can be observed from the cavitation damage sustained at the impeller trailing edge after only a few thousand seconds of operation (figure 1.1) (The author wants to thank the Rocketdyne Division of Rockwell International for providing the photograph). Thus, problems associated with rotor-

stator interaction have been observed for some time in one form or other. Still, there are few practical analytical or numerical methods or experimental results available to provide knowledge about the magnitude of the unsteadiness caused by rotor-stator interaction in diffuser pumps.

The rotor-stator interaction may be divided into two different mechanisms, potential flow interaction and wake interaction (Dring, 1982). The potential flow interaction between the two blade rows moving relative to each other arises because of the circulation about the blades and because of potential fields, other than circulation, about the blades that are due to the finite thickness of the blades (Lefcort 1965). The potential flow fields about a blade extend both upstream and downstream of the blade. Kemp and Sears (1955) reported a solution of linearized potential flow for two rows of thin airfoils with small turning moving relative to each other. The fluctuating part of the circulation normalized by the steady circulation was found to be larger for the upstream than for the downstream blade row. It may hence be expected that the flow unsteadiness induced by potential flow interaction between two blade rows moving relative to each other is larger on the upstream blade row than on the downstream blade row. The wake interaction refers to the unsteadiness induced at a blade of a blade row by wakes shed by the blades of an upstream blade row and convected downstream. Kemp and Sears (1955) computed the forces on an airfoil passing through wakes, and found that the unsteady forces on the airfoil are of about the same size as those due to potential flow interaction. Hence both potential flow interaction and wake interaction may result in unsteady forces of significant size on both the impeller blades and the diffuser vanes. If the radial gap between the impeller blades and the diffuser vanes is small both interaction mechanisms will occur simultaneously and may influence each other.

### 1.2. Survey of Current Knowledge

Before considering the complete problem of impeller-diffuser interaction, it may be worthwhile to consider briefly the flow discharged by a centrifugal impeller into

a vaneless diffuser. Thus, information can be obtained about how far downstream of the impeller blade trailing edge the flow nonuniformity, caused by the reduced relative velocity and the reduced relative total pressure in the impeller blade wakes, can be observed. Dean reported 1960 hot-wire measurements of the flow at the discharge of a centrifugal compressor, and presented what is known as the jet-wake model. It was concluded that, because of reversible work transfer between the wake and the jet, the rotating wakes should close up quickly. At about 5% downstream of the impeller trailing edge, any circumferential nonuniformities should have ceased to exist.

The jet-wake model was qualitatively confirmed by Eckhard (1975, 1976), who used the L2F technique to measure the flow field inside and at the discharge of a high speed centrifugal compressor. It was, however, observed that the compressor wakes could be observed much farther downstream than predicted by Dean. Furthermore, it was shown that the flow field was three-dimensional. Circumferential as well as hub-to-shroud flow nonuniformities were observed. The impeller blade wake was, for most flow coefficients, located in the shroud suction side corner of the blade passage. Measurements of the flow at the discharge of a centrifugal impeller were also made by Inoue and Cumptsy (1984) using hot-wires for velocity measurements. It was again found that the wake extends further downstream than predicted by the jet-wake model. Thus, wake interaction is very likely to contribute to the diffuser vane pressure fluctuations if the radial gap between impeller blades and diffuser vanes is small.

Flow field investigations of the flow inside a radial compressor rotor and in the vaneless space between the compressor rotor and the diffuser of a centrifugal compressor stage were made among others by Krain (1981) and Stein and Rautenberg (1988). The velocity field was investigated by means of the L2F technique. The researchers found that the velocity fluctuations were still of significance at the diffuser throat. In contrast to the early measurements in a diffuser pump made by Lalive (1936), Stein (1988) reported that the pressure fluctuations at the diffuser inlet were small.

Most of the experimental work on blade row interaction with the aim of measuring unsteady blade pressures has been in axial turbomachinery. Among others, Dring et al. (1982) investigated blade row interaction in an axial turbine and found both potential flow and wake interaction for closely spaced blade rows (15% based on chord). Significant pressure fluctuations of up to 72% of the exit dynamic pressure were measured near the leading edge of the rotor. Gallus (1979) and Gallus et al. (1980) reported measurements on axial compressors. The blade rows were spaced relatively far apart (60% based on chord), such that the potential interaction between the rotor and the stator was weak; i.e., the pressure fluctuations on the compressor stator were found to be considerably larger than those on the compressor rotor. In radial turbomachinery, impeller blade pressure measurements were reported by Iino and Kasai (1985). The radial gap between impeller blades and diffuser vanes was small, so that significant pressure fluctuations on the impeller blades were observed. It was furthermore found that blade and vane angle may have an important influence on the blade pressure fluctuations.

Theoretical analyses of the unsteady flow in turbomachines have been made by several investigators. For axial turbomachines or cascades, Kemp and Sears calculated the unsteady force on blades moving through viscous wakes of preceding grids (1953), and the potential interaction between a stationary and a moving cascade (1955). Lienhart (1974) also computed a nonsteady solution for the two-dimensional incompressible flow through blade rows with relative motion using potential flow theory. Viscous effects, however, were neglected. Krammer (1982) computed unsteady blade forces in turbomachines by means of potential flow and by simulating viscous wakes by contra rotating vortex rows. For radial turbomachines, Iino reported a computation of potential flow interaction between a centrifugal impeller and a vaned diffuser (1982). But, as in Lienhart's computations (1974), viscous wakes were neglected. All the investigations mentioned were done for two-dimensional flow and infinitely thin blades and vanes, and, with the exception of Krammer (1982), did consider only potential flow effects or viscous wake effects. For closely spaced blade rows, however, both effects will occur simultaneously. Further-

more, experimental investigations of the flow in a centrifugal compressor impeller carried out by Eckhard (1975) have shown that the impeller blade wake at the impeller blade suction side is fed with low energy fluid from the blade channel surfaces by means of a vortex in the impeller blade channel. Therefore, the flow in centrifugal compressor impellers (and centrifugal pump impellers) is truly three-dimensional. Modelling these three-dimensional flows by a two-dimensional analysis may lead to useful results. However, experimental results are required to provide information about how to model the flow, and to validate the model.

Results obtained by numerically solving the two-dimensional and three-dimensional thin layer equations for rotor-stator interaction in axial turbines have been reported by Rai (1987). However, to this author's knowledge, no numerical solution of the Navier-Stokes equations or of the thin layer equations have been reported for centrifugal compressor impellers or centrifugal pump impellers with radial diffusers.

Considering the complexity of the problem, and the limitations of the theoretical and numerical methods available, it was decided that an experimental investigation would be the best and most appropriate approach to provide valid data about the magnitude of the unsteadiness, especially of the unsteady impeller blade and diffuser vane pressures, caused by rotor-stator interaction in diffuser pumps.

The references stated above are certainly not complete. However, they give an overview, especially of the experimental work that has been done on rotor-stator interaction. The selection of references showed that most of the experimental research for radial turbomachinery has been done for compressor flow. However, no investigation on both fluctuating blade and vane pressures in either a radial compressor or a radial pump has been reported. Recalling the problems experienced in diffuser pumps due to rotor-stator interaction, it was decided that a thorough investigation on rotor-stator interaction by measuring fluctuating impeller blade pressures and diffuser vane pressure might provide some useful insight into the problem. It was furthermore decided to make measurements of the unsteady flow at the discharge of a centrifugal impeller into a vaneless diffuser. As mentioned

above, many such investigations have been made for air compressors. However, the trailing edge of the air compressor blades was thin in comparison to the thick trailing edge found in centrifugal pump impellers as the double suction pump of the High Pressure Oxygen Turbopump (HPOTP) of the Space Shuttle Main Engine (SSME). Hence, it was felt that the unsteady measurements at the impeller discharge might give some insight into the influence of the thick impeller blade trailing edge on the flow at and downstream of the impeller discharge.

### 1.3. Outline of the Experimental Investigation

The present experimental investigation has the following objectives: measurement of the unsteady flow at the impeller discharge into a vaneless diffuser by using total pressure probes and a three-hole tube, measurements of the unsteady impeller blade and diffuser vane pressure, and front shroud pressure measurements on vaned and vaneless diffusers. Those last measurements were planned with the objective in mind to investigate whether the flow unsteadiness is increased by the presence of the diffuser vanes.

The measurements were done in the test section of the Rotor Force Test Facility at Caltech. The impellers, diffusers and measurement instrumentation used for the measurements are described in detail in Chapter 2. Results of the different measurements will be presented in Chapters 3 to 6. Steady diffuser vane pressure measurements, using mercury manometers, and unsteady diffuser vane pressure measurements, using piezoelectric pressure transducers, were made for one half of the double suction pump impeller of the High Pressure Oxygen Turbopump (HPOTP) of the Space Shuttle Main Engine (SSME), referred to as Impeller R, and a vaned diffuser, referred to as Diffuser S. Superimposing the steady and the ensemble averaged unsteady diffuser vane pressure measurements, the ensemble averaged vane pressure was obtained. It was assumed that the steady pressure value measured with mercury manometers was identical to the time mean value about which the piezoelectric pressure transducers measured the pressure fluctuations.

From the pressure measurements, the steady and unsteady lift on the vane and the steady and unsteady moment about the vane leading edge were computed. Surface pressure measurements were also made on the front shroud of the vaned diffuser and a vaneless diffuser of identical side wall geometry, referred to as Diffuser T. Those measurements are presented in Chapter 5.

Diffuser vane pressure measurements were also made for a two-dimensional impeller, referred to as Impeller Z1. Those measurements and blade pressure measurements on the impeller blades of an impeller of identical blade geometry as Impeller Z1, but permitting the installation of pressure transducers for blade pressure measurements, are reported in Chapter 6. The blade pressure measurements were done using Diffuser S and a diffuser allowing different diffuser vane configurations to permit investigations to be made on the influence of the number of diffuser vanes and the vane angle on the impeller blade pressure measurements. All measurements were made with the system pressure sufficiently high to ensure noncavitating flow.

Total pressure measurements were made for Impeller R and for Impeller Z1 in the vaneless diffuser of a volute. Those measurements are presented in Chapter 4.

The three-hole tube measurements made for Impeller Z1 and Impeller R in Diffuser T are presented in Chapter 3. The reason that the total pressure measurements and the three-hole tube measurements were done in two different diffusers is as follows. At the onset of the experiment, only two test impellers, Impeller R and Impeller Z1, and the volute with the vaneless diffuser were available. The others diffusers, Diffuser S, Diffuser T and the variable vane configuration diffuser for the blade pressure measurements, as well as the total pressure probes and the three-hole tube, had to be designed and built. Hence, the investigation got started with total pressure measurements in the vaned diffuser of the volute, since designing and building the total pressure probe were the least expensive and least time extensive of the design tasks. After the total pressure measurements were made, it turned out that due to limited space, the three-hole tube with the three pressure transducers could not be installed in Volute D. Hence, a new vaneless diffuser of identical side wall geometry as Diffuser S was designed and built for the three-hole tube measure-

ments. This diffuser was also used for diffuser front shroud pressure measurements. Time constraints prohibited to repeat all the total pressure measurements made in Volute D in the new diffuser. So, some total pressure measurements were made at mid channel height of Diffuser T with the objective of comparing those measurements to the three-hole tube measurements and to total pressure measurements made in the vaned diffuser in a channel between diffuser vanes.

During the tests, the impeller could only be positioned on locations on an orbit concentric to the diffuser center (orbit radius=0.050 inch), so that the radial gap between the impeller blades and a particular instrumented diffuser vane, or the orifice of the total pressure probe, or the head of the three hole tube could be varied by 3% of the impeller discharge radius, depending upon the position of the impeller on the orbit (for a more detailed description see Chapter 2). For both impellers used for the measurements in the stationary frame (i.e., the diffuser vane pressure measurements, the total pressure measurements, and the three-hole tube measurements) data were taken at the smallest and the largest radial gap possible. During the impeller blade pressure measurements (because of the eccentric position of the impeller with respect to the diffuser center), the radial gap between the instrumented impeller blade and the diffuser vanes varied between 5% and 8% during one impeller revolution. Data are presented both for the blade pressure fluctuations observed during one revolution and for the pressure fluctuations observed when the gap between the instrumented impeller blade and the diffuser vanes was smallest.

Are the blade and vane pressure fluctuations measured for the "local" radial gaps between impeller blades and diffuser vanes representative for diffuser pumps in which the radial gap between the impeller blades and the diffuser vanes is uniform? During one shaft revolution, the impeller flow is subjected to disturbances occurring at two different frequencies (low frequency disturbances such as rotating stall etc. are excluded from this discussion since the present investigation did not focus on such phenomena); namely a disturbance due to the presence of the diffuser vanes occurring at vane passage frequency,  $f_v$ , and a disturbance due to the varying radial gap between impeller blades and diffuser vanes during one shaft revolution

occurring at shaft frequency,  $f_s$ . For the centrifugal pump stages investigated, the vane passage frequency was an order of magnitude larger than the shaft frequency ( $6 \leq (f_v/f_s) \leq 12$ ). Hence, it is inferred that the flow about an impeller blade passing a diffuser vane at a certain radial gap can be considered "quasiperiodic", i.e., the pressure fluctuations experienced by that particular impeller blade and that particular diffuser vane are representative for the pressure fluctuations the impeller blades and the diffuser vanes in diffuser pumps with a uniform radial gap of that particular size are subjected to. The proximity of neighboring diffuser vanes (for the instrumented impeller blade) and neighboring impeller blades (for the instrumented diffuser vane) with a slightly different radial gap (i.e., the change of the radial gap to neighboring diffuser vanes (or impeller blades) is small compared to the radial gap between the impeller blade and the diffuser vane whose interactions are investigated) is considered a small perturbation with only a small effect on the blade and vane pressure fluctuations measured on the particular instrumented impeller blade and diffuser vane. To quantify the size of this small effect, however, it would be necessary to make these measurements in a diffuser pump with a uniform radial gap between the impeller blades and the diffuser vanes.

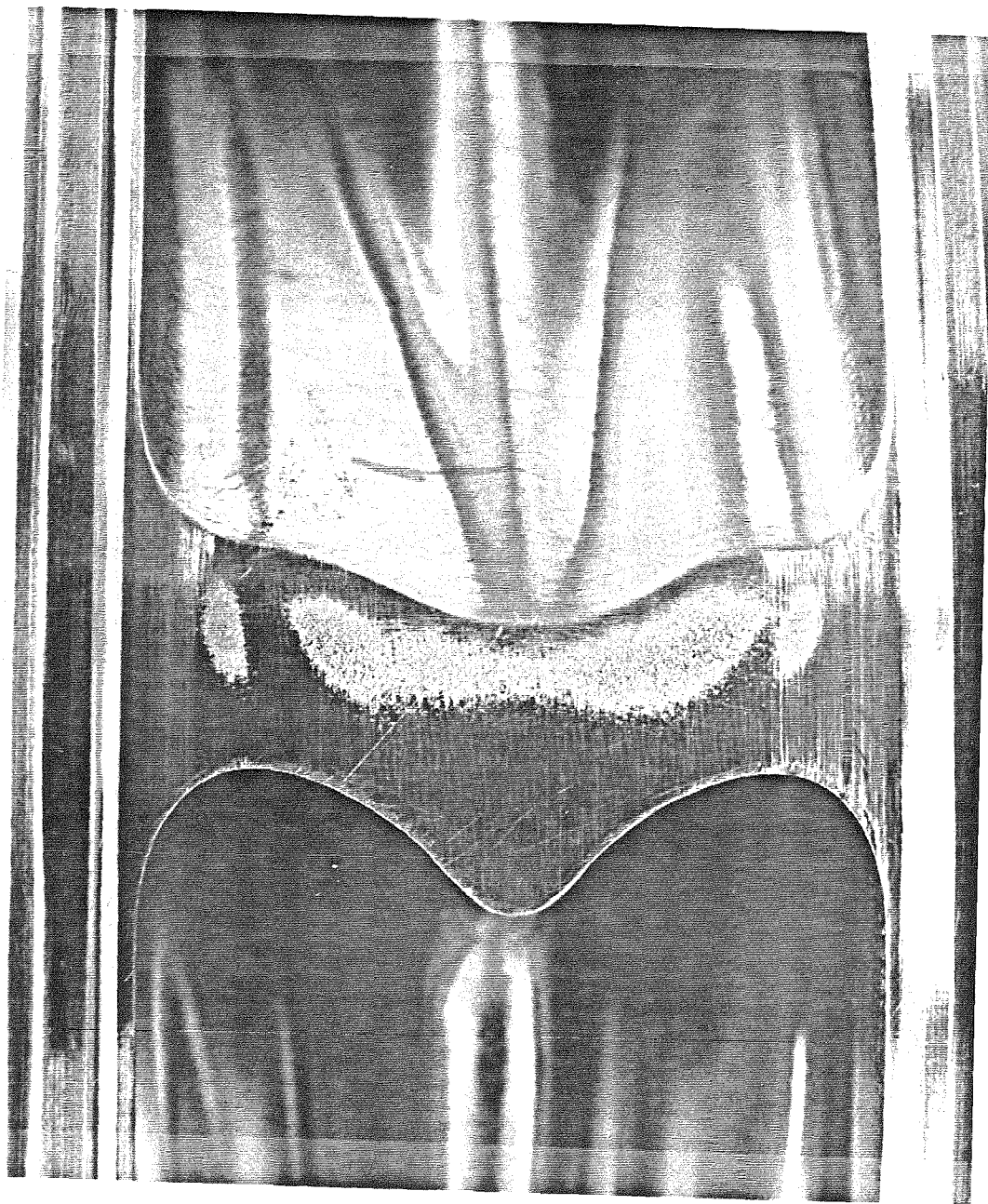


**Fig. 1.1.** Cavitation damage at the trailing edge of the impeller of the double suction pump of the HPOTP of the SSME.

## CHAPTER 2

### 2. Test Facility, Instrumentation and Data Acquisition

#### 2.1. Description of the Test Facility

The measurements made for this research were conducted in the RFTF (Rotor Force Test Facility) at the California Institute of Technology. This facility has been described in detail by Ng (1976), Braisted (1979), Chamieh (1983), and Jery (1986).

In figure 2.1, an overhead view of the RFTF that identifies its most important components is presented. The measurements (diffuser vane and impeller blade pressure measurements, and total pressure and three hole tube measurements) were made in the centrifugal pump test section. The pump located in this section circulates the water in the clockwise direction through the loop. The flow rate was measured by a turbine flow meter and was controlled by the "silent throttle" valve, which is servo-controlled, using the output of the turbine flow meter. The overall system pressure was regulated by the amount of pressurized air allowed inside a submerged air bag. A heat exchanger permitted maintaining a constant water temperature during the experiments. Upstream and downstream pump pressures were registered by two pressure transducers. In addition, a dial gage and a Heise gage were used for visual control. The flow fluctuators located on either side of the reservoir were used in earlier experiments designed to obtain transfer functions for cavitating turbomachinery (Ng, 1976, and Braisted, 1979). For the present work, the fluctuators were dismantled. In the upstream and downstream flow smoothing sections, honeycombs were used to provide a more uniform velocity profile. The pump impeller, mounted on the drive shaft, was driven by a 20 hp d.c. motor (the "main" motor). By using a 2:1 step-up gear box, shaft speeds up to 3500 rpm could be obtained. Since no impeller whirling was done for the measurements reported, the whirl motor was not used. A photograph of the test facility is presented in

figure 2.2. Several of the components described above such as the heat exchanger, the whirl motor, the step-up gear box and the drive shaft can easily be identified.

An assembly drawing of the components of the eccentric drive system and the test section with one of the two-dimensional impellers, Impeller Z2, installed is shown in figure 2.3. The eccentric drive system was designed to perform an experiment to measure forces on whirling impellers. The shaft that drives the impeller passes through an eccentrically drilled cylinder that causes a 0.050 in displacement of the center of rotation of the impeller from the center of the diffuser. The eccentrically drilled cylinder is located in the eccentric drive mechanisms. For force measurements on whirling impellers, this cylinder was rotated by the whirl motor in either direction up to 1750 rpm (as mentioned above, the whirl motor was not used for the measurements reported herein).

A photograph of the test section showing the inlet section, the housing and the eccentric drive is presented in figure 2.4. The pressure tap used for the reference pressure (upstream pressure) for the steady pressure measurements can be seen at the left edge of the photograph. The drive shaft, the slip ring assembly, the step-up gear box, the main shaft encoder, and the front part of the main motor casing as well as the whirl motor and the whirl shaft encoder are shown in the next photograph (figure 2.5).

Because of the eccentric drive system, the impeller could be positioned only on locations of a circular orbit concentric to the diffuser center (orbit radius=0.050 in). For the measurements in the stationary frame such as the diffuser vane and the diffuser front shroud pressure measurements as well as for the total pressure and for the three-hole tube measurements, the impeller was moved to different locations on its concentric orbit between measurements. Thus, data could be obtained for different radial gaps between the impeller blade trailing edge and the diffuser vane leading edge of a particular instrumented vane, and between the impeller blade trailing edge and the total pressure probe or the three-hole probe.

## 2.2. Description of the Impellers and Diffusers used in the Experiment

Three impellers were used in the course of the experiment, one half of the double suction pump impeller of the HPOTP (High Pressure Oxygen Turbopump) of the SSME (Space Shuttle Main Engine), referred to as Impeller R, and two two-dimensional test-impellers with identical blade number and blade geometry, referred to as Impeller Z1 and Z2.

**Table 2.1. Impellers.**

Impeller	$z_b$	$t^*$	$\alpha^*$	$d_2$	$b_2$
Imp. R	8	.155	$\approx 36^\circ$	6.6 in	0.57 in
Imp. Z1	5	.130	$25^\circ$	6.375 in	0.62 in
Imp. Z2	5	.130	$25^\circ$	6.375 in	0.62 in

Impeller R (figure 2.6) has eight blades in total with four partial blades and an inducer with four inducer blades. Before this research was started, force measurements on Impeller R whirling inside the vaned diffuser of a volute were made. In order to whirl inside the existing volute, the impeller discharge diameter had to be reduced from 6.85 in to 6.6 in. The blade angle of both full and partial blades at the impeller discharge is about 36 degrees. In figure 2.7, the impeller, installed in the test section, is shown. The position of the leading edge of the full and the partial impeller blades is indicated. Because of the eccentric position of the inducer of the impeller inside the intake, the inducer tip clearance varied from 0.150 in to 0.050 in. Hence, the mean clearance was 0.100 in. Impeller R was used extensively for diffuser vane pressure measurements. Total pressure measurements and three-hole tube measurements at the discharge were also made, using Impeller R. No impeller blade pressure measurements were made for Impeller R.

The two two-dimensional test-impellers are both five-bladed impellers, with logarithmic blades and a blade angle of 25 degrees. As mentioned previously, the blade number and the blade geometry of both impellers are identical. The reason of having two impellers is as follows. The "old" two-dimensional impeller, Impeller Z1,

was originally designed for the force measurements on whirling impellers. It turned out that this impeller could be used for diffuser vane pressure measurements without major modifications of the intake section used for Impeller R. Modification of this impeller for impeller blade pressure measurements appeared quite difficult. Instead, a "new" two-dimensional impeller was designed with identical blade number and identical blade geometry but permitting the possibility to insert pressure transducers in the impeller back plate to measure impeller blade pressure fluctuations. The impeller was subsequently built and is referred to as Impeller Z2. A photograph of Impeller Z2 is shown in figure 2.8 (the front shroud of the impeller was removed to show the impeller blade shapes). Impeller blade pressure measurements were made at three pressure taps on the impeller blades, one on the blade pressure side ( $R/R_2 = 0.987$ ), one at the impeller blade trailing edge ( $R/R_2 = 1.0$ ), and one on the impeller blade suction side ( $R/R_2 = 0.937$ ). The signal from the pressure transducer was transmitted by a cable from the pressure transducer to a slip ring assembly and from there to the pressure transducer power supply.

Diffuser vane pressure measurements were made using a straight wall constant width diffuser with nine vanes, referred to as Diffuser S. The diffuser and the vanes were milled out of one block of aluminum. No volute was used. Thus, the flow is discharged from the diffuser into a large housing (see figures 2.3, 2.7 and 2.12). The shape of a diffuser vane, with the locations of the pressure taps at vane mid height, is shown in figure 2.9. The vane shape is identical to the one used in an early version of the diffuser of the HPOTP of the SSME; however, the number of vanes was reduced from seventeen to nine in this experiment. This was done to permit space for total pressure measurements in the vane channels with a total pressure probe. The diffuser width was chosen to be half the width of the diffuser of the HPOTP in the SSME,  $b_3 = 0.59$  in (for this experiment, only one half of the pump impeller of the HPOTP of the SSME was tested; hence the reduction of the diffuser width by 1/2). Thus, the diffuser channel was wider than the blade channel of Impeller R ( $b_2 = 0.57$  in), but not as wide as the blade channel of the two two-dimensional impellers ( $b_2 = 0.62$  in). Diffuser vane pressure measurements

were made at fourteen locations at mid vane height of the diffuser vane pressure side and the diffuser vane suction side. Six more pressure taps were distributed axially between front shroud and hub (or back shroud) at two different locations downstream of the leading edge on the suction side of the vane. The size of the pressure transducer did not permit arbitrarily close spacing of the pressure taps on a single vane, so that a total of seven vanes were used for the twenty pressure taps. Pressure measurements were also made on the front shroud of the diffuser. The location of the pressure taps on the diffuser vanes, the front shroud pressure taps, and the position of the orifice of the total pressure probe during the total pressure measurements are given in the appendix. A photograph of Diffuser S with the total pressure probe installed is presented in figure 2.10. The front shroud pressure taps can be seen as well. In figure 2.11 and 2.12, a photograph and an assembly drawing of Diffuser S and Impeller R installed in the test section are shown. In the photograph, two pressure transducers installed for vane pressure measurements can be seen. The cables transmitting the signal from the pressure transducer to the power supply are led through flexible tubing from diffuser to the housing. During operation, a lid is attached to the diffuser to waterproof the annular cavity in which the transducers are mounted.

A second diffuser, referred to as Diffuser T, of identical geometry as Diffuser S but vaneless, was used for front shroud pressure measurements as well as for total pressure and three-hole tube measurements.

A third diffuser, again of identical side wall geometry and diffuser channel width as Diffuser S, but permitting variable diffuser vane configurations was designed and built to investigate the effects of the number of diffuser vanes and of the diffuser vane angle on the impeller blade measurements. This employed circular arc vanes available from previous research work done in the RFTF with the geometry listed in Table 2.2.

**Table 2.2. Geometry of the Circular Arc Vanes.**

$R_{mean}$	3.500 in (88.91 mm)
$c$	2.24 in (56.90 mm)
$t_v$	0.165 in (4.19 mm)

Three diffuser vane configurations were tested. The different vane configurations, with the number of diffuser vanes,  $z_v$ , and the vane leading edge mean line angle (in the following also simply referred to as the vane angle),  $\beta^*$ , and the name of the respective diffusers are referred to are presented in Table 2.3. Photographs showing Diffuser G and Diffuser F installed in the test facility are presented in figures 2.13 and 2.14.

**Table 2.3. Diffusers.**

Diffuser	Vane Type	$z_v$	$\beta^*$	$d_3$	$b_3$
Diff. F	cir. arc	12	20°	6.8 in	0.59 in
Diff. G	cir. arc	6	20°	6.8 in	0.59 in
Diff. H	cir. arc	6	10°	6.8 in	0.59 in
Diff. S	see App.	9	18.4°	6.8 in	0.59 in
Diff. T		0		6.8 in	0.59 in

Using Diffusers F, G, and H permitted an investigation of the influence of the number of diffuser vanes,  $z_v$ , and of the influence of the vane leading edge mean line angle,  $\beta^*$ , on the impeller blade pressure measurements by comparing the measurements for Diffuser G and Diffuser F, and Diffuser G and Diffuser H, respectively.

Total pressure measurements were also made in the vaneless diffuser of a volute of trapezoidal cross section, referred to as Volute D. The installation of the total pressure probe in Volute D is shown in figure 2.15.

### 2.3. Pressure Measurement Techniques

Machine drawings of the two total pressure probes used for the total pressure measurements and the total pressure probe holding device are presented in figures 2.16 and 2.17. For the total pressure measurements the total pressure probes were mounted onto the holding device (figure 2.18). The geometry of the pressure taps for the pressure measurements on the diffuser vanes and the impeller blades is shown in figure 2.19.

A static calibration curve for the total pressure probe with the 0.025 in orifice is shown in figure 2.20. It can be seen that the probe is not very sensitive to flow angle variations of  $\pm 15$  degrees (the measurement error from the calibration is 2% of the dynamic head). Details of the calibration procedure can be found in Chapter 3, in which the calibration of the three-hole tube is described in detail.

The resonant frequency of the pressure taps was estimated, using a Helmholtz resonator model, to be approximately 5000 Hz for the total pressure probe pressure tap and 8000 Hz for the vane and blade pressure taps. Spectra of unsteady total pressure measurements for Impeller R ( $\phi = 0.135, r_3/R_2 = 1.02, \text{ rpm} = 1200$ ), using the total pressure probe with the 0.025 in orifice, and unsteady vane pressure measurements for Impeller R at vane pressure tap S2C ( $\phi = 0.12, R_3/R_2 = 1.015, \text{ rpm} = 1800$ ) are presented in figures 2.21 and 2.22. It can be seen that the estimates on the resonant frequencies of the pressure taps were reasonable.

No dynamic calibration of the vane pressure or the total pressure tap was made. Instead, it was inferred from the spectra of the unsteady measurements, showing that the impeller blade passage frequency and its higher harmonics were “far” removed from the resonant frequency of the pressure tap, that amplification and phase shift were negligible.

The performance of the total pressure probe was in addition investigated by comparing results obtained with the two probes of different orifice size (the resonant frequency of the pressure probe with the 0.050 in orifice was found to be approximately twice as large as the resonant frequency for the probe with the 0.025 in

orifice). In figure 2.23, the ensemble averaged measurements made with the two tubes are presented for maximum flow,  $\phi=0.135$ , and 1200 rpm. It can be seen that both the magnitude and the phase of the two ensemble averaged total pressure measurements are nearly identical. The steeper increase of the total pressure from its minimum to its maximum value for the total pressure probe with the smaller orifice can be explained by the fact that the smaller orifice does less "spatial averaging" than the larger orifice, and is hence more suited to resolve strong gradients in the flow. Since the total pressure curves for the two tubes are in good agreement it can be inferred that the tubes were sufficiently small to resolve the total pressure gradients in the flow, although it has to be remarked that using the smaller probe did still result in a small improvement in resolving the very steep total pressure increase from the total pressure minimum to the total pressure maximum. Furthermore, it can, as already mentioned above, be inferred that the resonant frequency of the probe with the 0.025 in orifice is sufficiently large for the measurements since, in comparison with the tube with the larger orifice, no phase shift of the ensemble averaged total pressure could be detected.

Front shroud pressure measurements were made with the transducers flush-mounted.

The three-hole tube calibration and the three-hole tube performance will not be described herein but will be instead described in Chapter 3, in which the three-hole tube calibration and the three-hole tube measurements will be discussed.

#### 2.4. Instrumentation

Piezoelectric pressure transducers with built-in amplifiers from PCB Inc. were used for the unsteady pressure measurements. The Model 105B02 was used for all measurements. The transducer was selected because of its small size (diaphragm diameter: 0.1 in), high resonant frequency (250 kHz) and good resolution (0.01 psi). The stainless steel diaphragm permitted long time exposure to water. Because of the built-in amplifier, the transducer calibration is independent of the cable length

or the cable capacitance. Hence, the transducer could be used for impeller blade pressure measurements in the rotating impeller frame, with the transducer power supply located in the stationary laboratory frame. Because of the relatively short discharge time constant of the transducer of 1 sec, static calibration means could not be used. Instead, the dynamic calibration provided by the manufacturer was used. The linearity of the calibration was within 2%. A calibration curve and a list with the pressure transducer specifications is provided in the appendix.

Since the piezoelectric transducers measured only dynamic pressure, i.e., the pressure fluctuations about the time mean pressure, steady pressure measurements could not be made with those transducers. Instead, steady pressure measurements were obtained with mercury manometers. As reference pressure, the wall pressure at a pressure tap about 17 in upstream of the inducer blade leading edge of Impeller R was used (see figure 2.4). The experimental error on those measurements was estimated to be  $\pm 0.5\%$ . For impeller back flow observations, tufts were placed at different locations upstream of the inducer blade leading edge (these observations were made only for Impeller R). For flow coefficients  $\phi \geq 0.09$ , the region of impeller back flow did at most extend to about 2.5 in upstream of the inducer blade leading edge. Most of the tests were made for  $\phi = 0.15, 0.12$  and  $0.09$ . For those flow coefficients, the reference pressure was taken sufficiently far upstream of the inducer. For flow coefficients  $\phi \leq 0.06$ , however, impeller back flow extended beyond the tuft farthest away from the inducer ( $\approx 8$  in), and thus for very low flow coefficients, the reference pressure may not have been taken sufficiently far upstream to eliminate the possible influence of impeller back flow on the reference pressure.

The flow rates were measured with a 1250 GPM Potter turbine flow meter. Comparing the measurements obtained with the turbine flow meter to those obtained with an electromagnetic flow meter, it was found that the turbine flow meter was accurate for flow rates larger than 50 gpm.

A magnetic pick-up transducer in conjunction with an HP 5302 universal counter was used to find the rotational speed of a 64 tooth steel wheel mounted on the main shaft. The rotational speed was controlled by the motor control (open-

loop potentiometer). The shaft speed during a run was observed to fluctuate by at most  $\pm 1$  rpm. An optical encoder on the main shaft was used to provide an index pulse at every revolution for phase control and a clock, with 1024 cycles per revolution, for speed control.

## 2.5. Data Acquisition and Data Reduction

The data were sampled and discretized in a 16 channel data acquisition system and stored in the memory of a desktop computer. The main shaft encoder provided the data taker with a pulse index at every shaft revolution and a clock with 1024 clock pulses per revolution. The pulse index was used to trigger the data taker. Using one channel of the data acquisition system only, data were taken at every clock pulse for shaft speeds up to 1800 rpm, and at every other clock pulse for shaft speeds exceeding 1800 rpm. Hence, for shaft speeds up to 1800 rpm, 1024 data per impeller revolution were taken; for shaft speeds exceeding 1800 rpm, 512 data were taken. Both instantaneous and ensemble averaged data were stored.

During the last part of this research, a new data acquisition system was added. It consisted essentially of an integrated hardware and software package from RC Electronics, Santa Barbara, CA. It permitted taking a maximum of 64k instantaneous data at a maximum sampling rate of 1 MHz. Providing the trigger and the clock from the main shaft encoder, 1024 data per impeller revolution could be taken at speeds exceeding 1800 rpm. This new data acquisition system was used for most of the impeller blade pressure measurements.

The measurements will be presented, normalized by the dynamic pressure based on impeller tip speed,  $(1/2)\rho u_2^2$ . Since the unsteady measurements contained some noise they were ensemble averaged. In the remainder of this chapter, the data reduction procedure, i.e., the ensemble averaging and the superposition of unsteady and steady measurements, will be explained.

The steady pressure measurements are presented as a steady pressure coefficient

normalized by the dynamic head, based on impeller tip speed,

$$\bar{c}_p = \frac{(\bar{p}_v - \bar{p}_{up})}{(1/2)\rho u_2^2}. \quad (2.1)$$

The unsteady measurements are presented as an unsteady pressure coefficient, normalized by the dynamic pressure based on impeller tip speed,

$$\tilde{c}_p = \frac{\tilde{p}_v}{(1/2)\rho u_2^2}. \quad (2.2)$$

The unsteady measurements were ensemble averaged. The ensemble averaged unsteady pressure measurements are presented as an ensemble averaged pressure coefficient, and were obtained from the unsteady pressure coefficient by:

$$\tilde{c}_{p,av}(j) = \sum_{i=1}^N \frac{\tilde{c}_p(i,j)}{N}, \quad (2.3)$$

where  $i$  denotes the  $i$ th sampling period,  $j$  denotes the  $j$ th data point of the sampling period, and  $N$  denotes the total number of sampling periods. So in the process of ensemble averaging, an average is obtained for measurements made at identical orientations of impeller blades and diffuser vanes. The number of sampling periods used for the different measurements is given in Table 2.4.

**Table 2.4. Number of Sampling Periods for Ensemble Averaging.**

Type of Measurement	No. of Sampling Periods
Total Pressure	2048 (Imp. R), 512 (Imp. Z1)
Three Hole Tube	2048 (Imp. R), 512 (Imp. Z1)
Vane Pressure	2048 (Imp. R), 512 (Imp. Z1)
Blade Pressure	512 and 64 (Imp. Z2)

The large difference in the number of sampling periods used for the different measurements is directly related to the resonant frequency of the pressure tap used for a particular measurement, the shaft speed, and the radial gap between the impeller discharge and the pressure tap. For the impeller blade pressure measurements, that were made at shaft speeds from 1500 rpm to 2100 rpm and a radial

gap of 5% to 8% (of the impeller discharge radius) during one shaft revolution, 64 sampling periods were found to be sufficient to “average out” the high frequency noise. However, for the diffuser vane pressure measurements for Impeller R that were done for a radial gap of 1.5% and for shaft speeds up to 2400 rpm, 500–1000 sampling periods were needed to average out the high frequency noise.

The experimental error was found to be less than  $\pm 5\%$  for the magnitude and less than  $\pm 2$  degrees (360 degrees corresponding to one impeller blade passage) for the phase of the ensemble averaged unsteady pressure measurements.

Since the piezoelectric transducers measure pressure fluctuations about a time mean pressure value, the average of the ensemble averaged pressure fluctuations taken over the averaging period is zero.

$$\sum_{j=1}^M \frac{\tilde{c}_{p,av}(j)}{M} = 0, \quad (2.4)$$

where  $M$  is the number of measurements made per averaging period.

Therefore, the ensemble averaged pressure coefficient was obtained superimposing the ensemble averaged unsteady pressure coefficient to the steady vane pressure coefficient,

$$c_{p,av} = \bar{c}_p + \tilde{c}_{p,av}. \quad (2.5)$$

It is hereby assumed that the time mean value about which the piezoelectric pressure transducers measure the unsteady pressure is identical to the steady pressure obtained by the mercury manometer measurements.

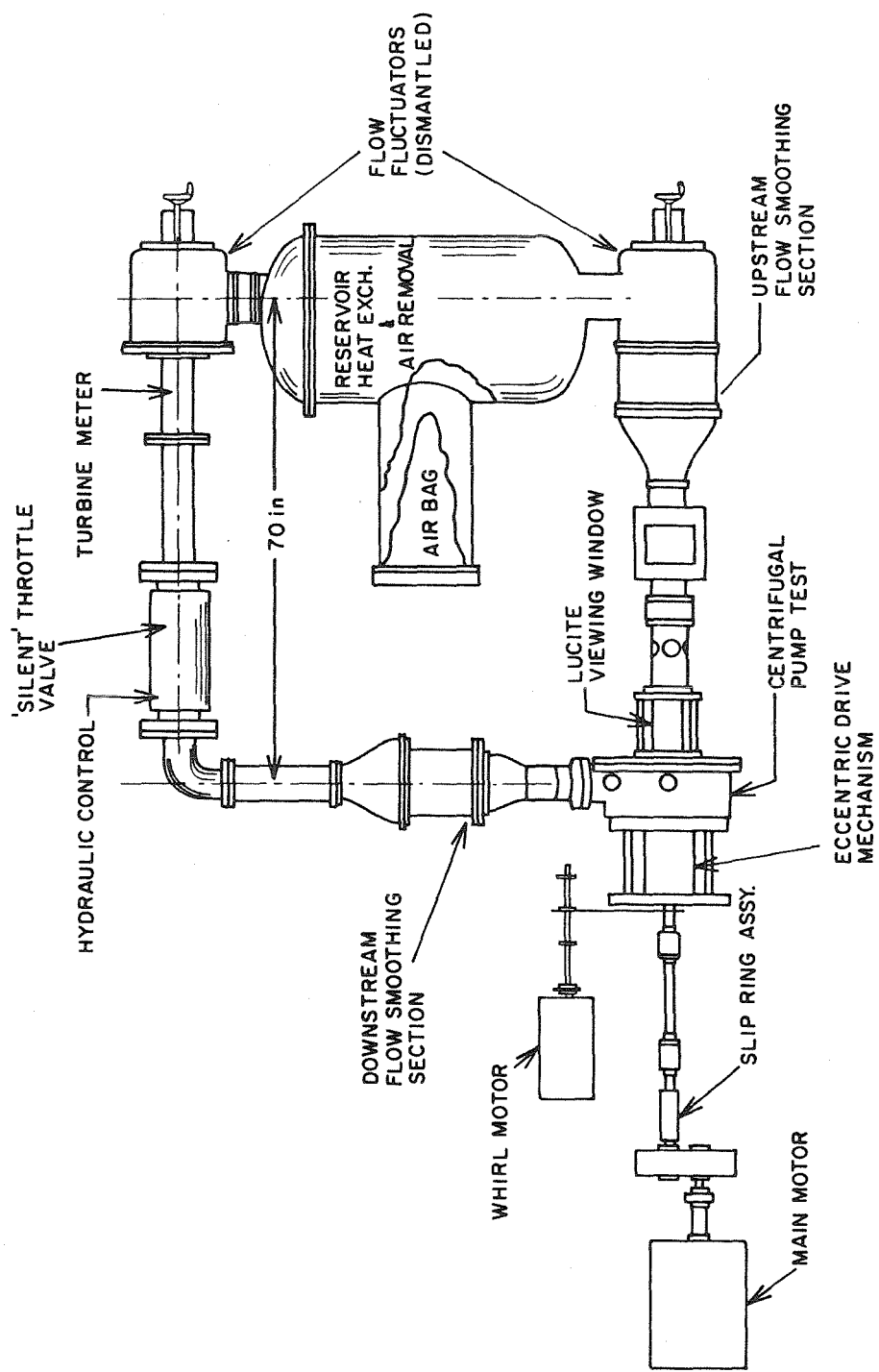


Fig. 2.1. Head view of the Rotor Force Test Facility.

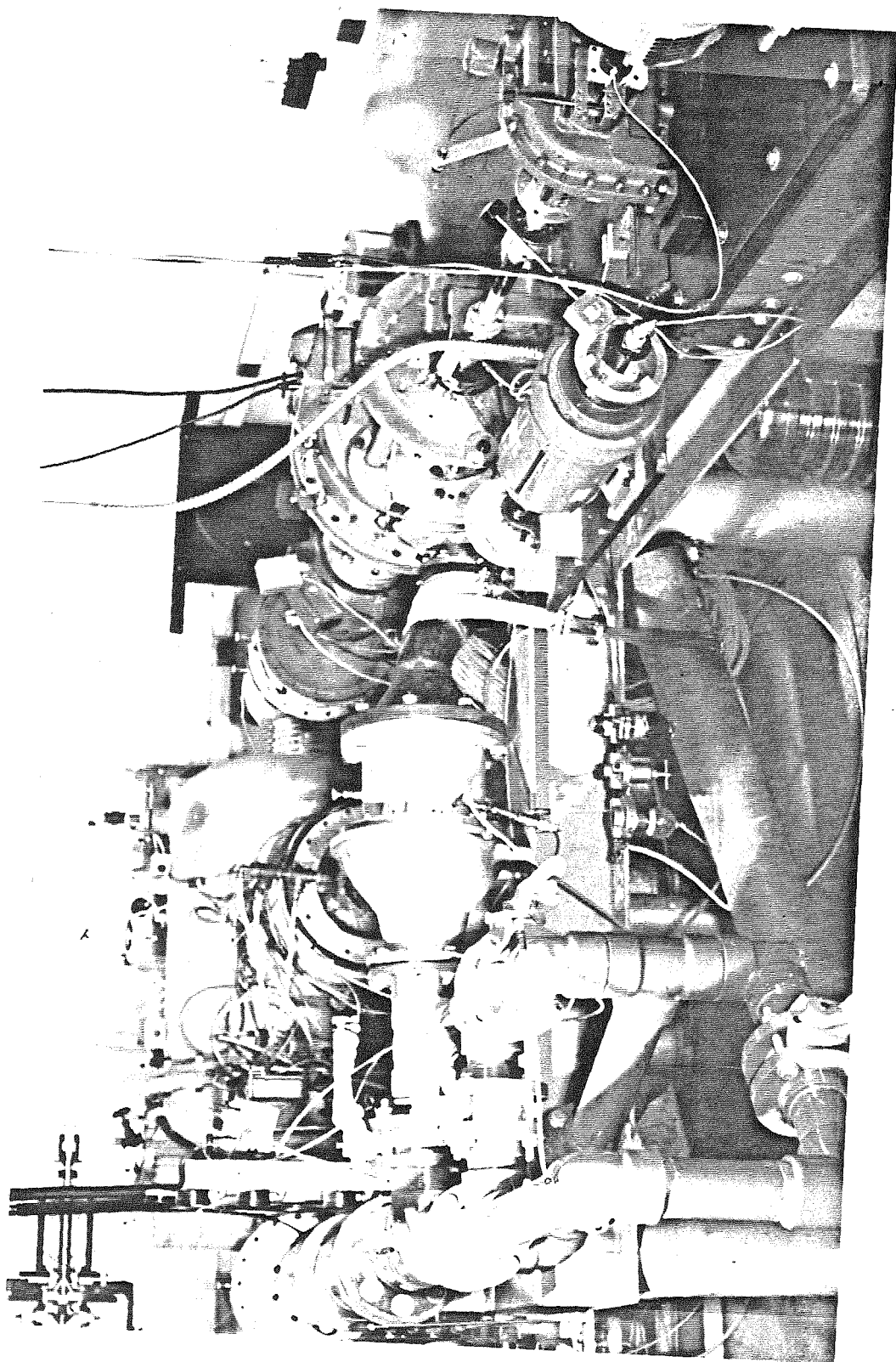


Fig. 2.2. Photograph of Rotor Force Test Facility.

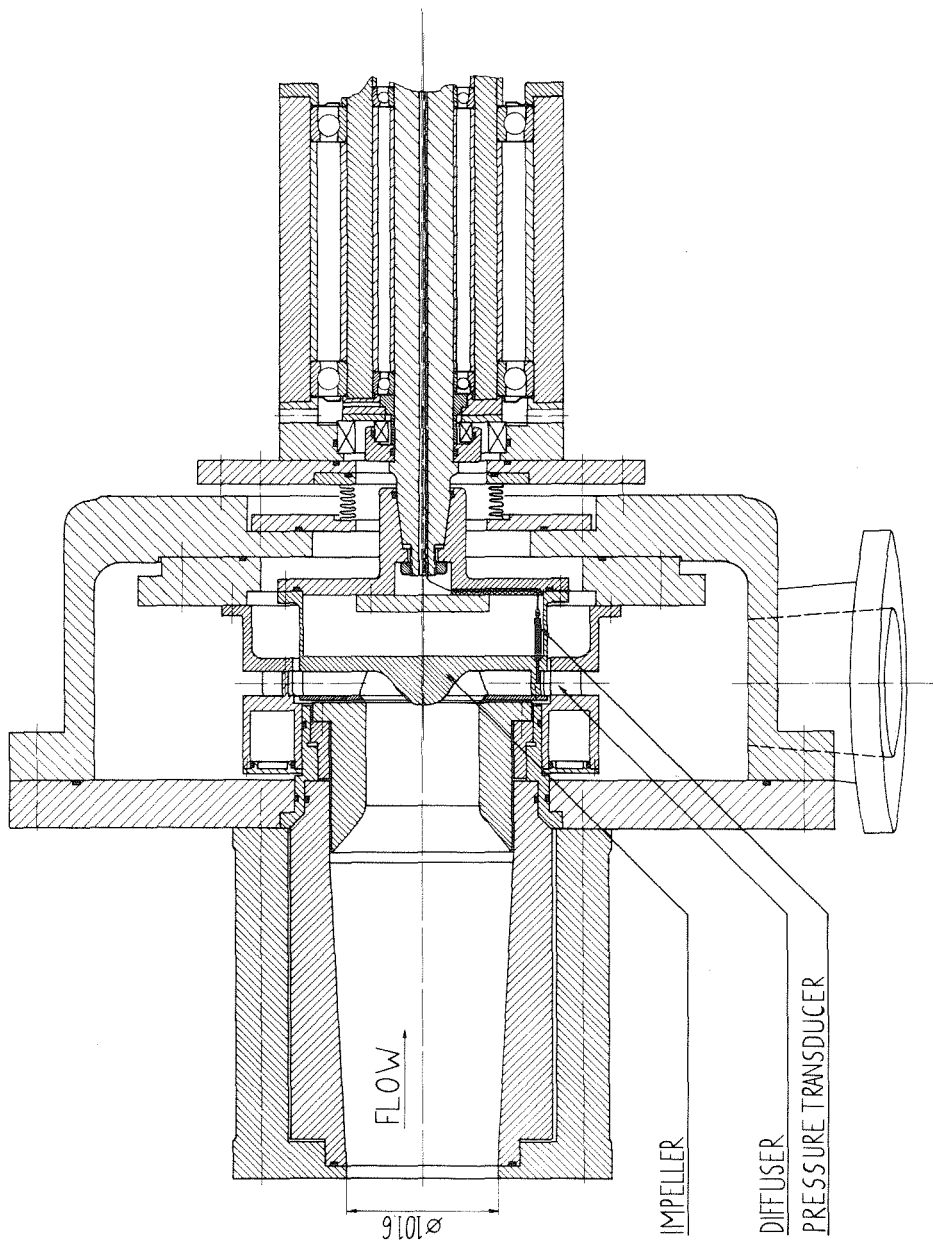


Fig. 2.3. Assembly drawing of the eccentric drive system and the test section with Impeller Z2 installed.

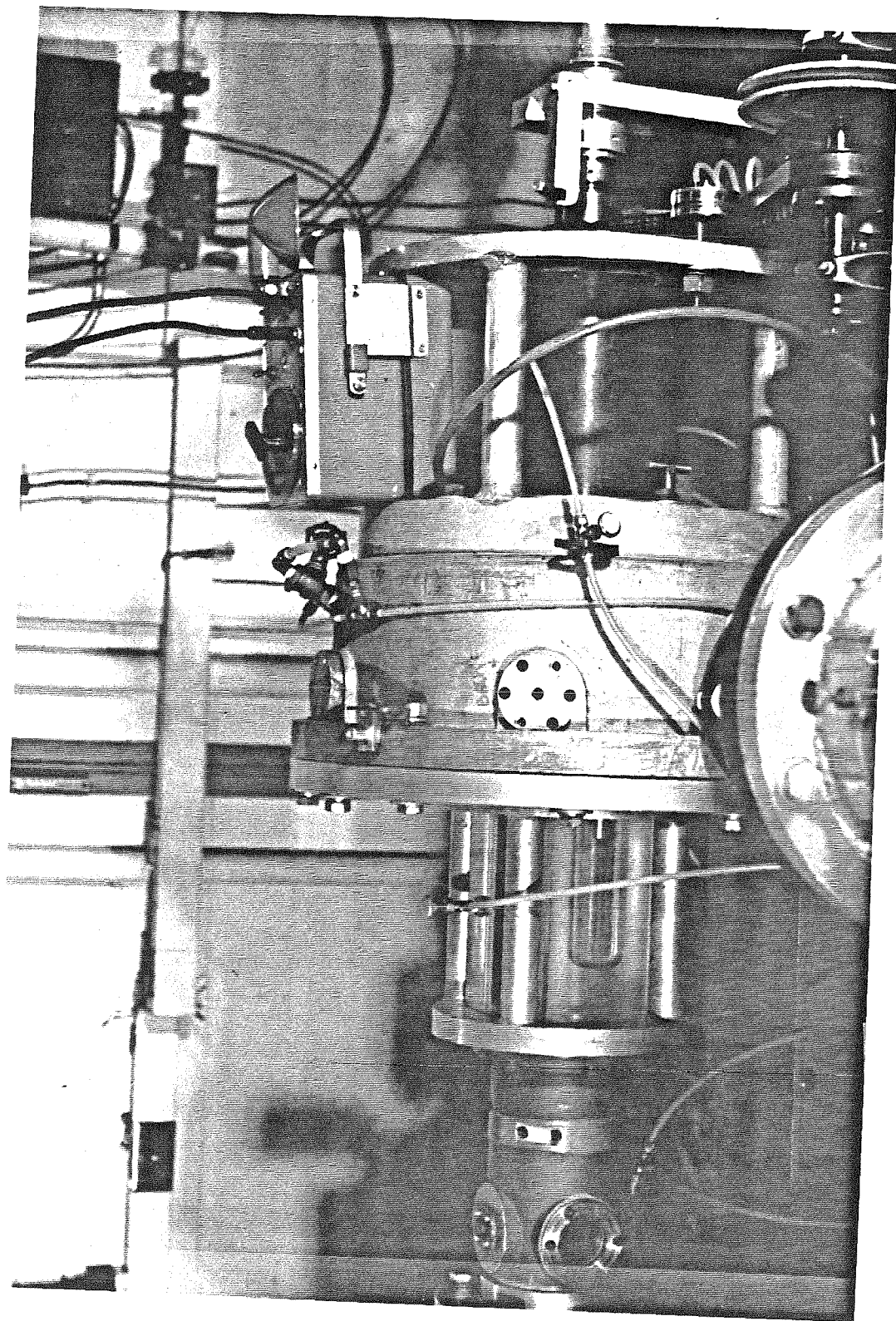


Fig. 2.4. Photograph of the test section of the RFTF.

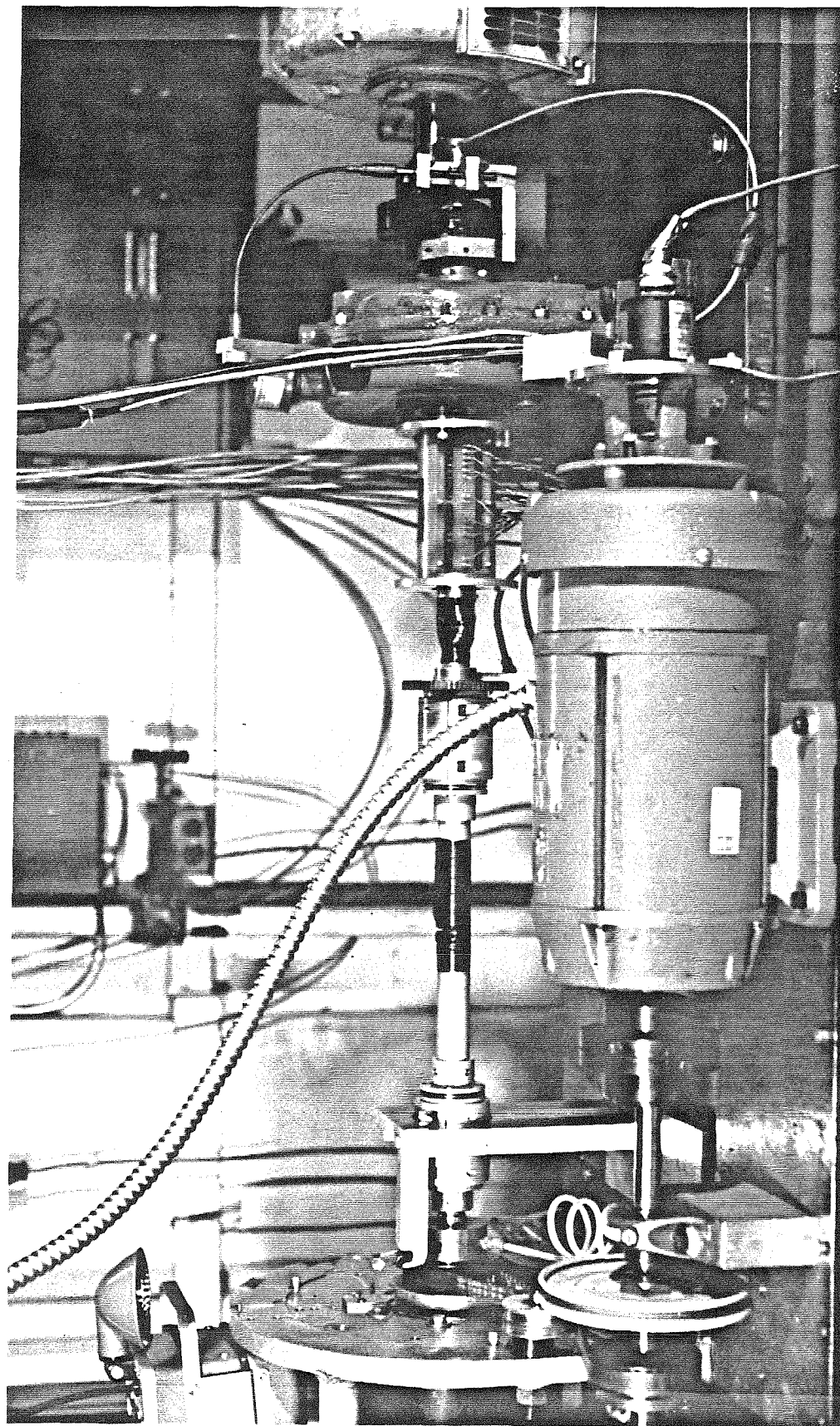
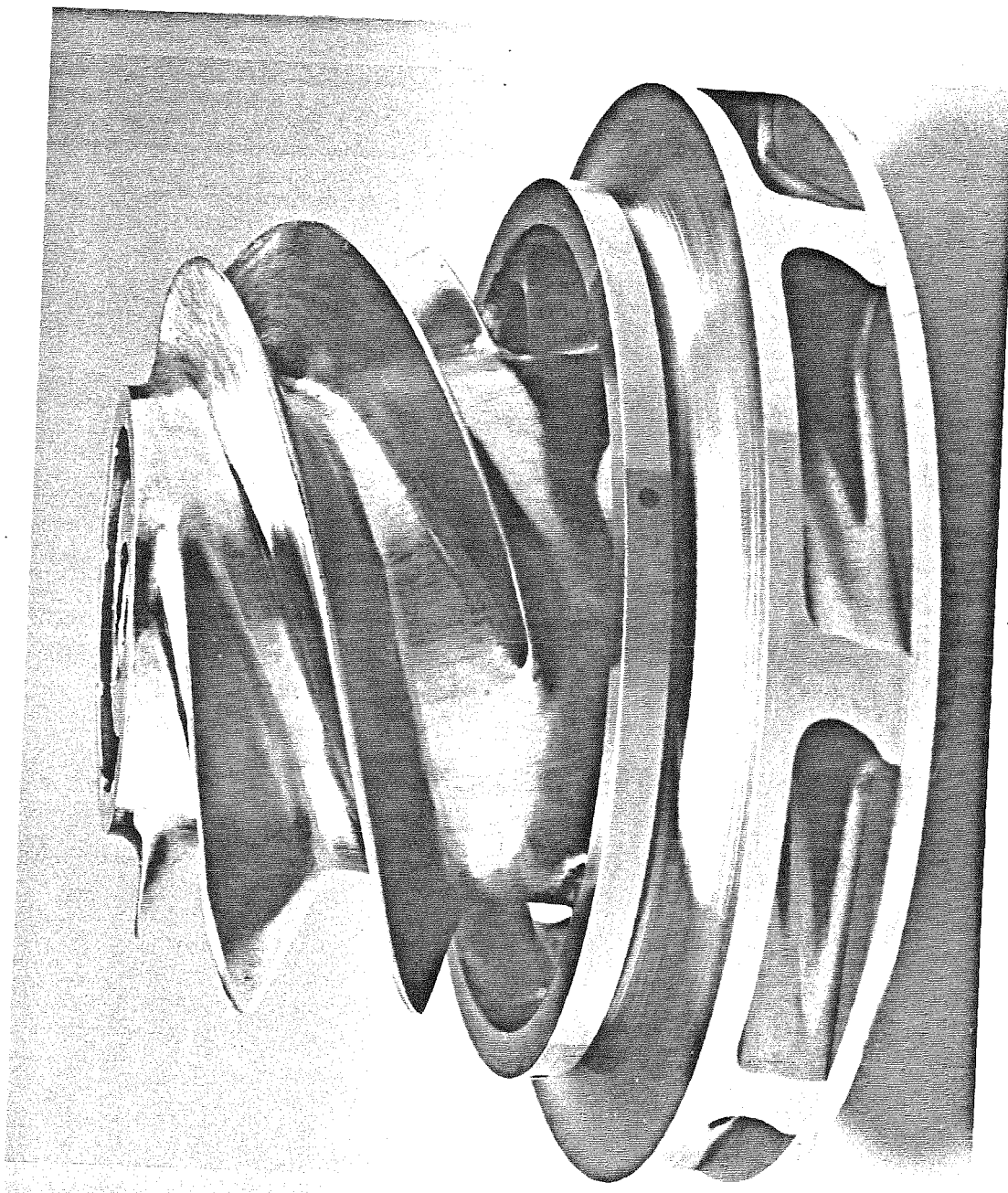


Fig. 2.5. Photograph showing the drive shaft, the slip ring assembly, and the drive shaft gear box.



**Fig. 2.6.** Photograph of Impeller R.

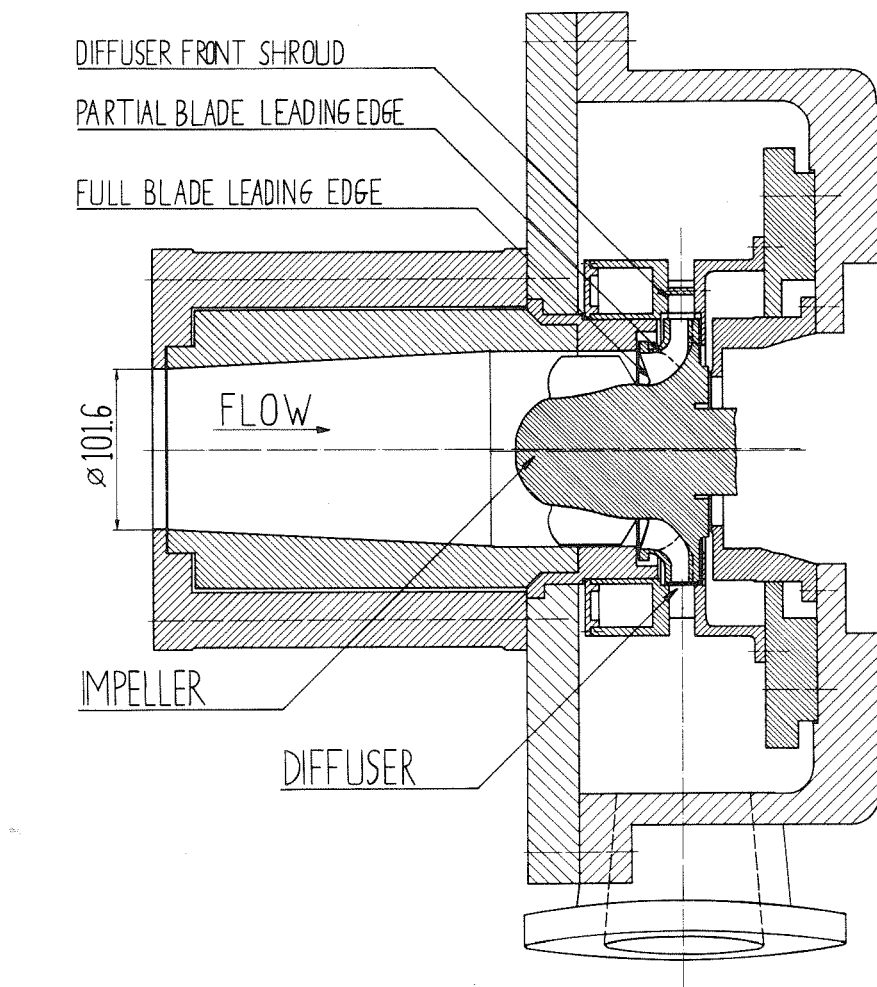
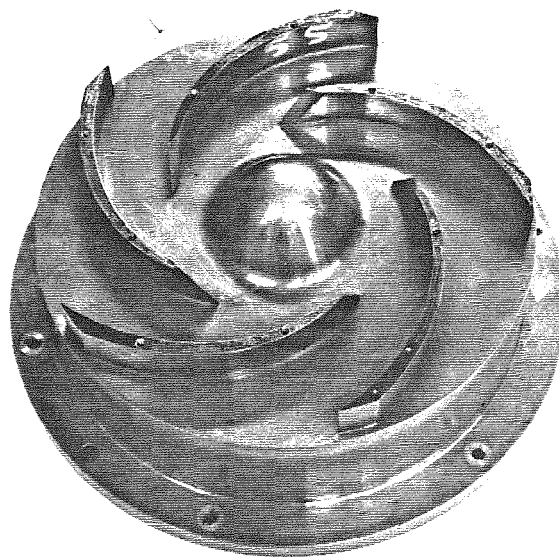


Fig. 2.7. Schematic assembly drawing of the test section with Impeller R installed.



**Fig. 2.8.** Photograph of Impeller Z2 (the front shroud of the impeller was removed to show the impeller blade shapes).

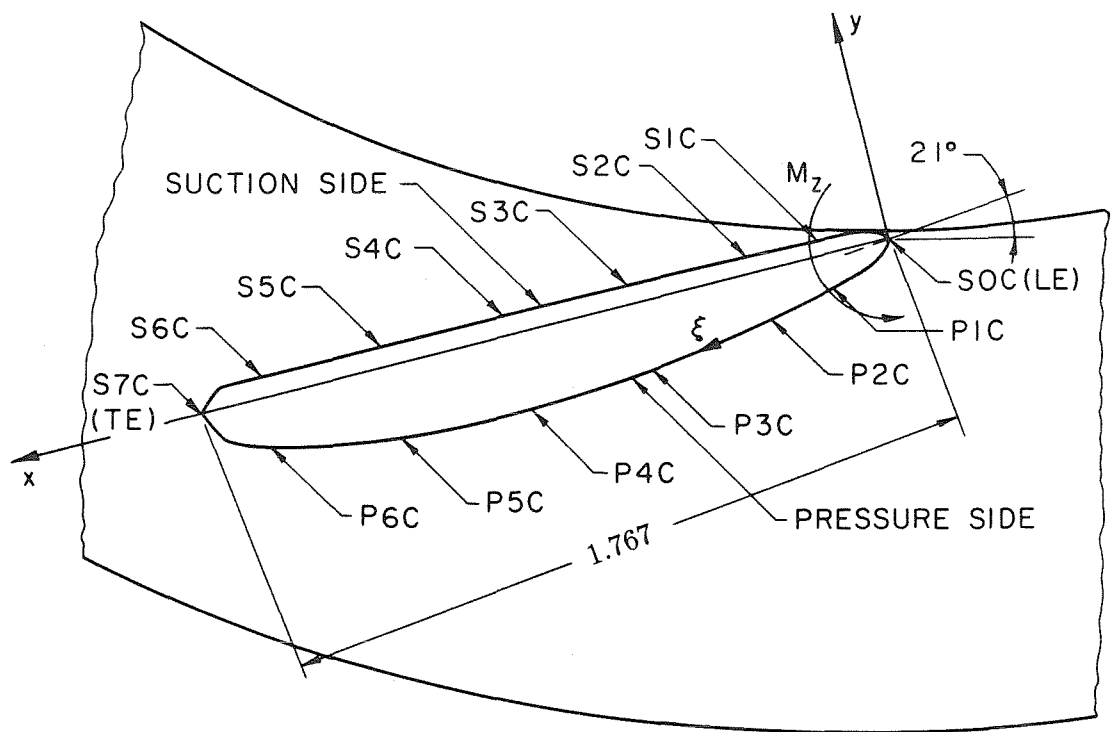


Fig. 2.9. Diffuser vane with pressure taps at mid vane height.

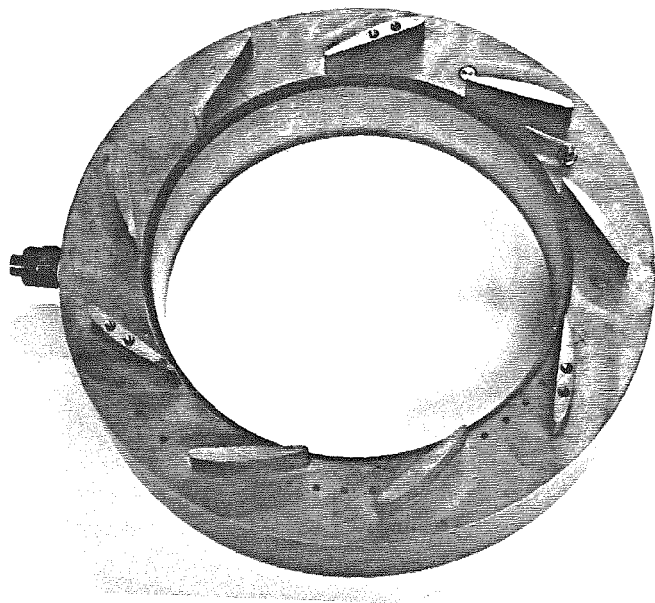


Fig. 2.10. Photograph of Diffuser S with the total pressure probe installed.

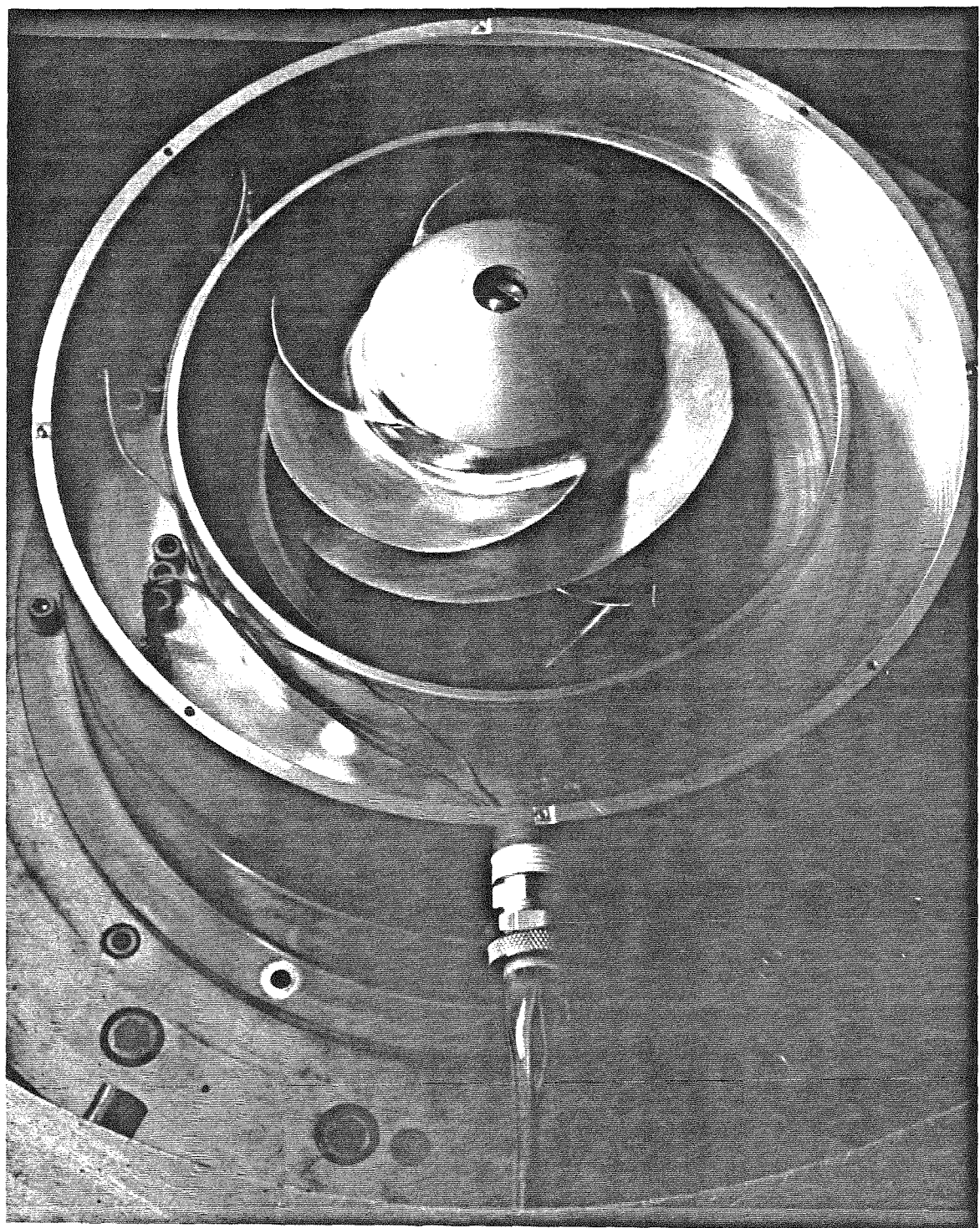


Fig. 2.11. Photograph of Impeller R and Diffuser S installed in the test section.

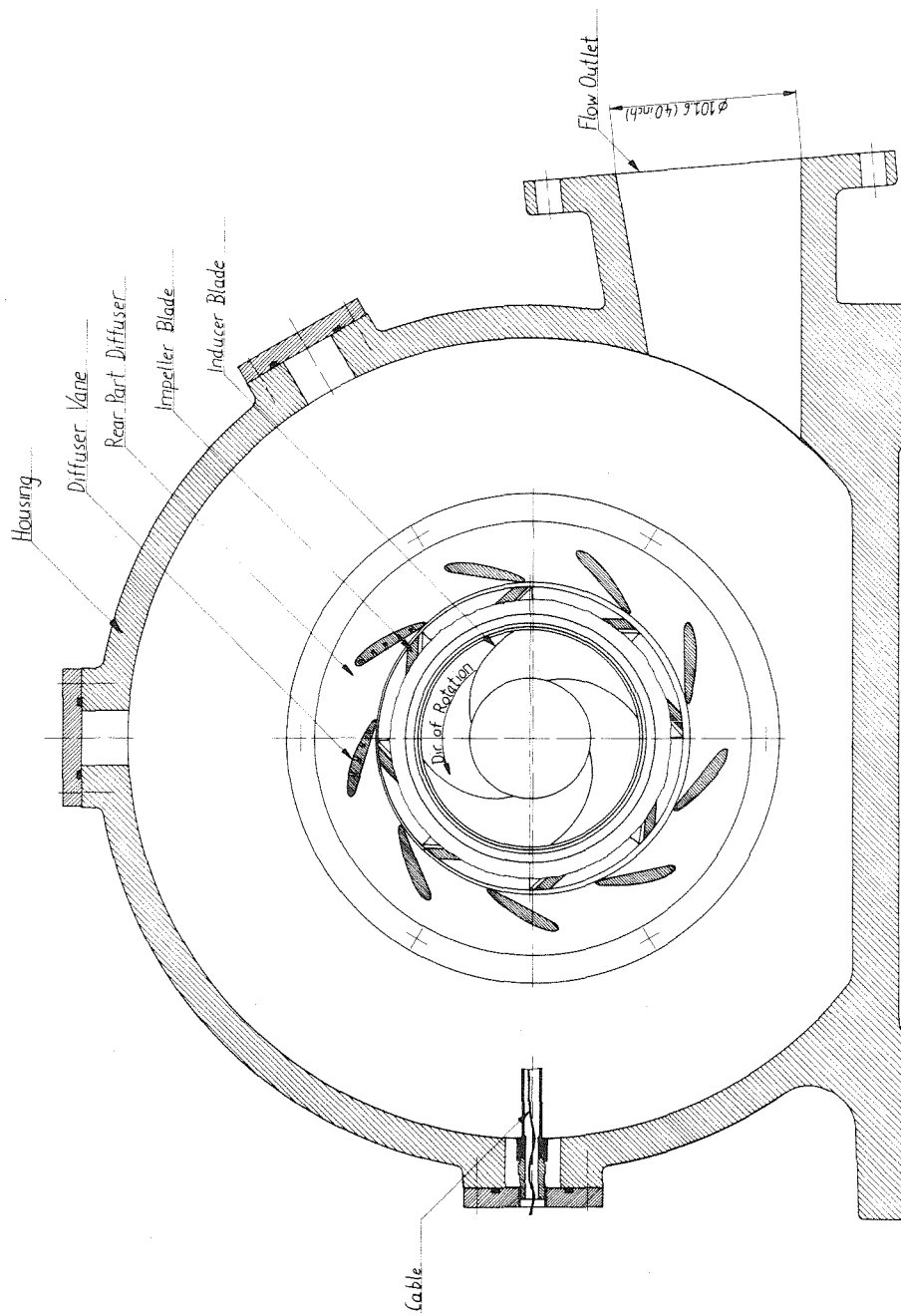
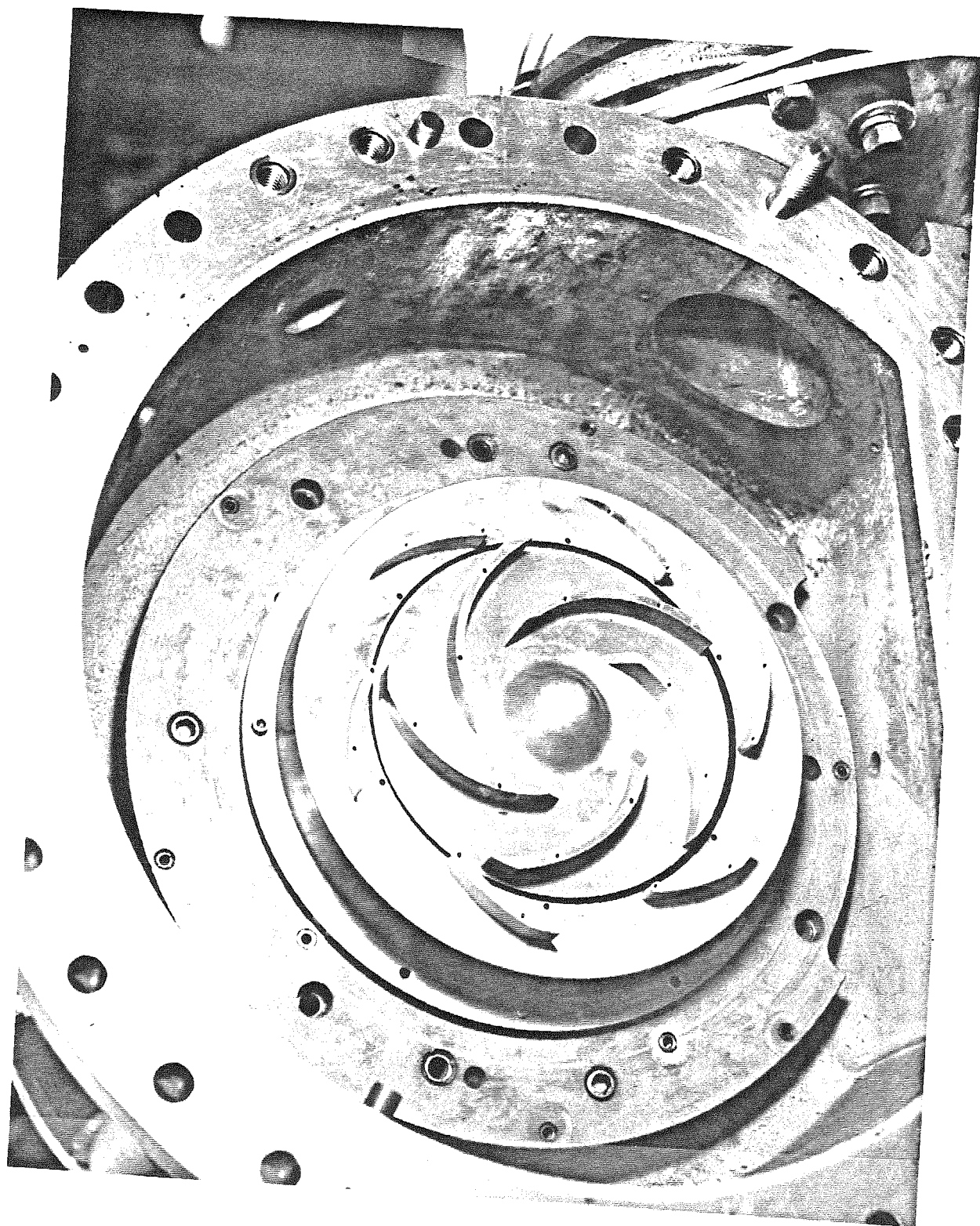
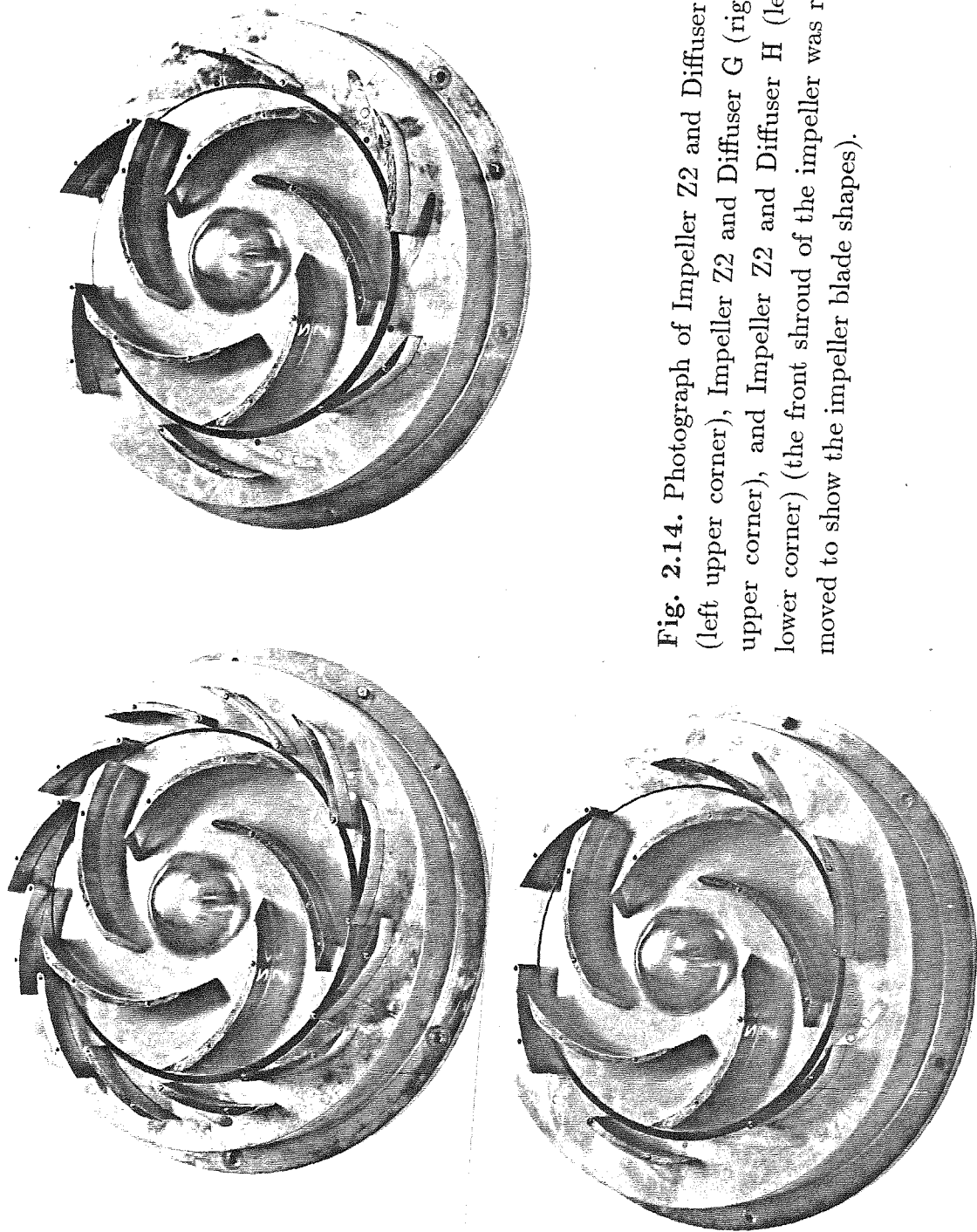


Fig. 2.12. Assembly drawing of Impeller R and Diffuser S installed in the test section.



**Fig. 2.13.** Photograph of Impeller Z2 and Diffuser G installed in the test section (the front shroud of the impeller was removed to show the impeller blade shapes).



**Fig. 2.14.** Photograph of Impeller Z2 and Diffuser F (left upper corner), Impeller Z2 and Diffuser G (right upper corner), and Impeller Z2 and Diffuser H (left lower corner) (the front shroud of the impeller was removed to show the impeller blade shapes).

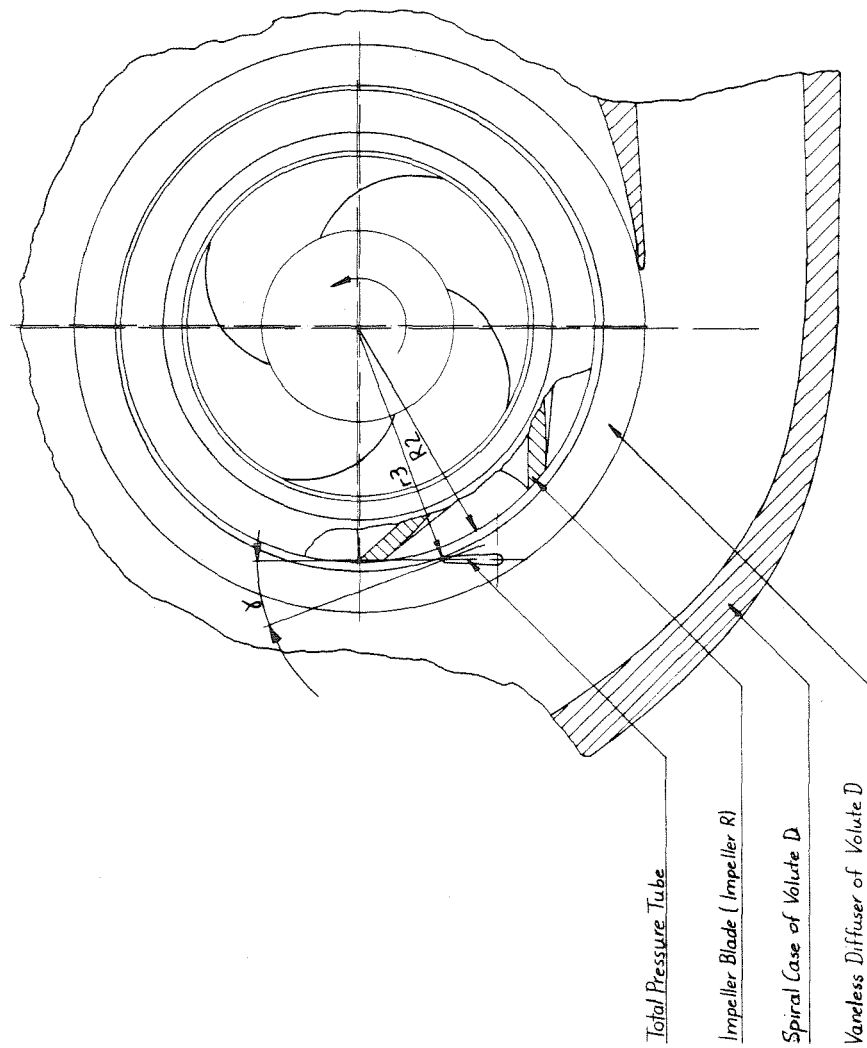


Fig. 2.15. Installation of the total pressure probe in Volute D.

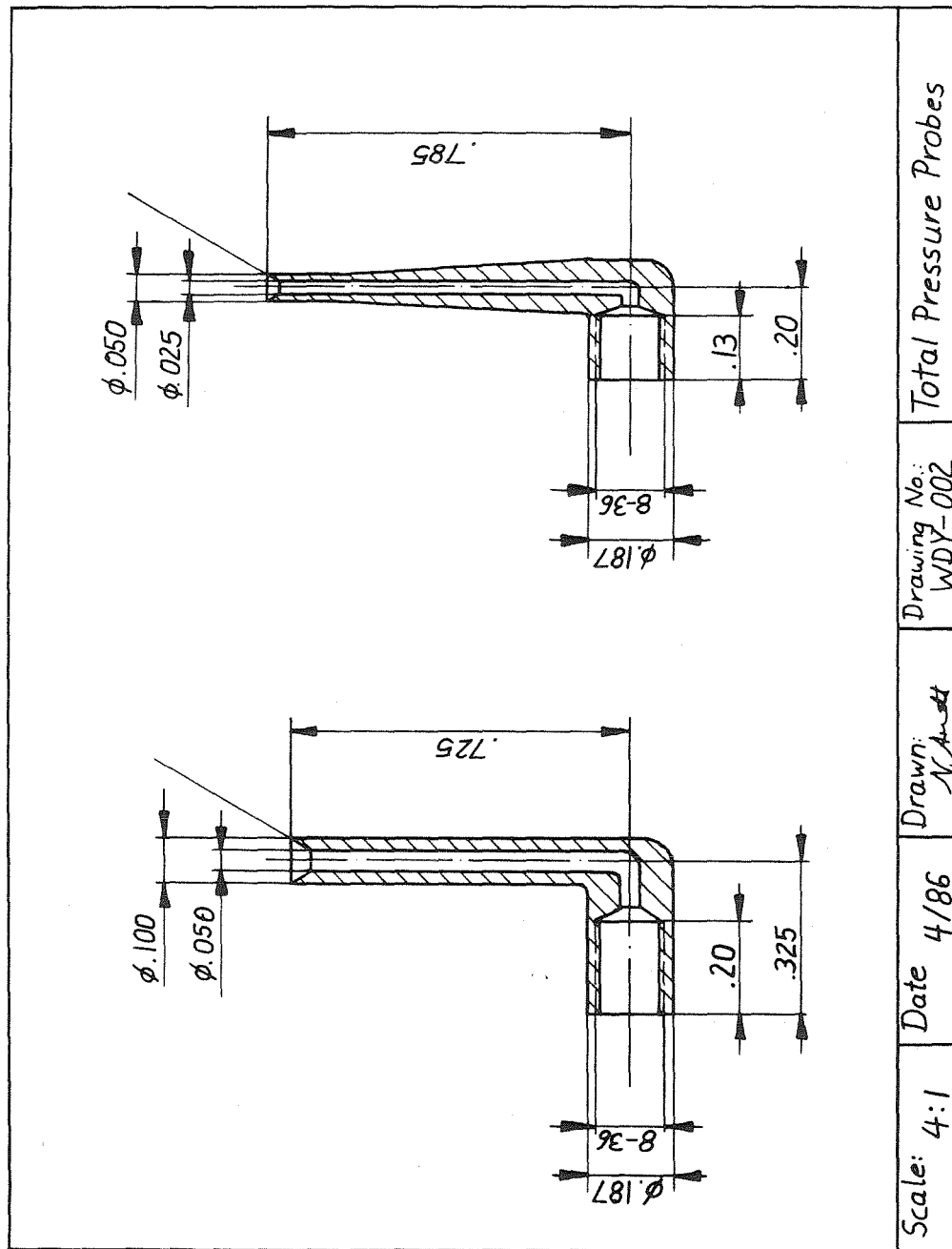


Fig. 2.16. Machine drawing of the total pressure probes.

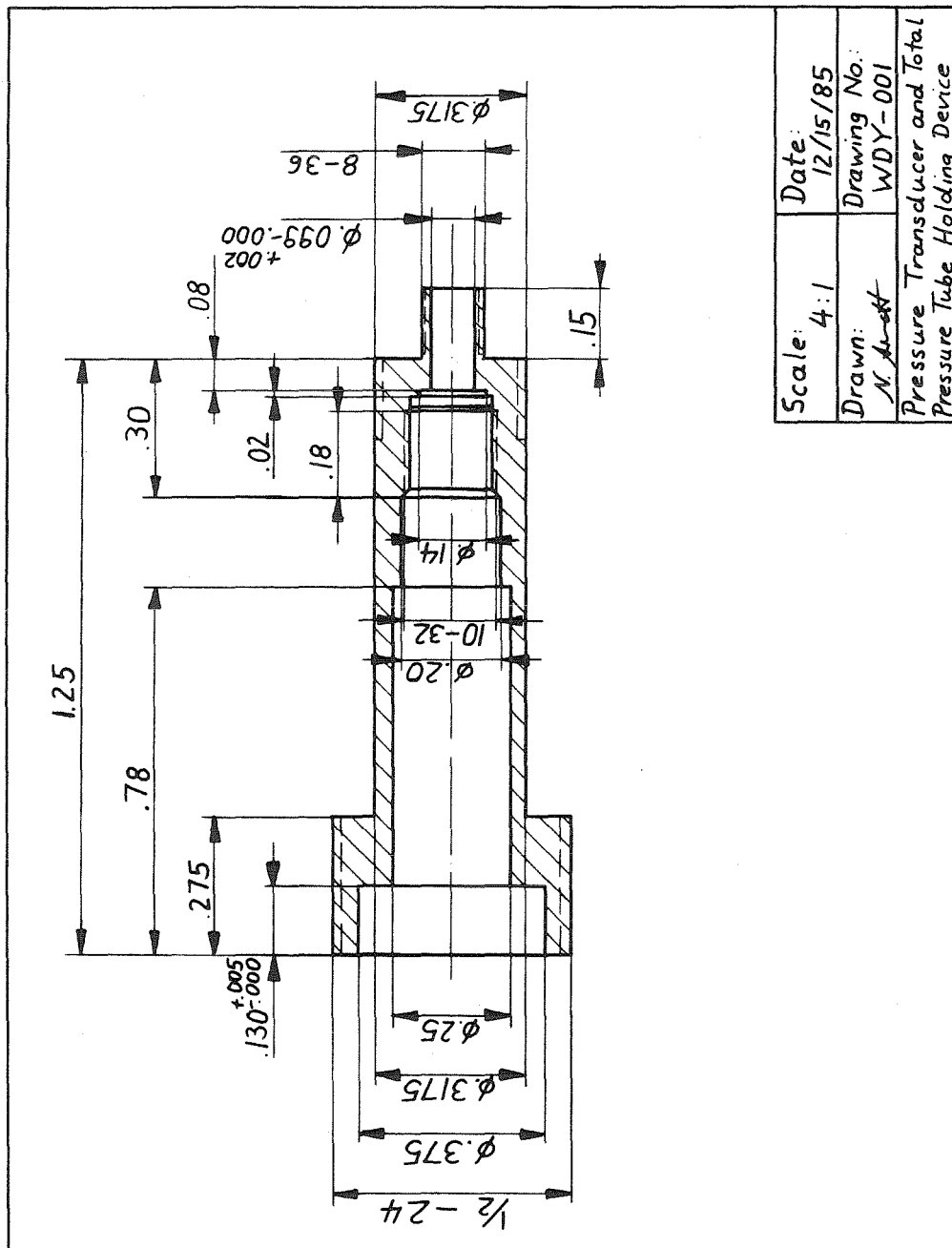
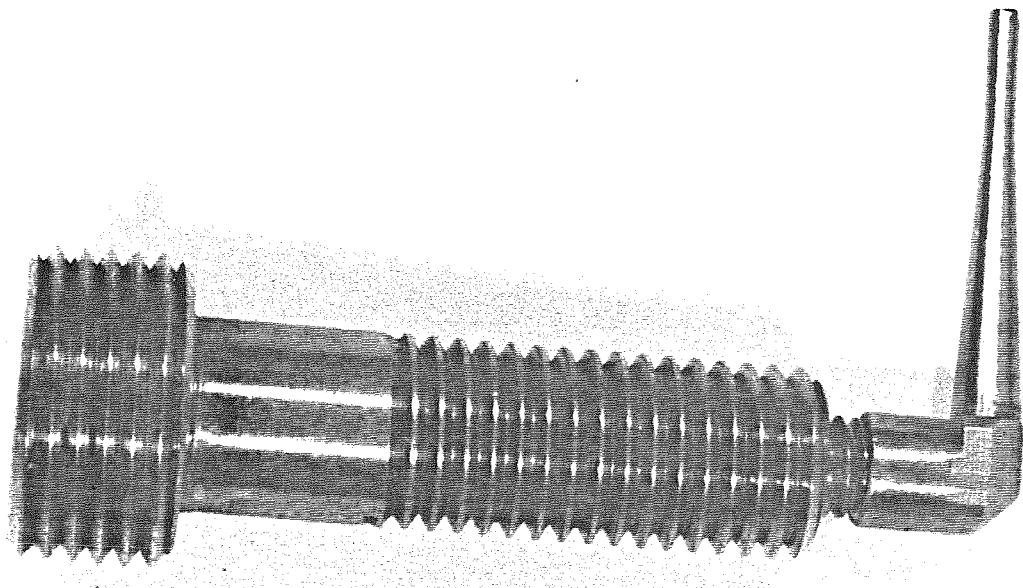


Fig. 2.17. Machine drawing of the total pressure probe holding device.



**0.5 inch**  
**12.7 mm**

**Fig. 2.18.** Photograph showing the total pressure probe mounted on the total pressure probe holding device.

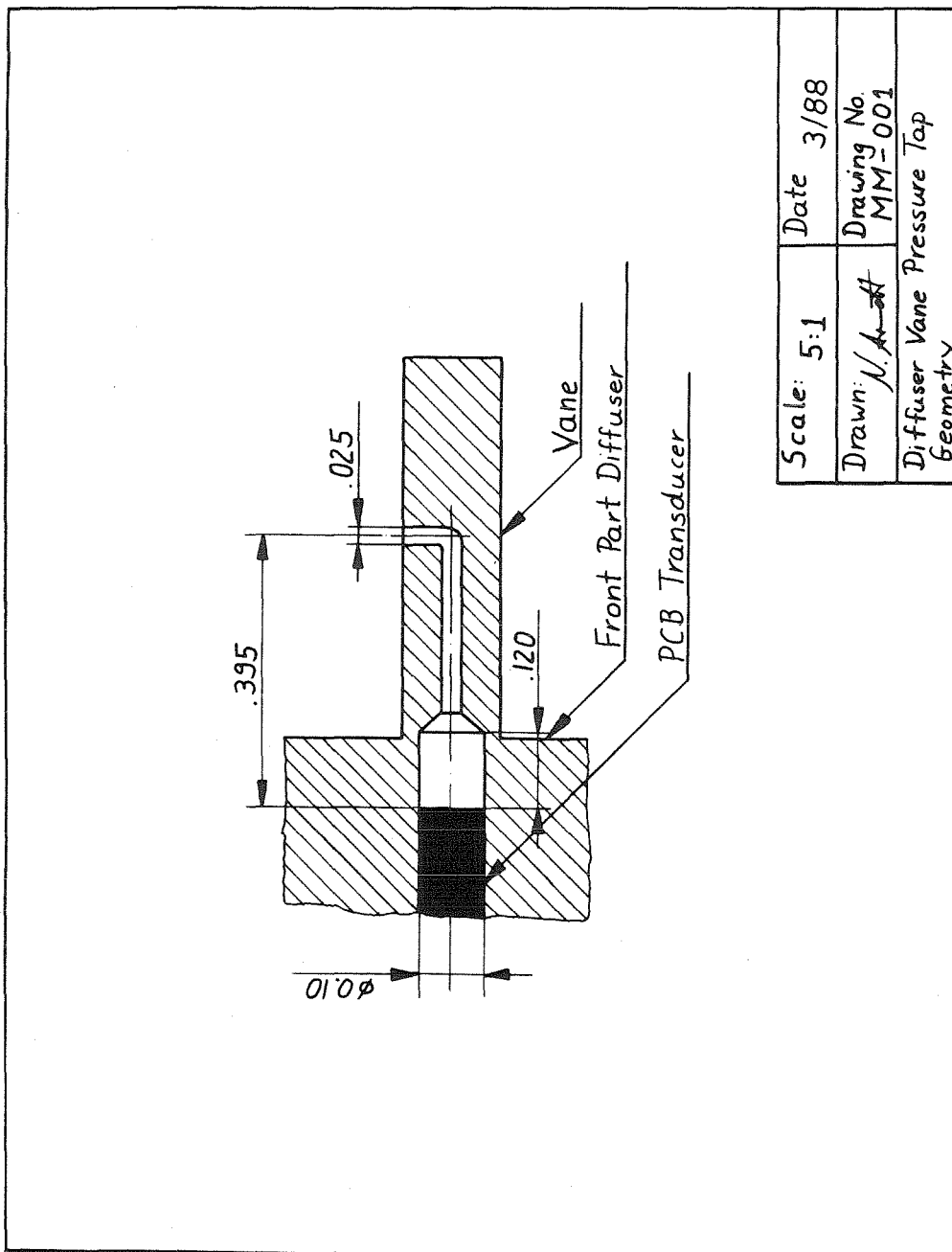


Fig. 2.19. Geometry of the vane (and blade) pressure tap.

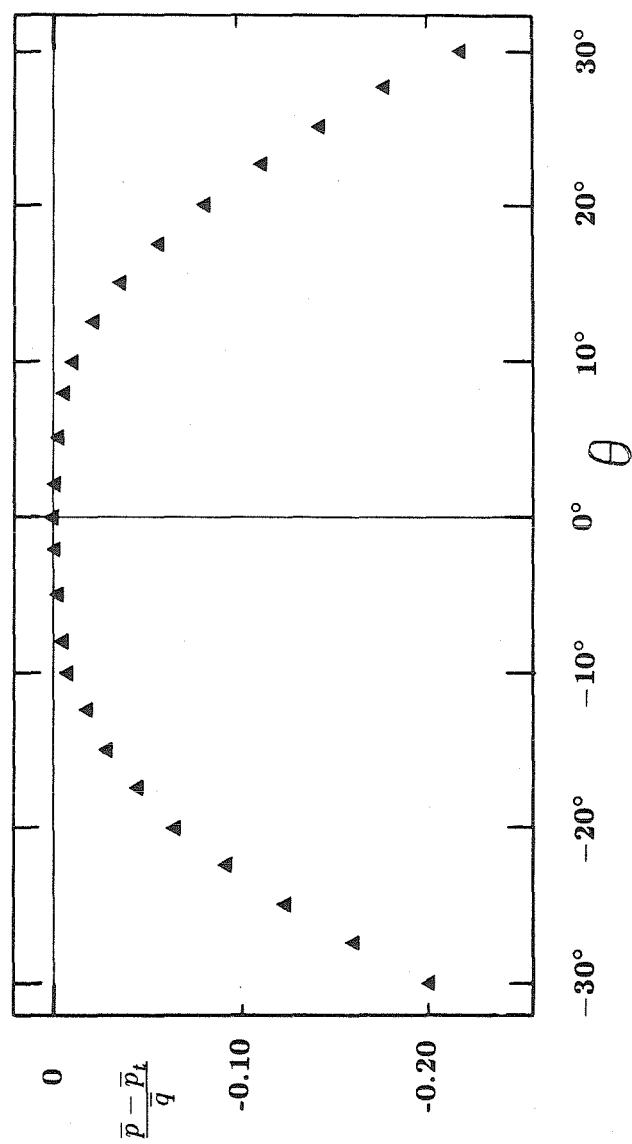


Fig. 2.20. Static calibration curve for the total pressure probe.

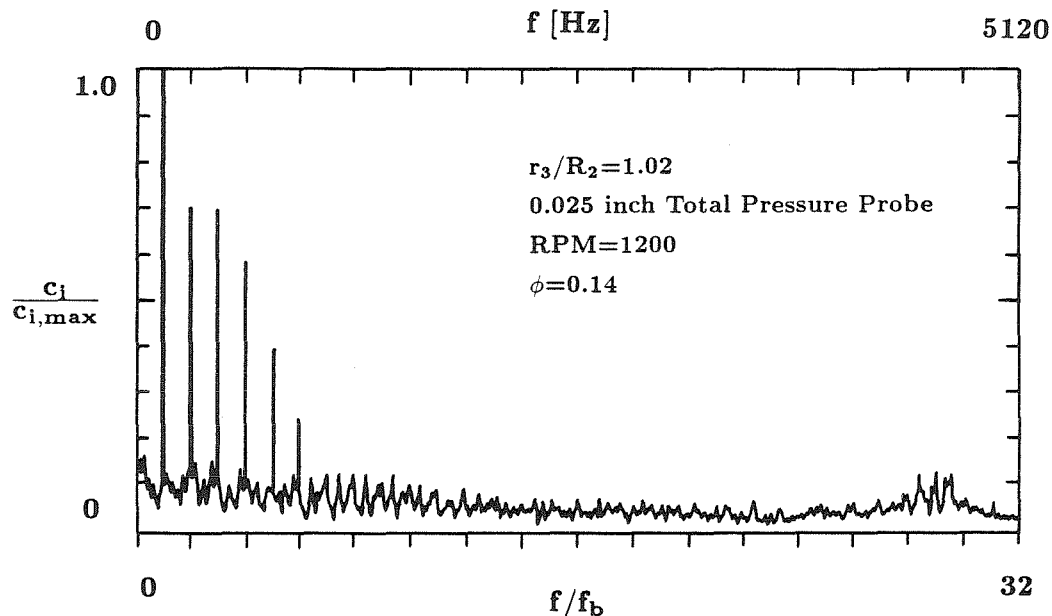


Fig. 2.21. Spectrum of unsteady total pressure measurements for Impeller R ( $\phi = 0.135$ ,  $r_3/R_2 = 1.02$ , rpm = 1200).

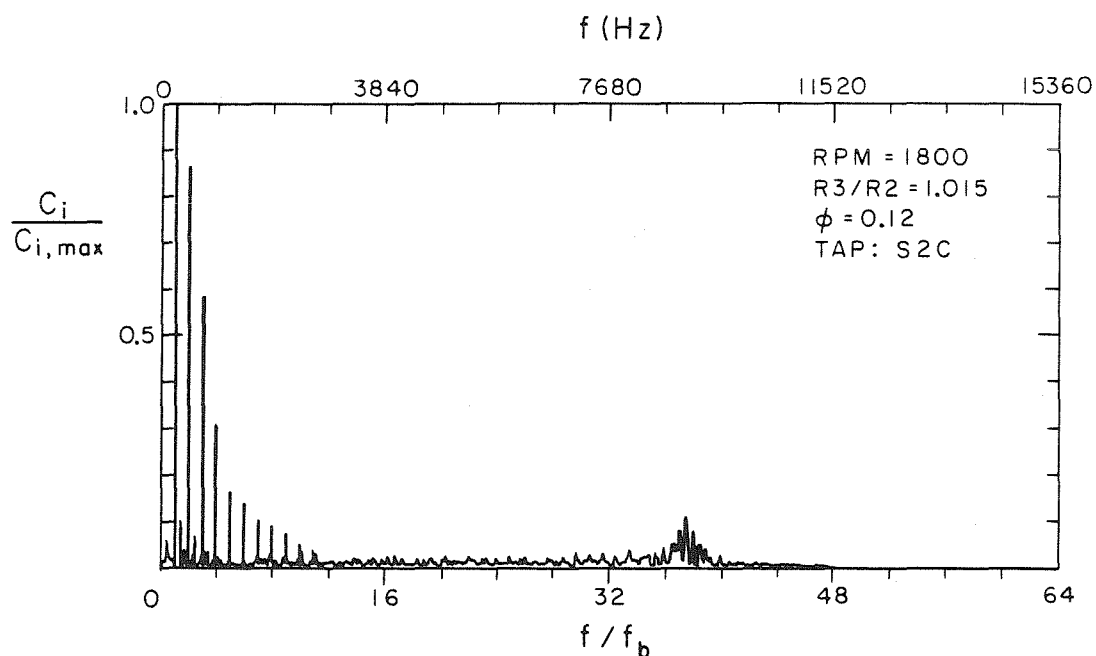
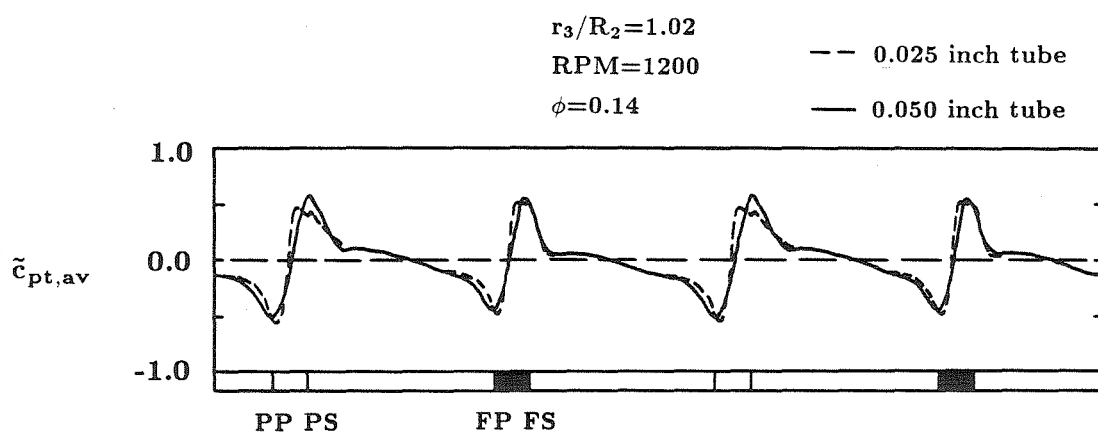


Fig. 2.22. Spectrum of unsteady diffuser vane pressure measurements for Impeller R and Diffuser S at pressure tap S2C ( $\phi = 0.12$ ,  $R_3/R_2 = 1.015$ , rpm = 1800).



**Fig. 2.23.** Ensemble average total pressure measurements for Impeller R with total pressure probes of different orifices, 0.025 and 0.050 inch. ( $\phi = 0.135, r_3/R_2 = 1.02, \text{ rpm} = 1200$ ).

## CHAPTER 3

### 3. Three-Hole Tube Measurements

#### 3.1 Three-Hole Tube Calibration

Total pressure measurements of the flow exiting centrifugal impellers were made, as mentioned previously, with a total pressure probe (those measurements will be discussed in Chapter 4). To measure other flow quantities, such as pressure, flow angle and dynamic pressure, a three-hole tube was designed and built for steady and unsteady measurements. The design of three-hole tubes for steady flow measurements is rather straightforward. For unsteady measurements, however, issues such as probe size, frequency response and mounting of the pressure transducers have to be considered. The probe size should be small compared to the length scale of the typical unsteadiness. For flows with large gradients in total pressure, that may be a requirement difficult to meet. To keep the frequency response of the "hydraulic line" from the probe head to the transducer high, the length of that line should be as short as possible. Furthermore, the effects of unsteady flow around the probe head are an important design consideration. If the probe head is spherical, the pressure around the probe head can be considered to consist of two terms (Kovasznay et al. 1981): one being proportional to the instantaneous dynamic pressure,  $1/2 \rho u^2$ , the other being proportional to the product of the sphere diameter and the time derivative of velocity,  $\rho D(du/dt)$ . If  $D$  is the sphere diameter,  $\rho$  the density,  $u$  the velocity,  $p$  the static pressure, and  $p_t$  the stagnation pressure, then

$$\frac{(p - p_t)}{\rho} = A \frac{u^2}{2} + BD \frac{du}{dt}. \quad (3.1)$$

The importance of the  $(du/dt)$  term is dependent on the relative magnitude of the coefficients  $A$  and  $B$ , both of which are dependent on the angular position around the sphere. Kovasznay et al. reported (1981) that at an angle of  $\approx 45^\circ$ , measured from the stagnation point of the steady flow on the sphere, the coefficient of the

derivative term, B, is nearly zero at 45 degrees. Thus, location of the side holes at this point will minimize dynamic effects. Therefore, the three-hole tube was designed with the side holes located on surfaces that intersect the surface on which the center hole is located at an angle of 45 degrees.

The three-hole tube design is shown in figures 3.1 and 3.2. The three leads are steel tubes with an outer diameter of .035 inch and an inner diameter of .023 inch, such that the total width,  $d_{th}$ , is .105 inch. The resonant frequency of the "hydraulic line" (or pressure tap) was calculated to be approximately 4000 Hz, which was considered sufficiently high for the measurements. The three-hole tube was permanently connected to a pressure transducer holding device, which could be installed in Diffuser T. The probe head of the three-hole tube was located at the mid channel height of Diffuser T. The alignment angle,  $\gamma$ , of the three-hole tube in the diffuser was 20 degrees. The alignment angle is defined as the angle between the centerline of the three-hole tube and the tangent to the circular orbit, centered at the center of the impeller rotation, through the center of the center hole of the three-hole tube. In figure 3a, a photograph is presented showing the three-hole tube with the PCB pressure transducers installed. The next figure, figure 3b, shows the three-hole tube installed in Diffuser T. In figures 3a and 3b, the left and the right hole of the three-hole tube are cut back by about one lead tube diameter (0.035 in). This was done after the measurements presented herein were made, i.e., the measurements presented herein were made for the probe head geometry shown in figure 3.1 and not for the probe head geometry shown in the photographs in figures 3a and 3b.

The steady calibration of the three-hole tube was made in an air jet (see figure 3.4). No dynamic calibration was made. A compressor discharges air into a large reservoir, from which the air leaves through a venturi nozzle. The nozzle diameter, 1.1 in, was sufficiently large to provide uniform flow around the three-hole tube for the calibration. The velocity of the discharged air can be regulated by partially closing the air inlet duct to the compressor, as well as by opening a second discharge from the reservoir. A honeycomb was placed at the inlet of the venturi nozzle for

flow smoothing purposes. Total pressure and dynamic pressure of the air at discharge were measured with a Prandtl-probe, using a water manometer permitting highly accurate readings. As reference pressure, the pressure in the reservoir was selected (see figure 3.4). Assuming first that the flow is incompressible and secondly that the flow leaves the venturi nozzle without any swirling velocity, the measurements with the Prandtl-probe determine the flow quantities of the jet at discharge, and are hence sufficient for the calibration of the three hole tube. The largest air speed attainable at the nozzle discharge was 124 ft/sec, measured with a Prandtl-probe. An important item of the calibration was similarity. The experiment in the test loop was conducted with water, and hence the flow was incompressible. For the air jet, the Ma number of the flow at nozzle discharge was about .11 for maximum velocity, approximately 124 ft/sec, such that the compressibility effects were considered negligible. The Reynolds number of the three-hole tube, based on three-hole tube width,

$$Re = \frac{d_{th}u}{\nu} \quad (3.2)$$

(where  $d_{th}$  is the three-hole tube width,  $u$  the velocity of the flow at the nozzle exit, and  $\nu$  the kinematic viscosity) was approximately 8000 for the three-hole tube in the air-jet, and approximately 27000 for the three-hole tube in the test loop experiment. As characteristic velocity in the test loop experiment, the impeller tip speed was chosen. Since the absolute velocity of the flow at the impeller discharge is, very approximately and depending upon flow coefficient, about half as large as the impeller tip speed, the Reynolds numbers for both calibration and test loop experiment were considered sufficiently close.

For calibrating purposes, the three hole tube was placed 1/8 in inside the nozzle and was turned from a position perpendicular to the nozzle plane up to 30 degrees to either side. During calibration, the three-hole tube was fastened such that the three-hole tube tip remained at the same position in the nozzle, independent of the turning angle. The pressure readings of the left, center, and right hole were measured, referenced to reservoir pressure, every two degrees. These curves,  $p_r - p_{res}$

vs.  $\theta$ ,  $p_c - p_{res}$  vs.  $\theta$ , and  $p_l - p_{res}$  vs.  $\theta$ , where  $\theta$  is the misalignment angle between the three-hole tube and the flow direction, are shown in figures 3.5–3.7. It can be seen that for the left and the right tap the pressure measurements are monotonic, whereas for the center hole they are similar to the calibration curve of the total pressure probe (figure 2.20).

For each angle  $\theta$  at which pressure measurements for the calibration were made, three calibration coefficients were defined, based on the pressure measurements obtained by the three-hole tube and the dynamic pressure and the total pressure measurements obtained with the Prandtl probe. The three calibration coefficients were defined by,

$$K_\theta = \frac{(p_l - p_{res}) - (p_r - p_{res})}{(p_c - p_{res}) - (1/2)((p_l - p_{res}) + (p_r - p_{res}))} \quad (3.3a)$$

$$= \frac{p_l - p_r}{p_c - (1/2)(p_l + p_r)} \quad (3.3b)$$

$$K_q = \frac{(p_c - p_{res}) - (1/2)((p_l - p_{res}) + (p_r - p_{res}))}{q} \quad (3.4a)$$

$$= \frac{p_c - (1/2)(p_l + p_r)}{q} \quad (3.4b)$$

$$K_T = \frac{(p_c - p_{res}) - (p_t - p_{res})}{q} \quad (3.5a)$$

$$= \frac{p_c - p_t}{q}. \quad (3.5b)$$

To obtain flow angle, total pressure and dynamic pressure from the three hole tube measurements, three calibration curves were defined:  $\theta$  vs.  $K_\theta$  (figure 3.8),  $K_q$  vs.  $K_\theta$  (figure 3.9), and  $K_T$  vs.  $K_\theta$  (figure 3.10). The calibration curves are then used the following way: During an experiment, pressures are measured at the right, center and left three-hole tube pressure taps, referenced to a common reservoir pressure, usually the wall pressure upstream of the pump. From  $p_r - p_{res}$ ,  $p_c - p_{res}$ , and  $p_l - p_{res}$ , the coefficient  $K_\theta$  is computed, from which by linear interpolation the flow angle  $\theta$  is obtained. Similarly,  $K_q$  and  $K_T$  are obtained by linear interpolation. Next, the dynamic pressure,  $q$ , and the total pressure,  $p_t$ , are

computed from

$$q = \frac{p_c - (1/2)(p_l - p_r)}{K_q} \quad (3.6)$$

$$p_t = p_c - K_T q. \quad (3.7)$$

Since the flow was considered incompressible, the pressure,  $p$ , and the two velocity components in the measurement plane could be obtained from  $p_t$ ,  $q$  and  $\theta$ .

It can be seen that the relationship between  $K_\theta$  and  $\theta$  is approximately linear. Furthermore, permitting an error of  $\pm 3\%$ ,  $K_q$  is constant over a wide range of  $K_\theta$  (corresponding to a range of  $\pm 20$  degrees) such that in that range the dynamic pressure,  $q$ , is approximately a linear function of  $p_c$ ,  $p_r$ , and  $p_l$ . Similarly, permitting an error of  $\pm 2.5\%$ ,  $K_T$  can be set constant in a range of  $\pm 15$  degrees from zero incidence angle, so that in that range

$$p_t = p_c + 0.0125p_c - (1/2)0.0125(p_r + p_l) \quad (3.8a)$$

(having used the previous approximation for  $K_q$ ). Noting that  $(1/2)(p_r + p_l)$  is  $0(p_c)$ , equation(3.8a) can be approximated by

$$p_t = p_c. \quad (3.8b)$$

introducing an additional error of less than 1%. Hence, as expected, the center hole gives a good total pressure reading for not too large an incidence angle. The calibration error was found to be less than 1% for the dynamic head and less than 0.2 degree for the flow angle.

### 3.2. Steady Three-Hole Tube Measurements

Steady three-hole tube measurements were made for the flow discharging from Impeller R and Impeller Z1 into Diffuser T, a vaneless straight wall constant width diffuser. The three hole tube was located at mid channel height of the diffuser and was aligned with an angle of 20 degrees (see figure 3.3b).

The measurements were made with mercury manometers. As reference pressure, the wall pressure about 17 in upstream of the respective impeller inlet was chosen. For Impeller R, measurements were made for four flow coefficients,  $\phi = 0.145$  (maximum flow), 0.12, 0.09 and 0.06, at  $r_3/R_2 = 1.04$  and 1.07. For Impeller Z1, measurements were made for five flow coefficients,  $\phi = 0.135$  (maximum flow), 0.12, 0.10, 0.08 and 0.06, at  $r_3/R_2 = 1.08$  and 1.11. The total pressure, dynamic pressure and the pressure were normalized by the dynamic head based on impeller tip speed,  $(1/2)\rho u_2^2$ ; the circumferential and radial velocity components were normalized by the impeller tip speed,  $u_2$ . Flow angle, and normalized total pressure, dynamic pressure and pressure as well as the radial and circumferential velocity components for the two impellers are presented in Table 3.1.

It can be seen that for both impellers, the steady flow angle in the absolute frame,  $\bar{\alpha}$ , is largest for maximum flow. It decreases with decreasing flow coefficient, from about  $20^\circ$  for maximum flow to about  $10^\circ$  for "medium" flow coefficients,  $\phi = 0.09$  for Impeller R, and  $\phi = 0.10$  for Impeller Z1. As the flow coefficient is further reduced, the steady flow angle increases slightly, to approximately  $12^\circ$  for  $\phi = 0.06$ . The flow angles for the two impellers are approximately equal for similar flow coefficients, although the blade angles at the impeller blade trailing edge are significantly different for the two impellers,  $\beta^* = 25^\circ$  for Impeller R, and  $\beta^* = 35^\circ$  for Impeller Z1. For all flow coefficients investigated, Impeller R produces a larger steady dynamic pressure than Impeller Z1. For high flow coefficients, the steady total pressure rise for Impeller R is also larger than for Impeller Z1, whereas the pressure rise is for all flow coefficients, with the exception of maximum flow, larger for Impeller Z1 than for Impeller R.

**Table 3.1. Steady Three-Hole Tube Measurements.**  
(for Impeller R and Impeller Z1)

**STEADY THREE-HOLE TUBE MEASUREMENTS**

**Impeller R**

$\phi$	$r_3/R_2$	$\bar{\alpha}$	$\bar{p}_t^*$	$\bar{q}^*$	$\bar{c}_u/u_2$	$\bar{c}_r/u_2$	$\bar{p}^*$
0.145	1.04	18.3°	0.648	0.180	0.403	0.133	0.468
0.12	1.04	13.5°	0.780	0.238	0.474	0.114	0.542
0.09	1.04	10.2°	0.916	0.320	0.556	0.100	0.598
0.06	1.04	11.9°	0.986	0.346	0.575	0.121	0.640
0.145	1.07	19.0°	0.622	0.148	0.364	0.125	0.476
0.12	1.07	12.8°	0.782	0.226	0.464	0.105	0.556
0.09	1.07	10.8°	0.894	0.284	0.523	0.100	0.612
0.06	1.07	12.7°	0.974	0.328	0.559	0.126	0.648

**Impeller Z1**

$\phi$	$r_3/R_2$	$\bar{\alpha}$	$\bar{p}_t^*$	$\bar{q}^*$	$\bar{c}_u/u_2$	$\bar{c}_r/u_2$	$\bar{p}^*$
0.135	1.08	20.0°	0.600	0.128	0.337	0.125	0.472
0.12	1.08	11.3°	0.744	0.176	0.411	0.082	0.568
0.10	1.08	10.5°	0.866	0.242	0.483	0.092	0.626
0.08	1.08	11.4°	0.969	0.263	0.503	0.101	0.706
0.06	1.08	12.0°	1.012	0.292	0.529	0.112	0.720
0.135	1.11	23.2°	0.600	0.135	0.337	0.144	0.464
0.12	1.11	12.1°	0.750	0.180	0.414	0.089	0.570
0.10	1.11	10.0°	0.849	0.210	0.451	0.079	0.638
0.08	1.11	11.9°	0.966	0.266	0.505	0.107	0.700
0.06	1.11	11.7°	0.984	0.242	0.482	0.100	0.742

where (see also figure 3.11)

$$\bar{\alpha} = \tan^{-1} \left( \frac{\bar{c}_r}{\bar{c}_u} \right) \quad (3.9)$$

$$\bar{p}_t^* = \frac{\bar{p}_t - \bar{p}_{up}}{(1/2)\rho u_2^2} = \bar{c}_{pt} \quad (3.10)$$

$$\bar{p}^* = \frac{\bar{p} - \bar{p}_{up}}{(1/2)\rho u_2^2} \quad (3.11)$$

$$\bar{q}^* = \frac{\bar{q}}{(1/2)\rho u_2^2} = \frac{(1/2)\rho(\bar{c}_u^2 + \bar{c}_r^2)}{(1/2)\rho u_2^2} = \left( \frac{\bar{c}_u}{u_2} \right)^2 + \left( \frac{\bar{c}_r}{u_2} \right)^2 \quad (3.12)$$

$$\left( \frac{\bar{c}_u}{u_2} \right) = \sqrt{\frac{\bar{q}^*}{1 + \tan^2 \alpha}} \quad (3.13)$$

$$\left( \frac{\bar{c}_r}{u_2} \right) = \left( \frac{\bar{c}_u}{u_2} \right) \tan \alpha \quad (3.14)$$

### 3.3. Unsteady Three-Hole Tube Measurements

#### 3.3.1. Data Reduction

Unsteady three-hole tube measurements were made on the flow exiting Impeller R and Impeller Z1 into Diffuser T. The radial gap between the three-hole tube and the impeller baled trailing edge during the measurements was, as for the steady measurements, 4% and 7% of the impeller discharge radius for Impeller R and 8% and 11% of the impeller discharge radius for Impeller Z1.

The unsteady measurements were made for each pressure tap of the three-hole tube (right, center and left pressure tap) in a separate run. 1024 data points were taken during one shaft revolution, corresponding to five impeller blade passages. The measurements contained a lot of high frequency noise, due to the resonant frequency of the pressure tap. Thus, they were ensemble averaged, and the ensemble averaged unsteady pressure of each pressure tap, normalized by the dynamic pressure based on impeller tip speed, was computed as

$$\tilde{p}_{c,av}^*(i) = \frac{1}{N} \sum_{j=1}^N \frac{\tilde{p}_c(i,j)}{(1/2)\rho u_2^2}, \quad (3.15)$$

where  $i$  is the  $i$ th data points taken during one averaging period (i.e., one shaft revolution),  $j$  is the  $j$ th averaging period, and  $N$  the total number of averaging periods. For this experiment, 512 periods were used for ensemble averaging. Next, the ensemble averaged unsteady pressure of each pressure tap was superimposed to the steady pressure, measured previously with mercury manometers, to obtain the ensemble averaged pressure at each pressure tap.

$$p_{c,av}^* = \bar{p}_c^* + \tilde{p}_{c,av}^* \quad (3.16)$$

This assumes, as for the ensemble averaged lift computations, that the steady pressure measured by the mercury manometers is equal to the time mean pressure about which the piezoelectric pressure transducers measure the unsteady pressure. Note that  $\sum_{i=1}^M \tilde{p}_{c,av}^* = 0$ , where  $M$  is the total number of data points taken during

one averaging period ( $M=1024$ ). The ensemble averaged pressure measurements at the three pressure taps were then used to compute the coefficients  $K_\theta$ ,  $K_q$  and  $K_T$  for all 1024 points of the averaging period. Applying the three-hole tube calibration curves to those coefficients,  $K_\theta$ ,  $K_q$  and  $K_T$ , the ensemble averaged total pressure, flow angle and dynamic pressure were obtained. Subsequently, the ensemble averaged static pressure, and the ensemble averaged velocity components in the circumferential and radial direction, normalized by the impeller tip speed,  $u_2$ , were computed by:

$$p_{av}^* = p_{t,av}^* - q_{av}^* \quad (3.17)$$

$$\left( \frac{c_{u,av}}{u_2} \right) = \sqrt{\frac{q_{av}^*}{1 + \tan^2 \alpha_{av}}} \quad (3.18)$$

$$\left( \frac{c_{r,av}}{u_2} \right) = \left( \frac{c_{u,av}}{u_2} \right) \tan \alpha_{av}. \quad (3.19)$$

Furthermore, the ensemble averaged circumferential velocity in the relative frame of reference,

$$\left( \frac{w_{u,av}}{u_2} \right) = \left( \frac{c_{u,av}}{u_2} \right) - \left( \frac{r_3}{R_2} \right), \quad (3.20)$$

the ensemble averaged flow angle in the relative frame of reference,

$$\beta_{av} = \tan^{-1} \left( \frac{w_{u,av}}{w_{r,av}} \right), \quad (3.21)$$

and the ensemble averaged relative total pressure

$$P_{t,av}^* = p_{av}^* + \left( \frac{w_{u,av}}{u_2} \right)^2 + \left( \frac{w_{r,av}}{u_2} \right)^2, \quad (3.22)$$

were computed.

The ensemble averaged quantities were then time averaged, and decomposed in a time mean and a fluctuating part, e.g., for the total pressure,

$$p_{t,av}^* = \bar{p}_{t,av}^* + \tilde{p}_{t,av}^*, \quad (3.23)$$

where  $\sum_{i=1}^M \tilde{p}_{t,av}^*(i) = 0$ . In Table 3.2., the time mean of the ensemble averaged flow angle, the total, the static and the dynamic pressure are compared to the steady flow angle, the total, the static, and the dynamic pressure obtained by the steady three-hole tube measurements. It can be seen that the differences between the time mean values and the steady values are smaller than 2%. Hence, the three-hole tube calibration is approximately “linear” for the flow conditions investigated.

**Table 3.2. Steady and Time Mean Flow Measurements.**

(Impeller Z1,  $r_3/R_2 = 1.08$ ,  $\phi = 0.135$ )

	steady	time mean
$\alpha$	$20.0^\circ$	$20.4^\circ$
$p_t^*$	0.600	0.601
$p^*$	0.472	0.474
$q^*$	0.128	0.126

### 3.3.2. Spectra of Unsteady Pressure Measurements

A spectrum of the unsteady pressure measurements at the left pressure tap of the three-hole tube using Impeller Z1 is shown in figure 3.12. The blade passage and the second and third harmonic blade passage harmonics can clearly be identified. The resonant frequency at about 4500 Hz can clearly be seen as well. As for the impeller blade, diffuser vane and the total pressure tap, the resonant frequency of the pressure tap is “far” removed from the impeller blade passage frequency and its higher harmonics, so that amplification and phase shift of the signal were negligible.

### 3.3.3. Comparing the Total Pressure Measurements Obtained by the Total Pressure Probe and the Three-Hole Tube

In figure 3.13, the ensemble averaged unsteady total pressure measurements obtained with the total pressure probe in Volute D for  $r_3/R_2 = 1.05$  and ensemble averaged unsteady total pressure obtained from the three-hole tube measure-

ments for  $r_3/R_2 = 1.04$ , are presented for Impeller R at maximum flow coefficient,  $\phi = 0.145$ . The total pressure probe measurements and the three-hole tube measurements show significant differences. The region of high total pressure on the impeller blade suction side could not be resolved by the three-hole tube. The total pressure minima, however, are only slightly larger for the total pressure probe than for the three-hole probe.

In figure 3.14, the same measurements are presented for a lower flow coefficient,  $\phi = 0.12$ . Again, the region of high total pressure at the suction side of the partial impeller blade is not resolved by the three-hole tube. The minima are, as for maximum flow ( $\phi = 0.145$ ), slightly larger for the total pressure probe than for the three-hole tube. However, the total pressure profile from the the suction side of the full impeller blade to the pressure side of the partial impeller blade is not significantly different for the three-hole tube and the total pressure probe. As already discussed for the total pressure measurements, the region of high total pressure on the full blade suction side has already mixed out at this radial measurement location ( $r_3/R_2 = 1.04$ ), and hence the transition from minimum to maximum total pressure is significantly smoother for the full blade passage than for the partial blade passage.

From figures 3.13 and 3.14 it appears that the three-hole tube is very limited in resolving strong total pressure gradients in the flow. This may be due to unsteady flow effects about the tip of the three-hole tube.

A similar comparison was made for the measurements using Impeller Z1. In figures 3.15-3.18 total pressure measurements are presented for the total pressure probe and the three-hole tube in Diffuser T for two flow coefficients, maximum flow,  $\phi = 0.135$ , and a medium flow coefficient,  $\phi = 0.10$ , for two ratios  $r_3/R_2$ , 1.08 and 1.11. Again, it can be seen that the total pressure fluctuations measured with the three-hole tube are smaller than those measured with the total pressure probe. In contrast to the measurements for Impeller R, the total pressure profiles are qualitatively similar; quantitatively, the extrema, both the minima and maxima, are larger for the total pressure probe than for the three-hole tube. The differences

in the magnitude of the fluctuations are largest for maximum flow,  $\phi = 0.135$  and  $r_3/R_2 = 1.08$ , and smallest for  $\phi = 0.10$  and  $r_3/R_2 = 1.11$ . If the occurrence of the total pressure minima during an impeller blade passage is taken as a criterion, the phase difference between the total pressure probe and the three-hole tube is virtually not noticeable.

Hence, as was shown both impellers tested, the three-hole tube does not permit accurate unsteady measurements if strong total pressure gradients are present in the flow. This prohibits accurate unsteady measurements "close" to the impeller blade trailing edge where the gradients in total pressure, etc. are strongest. From the total pressure measurements, a characteristic length over which the total pressure fluctuations occur can be defined by  $s_* = T_* u_2$ , where  $T_*$  is the time for the impeller blade trailing edge to pass the three-hole (or total pressure) probe. During that time the total pressure rises from its minimum to its maximum value for  $\phi = 0.145$  at  $r_3/R_2 = 1.04$ . The quotient of the so defined characteristic length,  $s^*$ , of the fluctuations and the three-hole tube width is about 2. Thus, the size of the three-hole tube is comparable to the length over which most of the total pressure fluctuation occur, and thus it is not surprising that the unsteady flow effects about the three-hole tube do not permit very accurate measurements for flows with strong gradients. As the distance to the impeller discharge is increased, the total pressure gradients in the flow decrease, and the length scale during which the fluctuations occur becomes larger and the three-hole tube results, at least qualitatively, better. In the following, only the three-hole tube measurements for the two-dimensional impeller, Impeller Z1, will be discussed, since for that impeller the total pressure profiles from three-hole tube measurements and total pressure probe measurements were found to be at least qualitatively similar.

Unsteady measurements of the flow at or close to the discharge of centrifugal impellers had been made by several investigators. Most of these investigations were done on air compressors. The measurements were made either with hot wires, Eckhard (1975), Inoue and Cumptsy (1984), and Dean and Senoo (1960), or with laser velocimeters, Eckhard (1976). Matsunaga et al. (1978) reported five-hole tube mea-

surements of the flow exiting a mixed-flow pump. The measurements were made rather "far" downstream of the impeller exit, not within a few percent of the impeller blade discharge as the laser measurements reported by Eckhard (1976) or the hot-wire measurements by Inoue and Cumptsy (1984). For the current experiment, hot-wire and/or hot film anemometry was considered not very suitable, since although hot-wire anemometry works well in gas flow, in water flow the fragility and the sensitivity to dirt contamination make hot-wire anemometry difficult to work with. Using a laser for velocity measurements would have necessitated a complete rebuilding of the test section and was hence not feasible. So, despite its limitations for measurements in flows with strong gradients, three-hole tube measurements were made and are presented for Impeller Z1.

### 3.3.4. Ensemble Averaged Unsteady Three-Hole Tube Measurements

Unsteady three-hole tube measurements using Impeller Z1 and Diffuser T will be presented for two flow coefficients,  $\phi = 0.135$  and  $0.10$ , for two radial gaps between the three-hole tube and the impeller discharge, 8% and 11% of the impeller discharge radius. For each test, the flow angle in both the absolute and the relative frame,  $\alpha$  and  $\beta$ , the total pressure in both the absolute and the relative frame,  $p_t^*$  and  $P_t^*$ , the dynamic and the static pressure,  $q^*$  and  $p^*$ , the circumferential velocity component in the absolute and rotating frame,  $(c_u/u_2)$  and  $(w_u/u_2)$ , and the radial velocity component,  $(c_r/u_2)$  are presented. Shown is the ensemble averaged unsteady component of those flow quantities, the time mean value and the magnitude of the peak to peak fluctuation during one shaft revolution are given in a table. The position of the impeller blades for the measurements is indicated by filled boxes.

Before turning to the results from the three-hole tube measurements, the ensemble averaged unsteady pressure measurements of the individual three-hole tube pressure taps (right, center, and left) are presented in figure 3.19 for maximum flow,  $\phi = 0.135$ , and  $r_3/R_2 = 1.08$ . It can be seen that the fluctuations are smallest for

the right pressure tap, and largest for the center pressure tap.

In figures 3.20–3.23, the three-hole tube measurements for  $\phi = 0.135$  and  $0.10$  and  $r_3/R_2 = 1.08$  and  $1.11$  are presented. All measurements were made at a shaft speed of 1200 rpm. The results for  $\phi = 0.135$  and  $r_3/R_2 = 1.08$ , figure 3.20, will be discussed first since they show, even at a radial position of 8% of the impeller discharge, a strong wake, and typical jet-wake behavior described by Dean and Senoo (1960), and observed among others by Inoue and Cumptsy (1984) and Eckhard (1976).

Turning first to the fluctuating pressure and total pressure measurements in the absolute frame of reference,  $\tilde{p}_{av}^*$  and  $\tilde{p}_{t,av}^*$ , it can be seen that distinct minima occur at the pressure side of the impeller blade trailing edge. There is virtually no phase difference between the minima for pressure and total pressure. The total pressure and pressure maxima, however, occur at different locations in the blade channel. The maximum total pressure occurs in the first half of the blade channel (between the blade suction side and the center of the blade channel), whereas the maximum pressure occurs in the second half of the blade channel (between the center of the blade channel and the blade pressure side).

The fluctuating dynamic pressure,  $\tilde{q}_{av}^*$ , (in the absolute frame of reference) does not have a distinct minimum at the impeller blade trailing edge, as the pressure and the total pressure do. Its maximum is in phase with the total pressure maximum. The minimum is attained at the center of the blade channel, approximately when the pressure reaches its maximum.

Turning to the fluctuating absolute circumferential velocity,  $\tilde{c}_{u,av}/u_2$ , two levels of different velocity can clearly be distinguished, a high velocity in the first half of the blade channel, and a level of low velocity in the second half of the blade channel. Maxima and minima are well in phase with maxima and minima of the dynamic pressure.

For the fluctuating radial velocity,  $\tilde{c}_{r,av}/u_2$ , the maximum occurs during the second half of the blade channel, the minimum at the channel center. In the first half of the blade channel, the radial velocity is smaller than in the second half.

The absolute flow angle,  $\tilde{\alpha}_{av}^*$ , fluctuates by about 20 degrees. It decreases sharply from its maximum value to its mean value before the impeller blade pressure side, and then decreases gradually to its minimum value at the center of the blade channel. A first very steep increase to its time mean value is followed by a more gradual increase to its maximum value.

The relative flow angle,  $\tilde{\beta}_{av}^*$ , fluctuates significantly less than the absolute flow angle, by approximately 10 degrees, compared to about 20 degrees for the absolute flow angle. It fluctuations occur approximately at the transition of high to low absolute circumferential velocity (or low to high relative circumferential velocity).

The fluctuating relative total pressure,  $\tilde{P}_{t,av}^*$ , has, similar to the relative and the absolute circumferential velocity, two distinct levels; the level of low relative total pressure occurs from the impeller blade suction side to the center of the impeller blade passage, whereas the high level of relative total pressure occurs from the center of the blade passage to the impeller blade pressure side. The transition from low to high relative total pressure occurs simultaneously to the transition from low to high relative circumferential velocity.

The distinct levels of absolute and relative circumferential velocity correspond well to the jet-wake model described by Dean and Senoo (1960). The wake is characterized by a low relative radial and circumferential velocity, whereas the jet is characterized by a large relative radial and circumferential velocity. In the absolute frame, that translates into a large absolute circumferential velocity in the wake and a small circumferential velocity in the jet. Similarly, the absolute flow angle is small in the wake and large in the jet. Further, following that jet-wake theory, two forces act on the border between the wake and the jet, the turbulent shear force tangential to the border, the usual force of wake mixing, and a pressure force between wake and jet rotating at shaft speed in the absolute frame of reference, and hence doing reversible work transfer between wake and jet, leading to an increase in angular momentum in the wake fluid at the expense of the jet fluid. This reversible work transfer is responsible for the rapid mixing of rotating wakes (in contrast to the slow, purely turbulent mixing of stationary wakes). For the flow

coefficient discussed above, the features of that wake-jet model can be observed in many of the presented flow quantities, such as the two rather distinct levels of relative and absolute circumferential velocity and the absolute flow angle variation. Furthermore, the large region of low relative total pressure on the impeller blade suction side shows clearly the existence of the impeller wake at the measurement location. Similar regions of low relative total pressure were found by Eckhard (1975) and Inoue and Cumptsy (1984). In contrast to the theory developed by Dean and Senoo (1960), the wake has not mixed out at a location of  $R/R_2 = 1.08$ . However, Eckhard (1976), and Inoue and Cumptsy (1984) as well, reported wakes that extended further in vaneless diffusers than the 5% margin of the impeller discharge radius obtained by the theory of Dean and Senoo (1960).

Increasing the radial gap between the three-hole tube and the impeller discharge from 8% to 11% of the impeller discharge radius for the maximum flow coefficient (figure 3.21) resulted in a significant decrease of the measured fluctuations; however, the wake clearly had not yet mixed out. This can best be seen from the absolute and relative circumferential velocities, which still do have two distinct levels, corresponding to wake and jet flow. But the relative width of the wake flow has increased significantly in comparison to the measurements made at the radial gap of 8%. The relative total pressure shows, with the region of low total pressure following the impeller blade suction side, the existence of the wake, too.

Next, the “medium” flow coefficient,  $\phi = 0.10$ , for  $r_3/R_2 = 1.08$ , (figure 3.22), will be considered. It can be seen that the wake is by far not as strong as for the maximum flow coefficient. The absolute flow angle fluctuations are significantly smaller, and the relative and absolute circumferential velocity do not have such distinct different velocity levels as for maximum flow. In fact, the relative total pressure, which showed the existence of the wake clearly for the maximum flow coefficient, does not give a clear indication of jet-wake flow for this particular flow coefficient,  $\phi = 0.10$ , at this measurement location.

In figure 3.23, the results from the three-hole tube measurements for the “medium” flow coefficient at  $r_3/R_2 = 1.11$  are presented. It can be seen that

the impeller wake has vanished at this measurement location; i.e., the absolute flow angle fluctuations and the dynamic pressure fluctuations are small, and the absolute and relative circumferential velocity fluctuations are small, too. Only the radial velocity fluctuations are still large, i.e., of about the same order of magnitude as the time-mean radial velocity. The observation that the radial velocity remains axisymmetrically nonuniform for significantly larger ratios  $R/R_2$  than the circumferential velocity has also been made by Inoue and Cumptsy (1984).

In contrast to the dynamic pressure fluctuations, which are very small for this particular run,  $r_3/R_2 = 1.11$  and  $\phi = 0.10$ , the static pressure still has a significant minimum at the impeller blade trailing edge. This minimum can also be seen in the absolute and relative total pressure data. Hence, it appears that the pressure and the total pressure also remain axisymmetrically nonuniform at larger ratios  $R/R_2$  than the circumferential velocity. This is in contrast to observations reported by Inoue and Cumptsy (1984) who observed that the total pressure attains axisymmetric uniformity at about the same ratio  $R/R_2$  as the circumferential velocity. However, Inoue's pressure measurements (1984) do not show a pressure minimum at the impeller trailing edge. The low pressure at the impeller trailing edge in the present experiment may result from the flow about the "thick" impeller blade trailing edge. Inoue and Cumptsy (1984) do not give data of the trailing edge thickness of the blades of the air-compressor used, but from figures included, it appears that the compressor blades are rather "thin," at least in comparison to the blades of Impeller Z1, and hence the different pressure at the impeller blade trailing edge may result from the different impeller blade thicknesses.

In fact, Furukawa et al. (1987) report that the unsteady pressure fluctuations on the shroud casing of a vaneless diffuser of a centrifugal pump depend strongly on the thickness of the impeller blade trailing edge. The measurements were made for two two-dimensional impellers with a blade outlet angle of 25 degrees and a normalized trailing edge thickness,  $t^*$ , of 0.328 and 0.117. For the zero incidence flow coefficient,  $\phi = 0.106$ , shroud casing pressure fluctuations were measured at  $R/R_2 = 1.072$ . The magnitude of the pressure fluctuations was reduced from  $|\tilde{p}_{fs,av}^*| \approx 0.18$  for the thick

blade to  $|\tilde{p}_{fs,av}^*| \approx 0.10$  for the thinner blade. The blade geometry of Impeller Z1 is actually quite similar to the thinner blade used by Furukawa et al. (1987) (Impeller Z1:  $\beta^* = 25^\circ$ ,  $t^* = 0.13$ ). For a flow coefficient of  $\phi = 0.10$  and  $r_3/R_2 = 1.08$ , the magnitude of the pressure fluctuations as measured with the three-hole tube was  $|\tilde{p}_{av}^* = 0.96|$ , very close to the shroud casing measurements made by Furukawa for his impeller with the thinner blades (1987). With the help of some theoretical computations, Furukawa et al. (1987) conclude that the low total pressure at the pressure side of the blade trailing edge is the result of the sharp turning and of the simultaneous acceleration the flow along the blade pressure side is subjected to as it reaches the corner of the blade pressure side with the trailing edge of a sufficiently thick impeller blade trailing edge.

### 3.4. Summary

Unsteady three-hole tube measurements of the flow discharged by a two-dimensional centrifugal impeller (Impeller Z1) into a vaneless diffuser were made at two radial locations,  $r_3/R_2 = 1.08$  and  $1.11$ , at the diffuser mid height. Comparing the fluctuating total pressure measurements obtained from the three-hole tube measurements to the fluctuating total pressure measurements obtained by a total pressure probe at the same radial position in the vaneless diffuser, it can be seen that the total pressure profiles are qualitatively similar; the magnitude of the fluctuations, however, are larger for the total pressure probe than for the three-hole tube. Hence, the three-hole tube may permit qualitative unsteady measurements, but not quantitatively accurate unsteady measurements. However, even the qualitative measurements provide some valuable information on the flow. The absolute circumferential distribution and the relative total pressure distribution showed, especially for the maximum flow coefficient, the existence of the wake at the impeller blade suction side, characterized by a low relative total pressure and a large absolute circumferential velocity. The known jet-wake model was qualitatively confirmed. However, the flow was axisymmetric at the radial distance away from the impeller

discharge predicted by Dean's model (1960) ( $R/R_2 = 1.05$ ). For the maximum flow coefficient,  $\phi = 0.135$ , axisymmetry was not yet achieved at  $R/R_2 = 1.11$ . For a lower flow coefficient ( $\phi = 0.10$ ), however, the circumferential velocity was approximately axisymmetric at  $R/R_2 = 1.11$ , whereas the fluctuations of the radial velocity were still large. In addition to the fluctuations predicted by the jet-wake model, a significant pressure fluctuation was observed at the impeller blade trailing edge, resulting in a region of low pressure and low absolute total pressure at the pressure side of the impeller blade trailing edge. This pressure minimum, like the radial velocity fluctuations, had not vanished at  $R/R_2 = 1.11$ . Hence, the pressure distribution, as well as the absolute total pressure distribution, was not axisymmetric at  $R/R_2 = 1.11$ .

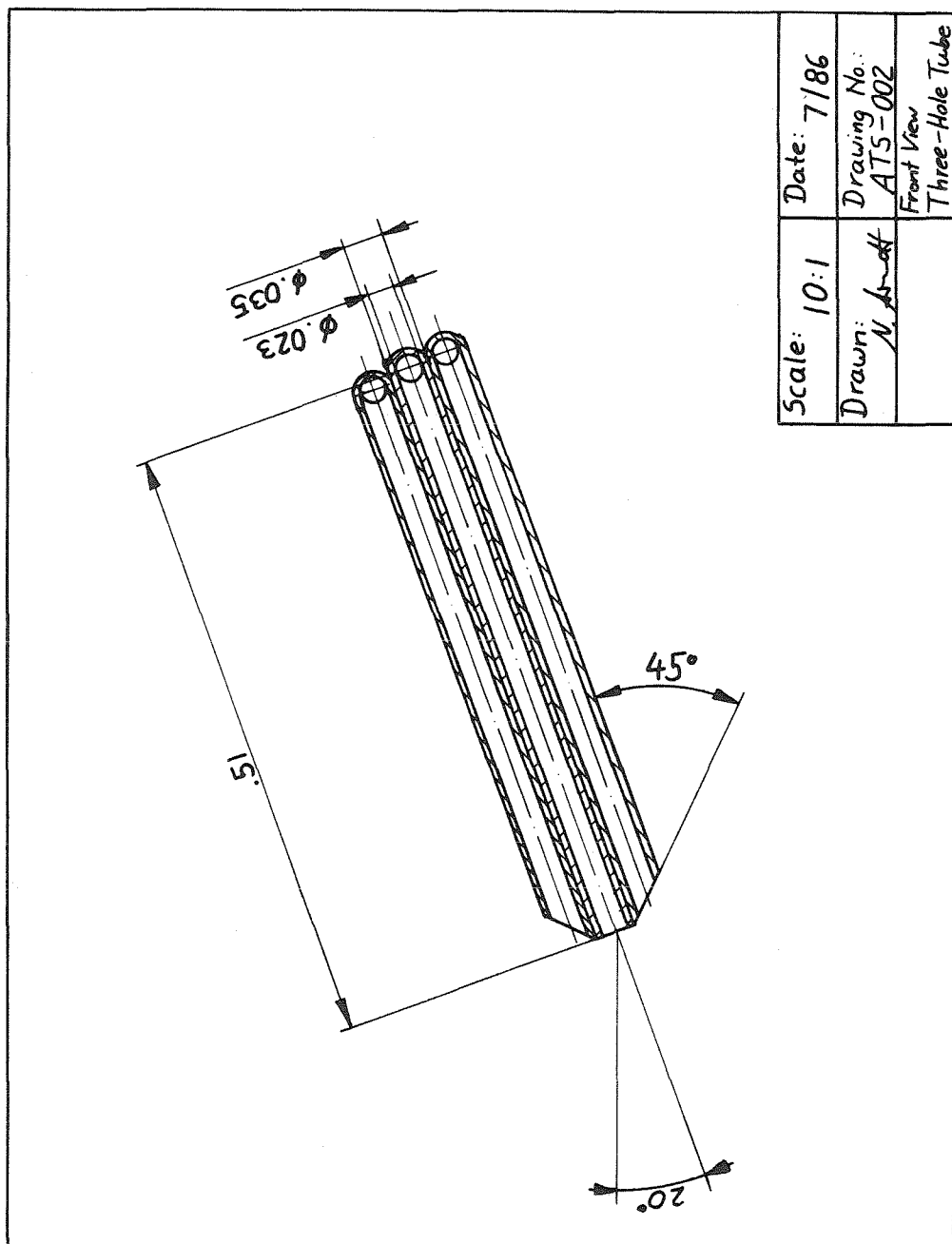


Fig. 3.1. Schematic three-hole tube drawing.

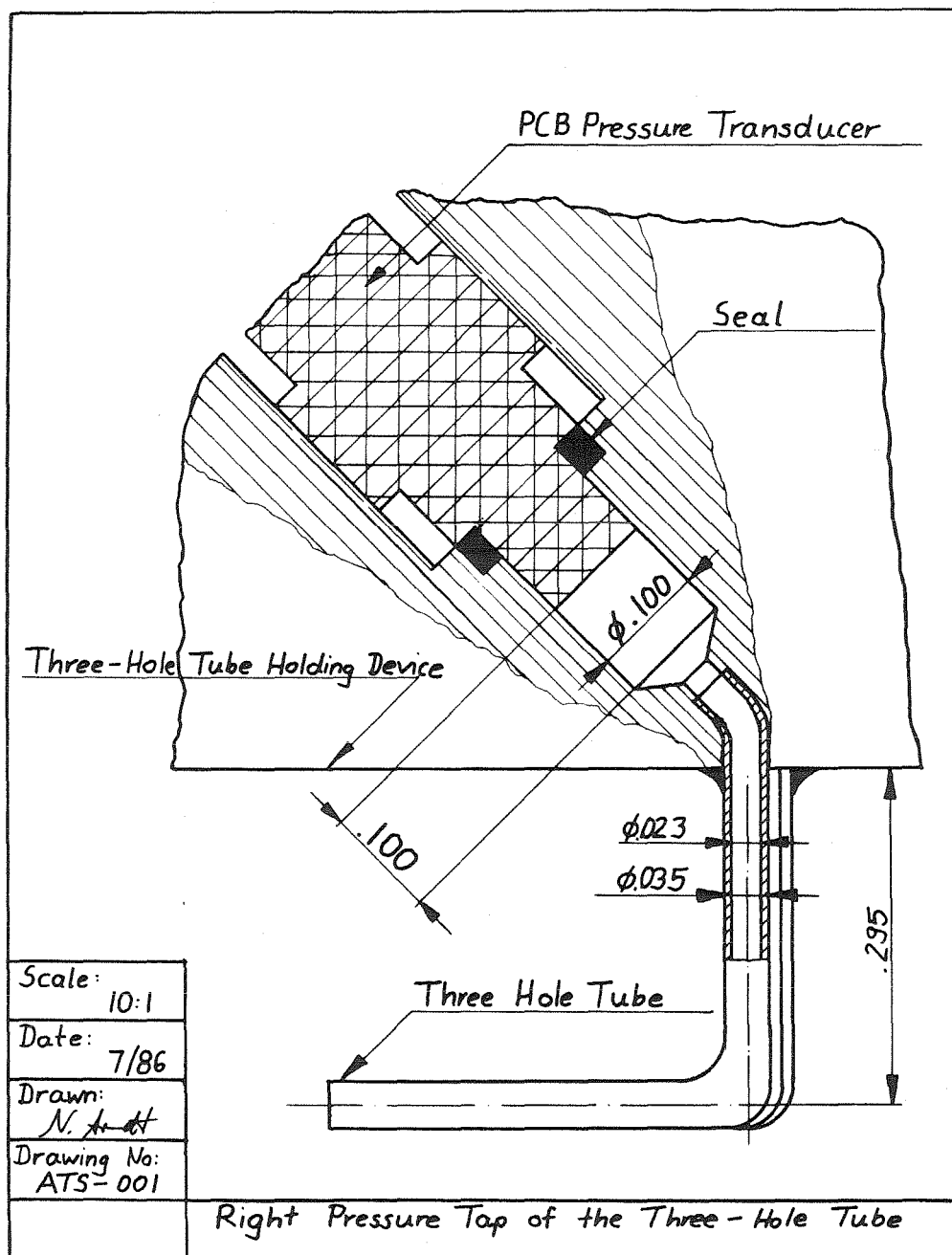


Fig. 3.2. Schematic three-hole tube drawing.

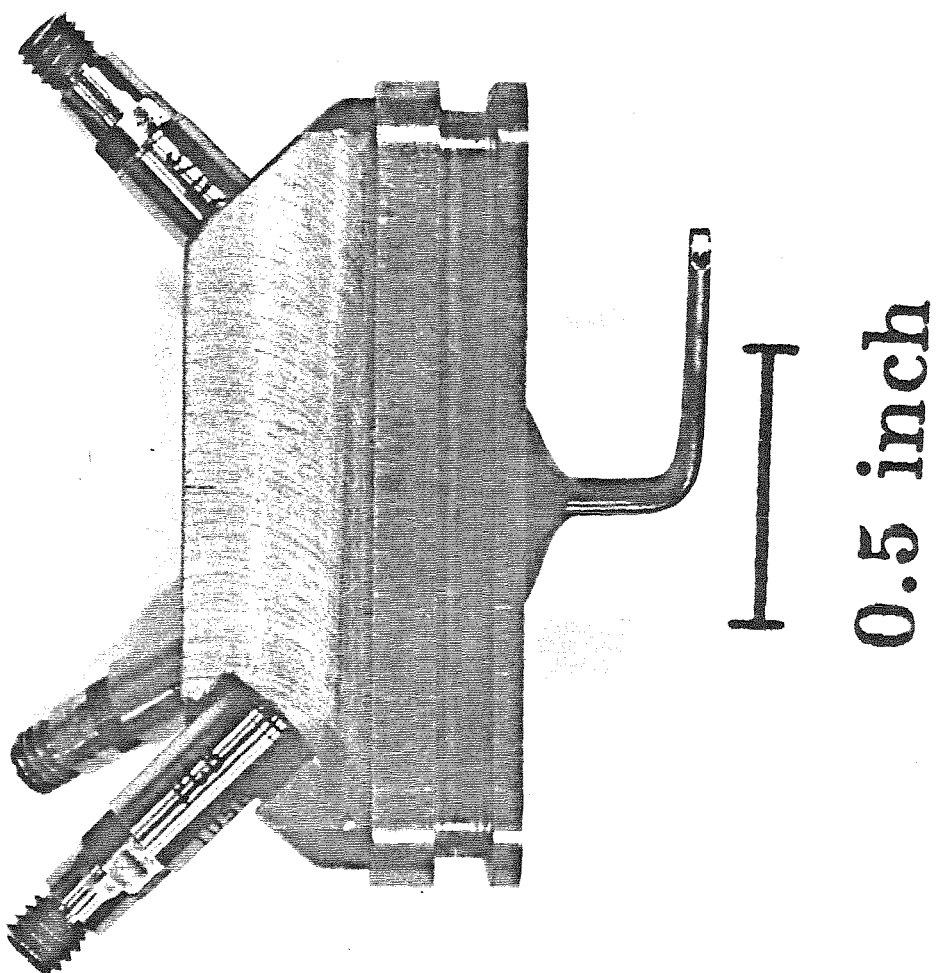


Fig. 3.3a. Photograph of the three-hole tube with the pressure transducers installed.

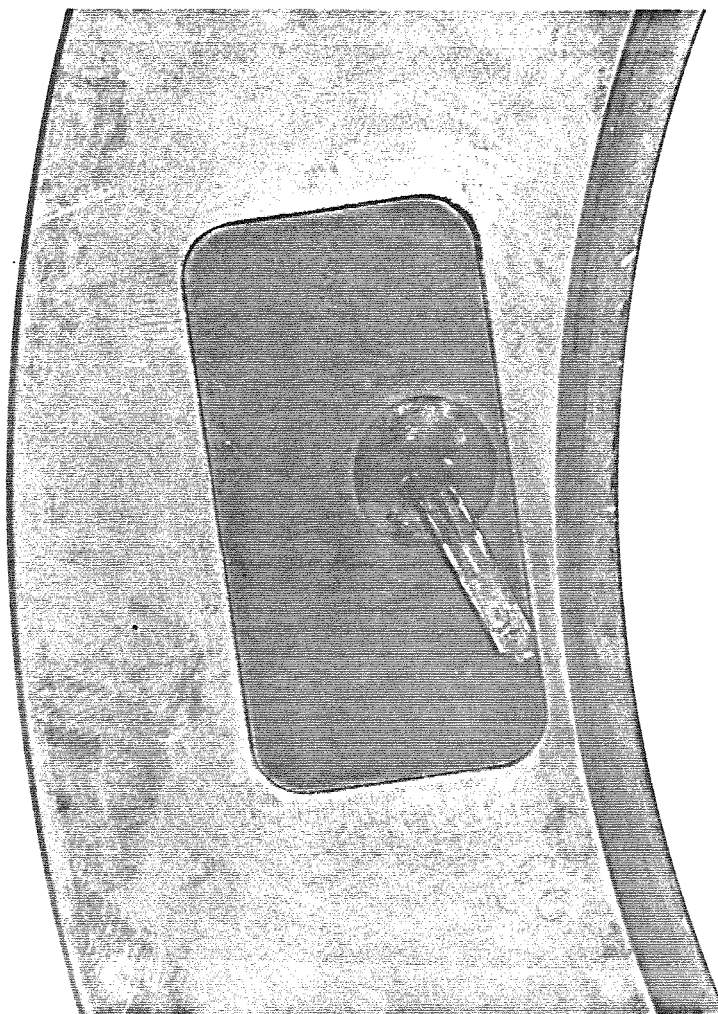


Fig. 3.3b. Photograph of the three-hole tube installed in Diffuser T.

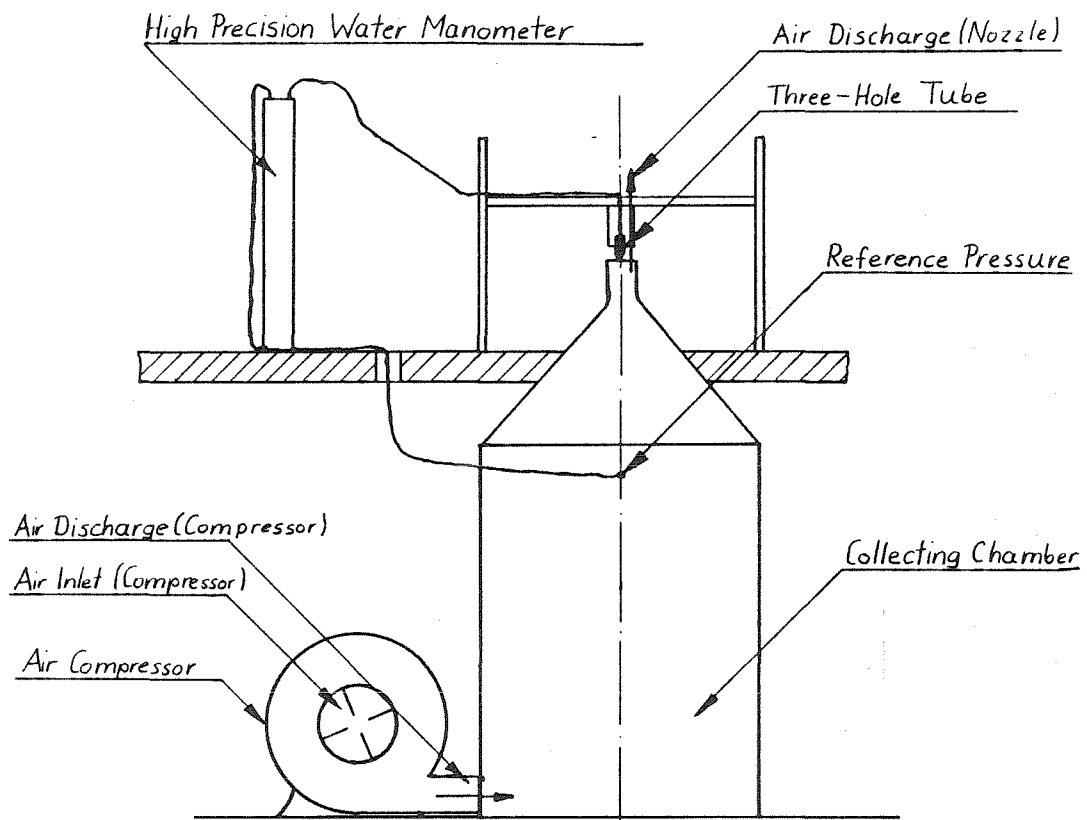


Fig. 3.4. Three-hole tube calibration facility.

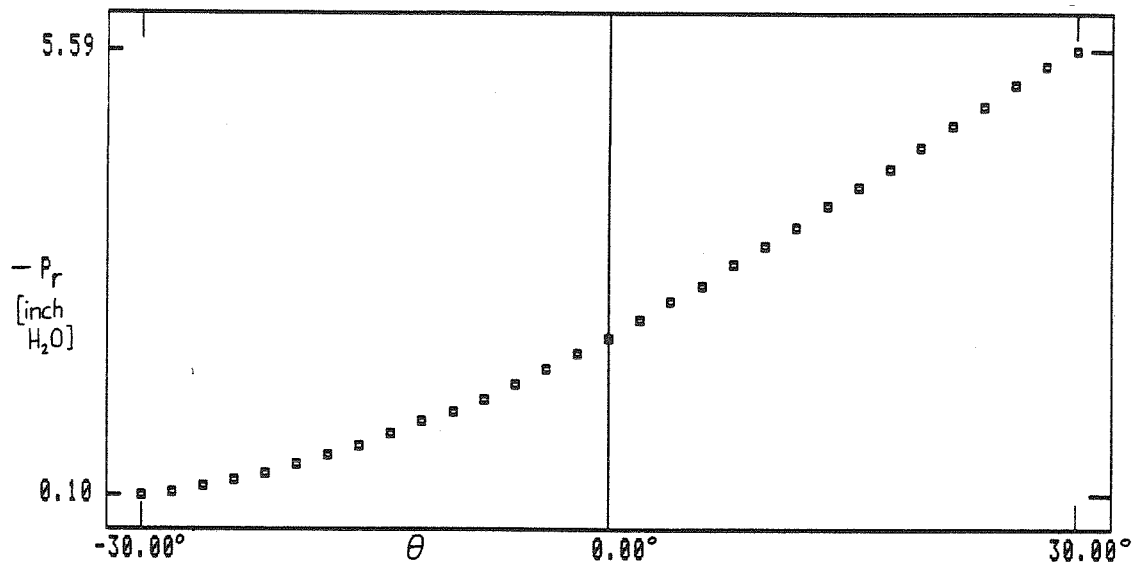


Fig. 3.5. Three-hole tube calibration measurements ( $(p_r - p_{res})$  vs.  $\theta$ ).

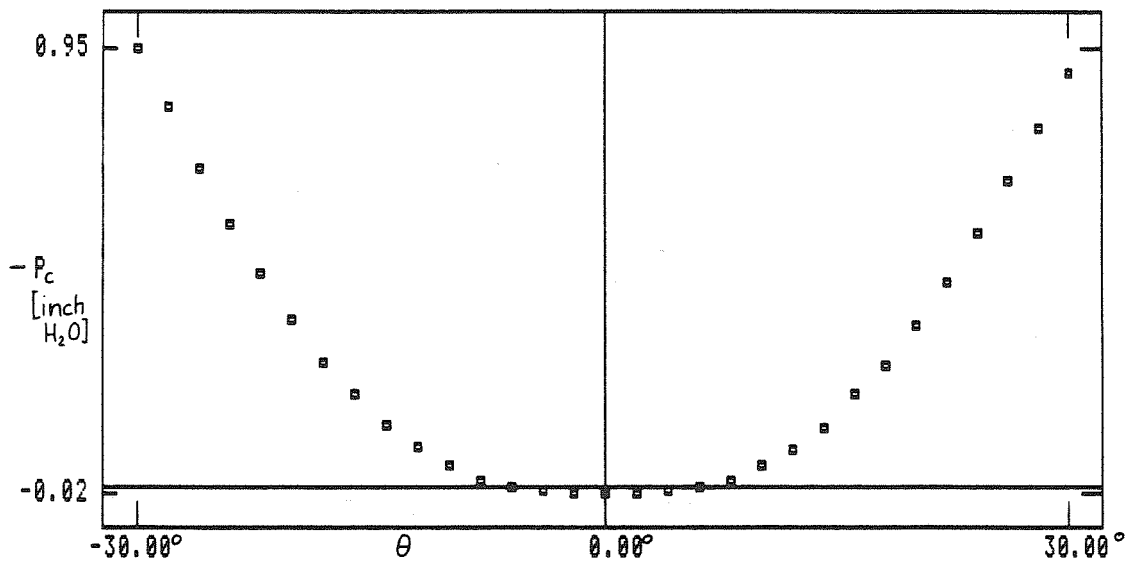


Fig. 3.6. Three-hole tube calibration measurements, ( $(p_c - p_{res})$  vs.  $\theta$ ).

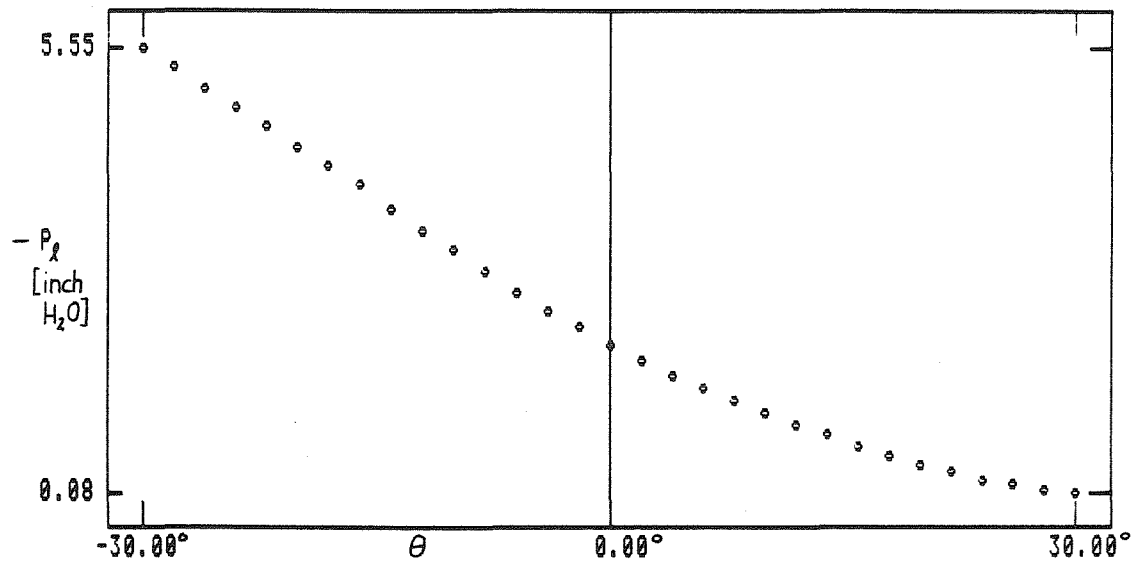


Fig. 3.7. Three-hole tube calibration measurements,  $((p_l - p_{res})$  vs.  $\theta$ ).

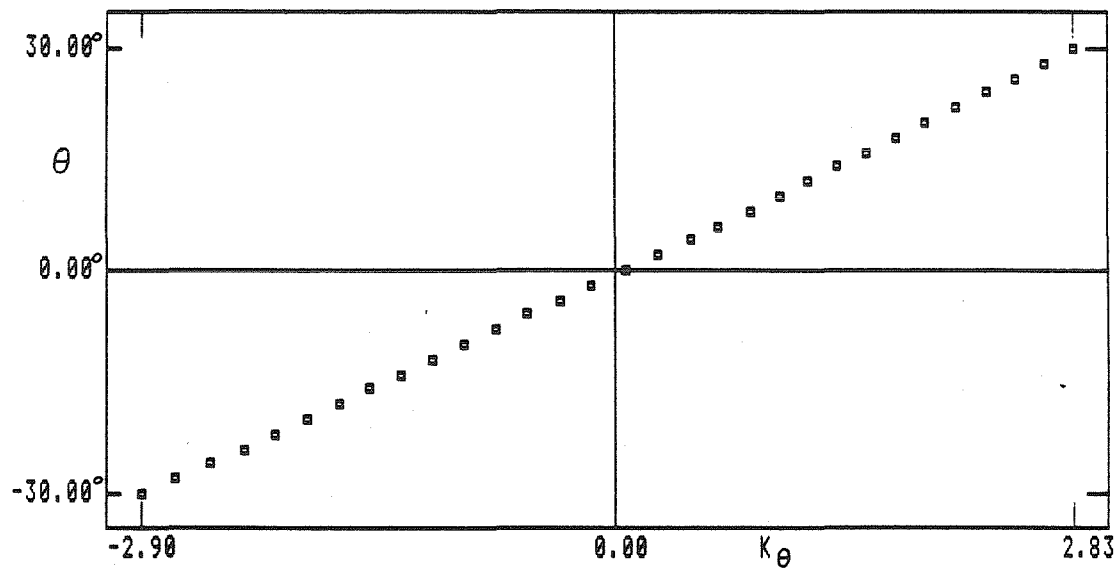


Fig. 3.8. Three-hole tube calibration curve ( $K_\theta$  vs.  $\theta$ ).

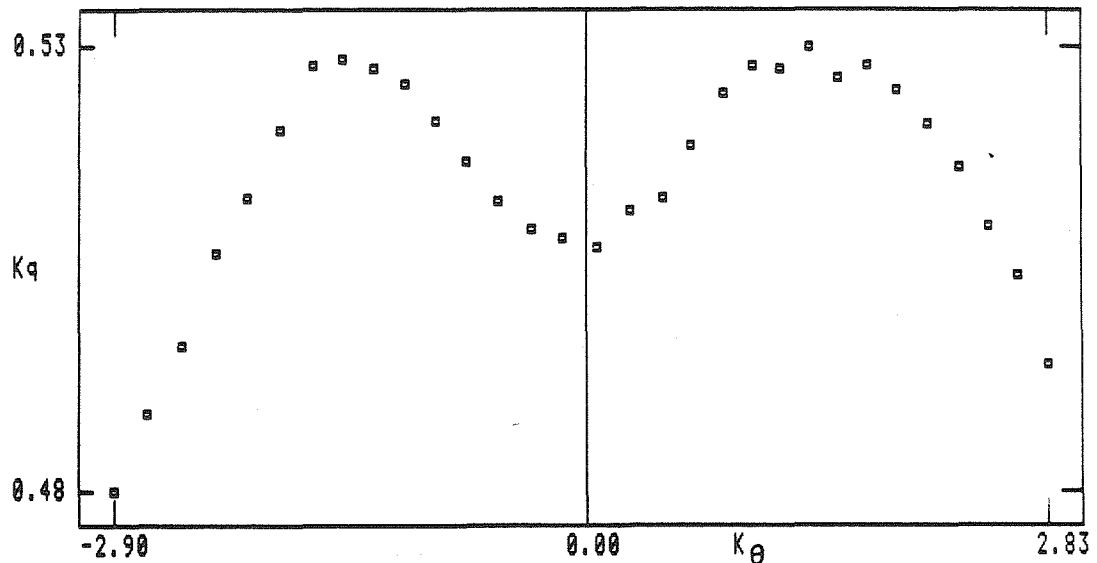


Fig. 3.9. Three-hole tube calibration curve ( $K_q$  vs.  $K_\theta$ ).

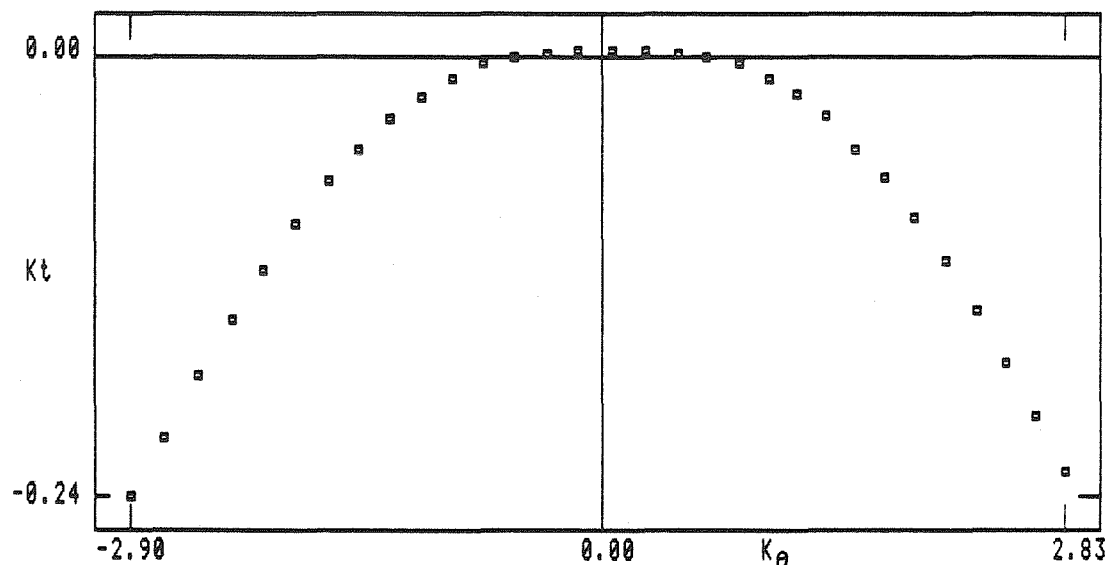


Fig. 3.10 Three-hole tube calibration curve ( $K_t$  vs.  $K_\theta$ ).

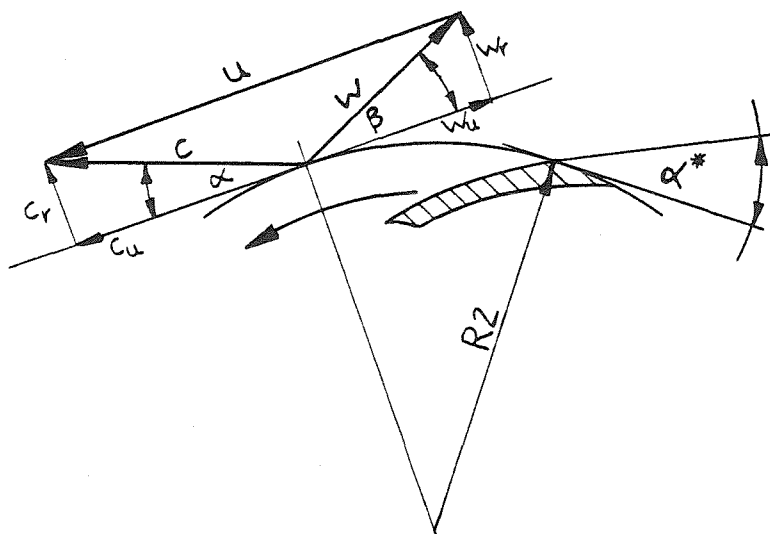


Fig. 3.11. Velocity triangle.

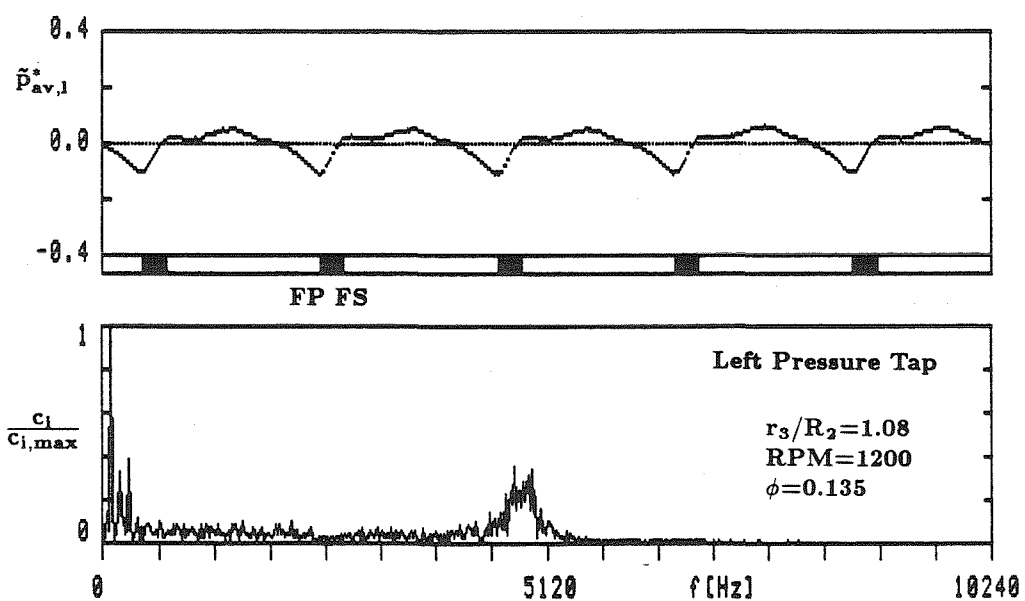
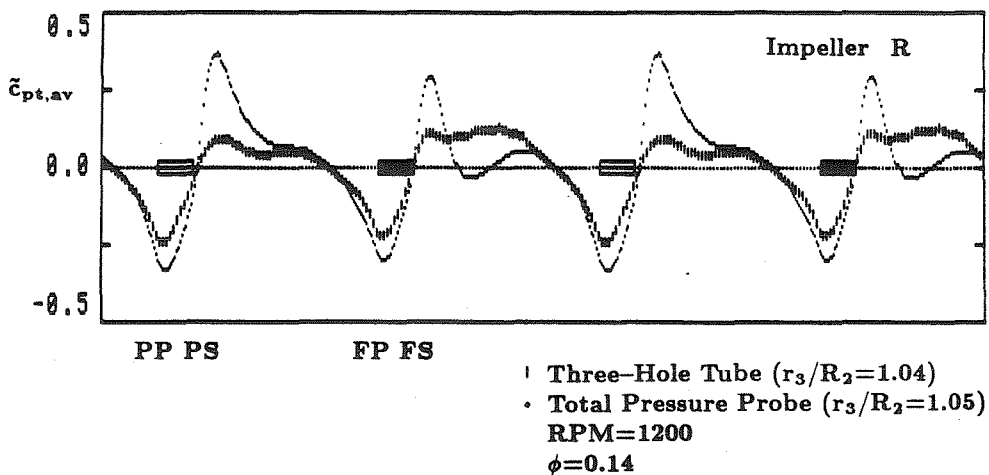
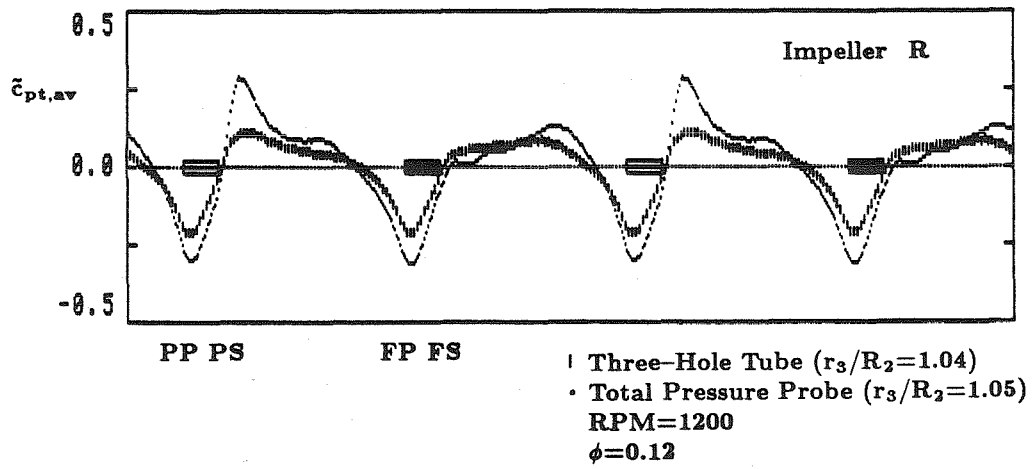


Fig. 3.12. Spectrum of unsteady three-hole tube measurements and ensemble averaged unsteady three-hole tube measurements (left pressure tap) for Impeller Z1 ( $\phi = 0.135$ ,  $r_3/R_2 = 1.08$ , rpm = 1200).



**Fig. 3.13.** Ensemble averaged unsteady total pressure measurements for Impeller R for  $\phi = 0.145$ ,  $r_3/R_2 = 1.05$  (comparing the three-hole tube to the total pressure probe).



**Fig. 3.14.** Ensemble averaged unsteady total pressure measurements for Impeller R for  $\phi = 0.12$ ,  $r_3/R_2 = 1.05$  (comparing the three-hole tube to the total pressure probe).

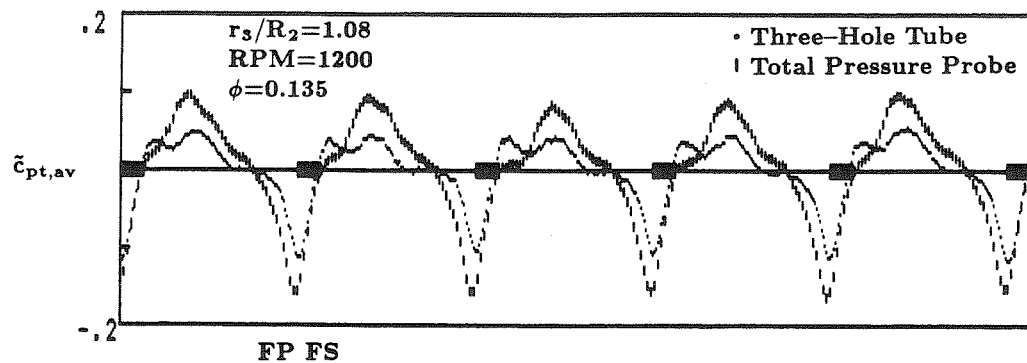


Fig. 3.15. Ensemble averaged unsteady total pressure measurements for Impeller Z1 for  $\phi = 0.135$ ,  $r_3/R_2 = 1.08$  (comparing the three-hole tube to the total pressure probe).

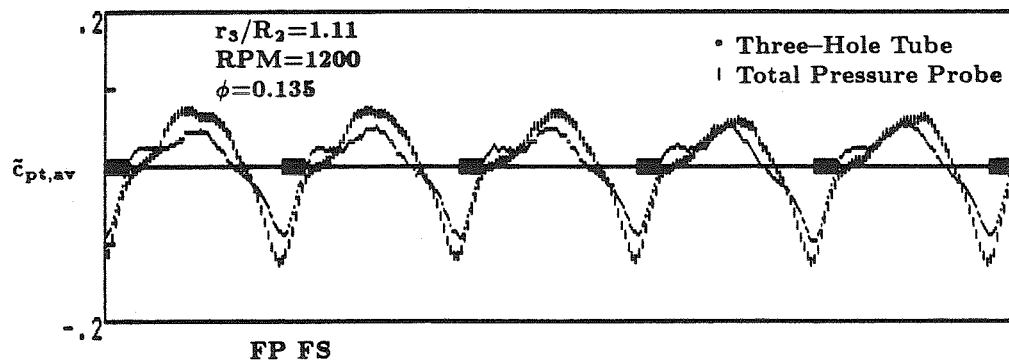


Fig. 3.16. Ensemble averaged unsteady total pressure measurements for Impeller Z1 for  $\phi = 0.135$ ,  $r_3/R_2 = 1.11$  (comparing the three-hole tube to the total pressure probe).

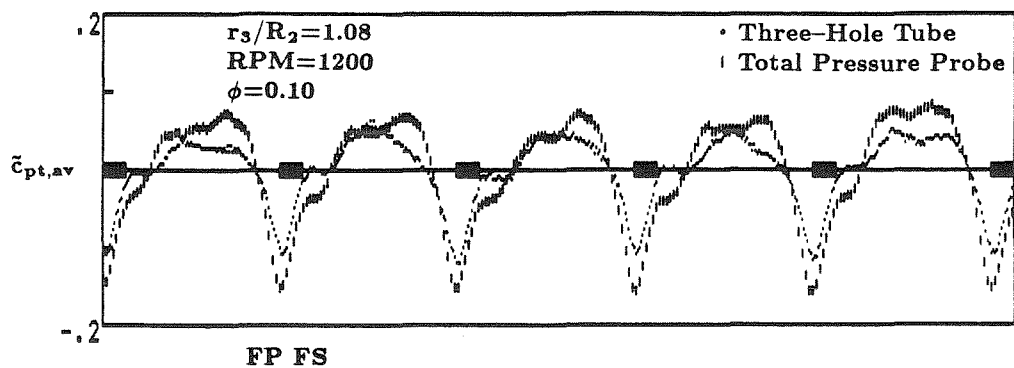


Fig. 3.17. Ensemble averaged unsteady total pressure measurements for Impeller Z1 for  $\phi = 0.10, r_3/R_2 = 1.08$  (comparing the three-hole tube to the total pressure probe).

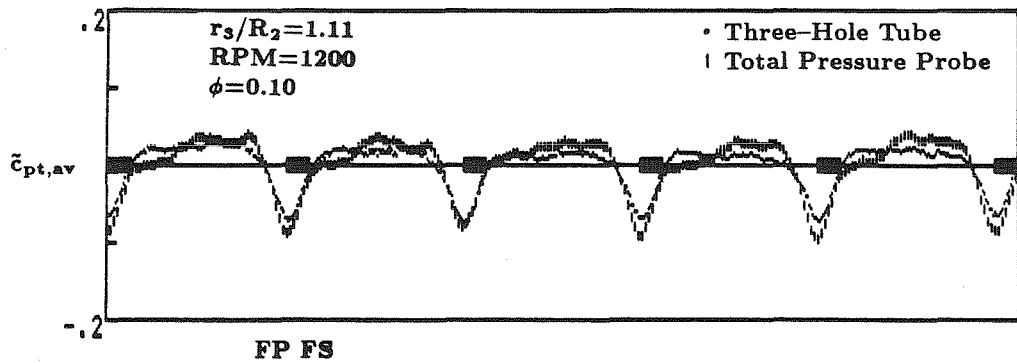


Fig. 3.18. Ensemble averaged unsteady total pressure measurements for Impeller Z1 for  $\phi = 0.10, r_3/R_2 = 1.11$  (comparing the three-hole tube to the total pressure probe).

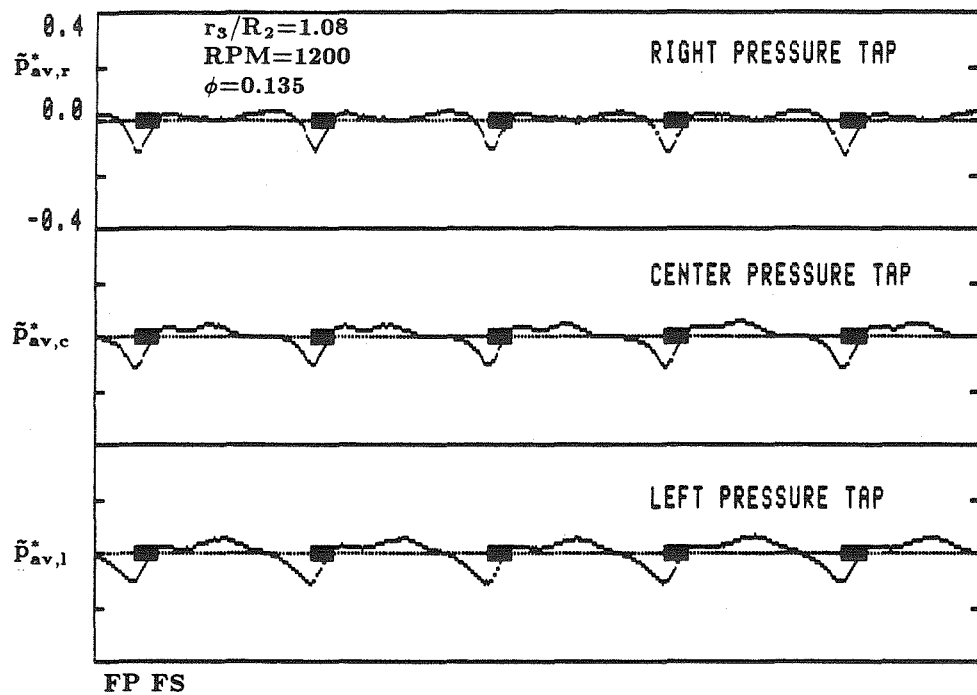


Fig. 3.19. Ensemble averaged unsteady pressure measurements of the right, center, and the left three-hole tube pressure tap for Impeller Z1 ( $\phi = 0.135, r_3/R_2 = 1.08$ , rpm = 1200).

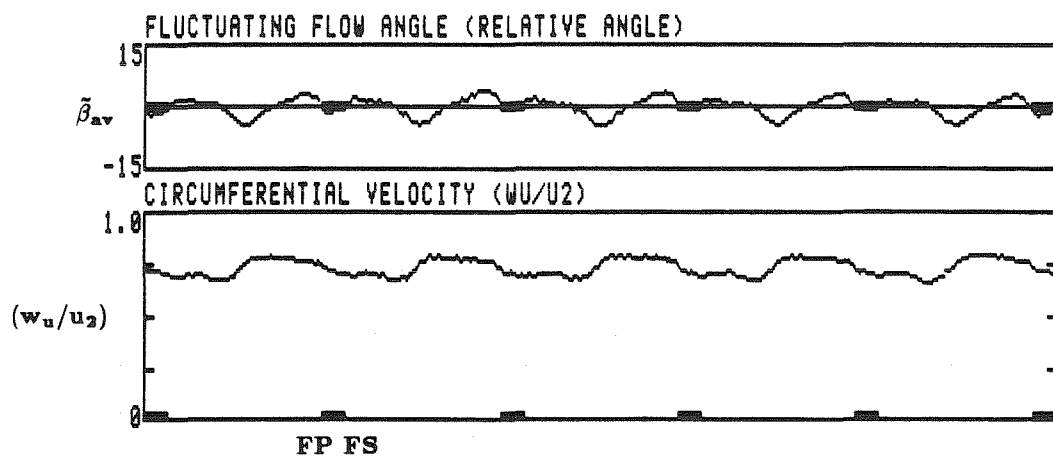
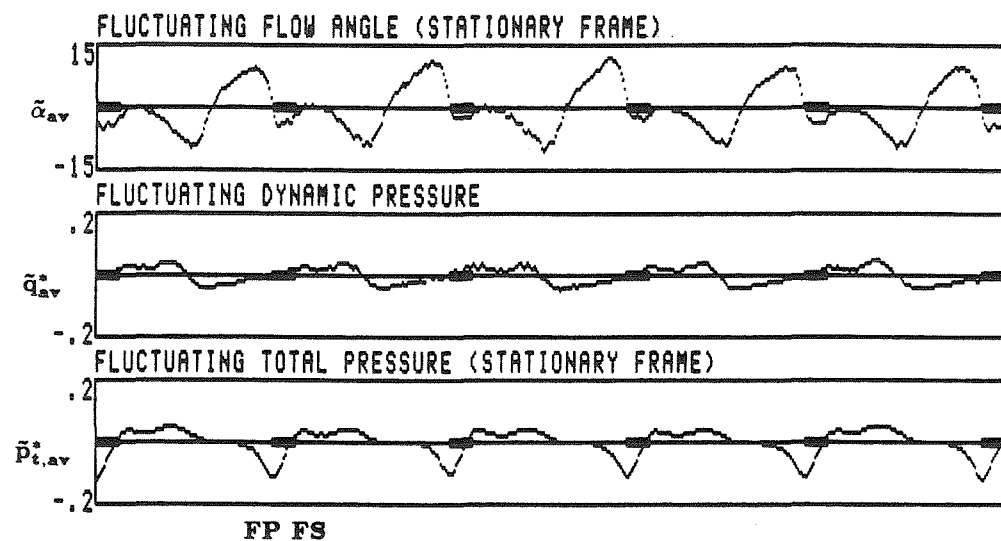


Fig. 3.20. Presenting the results from the three-hole tube measurements for Impeller Z1 ( $\phi = 0.135$ ,  $r_3/R_2 = 1.08$ , rpm = 1200).

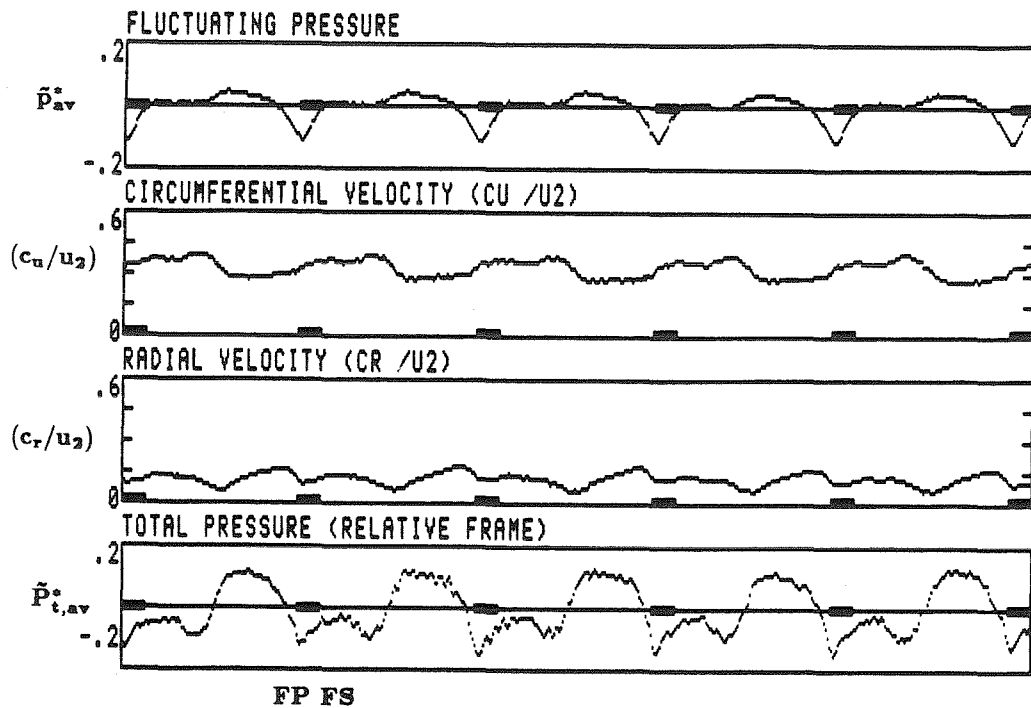


Table 3.3. Time Mean and Fluctuating Flow Measurements  
(Impeller Z1,  $r_3/R_2 = 1.08$ ,  $\phi = 0.135$ )

	Time Mean	Magnitude of Fluctuations
$\alpha$	$20.4^\circ$	$22.1^\circ$
$q^*$	0.126	0.095
$p_t^*$	0.601	0.172
$\beta$	$9.19^\circ$	$8.75^\circ$
$(w_u/u_2)$	0.749	0.133
$p^*$	0.475	0.159
$(c_u/u_2)$	0.331	0.133
$(c_r/u_2)$	0.121	0.123
$P_t^*$	1.05	0.282

Fig. 3.20. Presenting the results from the three-hole tube measurements for Impeller Z1 ( $\phi = 0.135$ ,  $r_3/R_2 = 1.08$ , rpm = 1200).

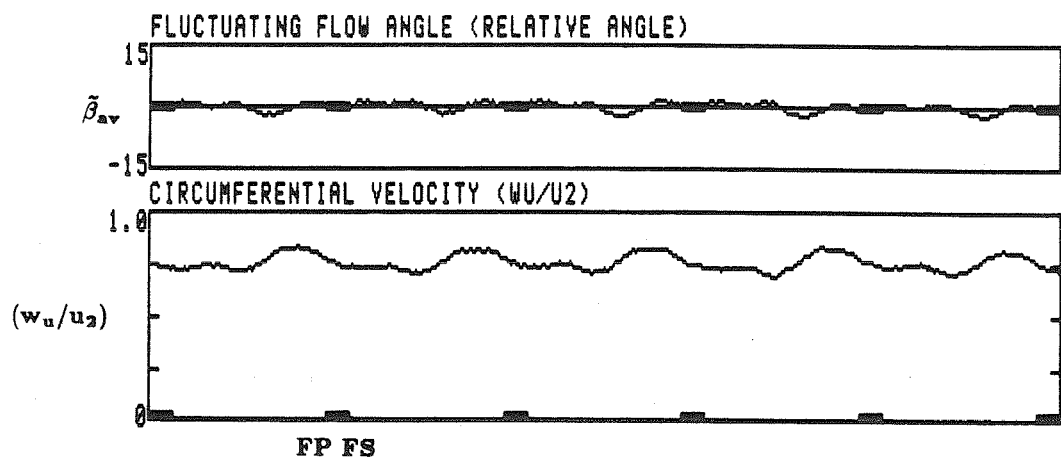
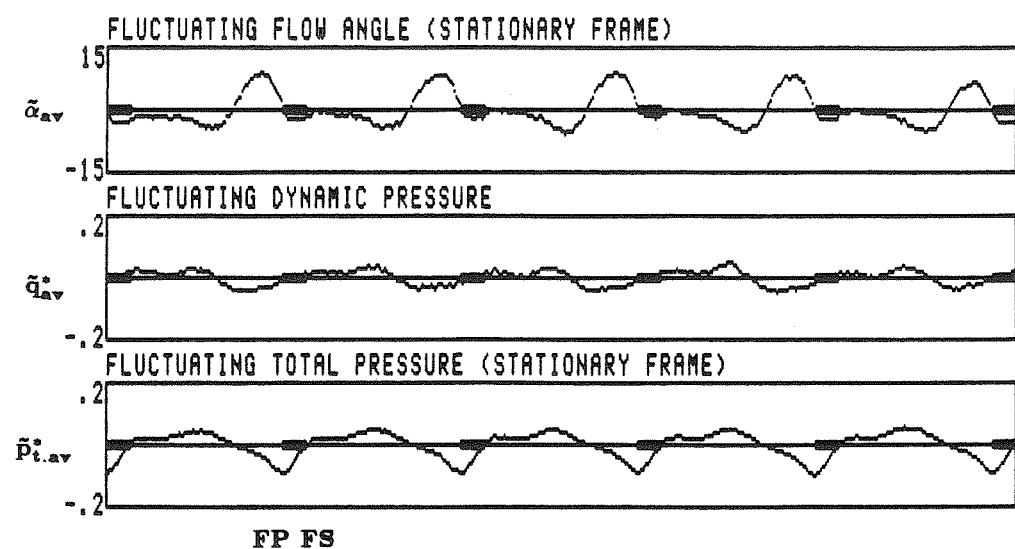


Fig. 3.21. Presenting the results from the three-hole tube measurements for Impeller Z1 ( $\phi = 0.135$ ,  $r_3/R_2 = 1.11$ , rpm = 1200).

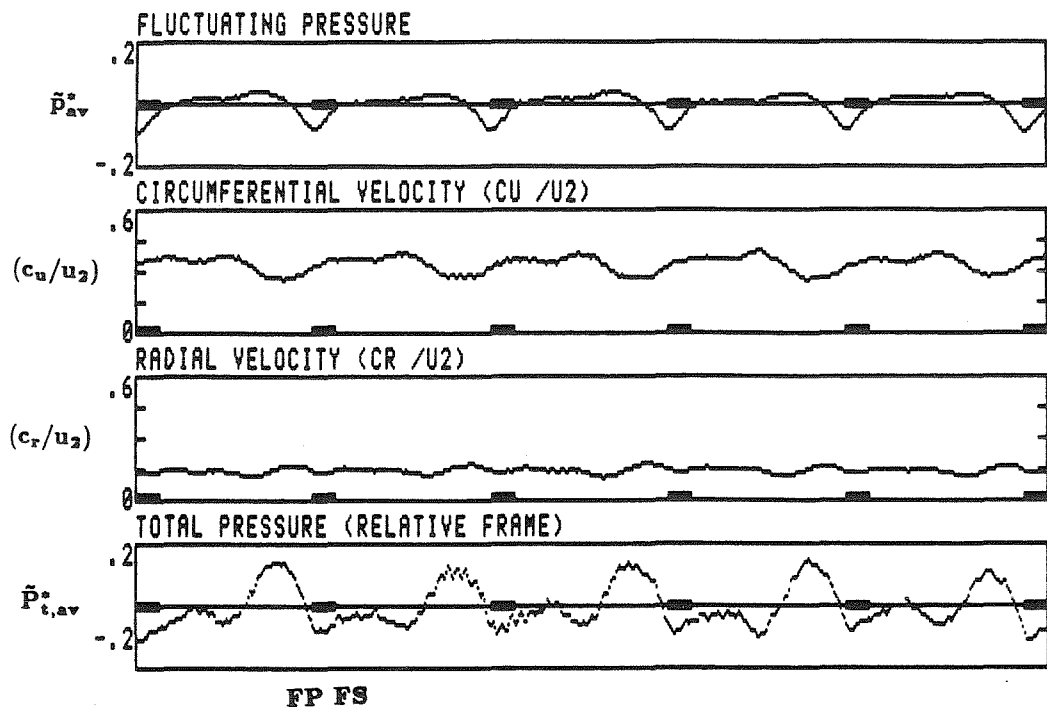


Table 3.4. Time Mean and Fluctuating Flow Measurements  
(Impeller Z1,  $r_3/R_2 = 1.11$ ,  $\phi = 0.135$ )

	Time Mean	Magnitude of Fluctuations
$\alpha$	$23.7^\circ$	$14.4^\circ$
$q^*$	0.134	0.094
$p_t^*$	0.600	0.152
$\beta$	$10.5^\circ$	$4.22^\circ$
$(w_u/u_2)$	0.775	0.142
$p^*$	0.464	0.128
$(c_u/u_2)$	0.334	0.142
$(c_r/u_2)$	0.145	0.067
$P_t^*$	1.09	0.258

Fig. 3.21. Presenting the results from the three-hole tube measurements for Impeller Z1 ( $\phi = 0.135$ ,  $r_3/R_2 = 1.11$ , rpm = 1200).

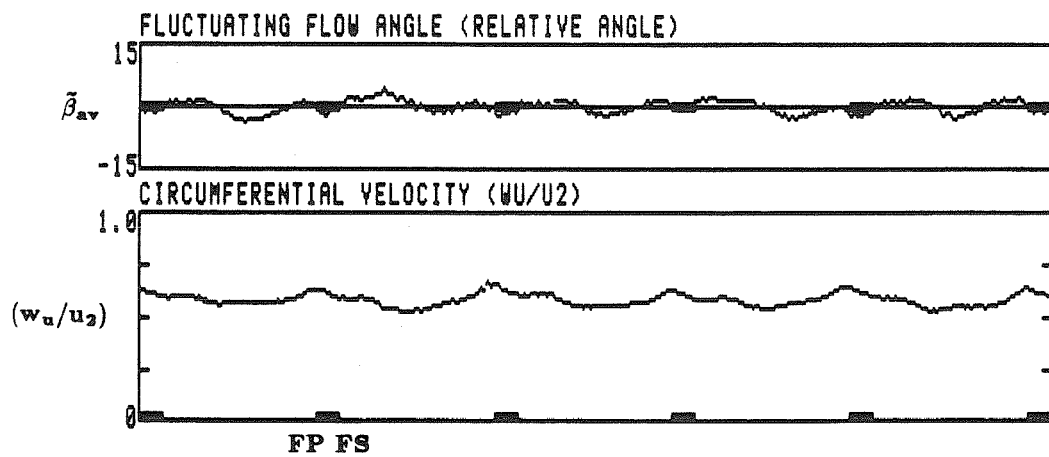
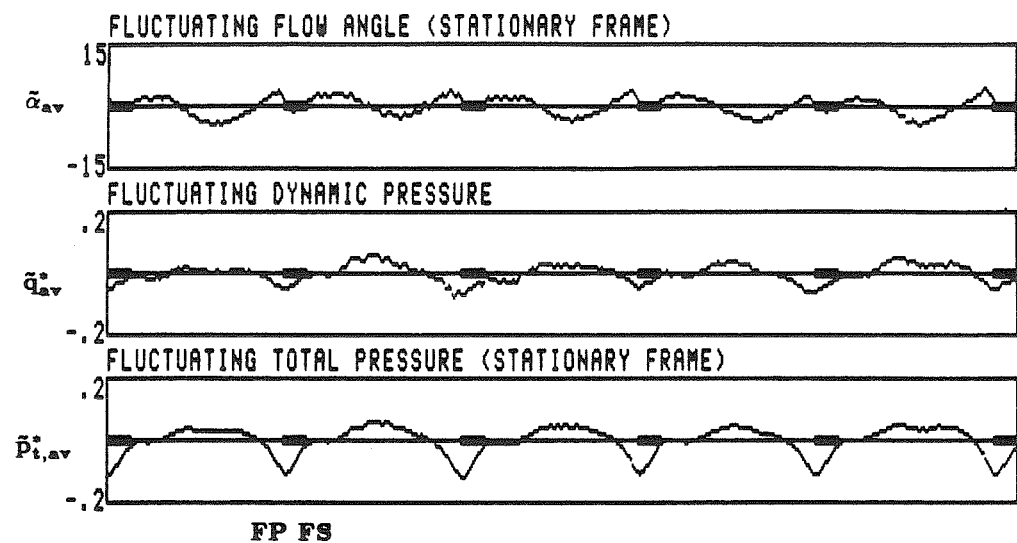


Fig. 3.22. Presenting the results from the three-hole tube measurements for Impeller Z1 ( $\phi = 0.10, r_3/R_2 = 1.08$ , rpm = 1200).

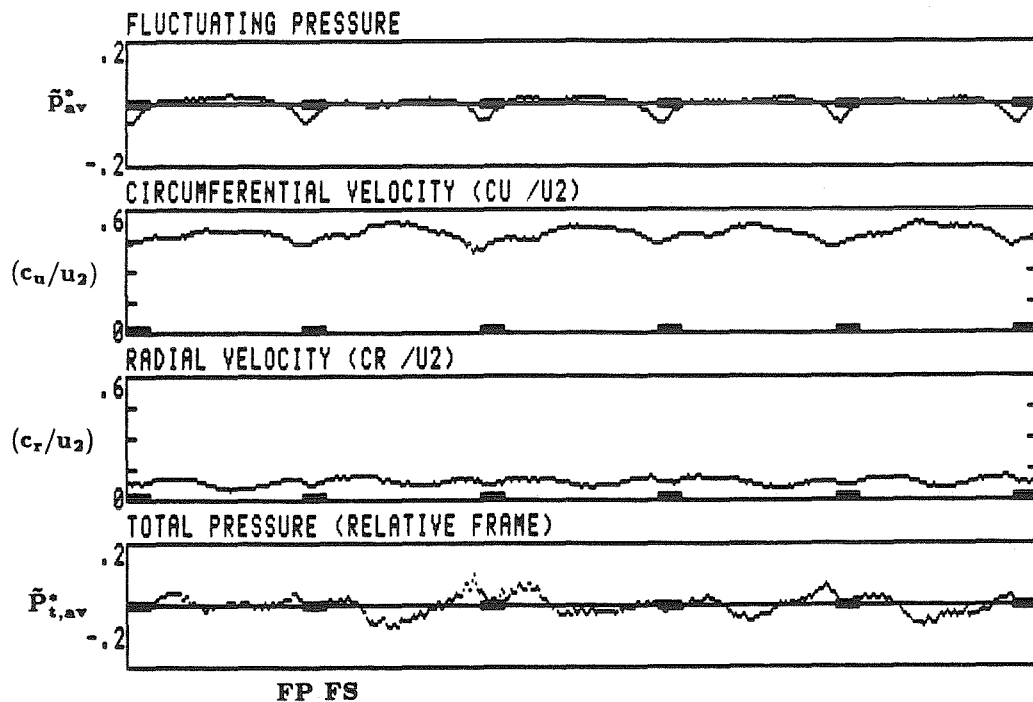


Table 3.5. Time Mean and Fluctuating Flow Measurements  
(Impeller Z1,  $r_3/R_2 = 1.08$ ,  $\phi = 0.10$ )

	Time Mean	Magnitude of Fluctuations
$\alpha$	$10.5^\circ$	$8.73^\circ$
$q^*$	0.242	0.142
$p_t^*$	0.866	0.183
$\beta$	$8.53^\circ$	$7.65^\circ$
$(w_u/u_2)$	0.597	0.150
$p^*$	0.625	0.090
$(c_u/u_2)$	0.482	0.150
$(c_r/u_2)$	0.090	0.079
$P_t^*$	0.999	0.168

Fig. 3.22. Presenting the results from the three-hole tube measurements for Impeller Z1 ( $\phi = 0.10$ ,  $r_3/R_2 = 1.08$ , rpm = 1200).

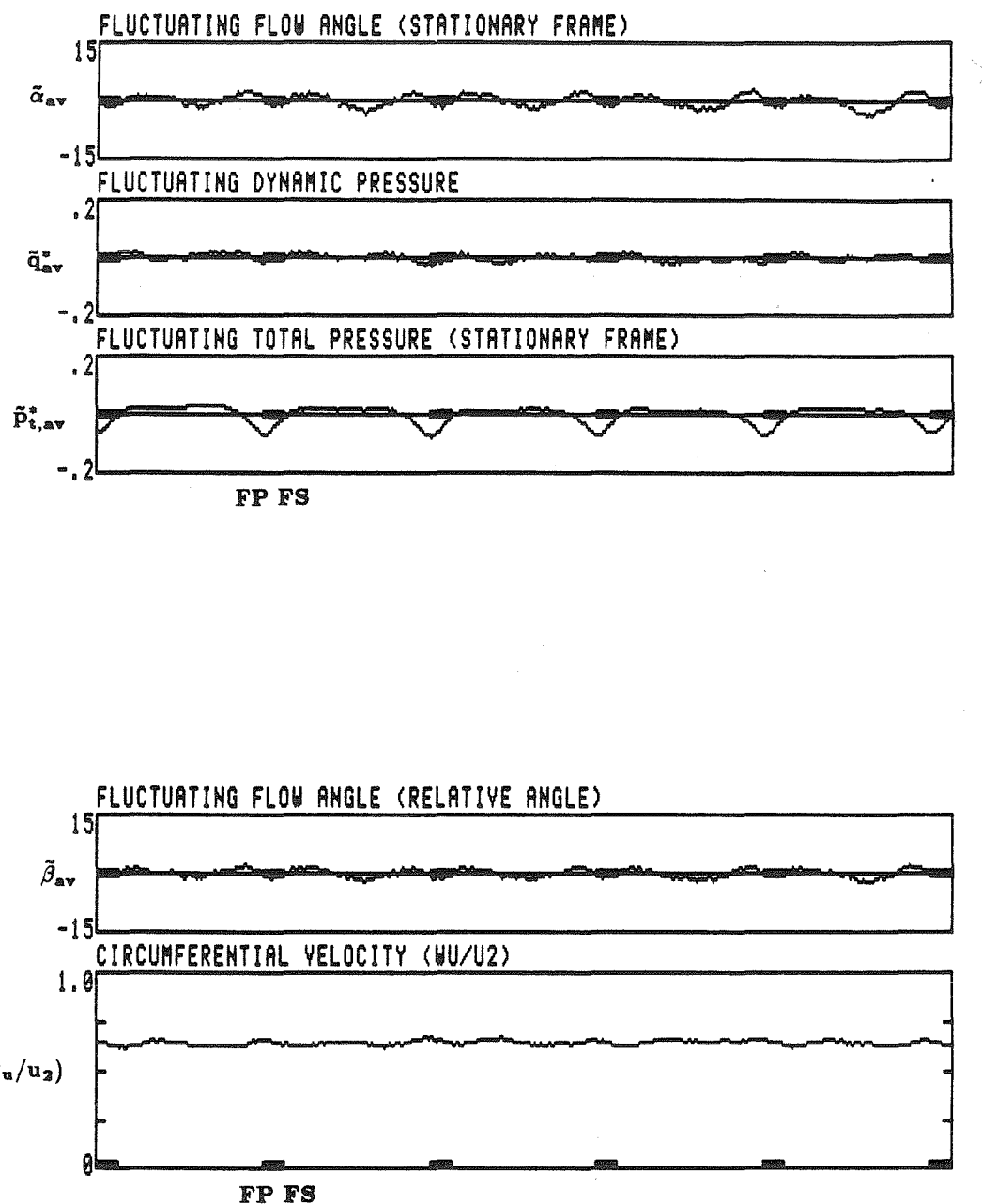


Fig. 3.23. Presenting the results from the three-hole tube measurements for Impeller Z1 ( $\phi = 0.10$ ,  $r_3/R_2 = 1.11$ , rpm = 1200).

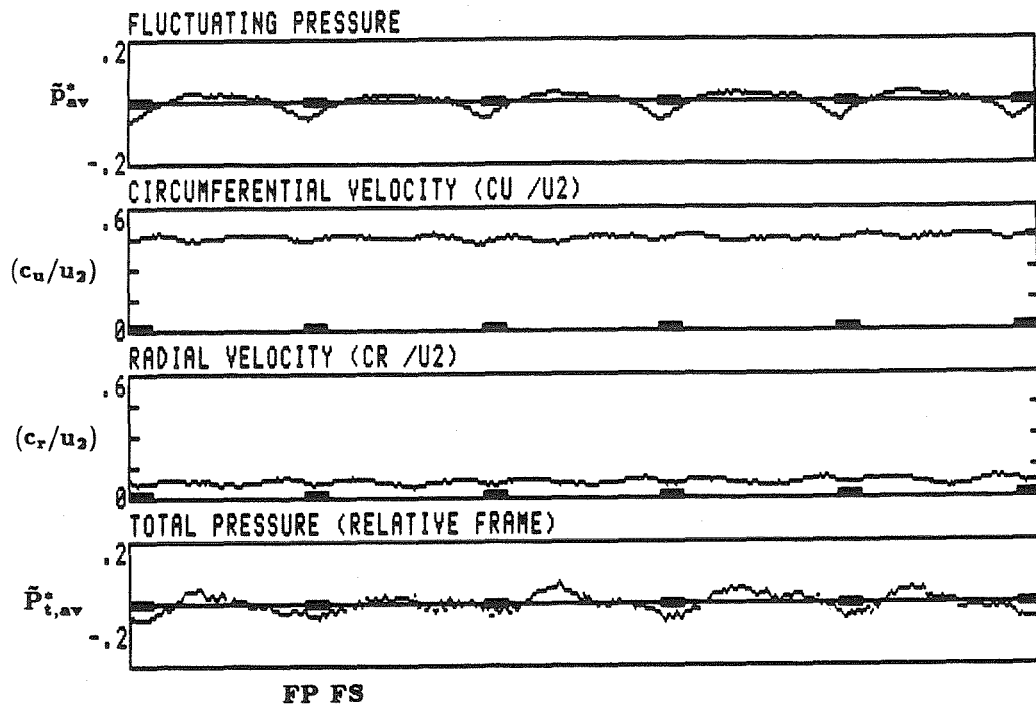


Table 3.6. Time Mean and Fluctuating Flow Measurements  
(Impeller Z1,  $r_3/R_2 = 1.11$ ,  $\phi = 0.10$ )

	Time Mean	Magnitude of Fluctuations
$\alpha$	9.95°	6.50°
$q^*$	0.210	0.050
$p_t^*$	0.848	0.108
$\beta$	6.90°	4.58°
$(w_u/u_2)$	0.658	0.053
$p^*$	0.638	0.095
$(c_u/u_2)$	0.452	0.053
$(c_r/u_2)$	0.079	0.063
$P_t^*$	1.07	0.127

Fig. 3.23. Presenting the results from the three-hole tube measurements for Impeller Z1 ( $\phi = 0.10$ ,  $r_3/R_2 = 1.11$ , rpm = 1200).

## CHAPTER 4

### 4. Total Pressure Measurements

#### 4.1. Introduction

Steady and unsteady total pressure measurements of the flow exiting two different centrifugal impellers, a two-dimensional impeller (Impeller Z1) and one half of the double suction pump impeller of the HPOTP (High Pressure Oxygen Turbopump) of the SSME (Space Shuttle Main Engine) into the vaneless diffuser of a volute with trapezoidal cross section (Volute D) are presented. The measurements were made by inserting a total pressure probe (figure 4.1) into the diffuser channel (figure 4.2). The total pressure probe with an inner diameter of 0.050 in (0.63 mm) was used for both the steady and unsteady total pressure measurements. The total pressure probe was aligned at an angle of 20 degrees. The total pressure probe alignment angle,  $\gamma$ , was defined as the angle between the centerline of the probe and the tangent to the circular orbit through the center of the probe at the orifice, centered at the center of the impeller rotation (see figure 4.2). Recalling from the total pressure calibration that the measurement error of the total pressure probe due to probe orientation flow direction misalignment was less than 2% of the dynamic pressure of the flow for misalignment angles smaller than  $\pm 15$  degrees, and less than 6% of the dynamic pressure of the flow for misalignment angles smaller than  $\pm 20$  degrees, the measurement error for the total pressure due to misalignment was considered negligible.

The total pressure probe could be positioned at different positions between the diffuser shroud (or front side wall) and the diffuser hub (or rear side wall). Thus, for both impellers, measurements were taken at different axial locations  $z/b$ , where  $z$  is the distance of the center of the total pressure probe from the diffuser shroud and  $b$  is the diffuser inlet width, and for different ratios  $r_3/R_2$  between the

center of the total pressure probe and the impeller blade trailing edge, where  $r$  is the distance of the total pressure probe center measured from the center of the impeller rotation and  $R_2$  is the impeller blade trailing edge (= impeller discharge) radius. Different ratios  $r_3/R_2$  were attained by positioning the impeller on different locations eccentric to the volute

The total pressure fluctuations were found to be of the same order of magnitude as the total pressure rise across the pump, and they decreased strongly with increasing  $r_3/R_2$ .

## 4.2. Measurements for Impeller R and Volute D

### 4.2.1. Steady Total Pressure Measurements

The steady total pressure measurements are presented as a steady total pressure coefficient, normalized by the dynamic pressure based on impeller tip speed,

$$\bar{c}_{pt} = \frac{(\bar{p}_t - \bar{p}_{up})}{(1/2)\rho u_2^2}. \quad (4.1)$$

Figure 4.3 shows the steady total pressure measurements for Impeller R and Volute D taken at five different axial locations  $z/b$  between the diffuser shroud and the diffuser hub for  $r_3/R_2 = 1.05$ , 1200 rpm, and for four flow coefficients,  $\phi = 0.14$  (maximum flow coefficient),  $\phi = 0.12$  (the "best efficiency" flow coefficient for Impeller R and Diffuser S),  $\phi = 0.09$  and  $0.06$ . It can be seen that the steady total pressure is largest for the smallest flow coefficient investigated,  $\phi = 0.06$ , and decreases with increasing flow coefficient. The total pressure increases across the volute from  $z/b = 0.20$  to  $z/b = 0.62$  and then decreases slightly from  $z/b = 0.62$  to  $z/b = 0.82$  for all four flow coefficients with the exception of  $\phi = 0.06$ , for which the total pressure continues to increase from  $z/b = 0.62$  to  $z/b = 0.82$ . The relative increase of the steady total pressure across the volute is largest for the smallest flow coefficient investigated,  $\phi = 0.06$ , and smallest for the two large flow coefficients,  $\phi = 0.14$  and  $\phi = 0.12$ .

#### 4.2.2. Ensemble Averaged Unsteady Total Pressure Measurements

The unsteady total pressure measurements were ensemble averaged and normalized by the dynamic pressure based on impeller tip speed. As an averaging period, a full and a partial impeller blade passage were used. For  $r_3/R_2 = 1.02$ , total pressure measurements were made only near the center of the diffuser center of Volute D,  $z/b = 0.47$ . For  $r_3/R_2 = 1.05$ , total pressure measurements were made at a total of five locations between the diffuser shroud and the diffuser hub,  $z/b = 0.20, 0.33, 0.47, 0.62$  and  $0.82$ . Thus, the variations of the unsteady total pressure fluctuations across the diffuser using Impeller R could be compared to those measured using Impeller Z1 for similar ratios  $r_2/R_3$  (1.05 and 1.055, respectively).

In figure 4.4, the magnitudes of the ensemble averaged total pressure fluctuations measured near the center of the diffuser,  $z/b = 0.47$ , are presented for  $r_3/R_2 = 1.02$  and  $1.05$  and four flow coefficients,  $\phi = 0.14, 0.12, 0.09$  and  $0.06$ . It can be seen that the total pressure fluctuations are of the same order of magnitude as the total pressure rise across the pump. The fluctuations are largest for maximum flow coefficient, and decreased with decreasing flow coefficient. Increasing the radial distance between the impeller discharge and the total pressure probe results in a significant decrease of the total pressure fluctuations for the flow coefficients investigated.

In the next figure (figure 4.5), ensemble averaged unsteady total pressure measurements for  $\phi = 0.12$  and  $r_3/R_2 = 1.02$  and  $1.05$  are shown for the passage of one full and one partial impeller blade. Discussing first the measurements for  $r_2/R_3 = 1.02$ , it can be seen that the total pressure increases very steeply from its minimum value which is attained at the pressure side of the trailing edge to its maximum value which is attained at the suction side of the blade trailing edge. The impeller wakes, characterized by high total pressure fluid in the absolute frame of reference (see also Chapter 3), are located on the suction side of both the full and the partial impeller blade. For the full blade, the wake is rather distinct, and its width is about 15% of one impeller blade passage. Furthermore, it can be seen that

the wakes shed by partial and full impeller blades are slightly different.

The measurements for  $r_3/R_2 = 1.05$  show the rapid mixing of the wake flow and the significant decrease of the total pressure fluctuations. The mixing of the wakes shed by partial and full impeller blades is very different. The wake of the partial impeller blade can still be noticed by the high total pressure fluid on the partial blade suction side. The wake of the full blade, however, seems to have mixed out entirely. The low total pressure regions at the pressure side of the blade trailing edges, however, are very similar for the full and the partial impeller blade. As already shown in the discussion of the three-hole tube measurements, this region of low total pressure fluid can still be found at large ratios  $r_3/R_2$  (i.e.,  $r_3/R_2 = 1.11$  for Impeller Z1). The reason why the wake, i.e., the high total pressure fluid on the blade suction side, mixes differently fast for full and partial impeller blades, and the low total pressure fluid at the pressure side of the blade trailing edge mixes similarly for the partial and the full blades may be explained as follows. The structure of the wake on the impeller blade suction side is influenced significantly by the length of the impeller blade. Thus, it is not surprising that differences of the wakes shed by full and partial blades may be found. The low total pressure fluid on the pressure side of the trailing edge, however, seems to stem from the turning of the pressure side fluid around the pressure side corner of the trailing edge. In the discussion for the three-hole tube measurements for Impeller Z1 it was found that total pressure and pressure minima were in phase at the pressure side corner at the trailing edge. The magnitude of those pressure fluctuations, as reported by Furukawa et al. (1987), seems to depend strongly upon the thickness of the trailing edge. If it is assumed that the jet flow in the impeller blade channel, in contrast to the wake flow, does not depend strongly upon the impeller blade length, then the flow around the pressure side corner of the impeller blade trailing edge will be similar for the full and the partial impeller blades, and hence the resulting pressure and total pressure fluctuations at the pressure side of the impeller blade trailing edge should be similar for the full and the partial blades.

In figure 4.6 the magnitudes of the ensemble averaged total pressure fluctu-

ations between the shroud and the hub of Volute D for  $r_3/R_2 = 1.05$  and three different flow coefficients,  $\phi = 0.14, 0.12$  and  $0.09$  are presented. Across the diffuser, the magnitude of the total pressure fluctuations varies significantly, increasing by about a factor of two for all flow coefficients from the measurement position near the shroud,  $z/b = 0.20$ , to the measurement position at  $z/b = 0.62$ , and then drops slightly at the measurement position near the hub,  $z/b = 0.82$ . With the exception of the measurement locations near the hub,  $z/b = 0.82$ , the fluctuations at all other measurement locations are largest for maximum flow,  $\phi = 0.14$ , and decrease with decreasing flow coefficient. Near the hub, the fluctuations are approximately equal for all three flow coefficients investigated ( $\phi = 0.14, 0.12$  and  $0.09$ ).

Not only the magnitude of the pressure fluctuations, but also the total pressure profile differs with the axial measurement location. In figures 4.7–4.9, the ensemble averaged total pressure fluctuations at the five axial measurements are presented for the three flow coefficients,  $\phi = 0.14$  (figure 4.7),  $\phi = 0.12$  (figure 4.8), and  $\phi = 0.09$  (figure 4.9). While the minimum total pressure always occurs at the pressure side of the impeller blades, the main difference in the total pressure profile for different axial measurement locations and flow coefficients is the occurrence or nonoccurrence of high total pressure fluid on the impeller blade suction side. At  $z/b = 0.82$  and  $0.62$ , high total pressure fluid is observed at the suction side of both full and partial impeller blades, for all flow coefficients. Near the center of the diffuser channel,  $z/b = 0.47$ , the total pressure profile for maximum flow,  $\phi = 0.14$ , is similar to the one at  $z/b = 0.62$ ; however, for lower flow coefficients,  $\phi = 0.12$  and  $0.09$ , the high total pressure fluid can only be found at the suction side of the partial blades but not at the suction side of the full blades. At  $z/b = 0.33$  and  $0.20$ , for the two larger flow coefficients,  $\phi = 0.14$  and  $0.12$ , the total pressure profile is different than it is at  $z/b = 0.82$  and  $0.62$ . The total pressure maxima occur closer to the impeller blade pressure side than to the impeller blade suction side. Thus, the locations of the maxima of the total pressure are different near the hub than near the shroud. Finally, the largest difference in the total pressure measurements between full and partial impeller blades was found at the center of the diffuser channel,  $z/b = 0.47$ ,

for  $\phi = 0.12$  and  $0.09$ .

### 4.3. Measurements for Impeller Z1 and Volute D

#### 4.3.1. Steady Total Pressure Measurements

Steady total pressure measurements for the two-dimensional test impeller, Impeller Z1, are presented in figure 4.10. The measurements were made at five locations,  $z/b$ , between the diffuser shroud and the diffuser hub of Volute D (the locations,  $z/b$ , are identical for Impeller R and Impeller Z1), for three flow coefficients,  $\phi = 0.133, 0.10$  and  $0.06$  and  $r_3/R_2 = 1.055$ . For the maximum flow coefficient,  $\phi = 0.133$ , the total pressure profile is nearly uniform across the volute. For the two lower flow coefficients,  $\phi = 0.10$  and  $0.06$ , however, the total pressure increases from shroud to hub. The increase is, as for Impeller R, strongest for the lowest flow coefficient,  $\phi = 0.06$ . The relative increase in total pressure from shroud to hub for Impeller R and Impeller Z1 is approximately equal.

#### 4.3.2. Ensemble Averaged Unsteady Total Pressure Measurements

Unsteady total pressure measurements for Impeller Z1 were made for two flow coefficients,  $\phi = 0.133$  and  $0.10$ , at five locations between the diffuser shroud and the diffuser hub, and two different radial gaps between the impeller discharge and the total pressure probe,  $r_3/R_2 = 1.055$  and  $1.085$ . The shaft speed was 1200 rpm. The unsteady measurements were ensemble averaged over one shaft revolution, corresponding to five impeller blade passages. The magnitude of the ensemble averaged total pressure fluctuations are presented in figure 4.11. In contrast to Impeller R, the magnitude of the total pressure fluctuations does not vary strongly between the diffuser shroud and the diffuser hub. Especially for maximum flow coefficient,  $\phi = 0.133$ , the total pressure fluctuations are nearly constant. For  $\phi = 0.10$ , they are largest at the measurement location near the hub,  $z/b = 0.82$ , and smallest near the shroud,  $z/b = 0.20$ . Furthermore, the fluctuations are at

most measurement locations larger for  $\phi = 0.10$  than for maximum flow,  $\phi = 0.133$ . Profiles of the ensemble averaged total pressure measurements for Impeller Z1 at 1200 rpm and  $r_3/R_2 = 1.055$  are presented for maximum flow,  $\phi = 0.133$ , in figure 4.12 and for  $\phi = 0.10$  in figure 4.13. Since the total pressure measurements made for Impeller Z1 and Diffuser T at the center of the diffuser have already been discussed in detail in the previous chapter, the total pressure measurements in Volute D will be discussed only briefly. Turning to the maximum flow coefficient,  $\phi = 0.133$ , first, it can be seen that the differences of the ensemble averaged unsteady total pressure profiles taken at different axial locations of the diffuser of Volute D are small. Comparing the measurements for the respective maximum flow coefficients for Impeller R and Impeller Z1 at nearly identical radial gaps to the respective impeller discharge,  $r_3/R_2 = 1.05$  and  $1.055$ , it is evident that the ensemble averaged unsteady total pressure profile has truly "three-dimensional" character for Impeller R (i.e., the profile varies strongly at the different axial measurement locations), and a nearly "two-dimensional" character for Impeller Z1 (i.e., the profile varies not significantly at the different axial measurement locations). At the measurement locations near the hub,  $z/b = 0.82$ , and near the shroud,  $z/b = 0.20$  and  $0.33$ , the magnitudes of the total pressure fluctuations are approximately equal for the two impellers; at the measurement locations at the diffuser center, however, they are significantly larger for Impeller R than for Impeller Z1.

Turning to the lower flow coefficient,  $\phi = 0.10$ , it can be seen that the location of the maximum total pressure changes with different axial measurement locations. Near the hub,  $z/b = 0.82$ , it is attained at the impeller blade suction side (similar to measurements for Impeller R), at the two "center" positions,  $z/b = 0.62$  and  $0.47$ , there are two maxima, one at the impeller blade suction side, the other closer to the blade pressure than the blade suction side (similar to Impeller R for  $\phi = 0.09$  at  $z/b = 0.47$  and  $0.33$ ), whereas at the two positions near the shroud the maximum total pressure is attained approximately at the center of the impeller blade channel. The unsteady ensemble averaged total pressure profiles between diffuser shroud and diffuser hub are not quite as uniform as they are for maximum flow,  $\phi = 0.133$ , but

are still more uniform than for a comparable flow coefficient for Impeller R.

#### 4.4. Ensemble Averaged Unsteady Total Pressure Measurements for Impeller Z1 and Diffuser S

Herein, total pressure measurements made between the vanes of a vaned diffuser, Diffuser S, will be presented. The measurements were made at four locations between the vane suction and the vane pressure side of adjacent vanes at the center of the diffuser for radial gaps between the total pressure probe tip and the impeller blade trailing edge of 7.2% and 10.3% of the impeller blade discharge radius (the angular position of the orifice of the total pressure probe with respect to the leading edge of a diffuser vane is given in the Appendix). Since the gap between diffuser vanes and impeller blades was 5% and 8%, the total pressure probe tip was positioned inside the vane channel ( $r_3/R_3 = 1.02$ ), not in the space between the impeller blades and the diffuser vanes. For comparison, total pressure measurements were made in a vaneless diffuser of identical sidewall geometry (Diffuser T) at identical ratios  $r_3/R_2$ . In figures 4.14 and 4.15, the ensemble averaged unsteady total pressure measurements are presented. In the upper part of each figure, the four measurements made between the diffuser vanes of Diffuser S are shown, with the uppermost of those four measurements corresponding to the measurement location closest to the vane suction side, and the lowermost of those four measurements corresponding to the measurement location closest to the vane pressure side. In the lower part of each figure, the measurements made with the vaneless diffuser, Diffuser T, are presented.

The measurements for the smaller radial gap,  $R_3/R_2 = 1.05$ , will be examined first. It can be seen that the total pressure fluctuations at all four measurement locations between the diffuser vanes of Diffuser S are larger than the total pressure fluctuations in the vaneless diffuser, Diffuser T. The largest total pressure fluctuations occur at the measurement location closest to the suction side. Thus, the presence of the diffuser vanes does increase the magnitude of the total pressure

fluctuations.

The measurements for the larger radial gap are presented in figure 4.15. As already pointed out for the smaller radial gap, the magnitude of the total pressure fluctuations is larger for the vaned than for the vaneless diffuser. Comparing the decrease in the magnitude of the total pressure fluctuations with increasing radial gap for the vaneless and the vane diffuser, it can be seen that the total pressure fluctuations decrease more strongly for the vaneless than for the vaned diffuser. Especially at the measurement location close to the vane suction side, where the total pressure fluctuations are largest, they decrease only by about 20%; whereas for the vaneless diffuser, they decrease by about 45%. Thus, for the larger radial gap, the fluctuations at the measurement location close to the vane suction side are nearly twice as large than the ones in the vaneless diffuser. In contrast, for the smaller radial gap, they are only about 40% larger.

#### 4.5. Summary

Steady and unsteady total pressure measurements were made at the discharge of two centrifugal impellers in the vaneless diffuser of a volute. The total pressure fluctuations "close" to the impeller discharge,  $r_3/R_2 = 1.02$ , were found to be of the same order of magnitude as the total pressure rise across the pump. The total pressure fluctuations were largest for maximum flow and decreased with decreasing flow coefficient. With increasing distance from the impeller discharge, the total pressure fluctuations decreased significantly. For some flow coefficients,  $\phi \leq 0.12$ , the impeller wakes shed by the full and the partial blades of Impeller R were found to mix out differently. The partial blade wakes were found to extend farther downstream from the impeller discharge than the full blade wakes. The low total pressure fluid on the pressure side of the blade trailing edge, however, was found to mix out similarly for full and partial impeller blades. For Impeller R, the magnitude of the total pressure fluctuations varied strongly between the volute shroud and the volute hub.

For Impeller Z1 (the two-dimensional test impeller), those axial variations of the total pressure fluctuations were found to be much smaller.

For Impeller Z1, total pressure measurements were also made at four locations between the vane suction side and the vane pressure side in Diffuser S. These measurements were compared to measurements made in the vaneless Diffuser T. It was found that the presence of the diffuser vanes increased the magnitude of the total pressure fluctuations. The largest total pressure fluctuations were found at the measurement location closest to the vane suction side.

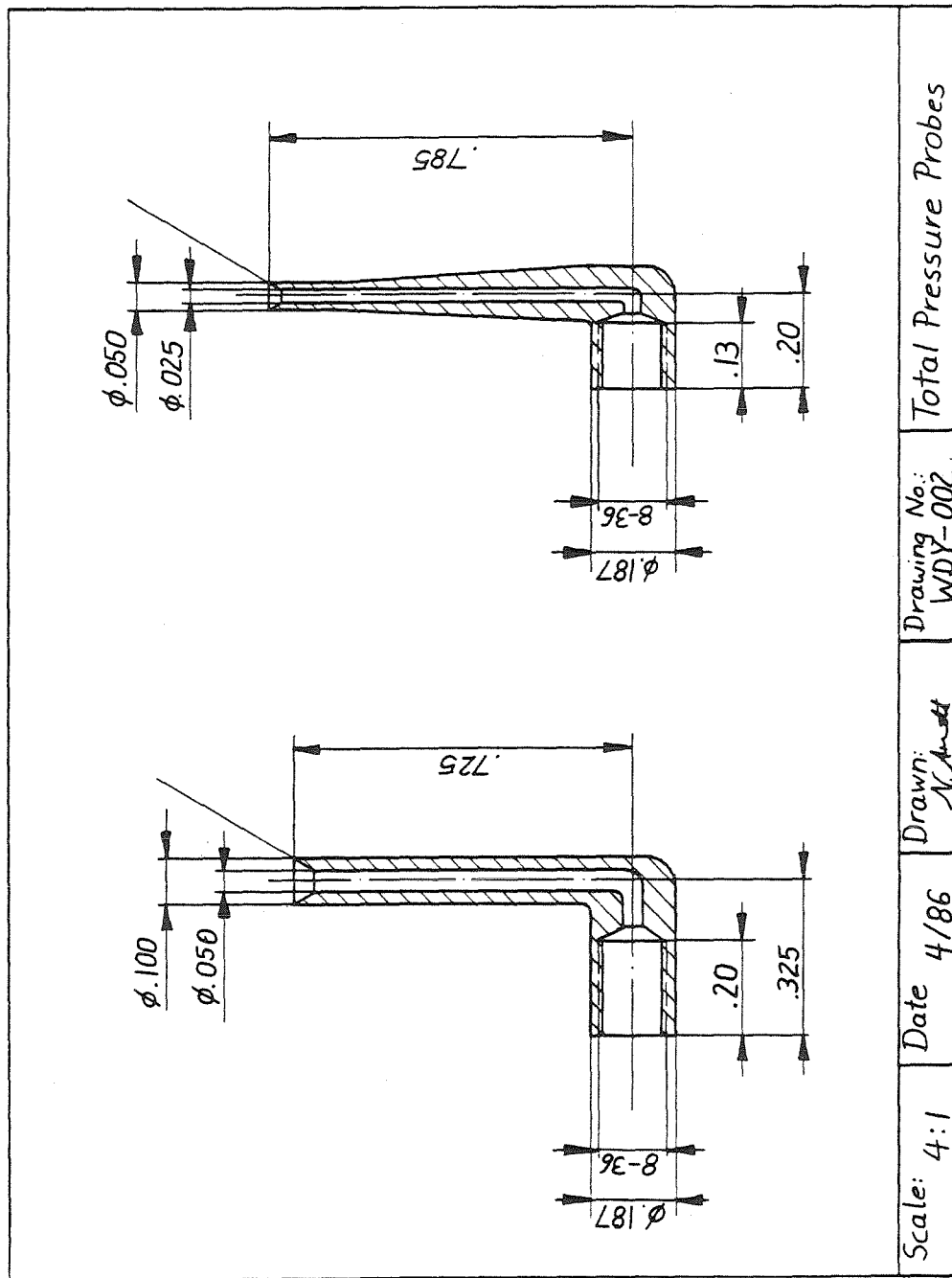


Fig. 4.1. Machine drawing of the total pressure probe.

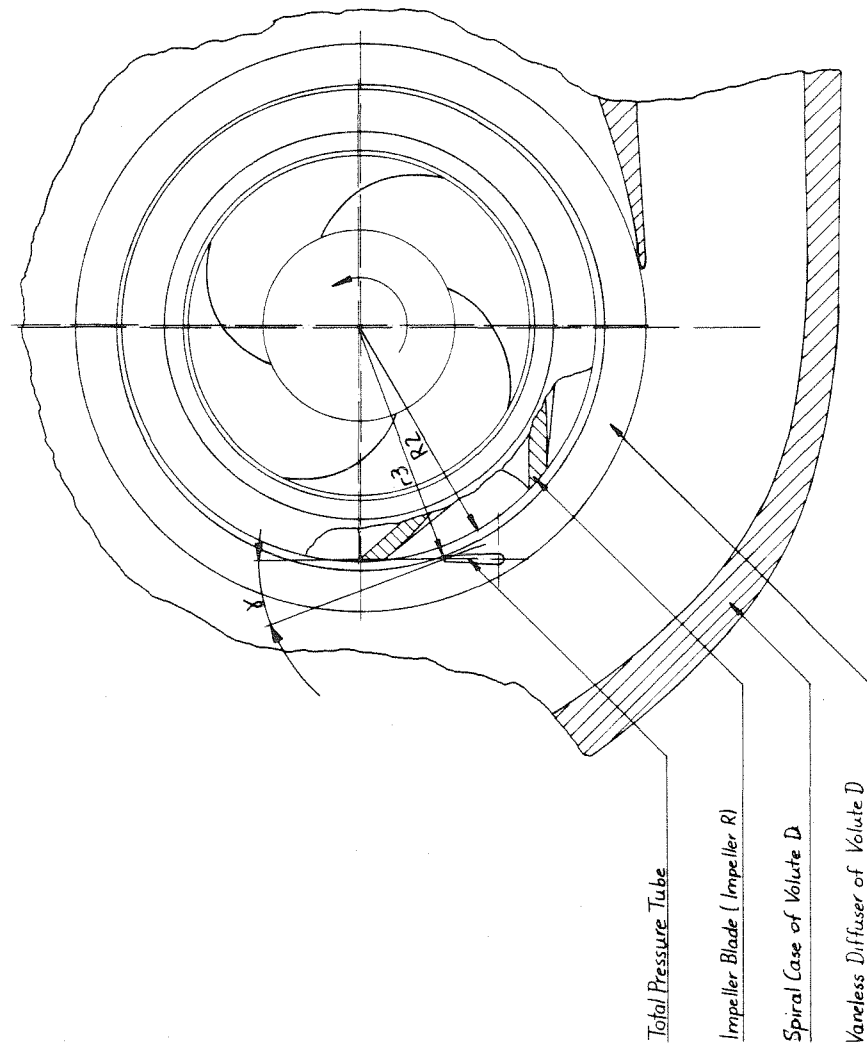


Fig. 4.2. Installation of the total pressure probe in Volute D.

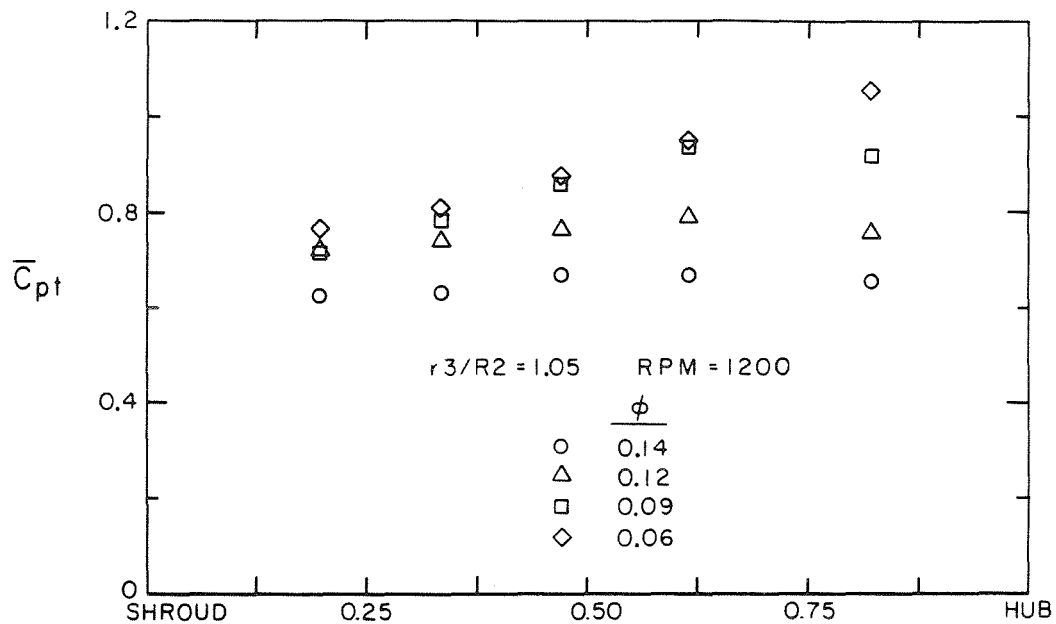


Fig. 4.3. Steady total pressure measurements for Impeller R and Volute D between the volute shroud and the volute hub ( $\phi = 0.14, 0.12, 0.09$  and  $0.06, r_3/R_2 = 1.05$ , rpm = 1200).

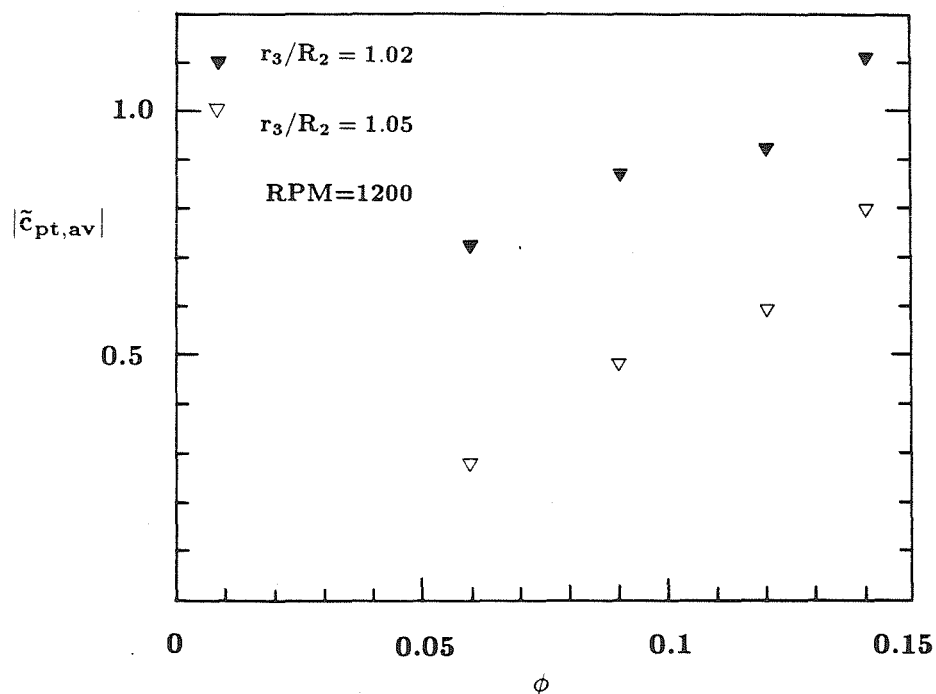
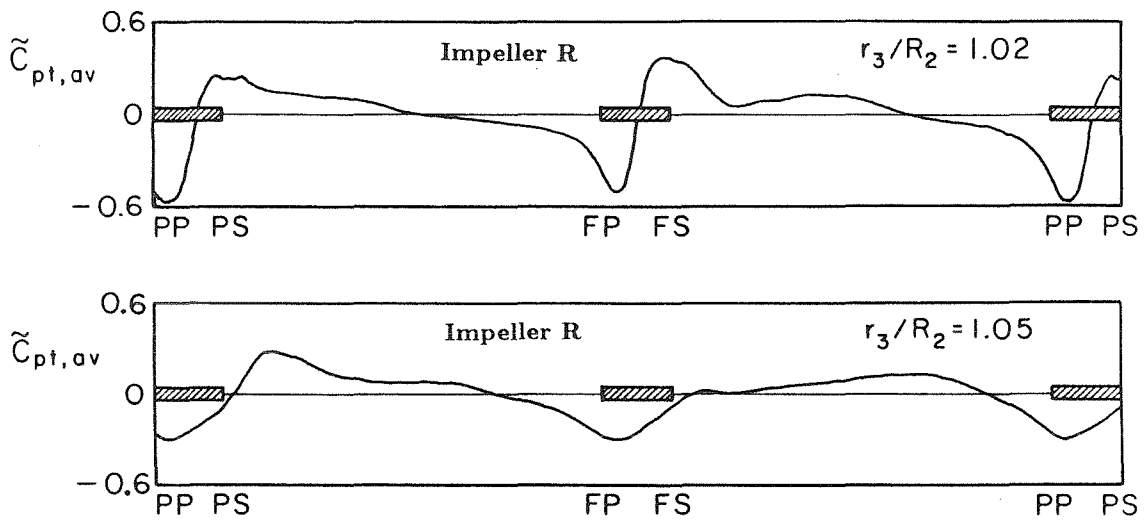
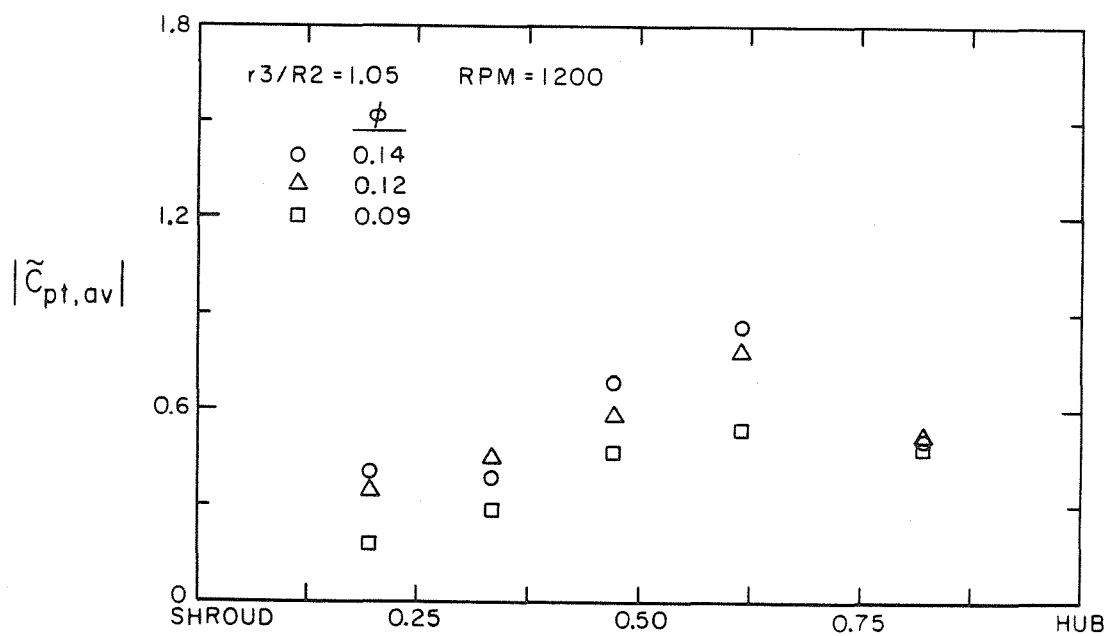


Fig. 4.4. Magnitude of ensemble averaged unsteady total pressure fluctuations for Impeller R and Volute D at  $z/b = 0.47$  ( $\phi = 0.14, 0.12$ , and  $0.09, r_3/R_2 = 1.02$  and  $1.05$ , rpm = 1200).



**Fig. 4.5.** Ensemble averaged unsteady total pressure measurements for Impeller R and Volute D at  $z/b = 0.47$  ( $\phi = 0.12$ ,  $r_3/R_2 = 1.02$  and  $1.05$ , rpm = 1200).



**Fig. 4.6.** Magnitude of ensemble averaged unsteady total pressure fluctuations for Impeller R and Volute D between the volute shroud and the volute hub ( $\phi = 0.14, 0.12$ , and  $0.09$ ,  $r_3/R_2 = 1.05$ , rpm = 1200).

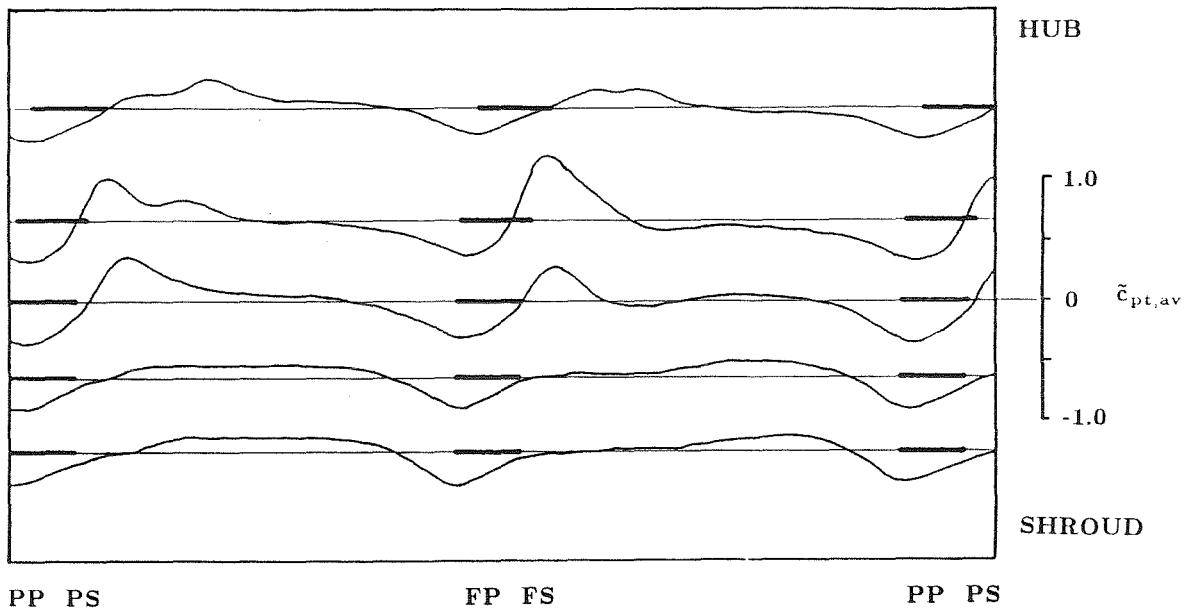


Fig. 4.7. Ensemble averaged unsteady total pressure measurements for Impeller R and Volute D between the volute shroud and the volute hub ( $\phi = 0.14, r_3/R_2 = 1.05$ , rpm = 1200).

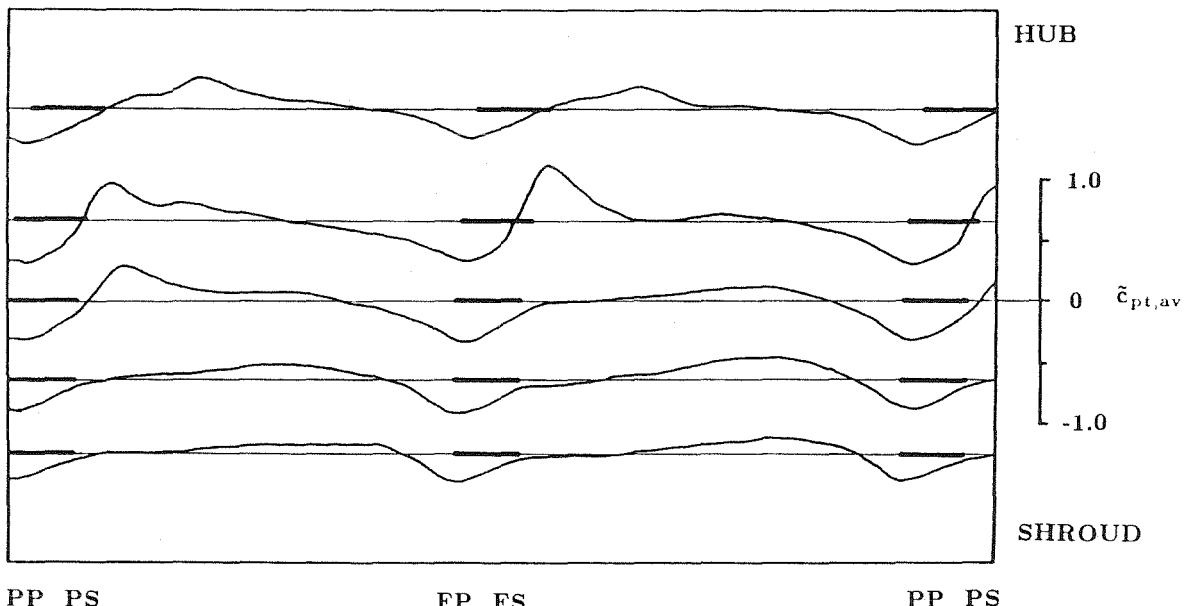
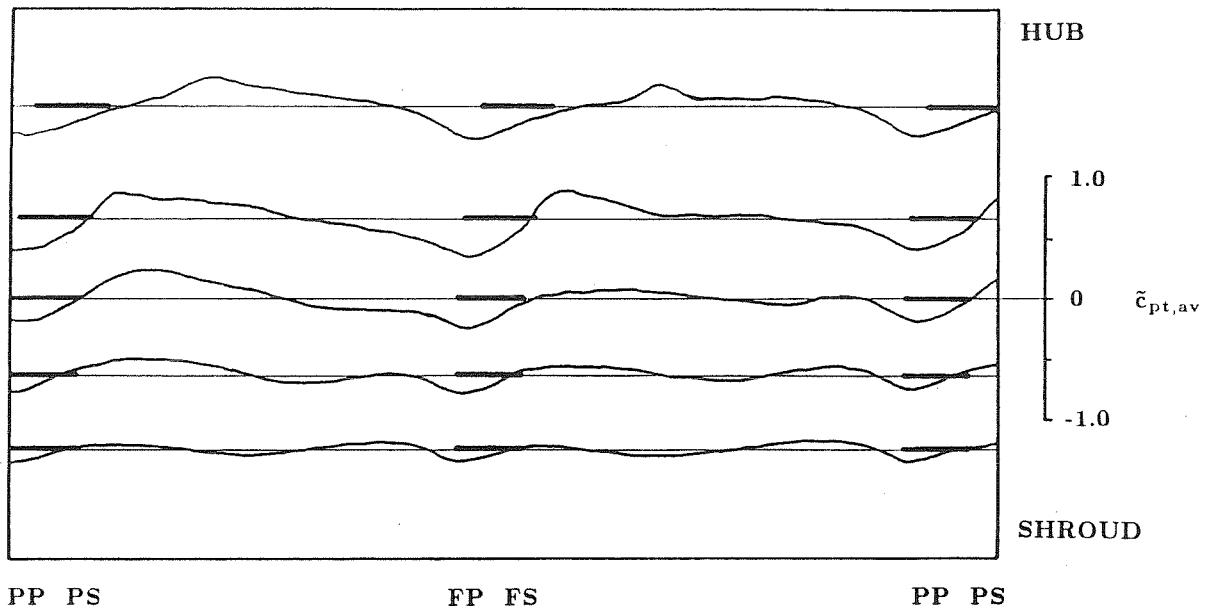


Fig. 4.8. Ensemble averaged unsteady total pressure measurements for Impeller R and Volute D between the volute shroud and the volute hub ( $\phi = 0.12, r_3/R_2 = 1.05$ , rpm = 1200).



**Fig. 4.9.** Ensemble averaged unsteady total pressure measurements for Impeller R and Volute D between the volute shroud and the volute hub ( $\phi = 0.09, r_3/R_2 = 1.05$ , rpm = 1200).

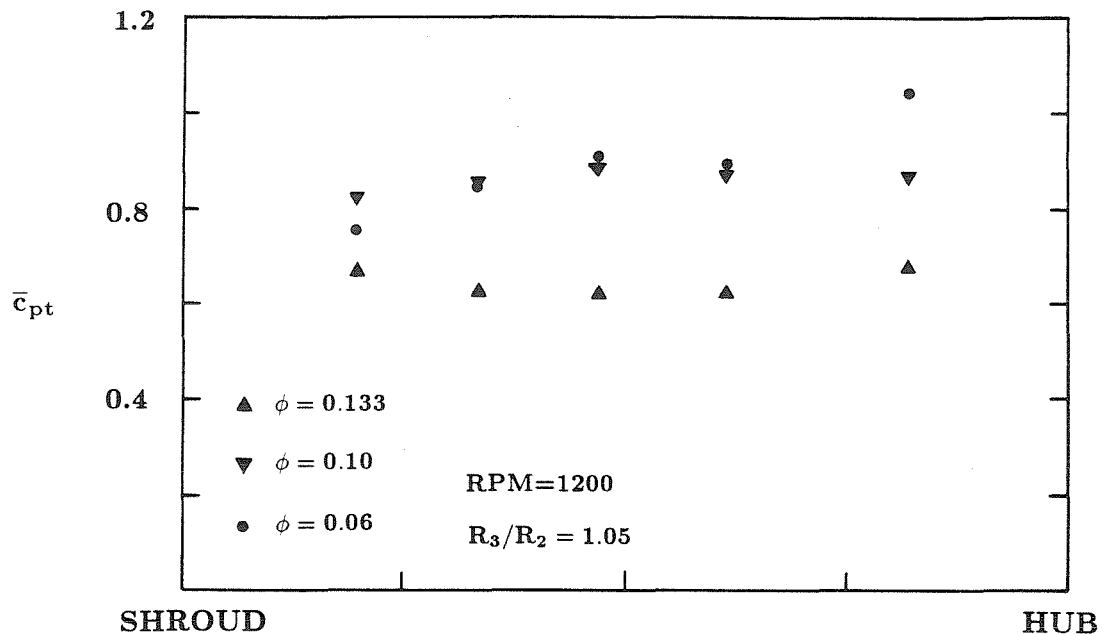


Fig. 4.10. Steady total pressure measurements for Impeller Z1 and Volute D between the volute shroud and the volute hub ( $\phi = 0.133, 0.10$ , and  $0.06, r_3/R_2 = 1.055$ , rpm = 1200).

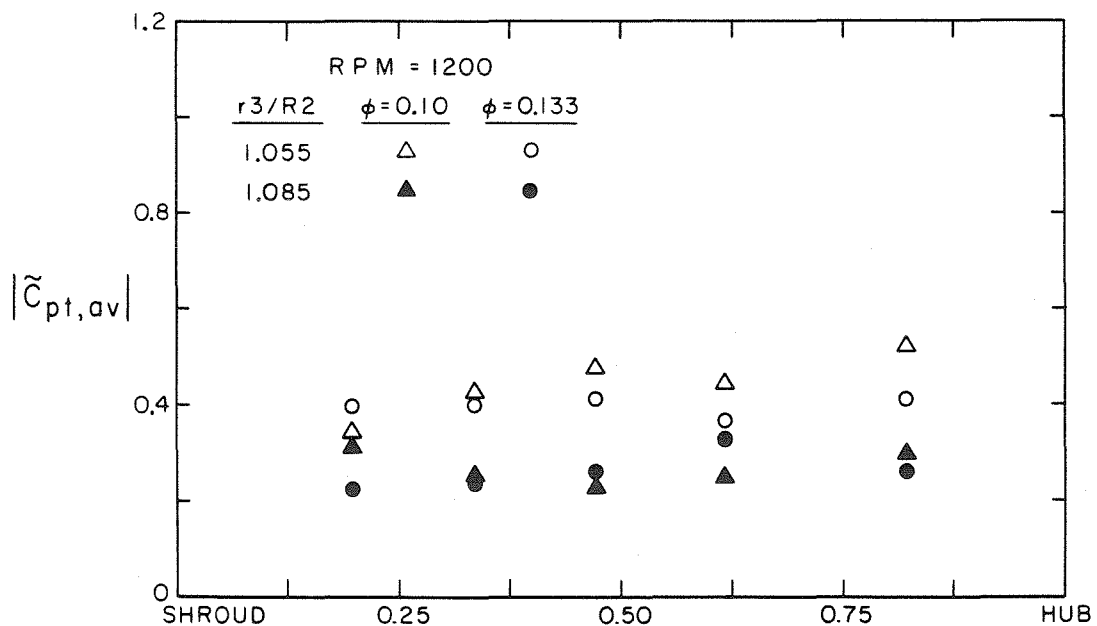


Fig. 4.11. Magnitude of ensemble averaged unsteady total pressure fluctuations for Impeller Z1 and Volute D between the volute shroud and the volute hub ( $\phi = 0.133$  and  $0.10, r_3/R_2 = 1.055$  and  $1.085$ , rpm = 1200).

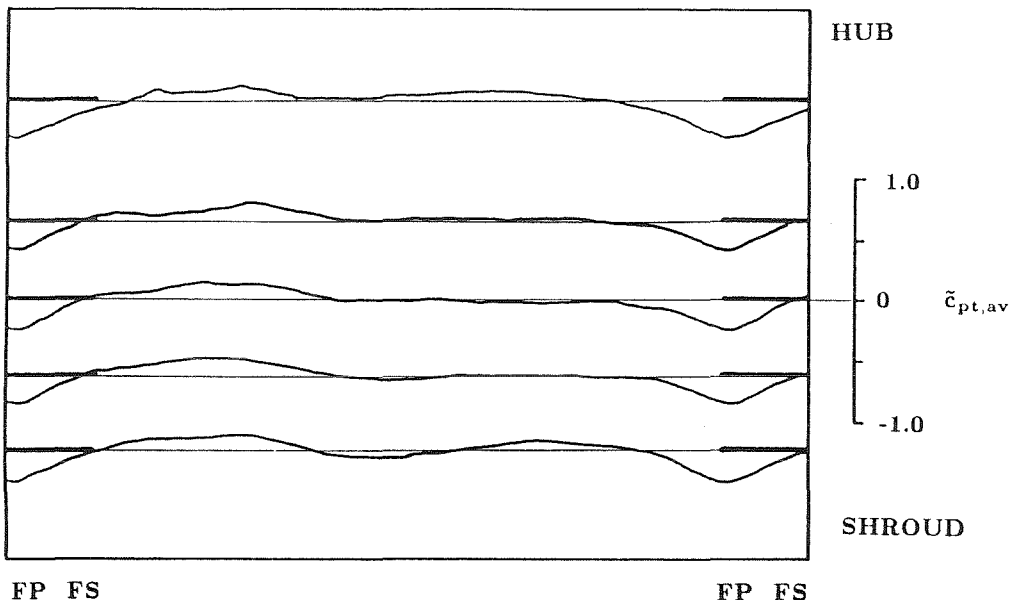


Fig. 4.12. Ensemble averaged unsteady total pressure measurements for Impeller Z1 and Volute D between the volute shroud and the volute hub ( $\phi = 0.133$ ,  $r_3/R_2 = 1.055$ , rpm = 1200).

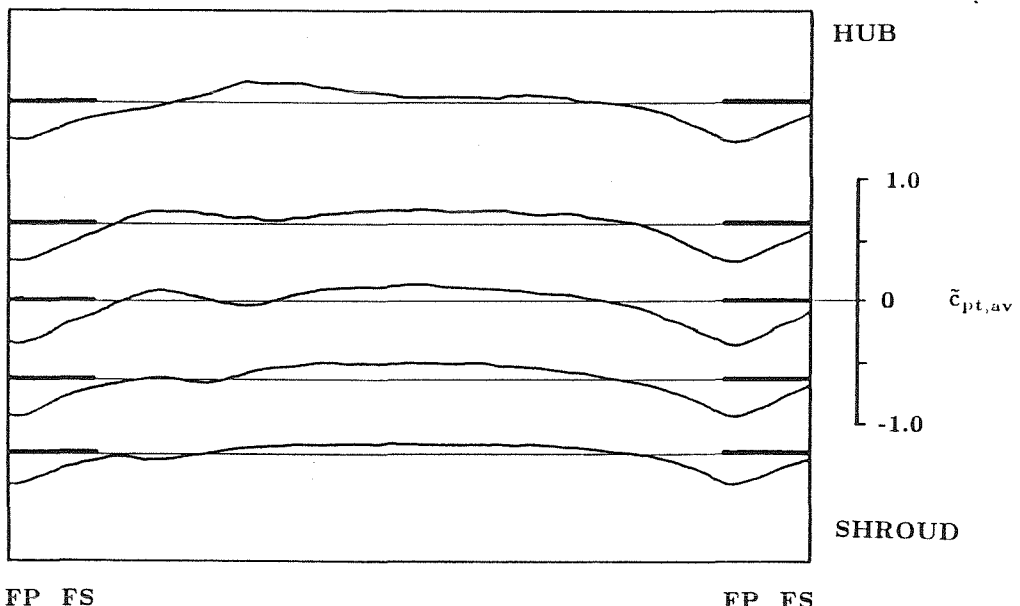


Fig. 4.13. Ensemble averaged unsteady total pressure measurements for Impeller Z1 and Volute D between the volute shroud and the volute hub ( $\phi = 0.10$ ,  $r_3/R_2 = 1.055$ , rpm = 1200).

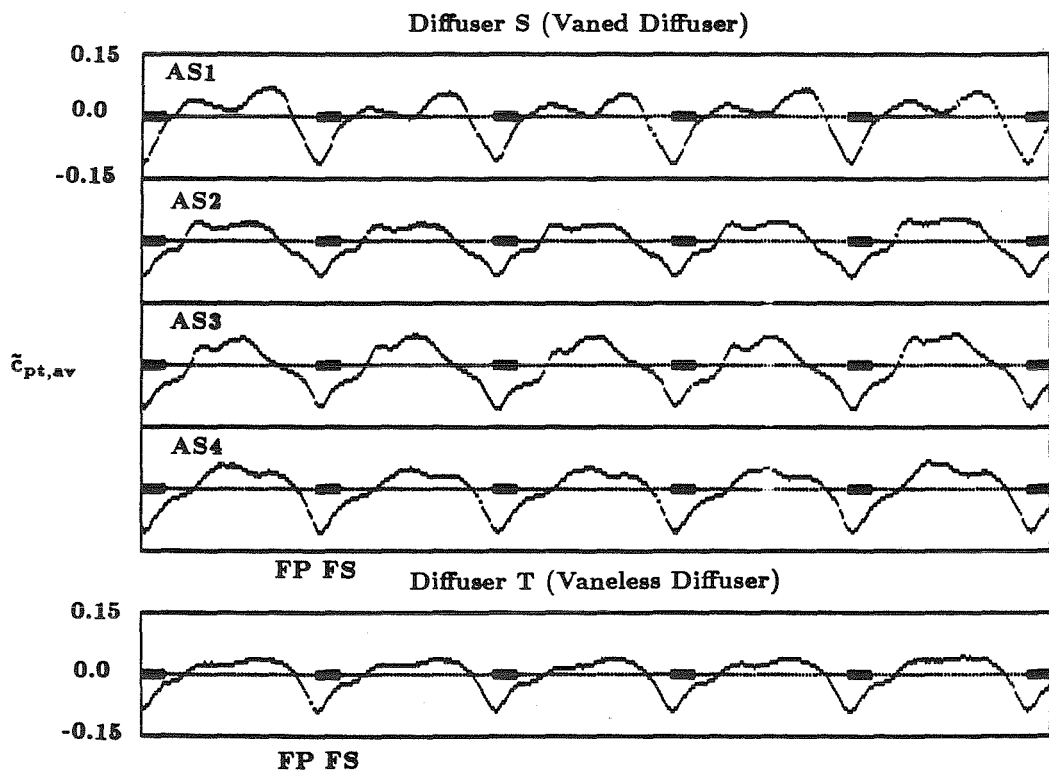


Fig. 4.14. Ensemble averaged unsteady total pressure measurements for Impeller Z1 and Diffusers S and T at the mid height of the diffuser channel ( $\phi = 0.10, r_3/R_2 = 1.07, R_3/R_2 = 1.05$ , rpm = 1200).

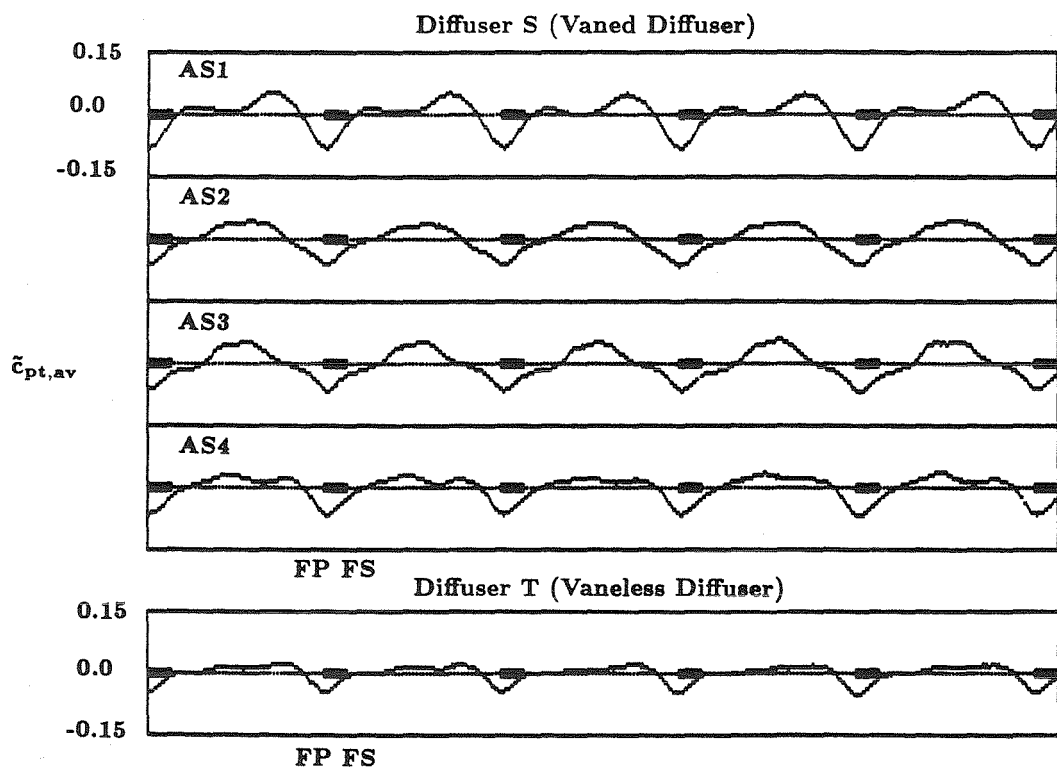


Fig. 4.15. Ensemble averaged unsteady total pressure measurements for Impeller Z1 and Diffusers S and T at the mid height of the diffuser channel ( $\phi = 0.10, r_3/R_2 = 1.10, R_3/R_2 = 1.08$ , rpm = 1200).

## CHAPTER 5

### 5. Diffuser Vane Pressure Measurements for the Pump Impeller of the HPOTP of the SSME

#### 5.1. Introduction

Herein, results on the interaction between a centrifugal impeller, namely, one half of the double suction pump of the HPOTP (High Pressure Oxygen Turbopump) of the SSME (Space Shuttle Main Engine), Impeller R, and a vaned diffuser, Diffuser S, are reported. Steady and unsteady pressure measurements along mid vane height and at different axial positions across the vane are presented. Superimposing the steady and ensemble averaged unsteady vane pressure measurements, the ensemble averaged vane pressure was obtained (it was assumed that the steady pressure value, measured with mercury manometers, was identical to the time mean pressure value about which the piezoelectric pressure transducers, used for the unsteady measurements, measured the unsteady pressure). Steady and unsteady computations of the force on the vane and the moment about the vane leading edge were made from the pressure measurements. The lift on the vane was defined as the force component normal to the chord joining the vane leading edge and the vane trailing edge. Surface pressure measurements were also made at the front shroud of the vaned and a vaneless diffuser.

Measurements were made for four flow coefficients, maximum flow coefficient ( $\phi = 0.15$ ), best efficiency flow coefficient ( $\phi = 0.12$ ), and two lower flow coefficients ( $\phi = 0.09$  and  $\phi = 0.06$ ), and three shaft speeds, 1200, 1800, and 2400 rpm. At one tap on both the vane suction and the vane pressure side (S2C and P1C, respectively), measurements were taken for a total of eleven flow coefficients, ranging from  $\phi = 0.05$  to  $\phi = 0.15$ .

During the tests, the impeller could only be positioned on locations on an

orbit concentric to the diffuser center (orbit radius=0.050 in), so that the radial gap between impeller blade trailing edge and the leading edge of any particular instrumented diffuser vane could be varied between 1.5% and 4.5%, based on the impeller discharge radius. The experiments were performed for radial gaps between the impeller blade trailing edge and the diffuser vane leading edge of 1.5% and 4.5%. Results of this work have been previously reported by Arndt et al. (1987, 1988).

### 5.2. Overall Performance

Performance curves for Diffuser S and Diffuser T are shown in figure 5.1. For the vaned diffuser, the maximum flow coefficient is about 2.5%, and the total head coefficient is up to 9% larger than for the vaneless diffuser. The design flow coefficient for the impeller was not known. Hence, efficiency measurements were made at a number of shaft speeds to determine the best efficiency flow coefficient for the impeller and Diffuser S. From these results, the best efficiency point was found to be at approximately  $\phi = 0.12$ , nearly independent of shaft speed.

### 5.3. Steady Vane Pressure Measurements and Steady Vane Lift Computations

Normalized by the dynamic pressure based on impeller tip speed, the steady vane pressure measurements will be presented as a steady vane pressure coefficient,

$$\bar{c}_p = \frac{(\bar{p}_v - \bar{p}_{up})}{(1/2)\rho u_2^2}. \quad (5.1)$$

Figures 5.2 and 5.3 show the steady vane pressure distribution at mid vane height. The measurements were taken at 1800 rpm, for two flow coefficients,  $\phi = 0.12$  and  $\phi = 0.09$ , and two different radial gaps,  $R_3/R_2 = 1.015$  and  $1.045$ . The vane loading is larger for  $\phi = 0.09$  than for  $\phi = 0.12$ . For both flow coefficients, however, the vane pressure increases on the suction side and remains unchanged on the pressure side with increasing radial gap. Hence, the steady lift on the vane decreases with increasing radial gap. Furthermore, the diffusion on the suction side is clearly noticeable.

Steady pressure measurements were also made on the vane suction side at four axial positions across the vane and two distances downstream of the vane leading edge,  $s=0.10$  and  $0.37$  (the two pressure taps at mid vane height corresponding to  $s=0.10$  and  $s=0.37$  are S1C and S3C). In figures 5.4 and 5.5, the steady measurements are presented for four flow coefficients,  $\phi = 0.15$  (maximum flow),  $0.12$  (best efficiency flow),  $0.09$  and  $0.06$ , a radial gap of  $1.5\%$  and  $1800$  rpm. It can be seen that the vane steady pressure, at both locations downstream of the leading edge and for all flow coefficients, does not vary significantly at the different axial measurement locations.

From the steady vane pressure measurements at mid vane height, the steady force on the vane at mid vane height was computed. The steady pressure distribution around the vane was obtained by fitting a third order periodic spline through the measured data. A periodic spline fit was chosen to get continuity for the pressure and the first two pressure derivatives at the vane leading and the vane trailing edge. Hence, the steady force was computed from

$$\bar{\mathbf{F}} = - \oint (\bar{p}_v - \bar{p}_{up})(\xi) \mathbf{n} d\xi. \quad (5.2)$$

The lift on the vane was defined as the component of the force on the vane normal to the chord joining the vane leading and the vane trailing edge. The lift on the vane was defined positive if the force component normal to the vane chord was in the positive  $y$  direction (figure (5.6)). Furthermore, the moment about the vane leading edge was computed from the vane pressure measurements at mid vane height,

$$\bar{\mathbf{M}}_z = - \oint (\bar{p}_v - \bar{p}_{up})(\xi) \mathbf{r} \times \mathbf{n} d\xi, \quad (5.3)$$

where  $\mathbf{r}$  is the vector from the vane leading edge to the diffuser vane surface. The lift and the moment are presented as lift and moment coefficients, normalized by the dynamic pressure based on impeller tip speed,  $(1/2)\rho u_2^2$ , and the vane chord,  $c$ ,

$$\bar{c}_L = \frac{L}{(1/2)\rho u_2^2 c} \quad (5.4)$$

$$\bar{c}_M = \frac{M_z}{(1/4)\rho u_2^2 c^2}. \quad (5.5)$$

In figure (5.7), the magnitude of the steady lift and the steady moment is presented versus flow coefficient for  $R_3/R_2 = 1.015$  and  $1.045$ . Both lift and moment increase significantly with decreasing flow coefficient. For the radial gap of  $1.5\%$ , the largest lift on the diffuser vane occurred for  $\phi = 0.09$ , whereas for the radial gap of  $4.5\%$ , the largest lift occurred for  $\phi = 0.06$ . The moment is for both radial gaps largest for  $\phi = 0.06$ . With the exception of  $\phi = 0.06$ , both lift and moment decrease with increasing radial gap.

**Table 5.1. Steady Lift and Moment on a Vane of Diffuser S.**  
(Impeller R and Diffuser S)

$\phi$	$R_3/R_2$	$\bar{c}_L$	$\bar{c}_M$
0.15	1.015	0.073	-0.059
0.15	1.045	0.056	-0.042
0.12	1.015	0.121	-0.075
0.12	1.045	0.099	-0.062
0.09	1.015	0.149	-0.087
0.09	1.045	0.126	-0.083
0.06	1.015	0.139	-0.090
0.06	1.045	0.143	-0.103

Summarizing, the steady vane pressure measurements showed that the steady lift on the vane and the steady moment about the vane leading edge increase significantly with decreasing flow coefficient. With the exception of the lowest flow coefficient investigated,  $\phi = 0.06$ , the steady lift and the steady moment decreased with increasing radial gap between the impeller blade trailing edge and the diffuser vane leading edge. For the flow coefficients investigated, the steady pressure measured at different axial locations on the diffuser vane suction side did not vary significantly.

#### 5.4. Unsteady Vane Pressure Measurements

The unsteady vane pressure measurements are presented as an unsteady vane pressure coefficient, normalized by the dynamic pressure based on impeller tip speed,

$$(1/2)\rho u_2^2,$$

$$\tilde{c}_p = \frac{\tilde{p}_v}{(1/2)\rho u_2^2}. \quad (5.6)$$

Figures 5.8 and 5.9 show the unsteady vane pressure measurements made at pressure tap S2C (on the suction side close to the leading edge). The measurements were made for four flow coefficients,  $\phi = 0.15$  (maximum flow),  $\phi = 0.12$  (best efficiency flow),  $\phi = 0.09$  and  $0.06$  and for radial gaps of 1.5% (figure 5.8) and 4.5% (figure 5.9) of the impeller discharge. A total of 4096 data points, corresponding to four main shaft revolutions or thirty-two blade passages, was taken. The spectra corresponding to those measurements are presented in figure 5.10 (for the radial gap of 1.5%) and in figure 5.11 (for a radial gap of 4.5%). The magnitude of the Fourier coefficients relative to the magnitude of the largest Fourier coefficient ( $c_i/c_{i,max}$ ) for a particular test is shown versus frequency (upper horizontal scale) and frequency normalized by impeller blade passage frequency ( $f/f_b$ ) (lower horizontal axis). The spectra were obtained using all 4096 data points (the relative magnitudes of the first 512 frequencies are shown). The magnitude of the ensemble averaged unsteady vane pressure fluctuations and the magnitude of the first impeller blade passage harmonic, as the pressure fluctuations normalized by the dynamic pressure based on impeller tip speed,  $(1/2)\rho u_2^2$ , are given in Table 5.2. The measurements at pressure tap S2C were selected for the representation of the unsteady pressure measurements, since for most flow coefficients the vane pressure fluctuations were largest at this particular pressure tap.

**Table 5.2. Magnitude of Vane Pressure Fluctuations at Vane Pressure Tap S2C**  
 (Impeller R and Diffuser S)

$\phi$	$R_3/R_2$	$ \tilde{c}_{p,av} $	$c_{fb}$
0.15	1.015	1.082	0.204
0.15	1.045	0.440	0.110
0.12	1.015	0.816	0.194
0.12	1.045	0.354	0.096
0.09	1.015	0.694	0.149
0.09	1.045	0.324	0.084
0.06	1.015	0.718	0.122
0.06	1.045	0.322	0.075

Note:  $|\tilde{c}_{p,av}|$  is the peak to peak fluctuation for a particular ensemble averaged unsteady measurement, whereas  $c_{fb}$  is the magnitude of the amplitude of the Fourier coefficients corresponding to the impeller blade passage frequency of the corresponding unsteady measurement.

Turning first to the measurements for the smaller radial gap,  $R_3/R_2 = 1.015$ , it can be seen that for all flow coefficients, the pressure fluctuations are of the same order of magnitude as the total pressure rise across the pump and that they are indeed periodic with impeller blade passage frequency. The high frequency "noise" in the measurements is due to the resonant frequency of the pressure tap. The steepest pressure increase and pressure decrease occur shortly after the impeller blade trailing edge has passed the diffuser vane leading edge. The ensemble averaged pressure fluctuations and the magnitude of the first impeller blade passage frequency are largest for maximum flow and smallest for the two low flow coefficients,  $\phi = 0.09$  and  $0.06$ . Furthermore, it can be seen that for the lowest flow coefficient,  $\phi = 0.06$ , "low frequency noise" is significant. A discrete low frequency harmonic can be observed at 15 Hz (the frequency resolution for these spectra was 7.5Hz). At  $f/f_b = 1/2, 3/2, 5/2$ , etc. the relative magnitudes of the Fourier coefficients corresponding to full impeller blade passage frequency,  $f_b$ , and its higher harmonics can be seen (since the impeller has a total of eight blades, four full and four partial

blades, the full impeller blade passage frequency,  $f_{fb}$ , is equal to the partial impeller blade passage frequency,  $f_{pb}$ , and furthermore,  $f_{fb} = (1/2)f_b$ . The relative magnitudes of the Fourier coefficients at those frequencies indicate the difference on the vane pressure measurements between a full and a partial impeller blade passing the diffuser vane. The relative magnitude of the full (or partial) impeller blade passage harmonic,  $f_{fb}$ , was found to be smallest for the best efficiency flow coefficient,  $\phi = 0.12$ , and to be largest for the smallest flow coefficient,  $\phi = 0.06$ .

Increasing the radial gap from 1.5% to 4.5% resulted in an approximately 60% decrease of the magnitude of the ensemble averaged vane pressure fluctuations. The relative decrease of the magnitude of the first blade pressure harmonic was found to be smaller than the relative decrease of the ensemble averaged vane pressure fluctuations. Furthermore, it was observed that the magnitude of the low frequency components in the spectra of the measurements increased significantly for the two lower flow coefficients,  $\phi = 0.09$  and  $0.06$ . For  $\phi = 0.06$ , the distinct peaks were found at shaft frequency, 30 Hz, and at 15 Hz; whereas for  $\phi = 0.09$ , peaks were found at 22.5 and 60 Hz. Since only data over a period of four shaft passages were taken, those discrete low frequency peaks were not found to repeat. The relative magnitude of the full (or partial) impeller blade passage frequency was seen to increase, especially for the two larger flow coefficients,  $\phi = 0.15$  and  $0.12$ .

Figure 5.12 shows the spectrum of unsteady measurements taken near the vane trailing edge on the vane suction side (tap S6C) for  $\phi = 0.12$  and a radial gap of 1.5%. The impeller blade passage frequency is dominant; however, its magnitude has decreased to about a third of the magnitude of the impeller blade passage frequency at the pressure tap S2C, and the higher harmonics decay much faster than at tap S2C. But even on the rear part of the vane the fluctuations are still periodic with impeller blade passage frequency.

Two spectra of vane pressure measurements at the pressure tap P1C, near the vane leading edge on the vane pressure side, are shown in figure 5.13. The measurements presented were made for the best efficiency flow coefficient,  $\phi = 0.12$ , and a lower flow coefficient,  $\phi = 0.08$ . The impeller blade passage harmonic is dominant

for both flow coefficients. As for the measurements made at the suction side pressure tap S2C, the relative magnitude of the full impeller blade passage harmonic is significantly larger for the lower flow coefficient than for the best efficiency flow coefficient (it increases from less than 0.1 for  $\phi = 0.12$  to approximately 0.55 for  $\phi = 0.08$ ). Hence, both at vane suction and pressure side pressure taps significant differences were found in the pressure fluctuations caused by full and partial impeller blades.

### 5.5. Magnitude and Phase of Fourier Coefficients of Ensemble Averaged Vane Pressure Fluctuations

Next, the magnitude and the phase of the Fourier coefficients corresponding to impeller blade passage frequency,  $f_b$ , two times impeller blade passage frequency,  $2f_b$ , and three times impeller blade passage frequency,  $3f_b$  will be presented for the best efficiency flow coefficient,  $\phi = 0.12$ , and a radial gap of 1.5%. At every pressure tap for this particular flow coefficient, the magnitude of the Fourier coefficients at full (or partial) impeller blade passage frequency was found to be an order of magnitude smaller than the magnitude of the Fourier coefficients at impeller blade passage frequency, and will therefore not be presented here (for pressure tap S2C, it was already shown that the magnitude of the full blade passage frequency components in the spectra was an order of magnitude smaller than the blade passage frequency components for the best efficiency flow coefficient; this was also found at all other pressure taps investigated for the best efficiency flow coefficient). The magnitudes of the Fourier coefficients are presented in figure 5.15. Note that the vertical scale, for the magnitude of the coefficients, is not a linear but a logarithmic one. It can be seen that the coefficients are significantly larger on the suction side than on the pressure side. Especially on the front part of the vane suction side, the higher harmonics, as already seen from the spectra in figure 5.10, contribute strongly to the vane pressure fluctuations. On the rear part of the suction side, however, the magnitude of the higher blade passage harmonics is small compared

to the magnitude of the blade passage harmonic. The phase angle of the blade passage harmonics is shown in figure 5.16. The reference configuration, i.e., the geometric configuration at which the data taking process was started, is shown in figure 5.14. (the phase angle was computed according to  $\phi_k = \tan^{-1}(a_k/b_k)$ , where  $a_k$  and  $b_k$  are the Fourier coefficients corresponding to the cos and sin terms in the Fourier series.) It can be seen that there is a significant difference in phase, of  $\approx 120$  degrees, between the first impeller blade passage harmonic on the front half of the vane suction side (pressure taps S1C–S4C) and the front half of the vane pressure side (pressure taps P1C–P4C).

## 5.6. Magnitude of Ensemble Averaged Vane Pressure Fluctuations

In figures 5.17–5.19 data on the magnitude of the ensemble averaged unsteady vane pressure fluctuations at mid vane height are presented. The fluctuations are defined as the difference between the maximum and minimum pressure value in the averaging period, which corresponds to one full and one partial impeller blade passage. It can be seen that the largest fluctuations independent of experimental parameters such as flow coefficient, shaft speed or radial gap occur on the front half of the suction side of the vane. Those fluctuations are of the same order of magnitude as the total pressure gain across the pump. Furthermore, the fluctuations on the pressure side are significantly smaller than those on the suction side. It is interesting to notice that, although the fluctuations decrease on both pressure and suction side along the vane, they attain a relative maximum on the rear half of the vane. This observation is similar to that made by Dring et al. (1982) in turbine rotor–stator interaction. Dring et al. (1982) also reported larger blade pressure fluctuations on the turbine rotor suction side than on the pressure side. In the compressor stage investigated by Gallus (1979) and Gallus et al. (1980), the largest fluctuations on the compressor stator were reported to occur at a tap on the pressure side. However, taking into account all the measurements reported on both pressure and suction side, it appears that the mean magnitude of the fluctuations is larger at the suction

side taps than at the pressure side taps.

Figure 5.17 shows the dependence of the fluctuations on the radial gap for  $\phi = 0.12$ . Increasing the radial gap resulted in a significant decrease, of about 50%, of the large fluctuations on the front half of the vane suction side and at the pressure tap on the pressure side closest to the leading edge. At most other measurement locations, the fluctuation decreased slightly or remained constant. Only at one pressure tap, P5C, on the rear half of the pressure side, did they increase with increasing radial gap. Figure 5.18 compares the magnitude of the fluctuations at different shaft speeds, where data are presented for  $\phi = 0.12$  and a radial gap of 1.5%. With the exception of the pressure tap at the vane trailing edge, there is hardly any speed dependence of the normalized pressure fluctuations at any of the pressure taps. In figure 5.19 the magnitude of the fluctuations for four different flow coefficients,  $\phi = 0.15, 0.12, 0.09$ , and  $0.06$  at 1800 rpm and for a radial gap of 4.5% is shown. At all pressure taps on the suction side, the fluctuations are largest for maximum flow,  $\phi = 0.15$ . At two suction side taps (S1C and S5C), the fluctuations decrease significantly with decreasing flow coefficient, whereas at all other suction side taps, they are not significantly different for  $\phi = 0.12, \phi = 0.09$ , and  $\phi = 0.06$ . On the vane pressure side, where the fluctuations are significantly smaller than on the suction side, the differences in magnitude of the fluctuations for the four flow coefficients investigated are small at most pressure taps except at P1C, where the fluctuations are largest for  $\phi = 0.09$  and for P2C, where they are largest for  $\phi = 0.15$ .

To investigate in more detail the dependence of the magnitude of the fluctuations on the flow coefficient, measurements were made for radial gaps of 1.5% and 4.5% for a total of eleven flow coefficients, ranging from  $\phi = 0.05$  to  $\phi = 0.15$ , on two pressure taps, P1C and S2C. The magnitude of the fluctuations as functions of flow coefficient and radial gap, relative to the magnitude of the fluctuations for maximum flow ( $\phi = 0.15$ ) at a radial gap of 1.5%, is presented for tap P1C in figure 5.20 and for tap S2C in figure 5.21. For both taps, the fluctuations are largest for maximum flow at the radial gap of 1.5%; however, they show different behavior

for decreasing flow coefficient. For P1C at the radial gap of 1.5%, they attain a minimum for  $\phi = 0.11$ , dropping about 40% below the maximum fluctuations for  $\phi = 0.15$ . Increasing the radial gap to 4.5% results in a shift of the minimum fluctuations from  $\phi = 0.11$  to  $\phi = 0.12$ . Furthermore, the largest fluctuations no longer occur for maximum flow, but for  $\phi = 0.09$ . For tap S2C, the fluctuations are largest, for both radial gaps, for maximum flow,  $\phi = 0.15$ , and decrease with decreasing flow coefficient. They attain relative minima and maxima for  $\phi = 0.09$  and  $\phi = 0.07$  (for the radial gap of 1.5%), and for  $\phi = 0.11$  and  $\phi = 0.07$  (for the radial gap of 4.5%).

Furthermore, the relative decrease of the pressure fluctuations with increasing radial gap is significantly different for the two taps. For tap P1C, the fluctuations decrease most strongly, by about 50%, for maximum flow,  $\phi = 0.15$ , and for the smallest flow coefficient investigated,  $\phi = 0.05$ , when increasing the radial gap from 1.5% to 4.5%. However, for medium flow coefficients such as  $\phi = 0.10$ , the fluctuations decrease only by about 10%. For pressure tap S1C, the pressure fluctuations decrease with increasing radial gap most strongly, by about 60%, for maximum flow,  $\phi = 0.15$ . Lowering the flow coefficient, the decrease of the fluctuations with increasing radial gap is reduced slightly, up to about 50% for  $\phi = 0.05$ .

Pressure measurements were also made on the suction side at four axial positions across the vane at two distances downstream of the leading edge ( $s=0.10$  and 0.37, the two pressure taps at mid vane height corresponding to  $s=0.10$  and  $s=0.37$  are S1C and S3C). Comparing the measurements for four flow coefficients ( $\phi = 0.15, 0.12, 0.09$  and  $0.06$  (figure 5.22)) at a radial gap of 1.5% shows that the fluctuations are largest for maximum flow, and that they decrease with decreasing flow coefficient. This was already previously reported in Chapter 5.4. for the pressure measurements at the mid vane height at pressure tap S2C. The differences of the magnitude of the fluctuations for the different flow coefficients increase from the shroud to the hub. At the hub, the fluctuations for maximum flow are about twice as large for maximum flow,  $\phi = 0.15$ , as for the smallest flow coefficient investigated,  $\phi = 0.06$ . Increasing the radial gap from 1.5% to 4.5% (figure 5.23)

resulted, as already seen from the figures presenting the pressure fluctuations at mid vane height, in a significant decrease of the pressure fluctuations. Furthermore, the magnitudes of the pressure fluctuations at  $s=0.37$  are nearly identical for  $\phi = 0.12, 0.09$  and  $0.06$ . But also for the radial gap of 4.5%, the vane pressure fluctuations are larger near the hub than near the shroud.

Recalling the results from the steady vane pressure measurements across the span of the vane that have been presented in Chapter 5.3., it can be seen that the magnitude of the vane pressure fluctuations across the span of the vane do not scale with steady vane pressure measurements. The measurements showed only slight variations of the steady vane pressure across the span of the vane, but significant variations of the magnitude of the pressure fluctuations. Comparing these measurements to the total pressure measurements of the flow discharging from Impeller R into the vaneless diffuser of Volute D, it can be seen that the vane pressure fluctuations and the total pressure fluctuations behave qualitatively similarly; i.e., they increase from shroud to hub, whereas the steady vane pressure and the steady total pressure behave differently; the steady total pressure increases strongly from shroud to hub; the steady vane pressure increases only slightly.

### **5.7. Ensemble Averaged Lift and Moment Computations**

From the vane pressure measurements described earlier, the force on the vane at mid vane height and the moment about the vane leading edge were computed. Since those measurements were obtained on different vanes, they had to be phase shifted to one reference vane for the force computations. The steady force was computed from the steady pressure distribution around the vane. Superimposing the steady and ensemble averaged unsteady pressure measurements, the ensemble averaged vane pressure distribution was obtained (it was assumed that the steady pressure value obtained by the mercury manometer measurements was identical to the time mean value about which the piezoelectric transducer measured the unsteady pressure). From the ensemble averaged pressure distribution, the ensemble

averaged force and the ensemble averaged moment were computed. The steady and the ensemble averaged pressure distribution on the vane was obtained by fitting a third order periodic spline through the measured pressure values. A periodic spline fit was chosen to get continuity for the pressure and the first two pressure derivatives at the leading edge and at the trailing edge. The ensemble averaged force was computed from,

$$\mathbf{F}_{av} = - \oint (\bar{p}_v + \tilde{p}_{v,av} - \bar{p}_{up})(\xi) \mathbf{n} d\xi. \quad (5.7)$$

The lift on the vane was defined as the component of the force on the vane normal to the chord joining the vane leading edge and the trailing edge. The lift on the vane was defined positive if the force component normal to the vane chord was in positive y direction (figure 5.6). Furthermore, the ensemble averaged moment about the vane leading edge was computed from the vane pressure measurements at mid vane height,

$$\mathbf{M}_{z,av} = - \oint (\bar{p}_v + \tilde{p}_{v,av} - \bar{p}_{up})(\xi) \mathbf{r} \times \mathbf{n} d\xi, \quad (5.7)$$

where  $\mathbf{r}$  is the vector from the vane leading edge to the diffuser vane surface. The ensemble averaged lift and the ensemble averaged moment are presented as ensemble averaged lift and ensemble averaged moment coefficients, normalized by the dynamic pressure based on impeller tip speed,  $(1/2)\rho u_2^2$ , and the vane chord,  $c$ ,

$$c_{L,av} = \frac{L_{av}}{(1/2)\rho u_2^2 c} \quad (5.8)$$

$$c_{M,av} = \frac{M_{z,av}}{(1/4)\rho u_2^2 c^2}. \quad (5.9)$$

In figure 5.24 the ensemble averaged vane pressure distribution at mid vane height is shown for two different locations of the impeller blades relative to the instrumented vane for best efficiency flow coefficient,  $\phi = 0.12$ , at 1800 rpm, and a radial gap of 1.5%. (The full circles indicate actual measurement points, the curve connecting those points the pressure distribution obtained by the interpolation scheme). As the impeller blade passes the diffuser vane, the vane pressure on the vane suction side drops below upstream pressure, resulting in a large pressure

difference between the vane suction and the pressure side. When the impeller blade is approximately halfway between two diffuser vanes, the vane pressure distribution is similar to the steady pressure distribution presented in figure 5.7, except for the pressure fluctuations at the trailing edge.

In figure 5.25 the ensemble averaged lift on a diffuser vane is presented for  $\phi = 0.12$ , rpm=1800, and radial gaps of 1.5% and 4.5%. The position of the impeller blades (shown is a full and a partial blade) is referenced to the diffuser vane leading edge of the instrumented vane. Maximum lift is attained immediately after the impeller blade suction side has passed the vane leading edge. As seen in figure 5.24, for a radial gap of 1.5%, the vane pressure on the suction side in the vicinity of the leading edge drops below upstream pressure at this instant of time. As the impeller blade moves on, the lift decreases, until the blade pressure side passes the vane leading edge. At this instant, the lift on the vane for the radial gap of 1.5% is slightly negative. Then, as the impeller blade trailing edge passes by, the lift increases sharply from its minimum to its maximum value. The increase of the radial gap from 1.5% to 4.5% results in a significant decrease in the fluctuating lift, as expected from a similar decrease of the magnitude of the vane pressure fluctuations. The occurrence of negative lift can be understood by recalling the significant phase difference, of about 120 degrees, between the impeller blade passage harmonic of the unsteady pressure measurements on the front half of the vane suction and the vane pressure side. Thus, the unsteady pressure minimum and maximum occur at different times on the vane suction and the vane pressure side. Since the magnitude of the fluctuating vane pressure is large for the small radial gap investigated, 1.5%, the pressure at the instant of time in which negative lift occurs is larger on the front half of the vane suction side than the front half of the vane pressure side resulting in negative lift. Similarly, during the instant of time where maximum lift occurs, the suction side pressure has attained its minimum and the pressure side pressure has attained its maximum value.

The ratio of ensemble averaged lift to steady lift is presented in figure 5.26. It was found that the magnitude of the ensemble averaged lift was up to three times

larger than the steady lift. Furthermore, the ratio of ensemble averaged lift to steady lift decreased with increasing radial gap, which was not obvious *a priori* since an increase in radial gap resulted in a decrease in both the steady lift, figure 5.7, and the magnitude of the pressure fluctuations, figure 5.17.

In figure 5.27 and 5.28, the ensemble averaged lift on the vane is presented for  $\phi = 0.15, 0.12, 0.09$  and  $0.06$  for a radial gap of  $4.5\%$ . The fluctuations are largest for  $\phi = 0.15$  and with decreasing flow coefficients. It has to be remarked, however, that the pressure fluctuations at low frequencies, which were observed especially for the lowest flow coefficient,  $\phi = 0.06$ , were “averaged out” during the ensemble averaging procedure. Differences in the magnitude of the lift fluctuations depending upon a partial or a full impeller blade passing the diffuser vane were observed. The differences were smallest for the “best efficiency” flow coefficient for which the lift fluctuations were about  $5\%$  smaller for the partial blade than for the full blade. For the lower flow coefficient, the differences increased. The lift fluctuations were found to be about  $22\%$  and  $39\%$  smaller for the partial blade than for the full blade for  $\phi = 0.09$  and  $0.06$ . In contrast, for the maximum flow coefficient, the lift fluctuations were about  $8\%$  larger for the partial blade than for the full blade. The large difference in lift fluctuation between a full and a partial impeller blade passing the diffuser vane for the low flow coefficients,  $\phi = 0.09$  and  $0.06$ , coincides with the results of the spectra presented earlier. The spectra showed that with decreasing flow coefficient the relative magnitude of the full blade passage frequency may increase significantly. The observations that the fluctuating lift decreases with decreasing flow coefficient is different from that reported by Gallus (1979) and Gallus et al. (1980), where the fluctuating lift on the stator blades was smallest for maximum flow, and increased with decreasing flow coefficient.

The ratio of the ensemble averaged lift to the steady lift during the passage of a full and a partial impeller blade is presented (for the same flow coefficients as the ensemble averaged lift) in figures 5.29 and 5.30. It can be seen that the maximum ratio of ensemble averaged lift to steady lift occurs for maximum flow ( $c_{L,av}/\bar{c}_L \approx 3$ ), and decreases significantly with flow coefficient, to  $c_{L,av}/\bar{c}_L \approx 1$

for  $\phi = 0.06$ . This decrease is not surprising since the steady lift for a radial gap of 4.5%, for which the lift computations are presented, increased with decreasing flow coefficient, whereas the pressure fluctuations decreased with decreasing flow coefficient.

Finally, the ensemble averaged moment about the diffuser vane leading edge and the ratio of the ensemble averaged moment to the steady moment about the diffuser vane leading edge are presented in figures 5.31 and 5.32 for the best efficiency flow coefficient,  $\phi = 0.12$ , and radial gaps of 1.5% and 4.5%. It can be seen that the moment fluctuations are approximately in phase with the lift fluctuations. The maximum ratio of ensemble averaged moment to steady moment is approximately the same as the maximum ratio of ensemble averaged lift to steady lift,  $\approx 3$  for a radial gap of 1.5% and  $\approx 2$  for a radial gap of 4.5%.

## 5.8. Magnitude of Ensemble Averaged Front Shroud Pressure Fluctuations

Unsteady pressures measurements were made on the front shroud of the vaned diffuser (Diffuser S), and a second diffuser of identical geometry, but vaneless (Diffuser T). For Diffuser T, the measurements were made at three distances to the diffuser inlet; for Diffuser S at any of those three distances to the diffuser inlet four measurements were made between the pressure and the suction side of two adjacent diffuser vanes. In figure 5.33, data on the magnitude of the ensemble averaged front shroud pressure fluctuations are presented for  $\phi = 0.12$  and radial gaps of 1.5% and 4.5% between impeller discharge and the diffuser inlet. The ratio  $R/R_2$  in figure 5.33 describes the ratio of the radius of the particular front shroud pressure measurement location to the impeller discharge radius for the different radial gaps between impeller discharge and diffuser inlet (for Diffuser S the radial gaps between impeller discharge and diffuser vane leading edge and between impeller discharge and diffuser inlet are identical). It can be noticed that the fluctuations on the front shroud of the vaned diffuser are about twice as large as those on the vaneless dif-

fuser. This is a clear indication that for the range of radial gaps investigated in this experiment both the potential interaction between impeller blades and diffuser vanes and the convection of the wakes shed by the impeller blades contribute to the unsteadiness of the flow. Furthermore, for the vaned diffuser, the magnitude of the front shroud pressure fluctuations depends on the circumferential position between suction and pressure side of two adjacent vanes. The fluctuations seem to be smaller and to decay faster in the vicinity of the pressure side than the vicinity of the suction side.

### 5.9. Summary

Steady and unsteady vane and front shroud pressure measurements were made for one half of the double suction pump impeller of the HPOTP (High Pressure Oxygen Turbopump) of the SSME (Space Shuttle Main Engine) and a vaned and a vaneless diffuser to investigate rotor-stator interaction in diffuser pumps. Spectra of the unsteady vane pressure measurements showed that the pressure fluctuations were periodic with impeller blade passage frequency. The vane pressure fluctuations were found to be larger on the suction side than on the pressure side attaining their maximum value, of about the same order of magnitude as the total pressure rise across the pump, in the vicinity of the leading edge. For a radial gap of 1.5% (based on impeller discharge radius) between impeller discharge and diffuser vane leading edge, the pressure on the vane suction side was observed to drop locally below upstream pressure immediately after the impeller blade trailing edge has passed the vane leading edge. The large pressure fluctuations on the front half of the vane suction side decreased by about 50% when the radial gap was increased from 1.5% to 4.5%. The lift on the vane, steady and unsteady, was computed from the vane pressure measurements. The magnitude of the fluctuating lift was found to be larger than the steady lift thus subjecting the vane to a large periodic load. Fluctuating lift as well as ratio of lift to steady lift decreased strongly when the radial gap was increased from 1.5% to 4.5%. Unsteady pressure measurements at different

locations across the span of the vane showed that the pressure fluctuations near the hub were considerably larger than those near the shroud. The unsteady front shroud pressure fluctuations on the vaned diffuser were found to be considerably larger than those on a vaneless diffuser, indicating that the close spacing of impeller and diffuser strongly increased the unsteadiness of the flow.

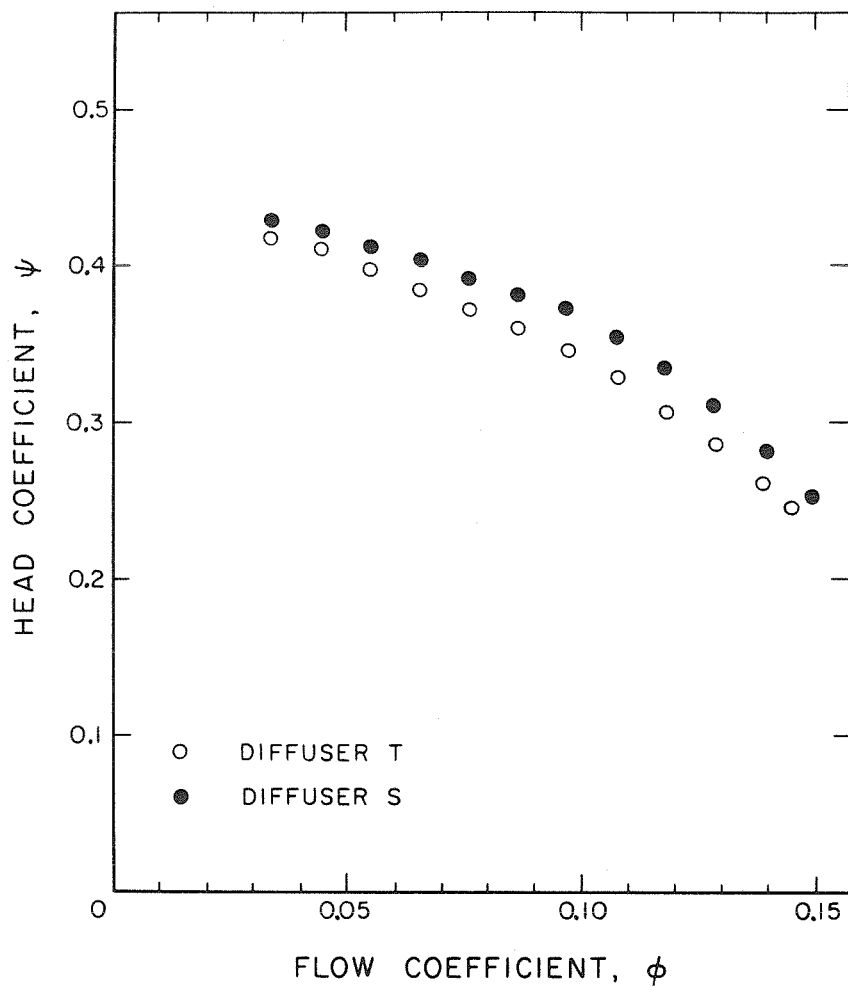


Fig. 5.1. Performance curves for Diffuser S and Diffuser T.

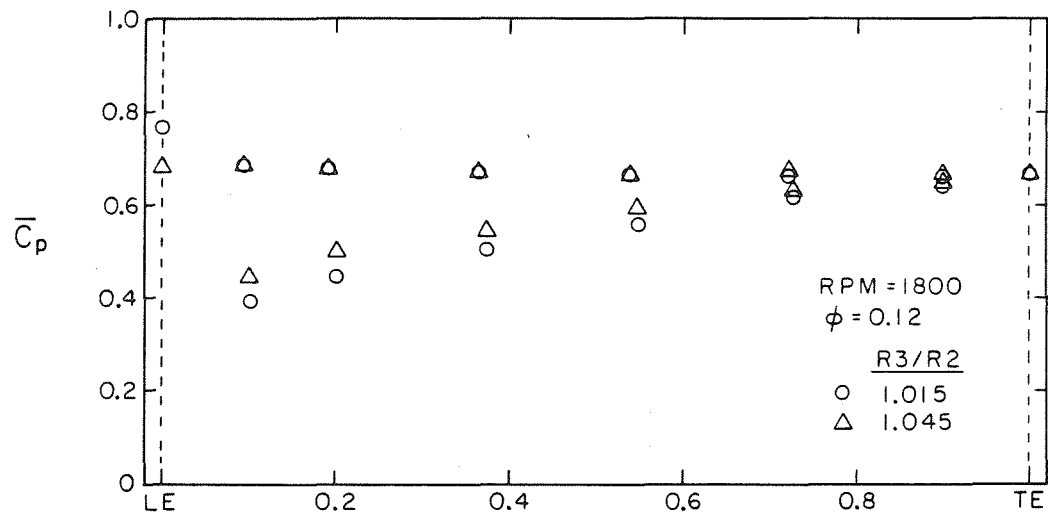


Fig. 5.2. Steady pressure measurements at mid vane height for Impeller R and Diffuser S ( $\phi = 0.12$ ,  $R_3/R_2 = 1.015$  and  $1.045$ , rpm 1800).

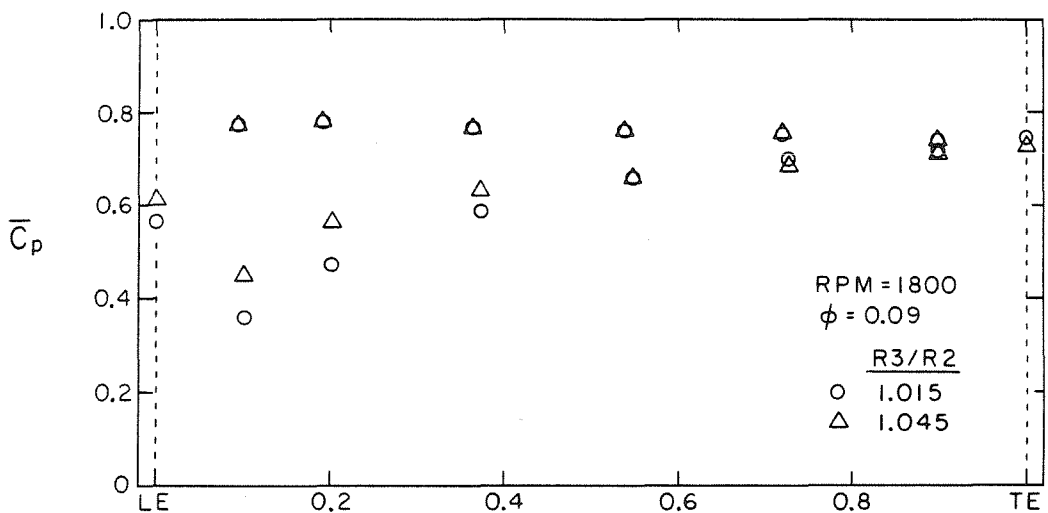


Fig. 5.3. Steady pressure measurements at mid vane height for Impeller R and Diffuser S ( $\phi = 0.09$ ,  $R_3/R_2 = 1.015$  and  $1.045$ , rpm 1800).

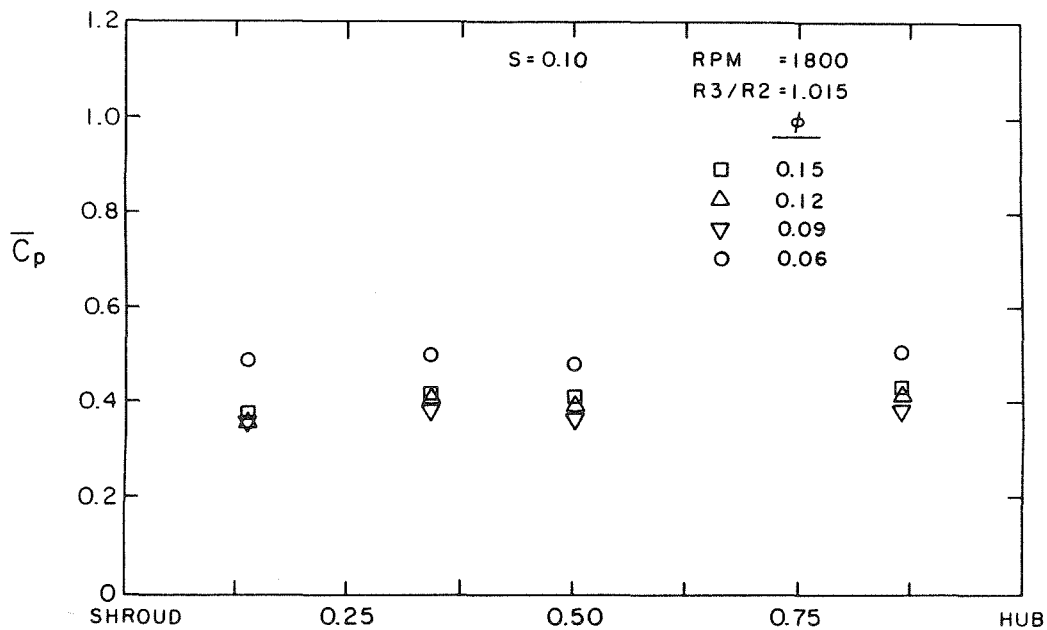


Fig. 5.4. Steady pressure measurements across the span of the vane for Impeller R and Diffuser S ( $\phi = 0.15, 0.12, 0.09$  and  $0.06, s = 0.10, R_3/R_2 = 1.015$ , rpm = 1800).

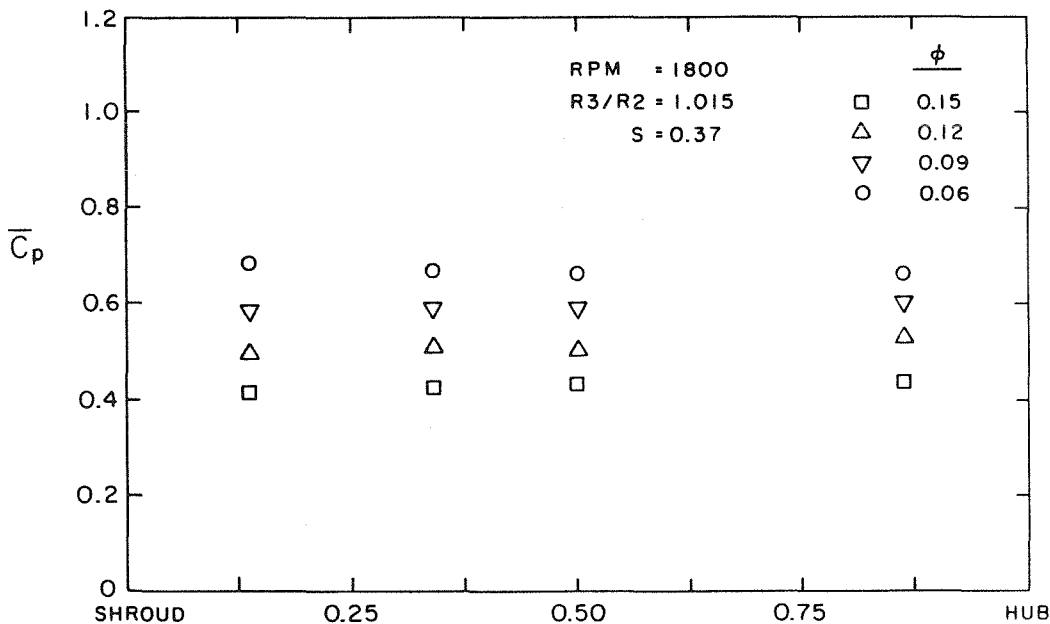


Fig. 5.5. Steady pressure measurements across the span of the vane for Impeller R and Diffuser S ( $\phi = 0.15, 0.12, 0.09$  and  $0.06, s = 0.37, R_3/R_2 = 1.015$ , rpm = 1800).

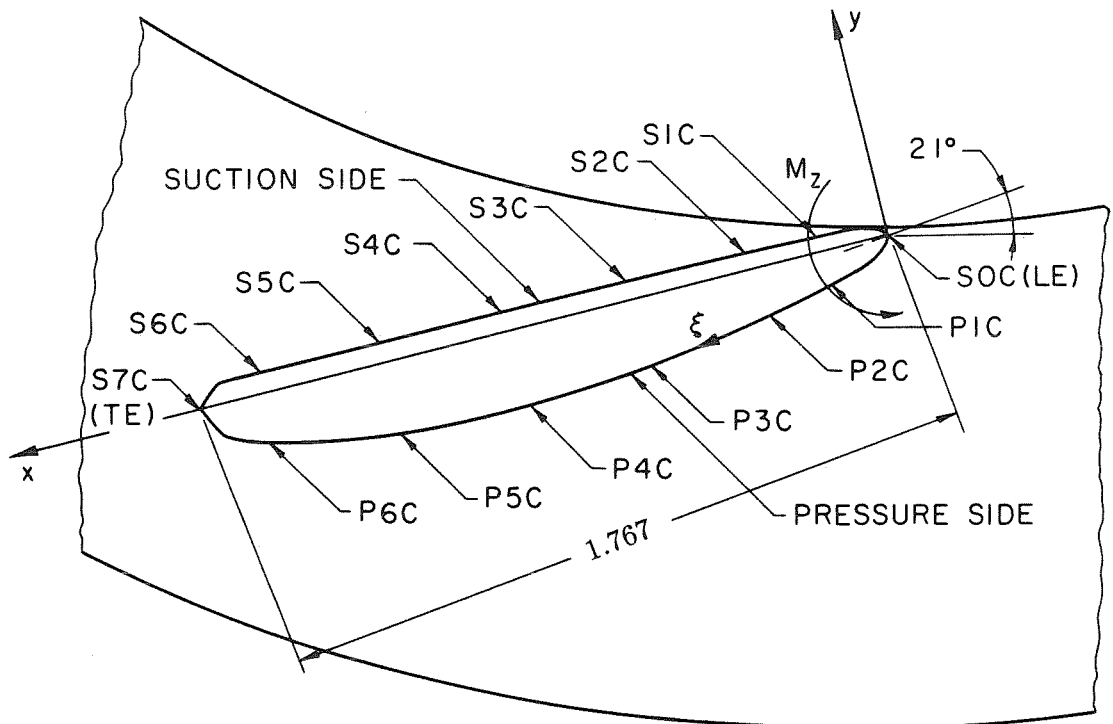


Fig. 5.6. Diffuser vane with pressure taps at mid vane height.

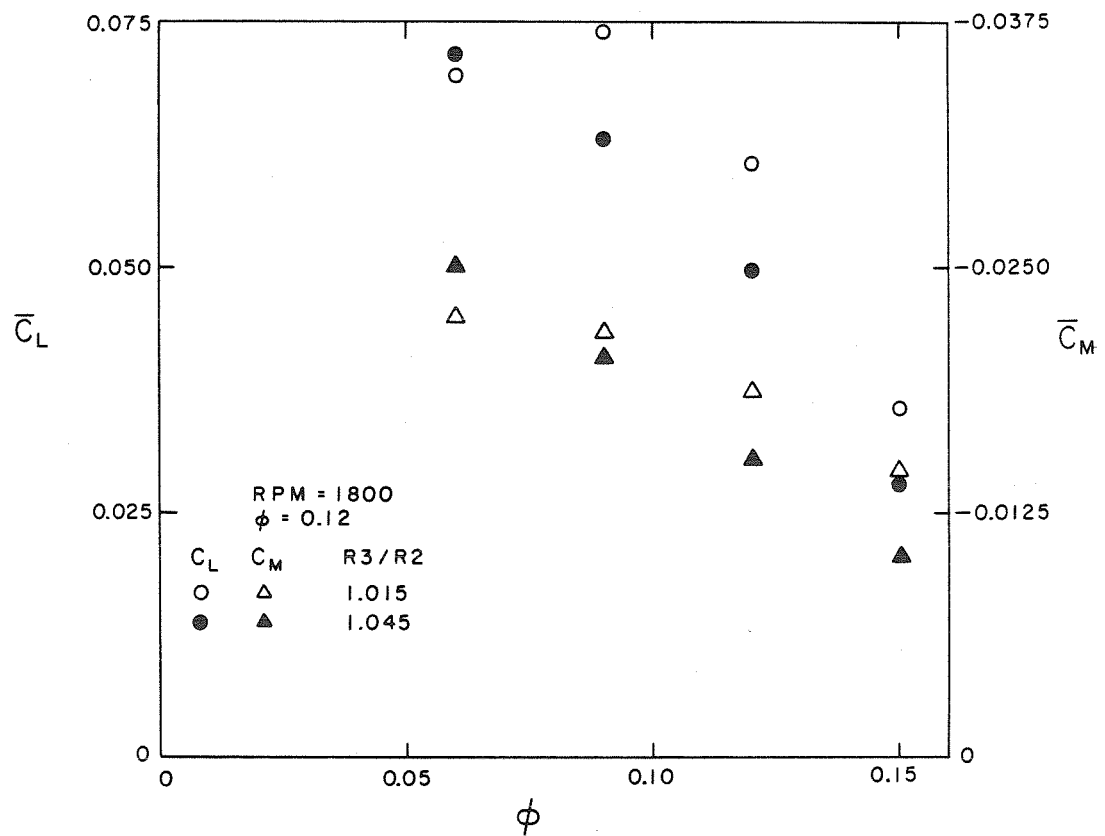


Fig. 5.7. Steady lift and steady moment versus flow coefficient for Impeller R and Diffuser S ( $R_3/R_2 = 1.015$  and  $1.045$ ,  $\text{rpm} = 1800$ ).

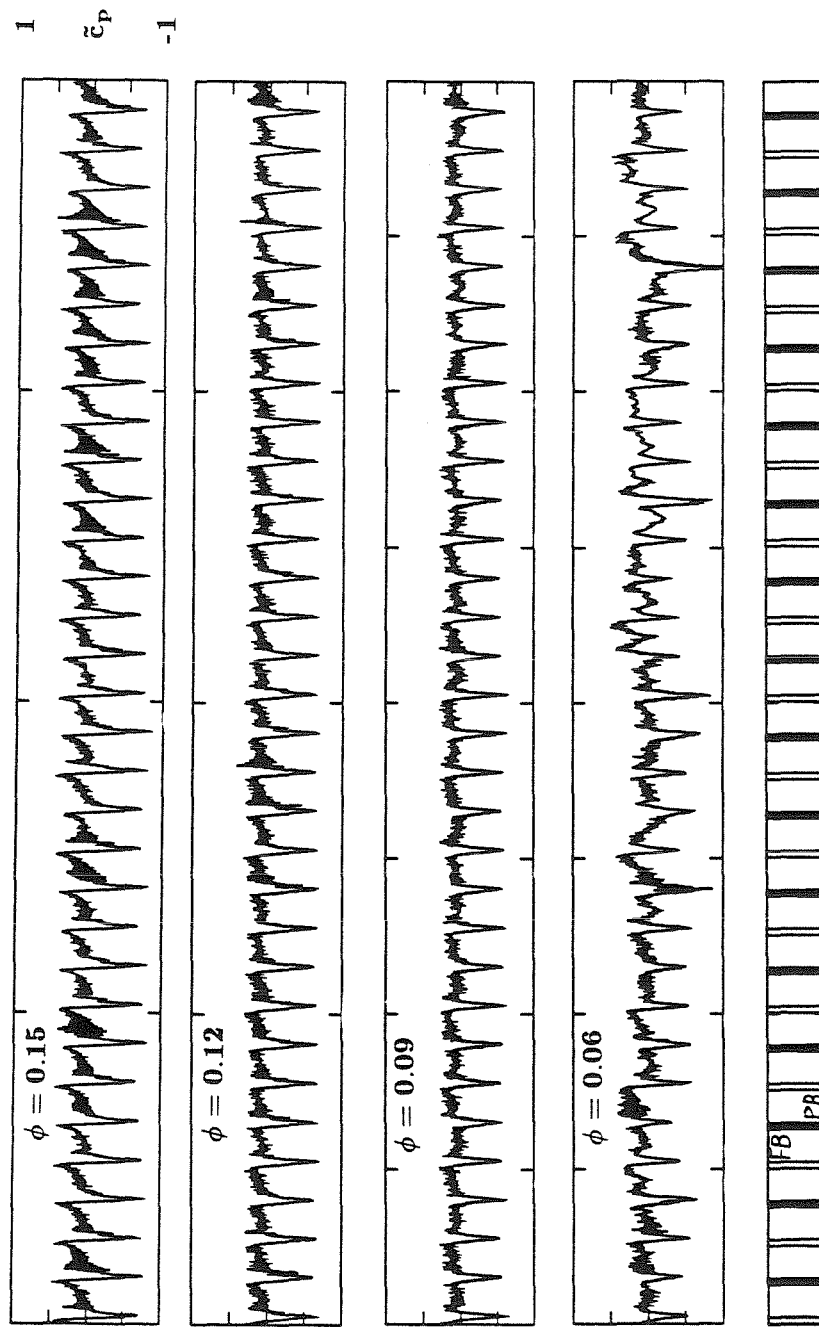


Fig. 5.8. Unsteady diffuser vane pressure measurements at pressure tap S2C for Impeller R and Diffuser S ( $\phi = 0.15, 0.12, 0.09$  and  $0.06$ ,  $R_3/R_2 = 1.015$ , rpm = 1800).

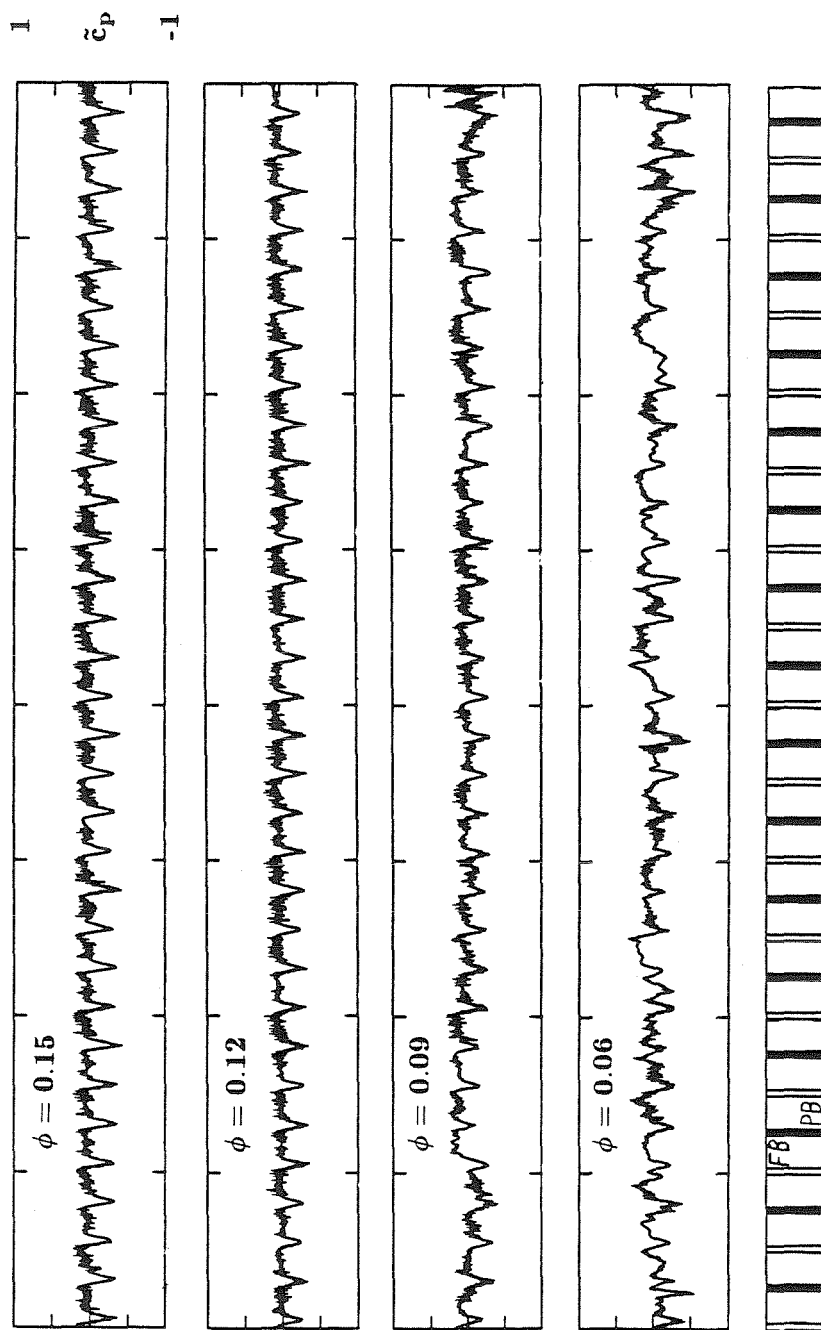
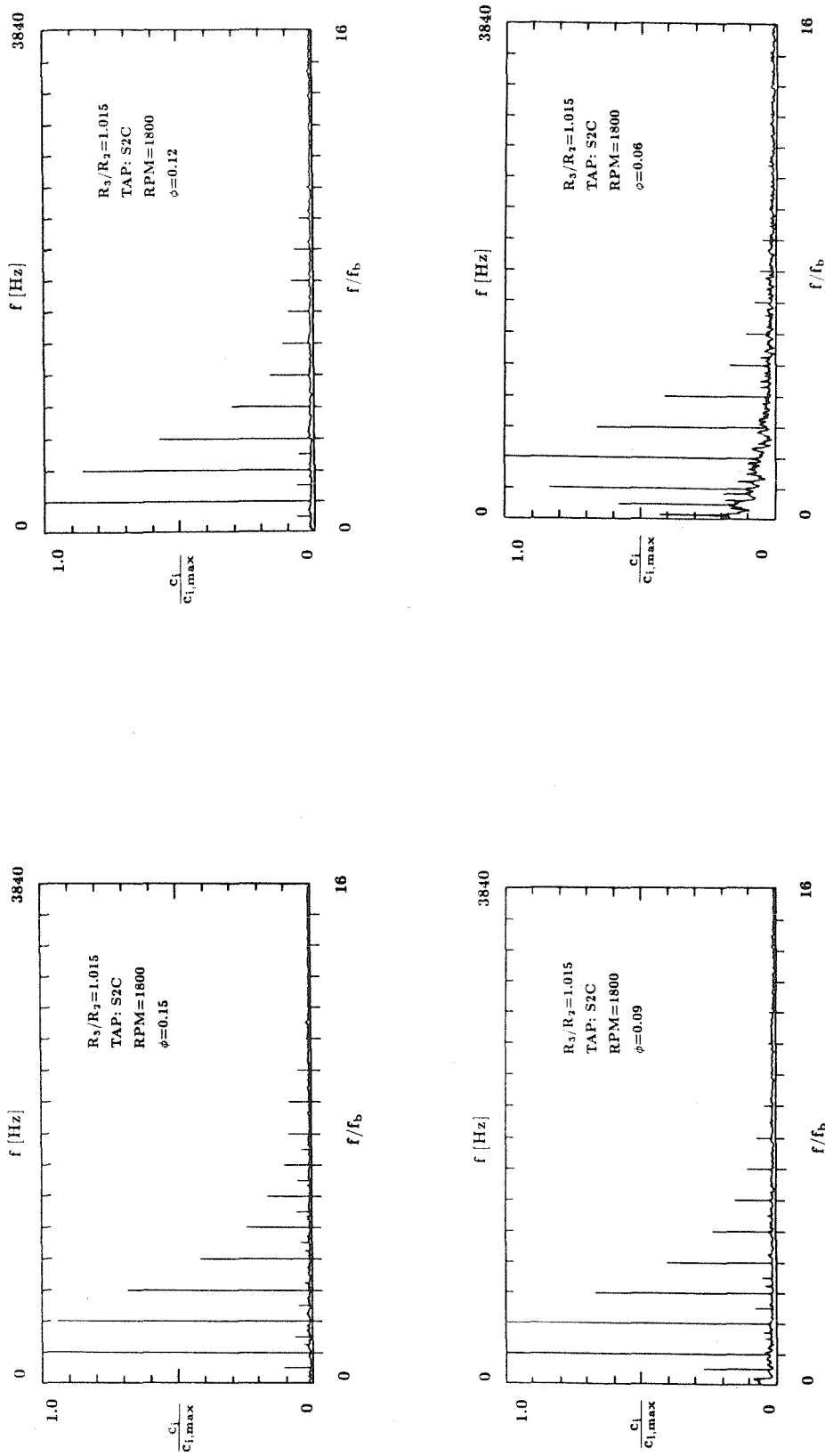


Fig. 5.9. Unsteady diffuser vane pressure measurements at pressure tap S2C for Impeller R and Diffuser S ( $\phi = 0.15, 0.12, 0.09$  and  $0.06, R_3/R_2 = 1.045$ ,  $\nu_{\text{pm}} = 1800$ ).



**Fig. 5.10.** Spectra of unsteady diffuser vane pressure measurements at pressure tap S2C for Impeller R and Diffuser S ( $\phi = 0.15, 0.12, 0.09$  and  $0.06, R_3/R_2 = 1.015$ , rpm = 1800).

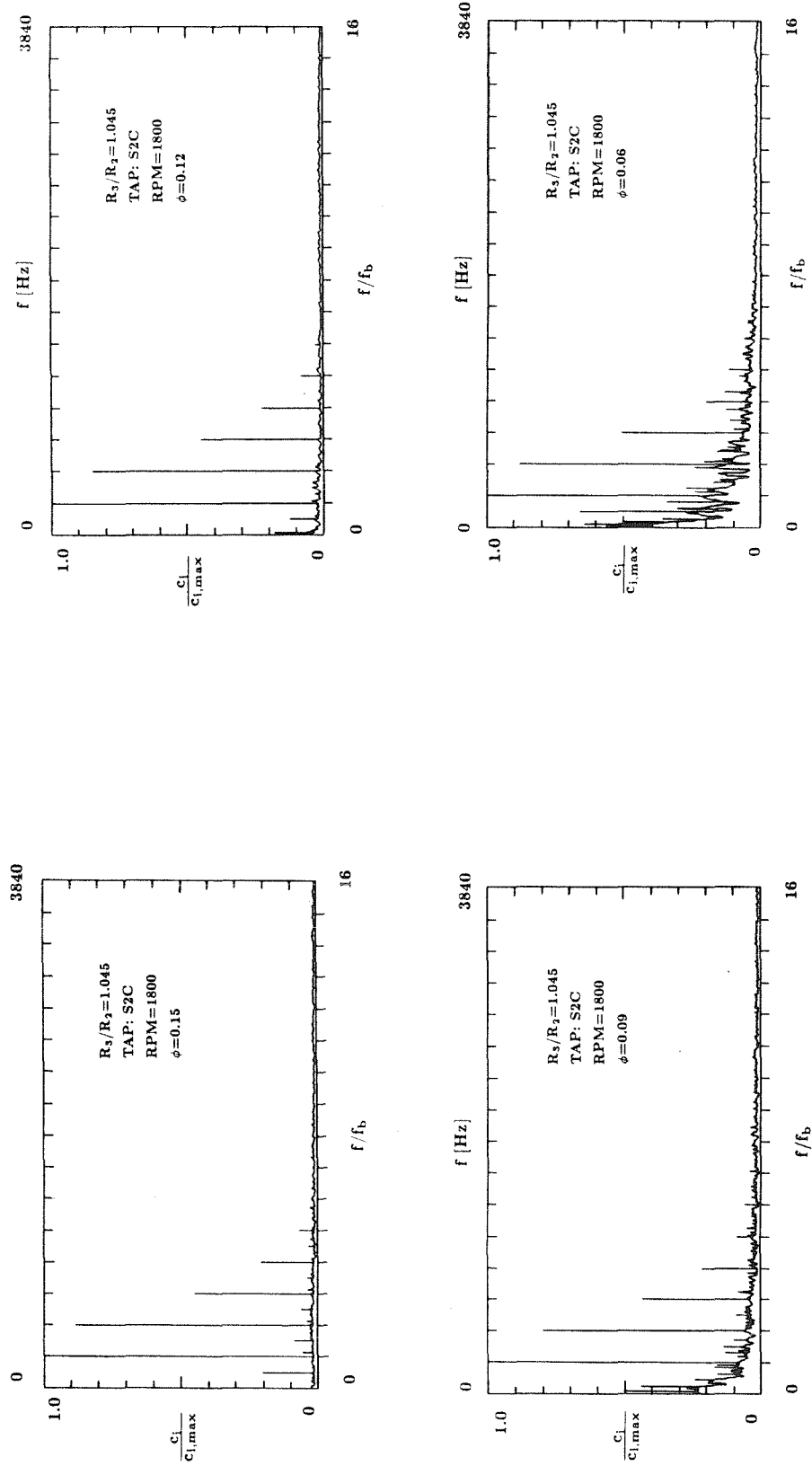


Fig. 5.11. Spectra of unsteady diffuser vane pressure measurements at pressure tap S2C for Impeller R and Diffuser S ( $\phi = 0.15, 0.12, 0.09$  and  $0.06, R_3/R_2 = 1.045$ , rpm = 1800).

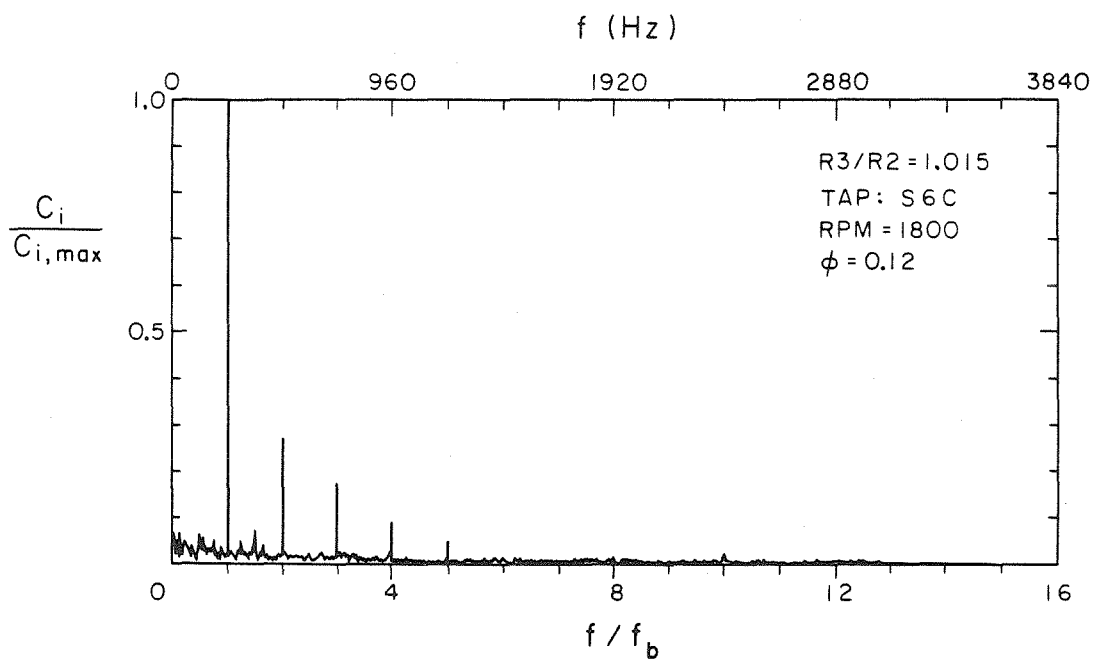


Fig. 5.12. Spectrum of unsteady vane pressure measurements at pressure tap S6C for Impeller R and Diffuser S ( $\phi = 0.12$ ,  $R_3/R_2 = 1.015$ , rpm = 1800,  $c_{i,\max} = 0.070$ ).

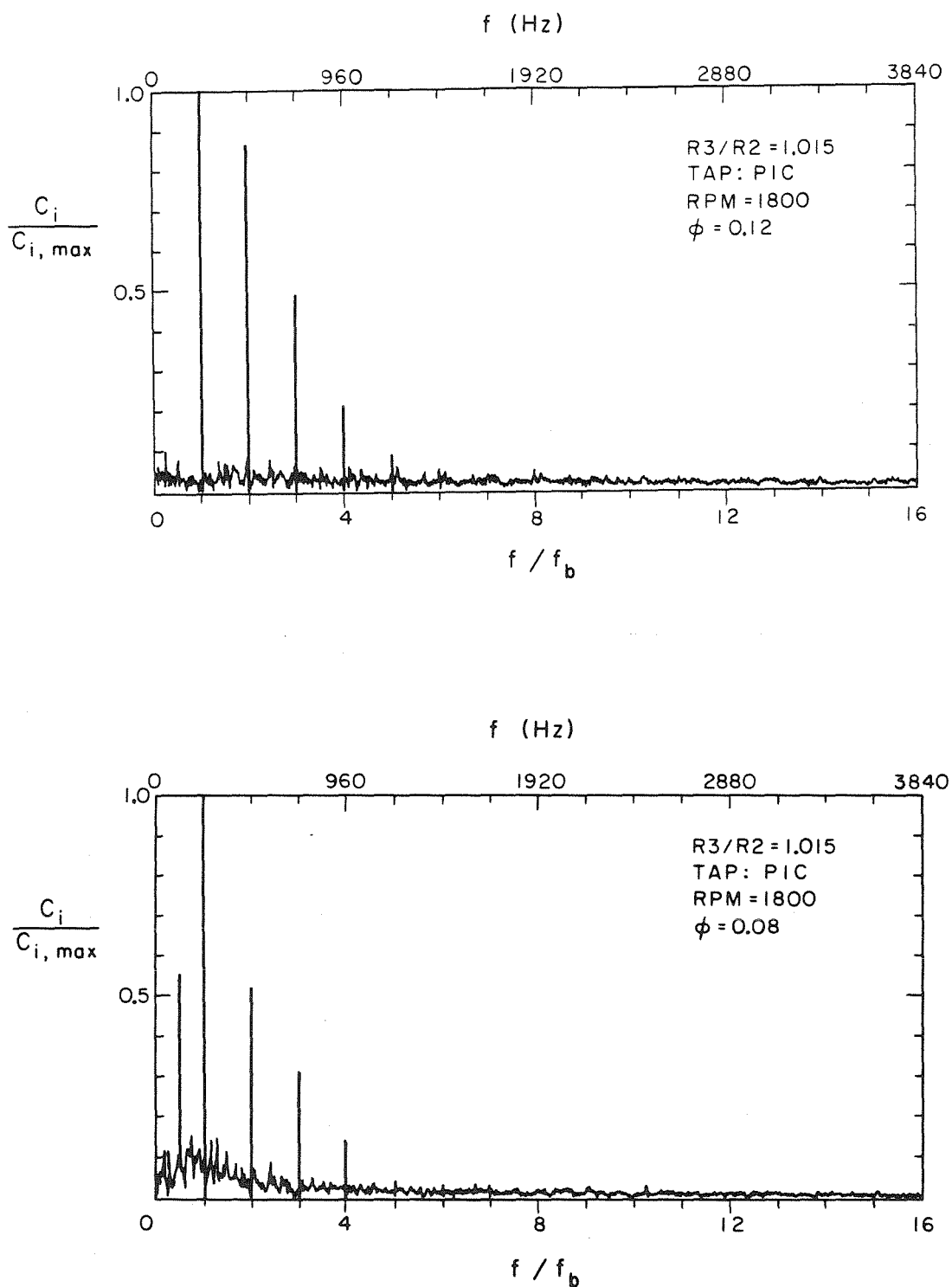


Fig. 5.13. Spectra of unsteady vane pressure measurements at pressure tap P1C for Impeller R and Diffuser S ( $\phi = 0.12$  and  $0.08$ ,  $R_3/R_2 = 1.015$ , rpm = 1800,  $c_{i,\max} = 0.060$  and  $0.071$ ).

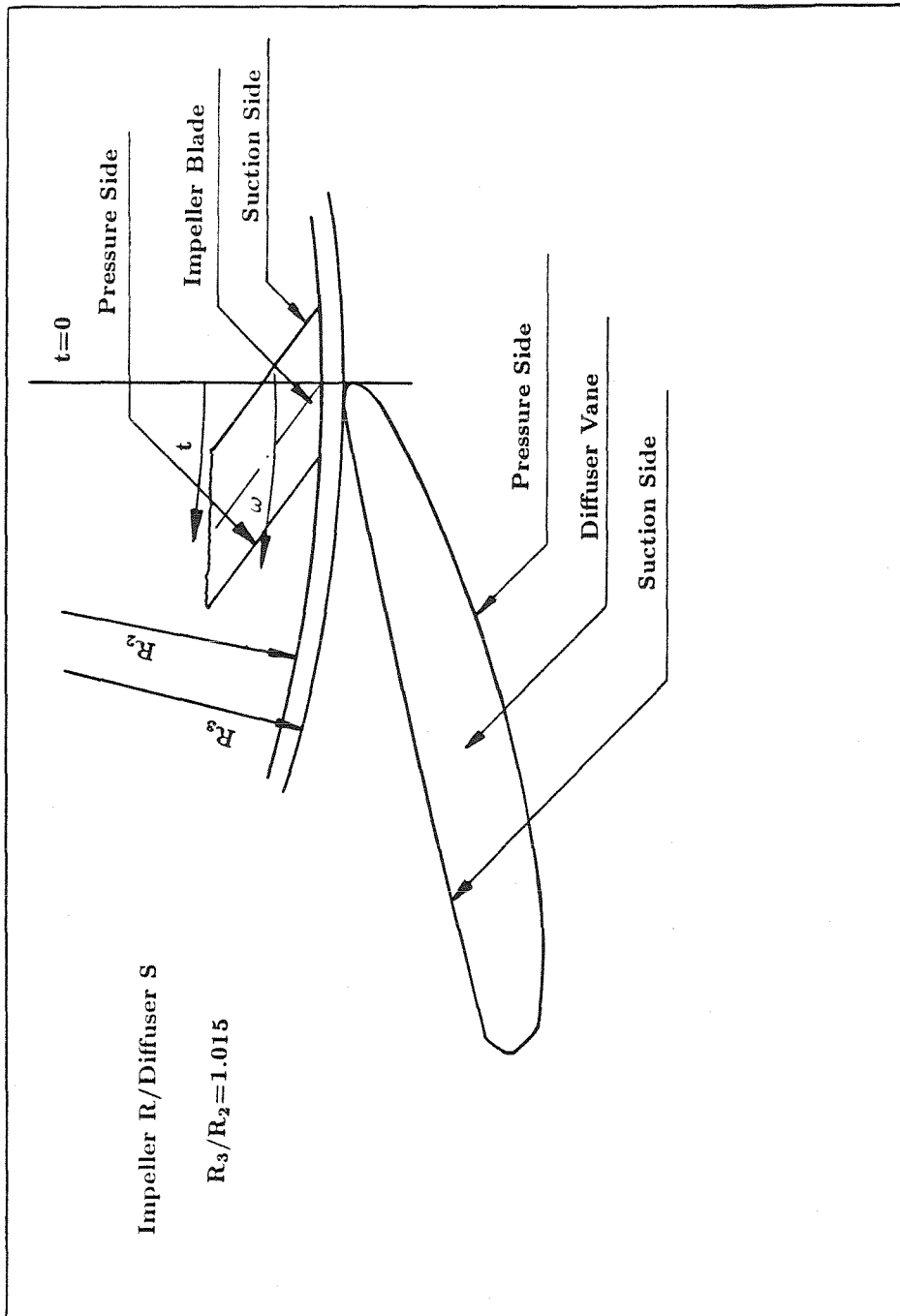
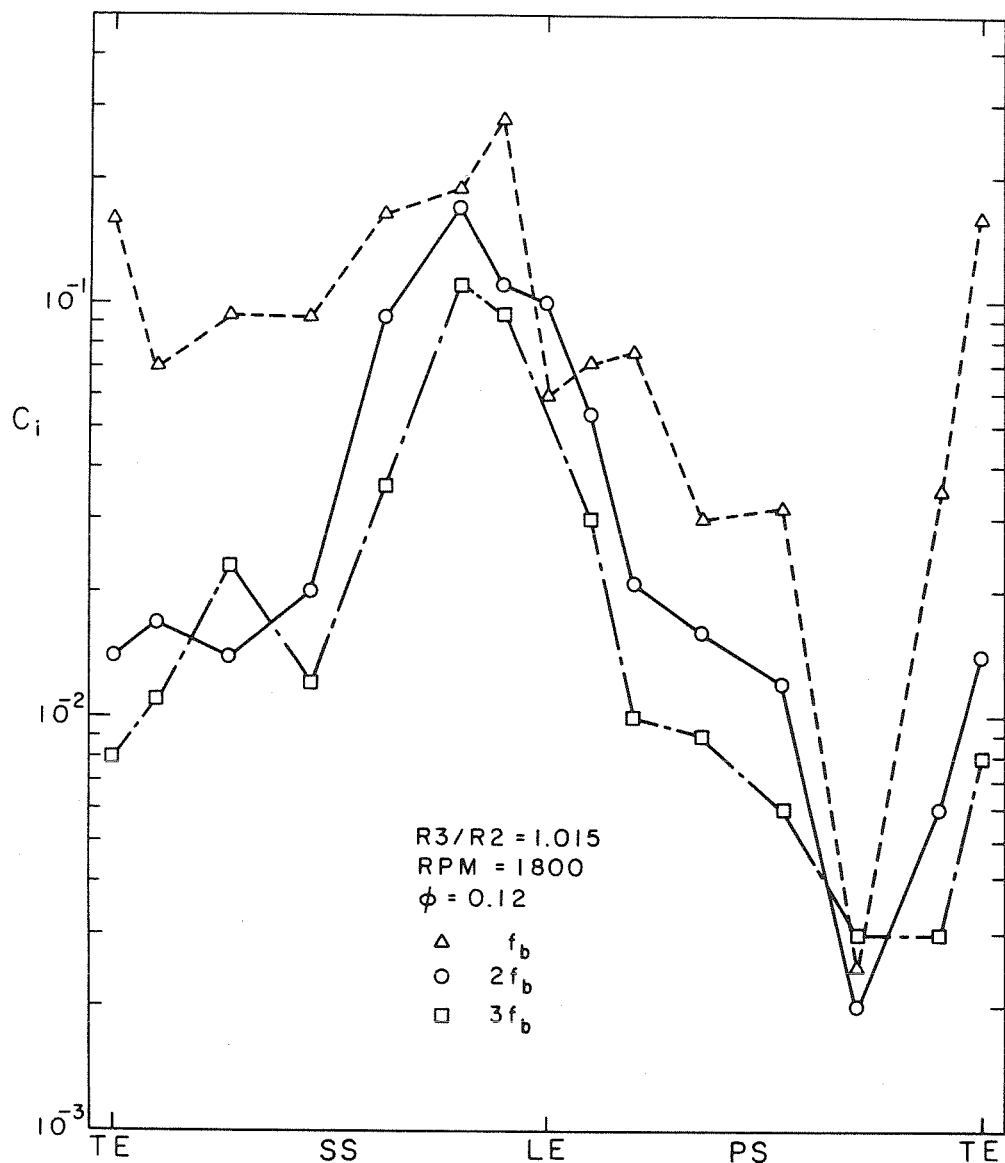


Fig. 5.14. Geometric reference configuration for the phase computation.



**Fig. 5.15.** Magnitude of Fourier coefficients of impeller blade passage harmonics for Impeller R and Diffuser S ( $\phi = 0.12$ ,  $R_3/R_2 = 1.015$ , rpm = 1800).

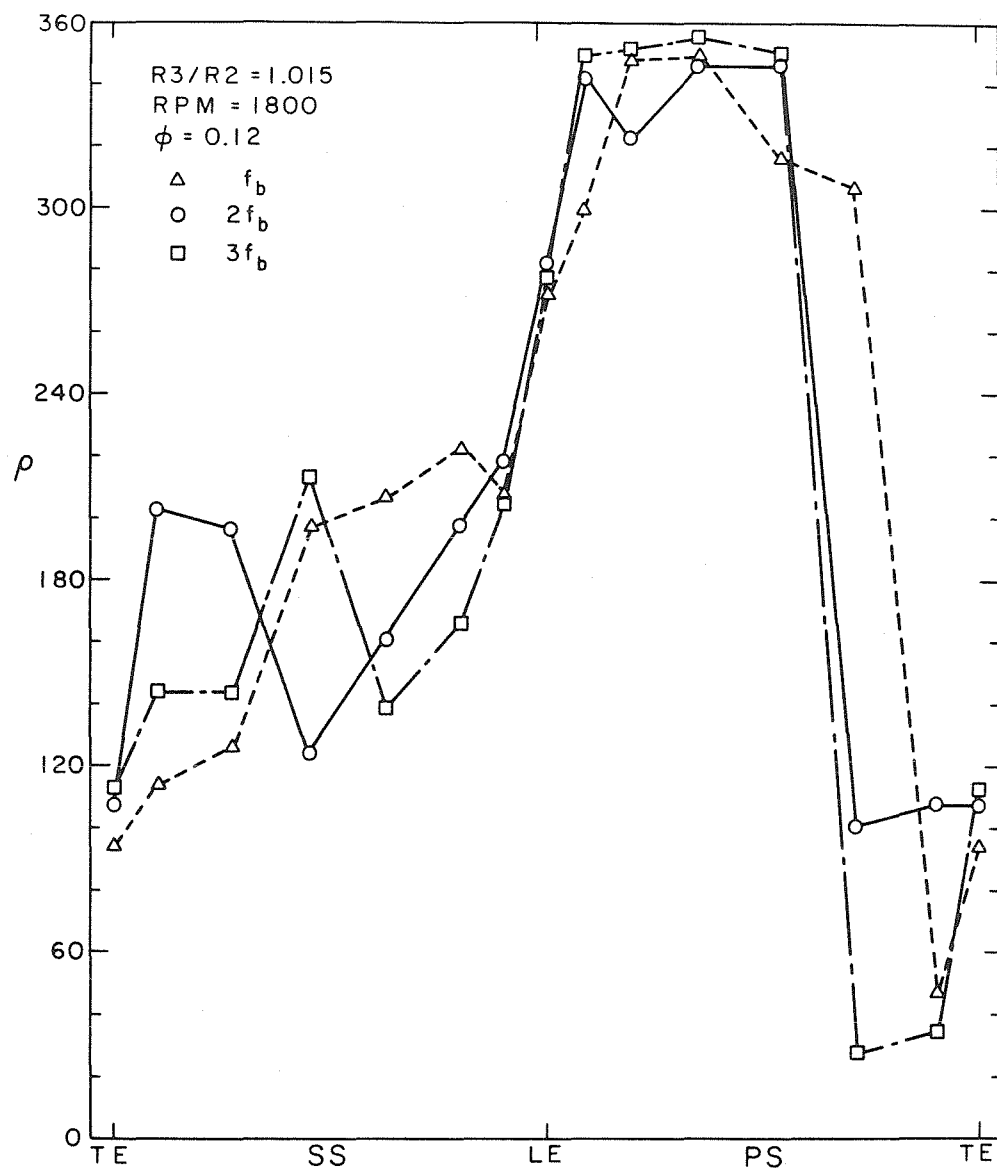


Fig. 5.16. Phase of Fourier coefficients of impeller blade passage harmonics for Impeller R and Diffuser S ( $\phi = 0.12, R_3/R_2 = 1.015, \text{ rpm} = 1800$ ).

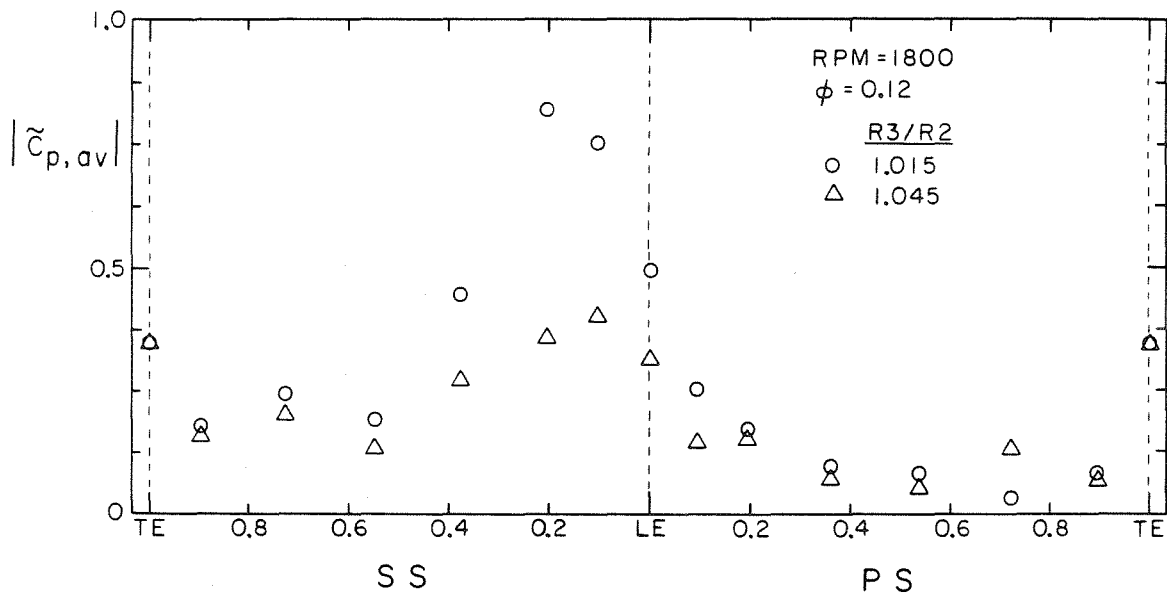


Fig. 5.17. Magnitude of ensemble averaged pressure fluctuations at mid vane height for Impeller R and Diffuser S ( $\phi = 0.12$ ,  $R_3/R_2 = 1.015$  and  $1.045$ , rpm = 1800).

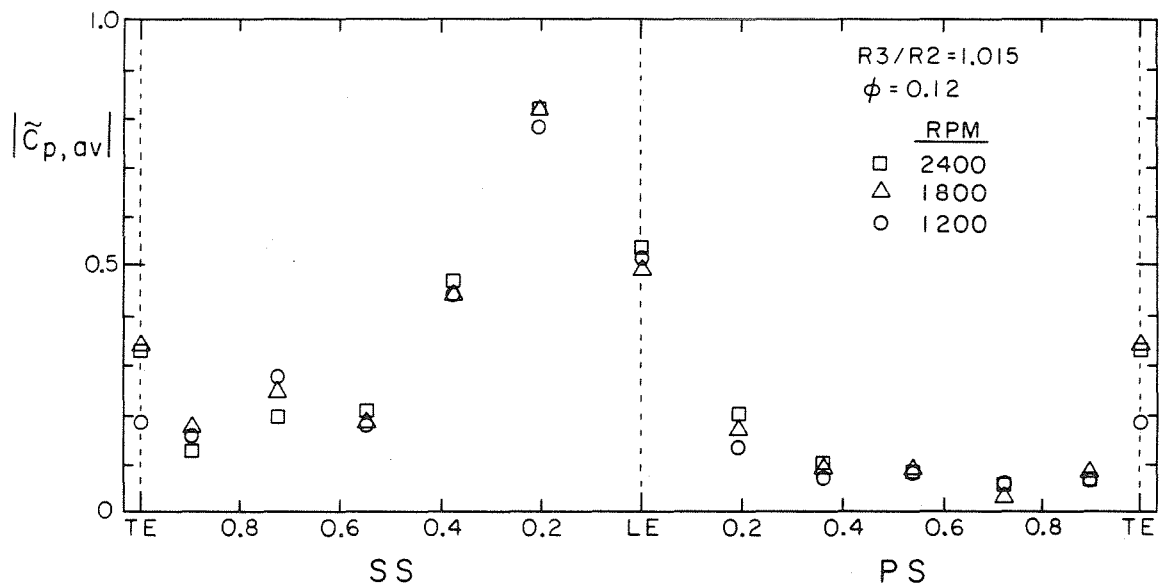
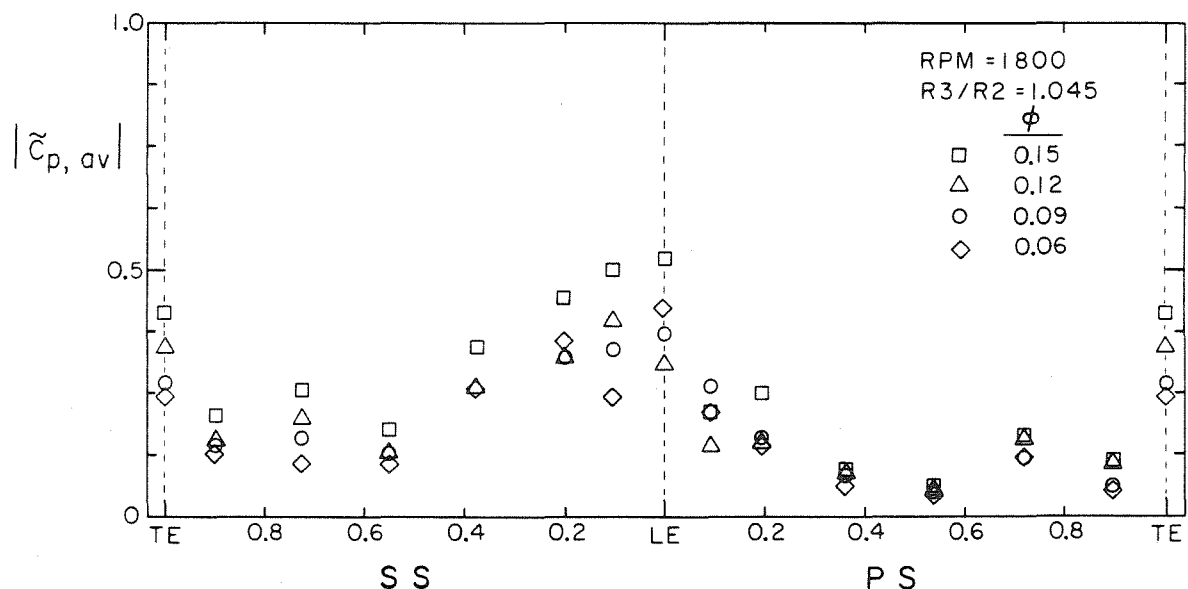
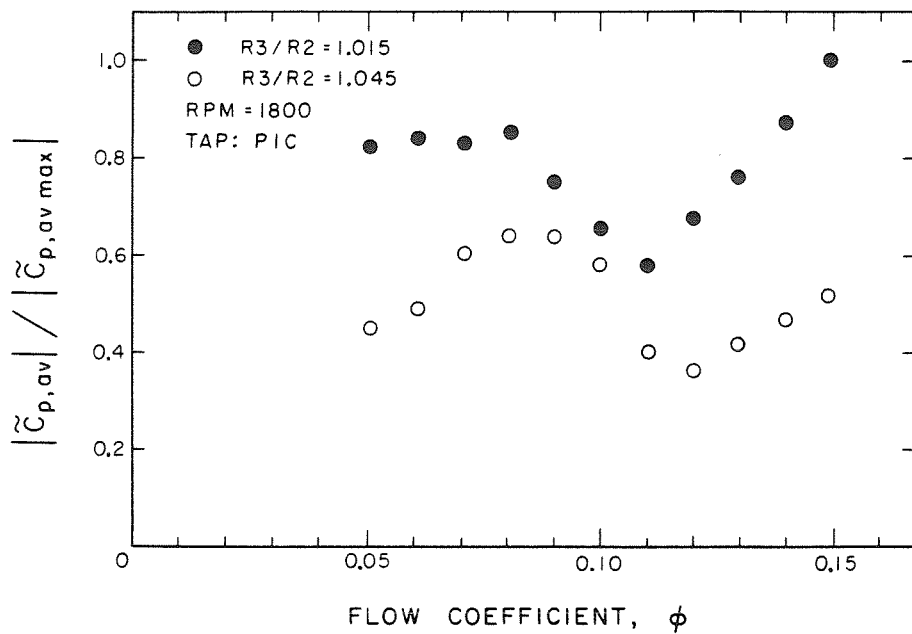


Fig. 5.18. Magnitude of ensemble averaged pressure fluctuations at mid vane height for Impeller R and Diffuser S ( $\phi = 0.12$ ,  $R_3/R_2 = 1.015$ , rpm = 1200, 1800 and 2400).



**Fig. 5.19.** Magnitude of ensemble averaged pressure fluctuations at mid vane height for Impeller R and Diffuser S ( $\phi = 0.15, 0.12, 0.09$  and  $0.06, R_3/R_2 = 1.045$ , rpm = 1800).



**Fig. 5.20.** Magnitude of ensemble averaged pressure fluctuations at pressure tap P1C for Impeller R and Diffuser S ( $\phi = 0.05 - 0.15$ ,  $R_3/R_2 = 1.015$  and  $1.045$ , rpm = 1800). Best efficiency flow coefficient:  $\phi = 0.12$ .

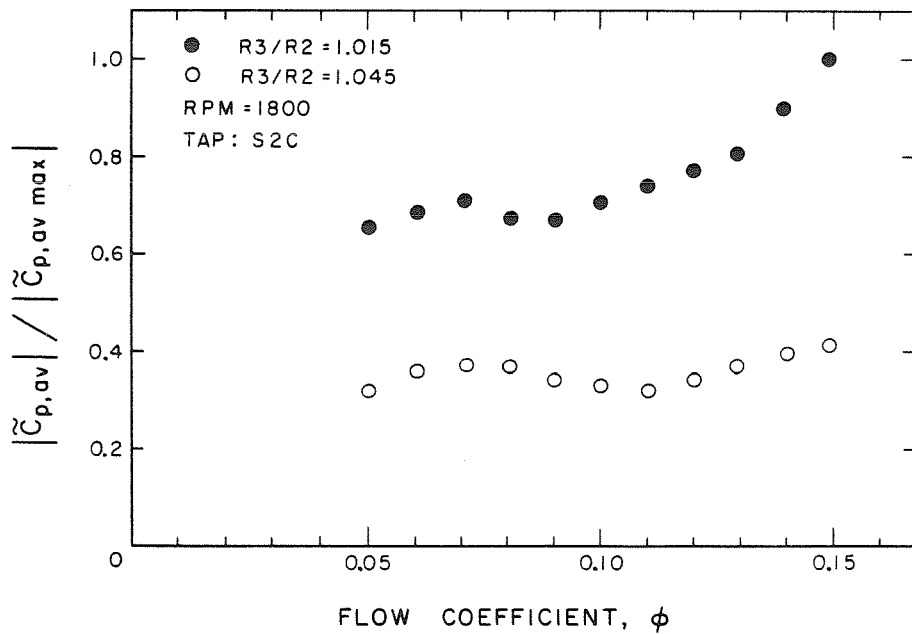


**Fig. 5.21.** Magnitude of ensemble averaged pressure fluctuations at pressure tap S2C for Impeller R and Diffuser S ( $\phi = 0.05 - 0.15$ ,  $R_3/R_2 = 1.015$  and  $1.045$ , rpm = 1800). Best efficiency flow coefficient:  $\phi = 0.12$ .

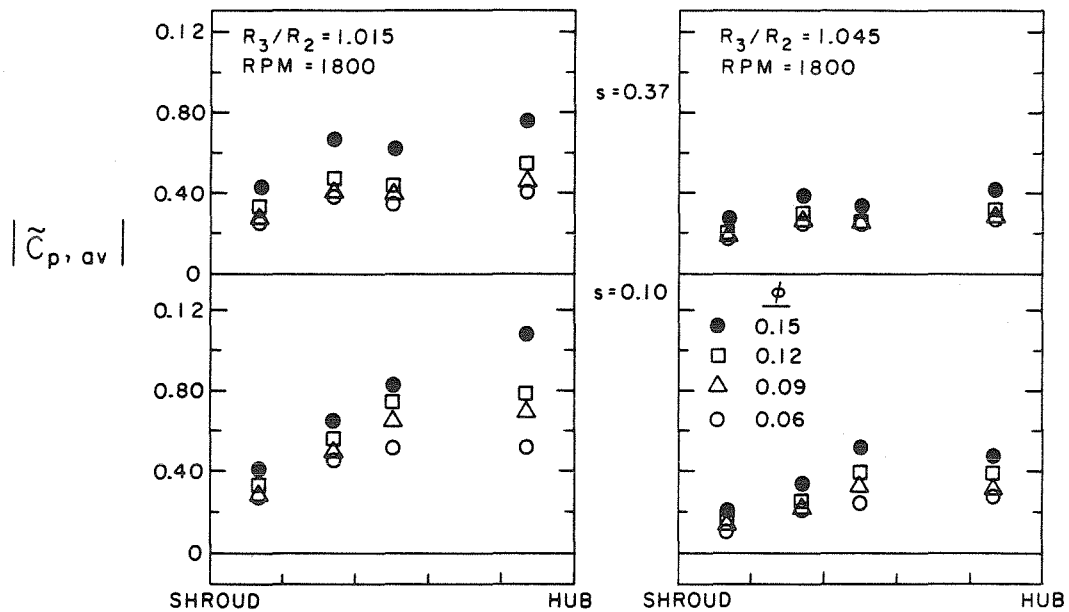


Fig. 5.22. Magnitude of ensemble averaged pressure fluctuations across the span of the vane for Impeller R and Diffuser S ( $\phi = 0.15, 0.12, 0.09$  and  $0.06$ ,  $R_3/R_2 = 1.015$ , rpm = 1800).

Fig. 5.23. Magnitude of ensemble averaged pressure fluctuations across the span of the vane for Impeller R and Diffuser S ( $\phi = 0.15, 0.12, 0.09$  and  $0.06$ ,  $R_3/R_2 = 1.045$ , rpm = 1800).

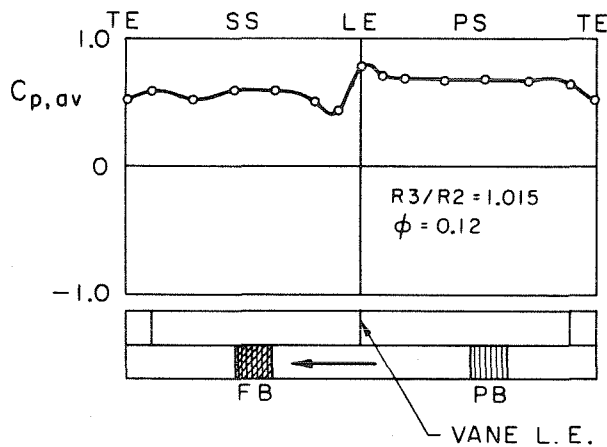
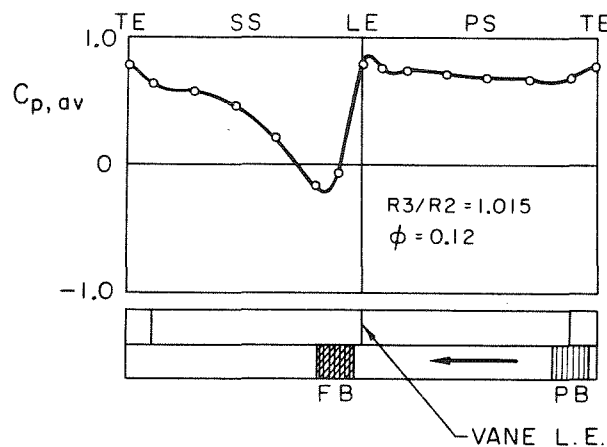


Fig. 5.24. Ensemble averaged pressured distribution at mid vane height for Impeller R and Diffuser S ( $\phi = 0.12$ ,  $R_3/R_2 = 1.015$ , rpm = 1800).

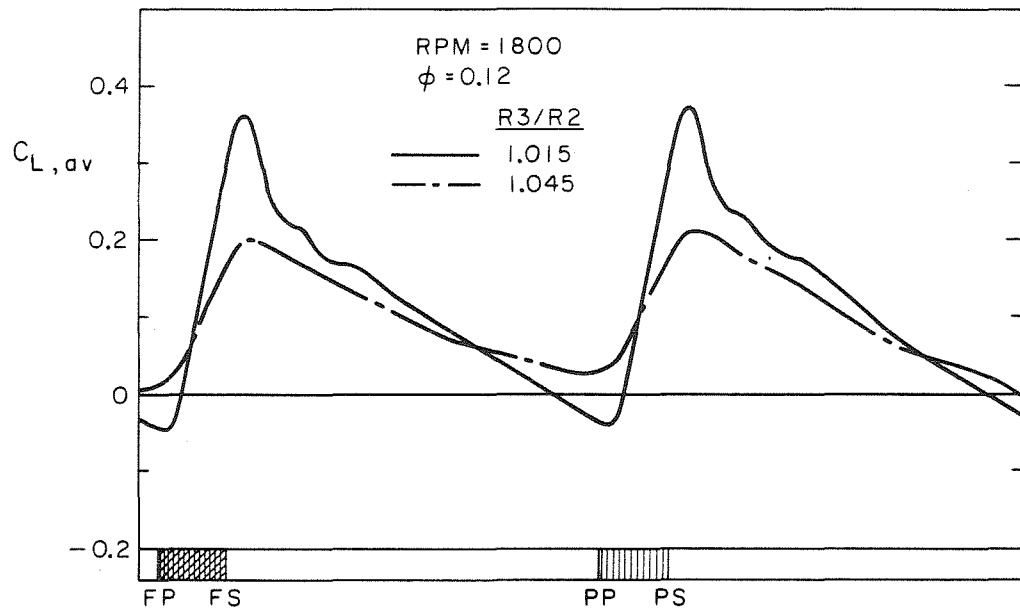


Fig. 5.25. Ensemble averaged lift on diffuser vane at mid vane height for Impeller R and Diffuser S ( $\phi = 0.12$ ,  $R_3/R_2 = 1.015$  and  $1.045$ , rpm = 1800).

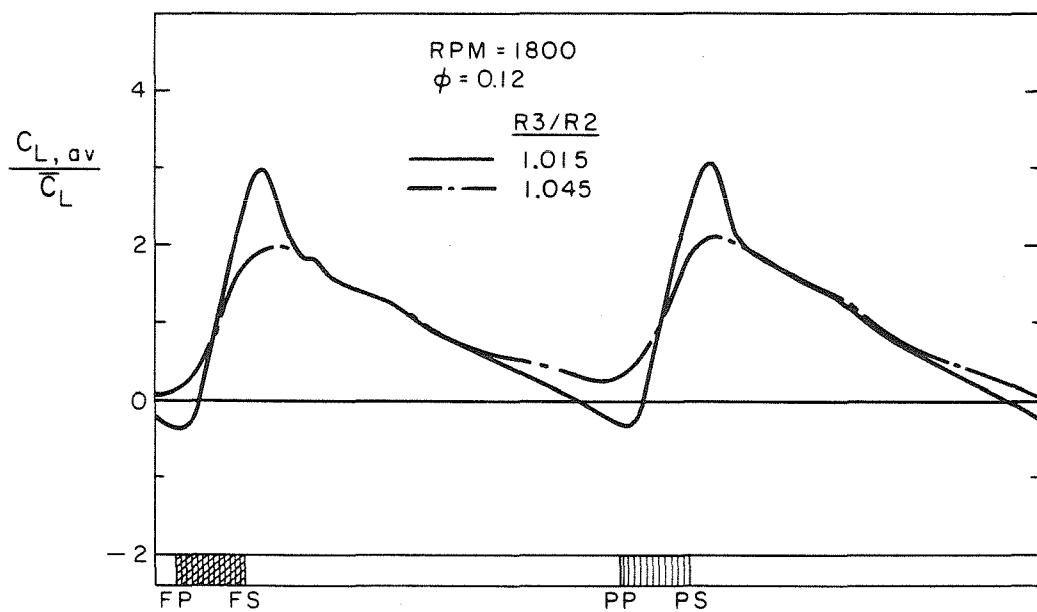


Fig. 5.26. Ratio of ensemble averaged lift to steady lift at mid vane height for Impeller R and Diffuser S ( $\phi = 0.12$ ,  $R_3/R_2 = 1.015$  and  $1.045$ , rpm = 1800).

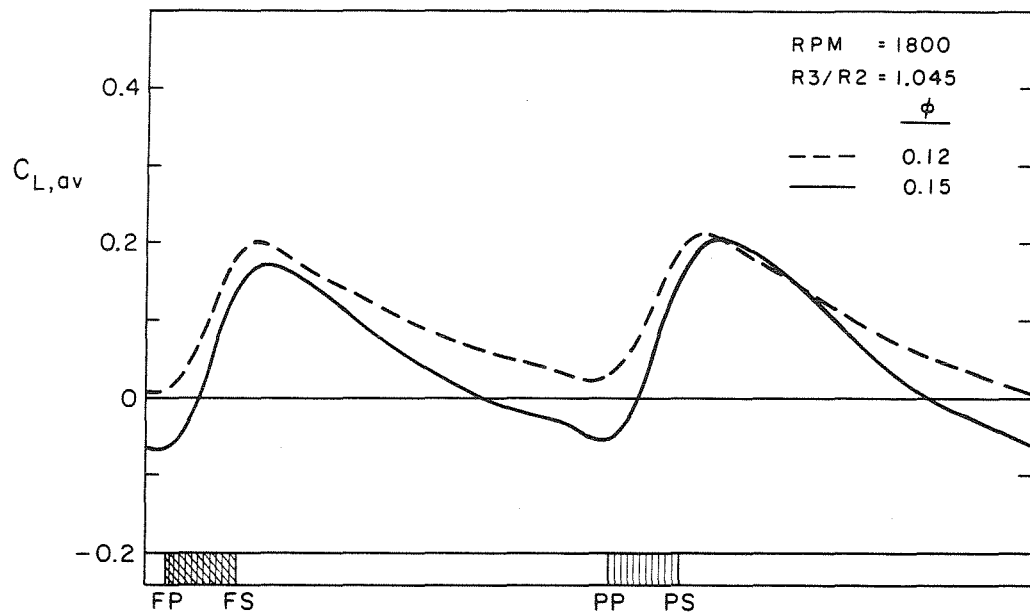


Fig. 5.27. Ensemble averaged lift on diffuser vane at mid vane height for Impeller R and Diffuser S ( $\phi = 0.15$  and  $0.12$ ,  $R_3/R_2 = 1.045$ , rpm = 1800).

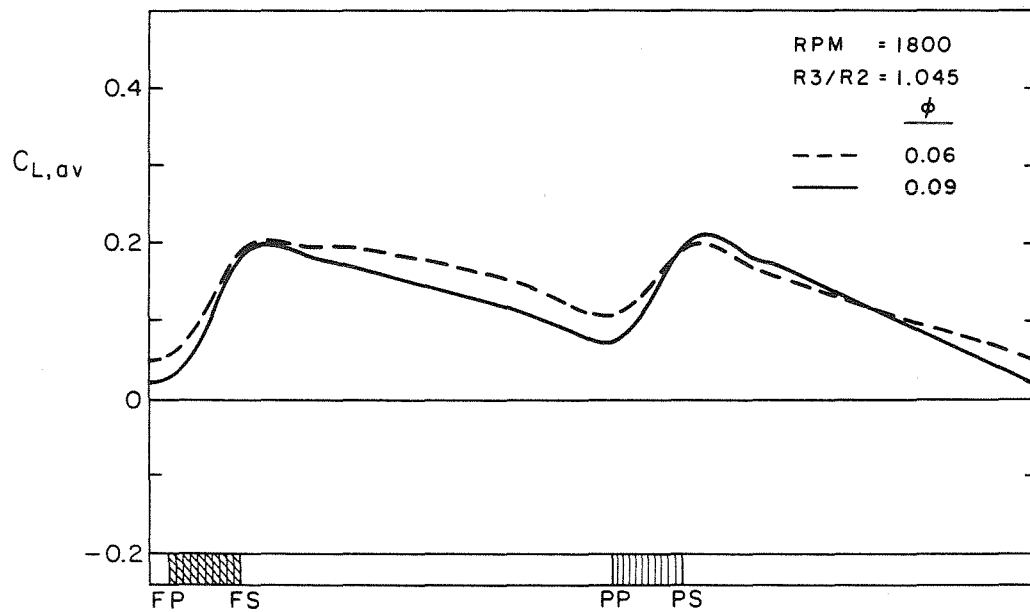


Fig. 5.28. Ensemble averaged lift on diffuser vane at mid vane height for Impeller R and Diffuser S ( $\phi = 0.09$  and  $0.06$ ,  $R_3/R_2 = 1.045$ , rpm = 1800).

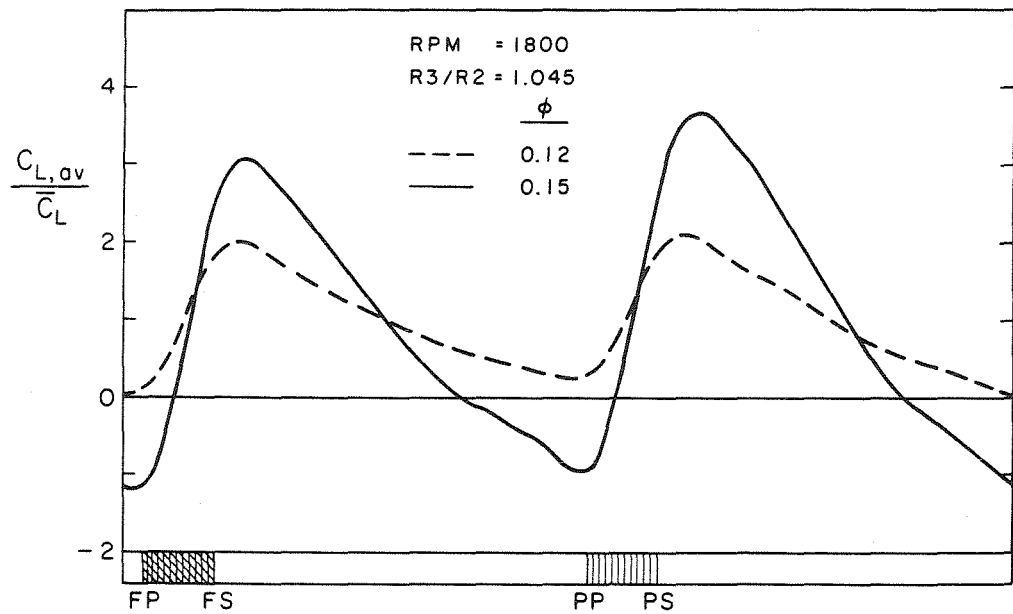


Fig. 5.29. Ratio of ensemble averaged lift to steady lift at mid vane height for Impeller R and Diffuser S ( $\phi = 0.15$  and  $0.12$ ,  $R_3/R_2 = 1.045$ , rpm = 1800).

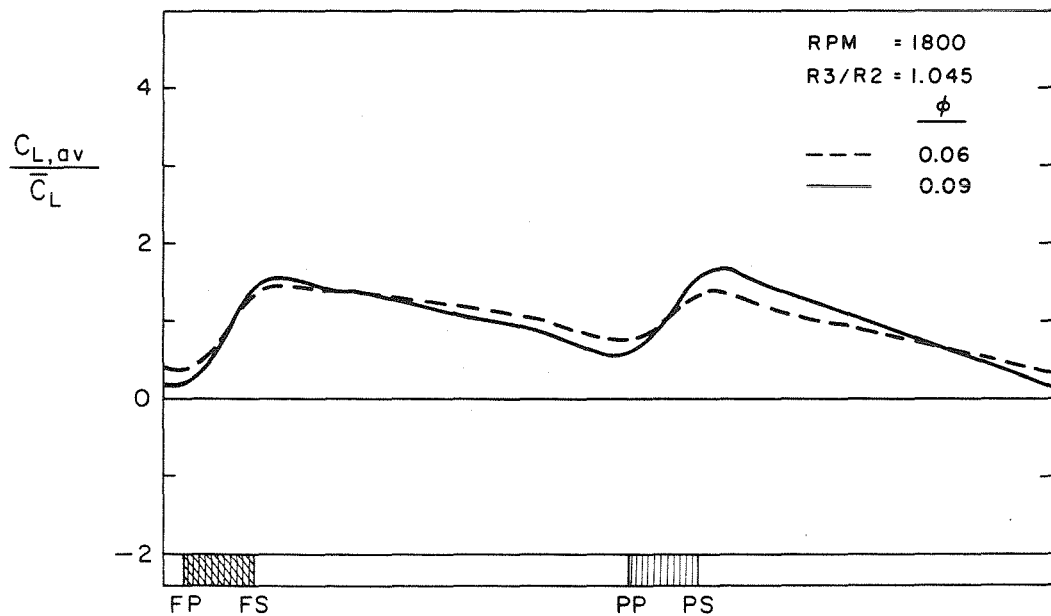


Fig. 5.30. Ratio of ensemble averaged lift to steady lift at mid vane height for Impeller R and Diffuser S ( $\phi = 0.09$  and  $0.06$ ,  $R_3/R_2 = 1.045$ , rpm = 1800).

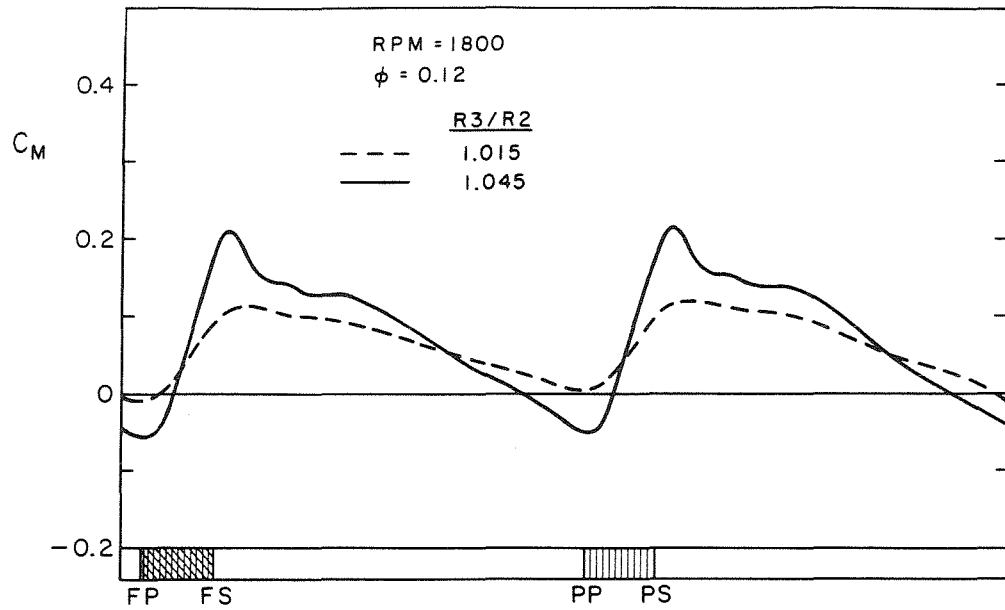


Fig. 5.31. Ensemble averaged moment about the diffuser vane leading edge for Impeller R and Diffuser S ( $\phi = 0.12$ ,  $R_3/R_2 = 1.015$  and  $1.045$ , rpm = 1800).

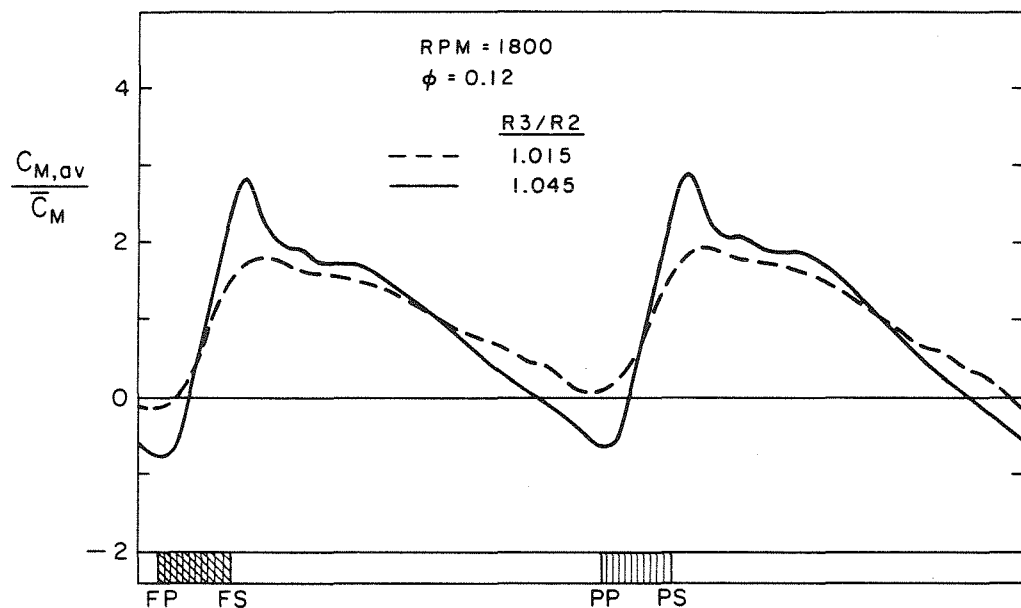


Fig. 5.32. Ratio of ensemble averaged moment to steady moment (about the diffuser vane leading edge) for Impeller R and Diffuser S ( $\phi = 0.12$ ,  $R_3/R_2 = 1.015$  and  $1.045$ , rpm = 1800).

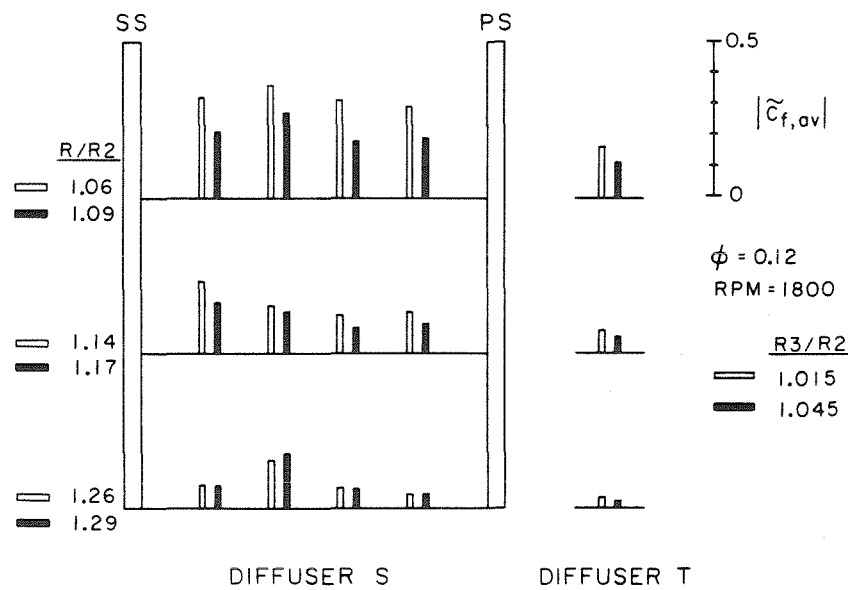


Fig. 5.33. Magnitude of ensemble averaged front shroud pressure fluctuations on Diffuser S and Diffuser T using Impeller R ( $\phi = 0.12, R_3/R_2, \text{ rpm} = 1800$ ).

## CHAPTER 6

### 6. Impeller Blade and Diffuser Vane Pressure Measurements in a Radial Pump

#### 6.1. Introduction

In the previous chapter, the diffuser vane pressure measurements using one half of the double suction pump impeller of the HPOTP (High Pressure Oxygen Pump) of the SSME (Space Shuttle Main Engine), Impeller R, were presented. Here, results of the diffuser vane pressure measurement using a two-dimensional impeller, Impeller Z1, will be reported. A second two-dimensional impeller of identical blade number and identical blade geometry, Impeller Z2, was designed and built to measure unsteady impeller blade pressures. This permitted a "complete" investigation of the rotor-stator interaction: impeller blade and diffuser vane pressure measurements. The impeller blade pressure measurements were made for Diffuser S, and for a second diffuser, of identical side wall geometry as Diffuser S, that permitted variable diffuser vane configurations to investigate the effects of the number of diffuser vanes and the diffuser vane angle on the impeller blade pressure measurements (the diffuser vane geometry and the diffuser vane configuration are given in Chapter 3). During the experiment, the impeller could only be positioned at locations on an orbit concentric to the diffuser center (orbit radius=0.050 in., impeller blade trailing edge radius= 3.1875 in.). Hence, during one impeller revolution, the radial gap between an impeller blade trailing edge and the diffuser vane leading edges varied between 5% and 8% of the impeller discharge radius. Some preliminary results on diffuser vane pressure measurements for the two-dimensional test impeller have been previously reported by Arndt et al. (1987).

## 6.2. Overall Performance

Performance curves, showing the normalized total pressure rise across the pump ( $\psi = (p_{down} - p_{up})/(\rho u_2^2)$ ), versus flow coefficient ( $\phi = Q/(u_2 A_2)$ ) are presented in figure 6.1 for Diffusers F, G, H and S. The largest flow coefficient was obtained for Diffuser S,  $\phi = 0.135$ . For large flow coefficients,  $\phi \geq 0.10$ , the total pressure rise was largest for Diffuser S, and smallest for Diffusers F (twelve vanes at 20 degrees) and H (six vanes at 10 degrees). At  $\phi = 0.09$ , the total pressure rise was approximately equal for Diffusers S, F and G (six vanes at 20 degrees), whereas the total pressure rise for Diffuser H was about 12% smaller. For low flow coefficients,  $\phi \leq 0.08$ , the total pressure increase for Diffuser S with decreasing flow coefficient was significantly smaller than for Diffusers F, G and H, so that for  $\phi = 0.06$  the total pressure rise for Diffuser S was even slightly smaller than for Diffuser H. The largest total pressure rise at that flow coefficient was attained for Diffuser F (twelve vanes at 20 degrees). Summarizing, it can be seen that for large flow coefficients, Diffuser S and G produced the largest total pressure rise, whereas for low flow coefficients, Diffusers F and G produced the largest total pressure rise. Diffuser H had at most flow coefficients the smallest total pressure rise.

## 6.3. Diffuser Vane Pressure Measurements

### 6.3.1. Steady Vane Pressure Measurements and Steady Vane Lift Computations

The steady vane pressure measurements are presented as a steady pressure coefficient, normalized by the dynamic pressure based on impeller tip speed,  $(1/2)\rho u_2^2$ ,

$$\bar{c}_p = \frac{\bar{p}_v - \bar{p}_{up}}{(1/2)\rho u_2^2}. \quad (6.1)$$

Steady diffuser vane pressure measurements were made for three flow coefficients,  $\phi = 0.135, 0.10$  and  $0.06$ , two radial gaps between diffuser vanes and impeller blades (5% and 8%) and a rotational speed of 1200 rpm. The steady vane pressure distribution for the medium flow coefficient,  $\phi = 0.10$ , is shown in figure 6.2. The

pressure distribution on the vane changes only marginally with increasing radial gap. Steady vane pressure measurements were also made on the vane suction side across the span of the vane at two locations downstream of the vane leading edge,  $s=0.10$  and  $0.37$  (at vane mid height, the pressure taps corresponding to  $s=0.10$  and  $0.37$  are S1C and S3C). The results, for a radial gap of 5%, are presented in figures 6.3 and 6.4. As for Impeller R, it can be seen that the steady vane pressure for all three flow coefficients investigated does not vary significantly across the span of the vane.

From the steady vane pressure measurements at mid vane height, the steady force on the vane at mid vane height was computed. The steady pressure distribution around the vane was obtained by fitting a third order periodic spline through the measured data. A periodic spline fit was chosen to get continuity for the pressure and the first two pressure derivatives at the vane leading and the vane trailing edge. Hence, the steady force was computed from

$$\bar{\mathbf{F}} = - \oint (\bar{p}_v - \bar{p}_{up})(\xi) \mathbf{n} d\xi. \quad (6.2)$$

The lift on the vane was defined as the component of the force on the vane normal to the chord joining the vane leading and the vane trailing edge. The lift on the vane was defined as positive if the force component normal to the vane chord was in the positive  $y$  direction (figure 6.5). Furthermore, the moment about the vane leading edge was computed from the vane pressure measurements at mid vane height,

$$\bar{\mathbf{M}}_z = - \oint (\bar{p}_v - \bar{p}_{up})(\xi) \mathbf{r} \times \mathbf{n} d\xi, \quad (6.3)$$

where  $\mathbf{r}$  is the vector from the vane leading edge to the diffuser vane surface. The lift and the moment are presented as lift and moment coefficients, normalized by the dynamic pressure based on impeller tip speed,  $(1/2)\rho u_2^2$ , and the vane chord,  $c$ ,

$$\bar{c}_L = \frac{L}{(1/2)\rho u_2^2 c} \quad (6.4)$$

$$\bar{c}_M = \frac{M_z}{(1/4)\rho u_2^2 c^2}. \quad (6.5)$$

The steady lift and the steady moment about the vane leading edge are given in Table 6.1.

**Table 6.1. Steady Lift and Moment on a Vane of Diffuser S.**  
(Impeller Z1 and Diffuser S)

$\phi$	$R_3/R_2$	$\bar{c}_L$	$\bar{c}_M$
0.135	1.05	0.0176	-0.0133
0.135	1.08	0.0138	-0.0110
0.10	1.05	0.0378	-0.0229
0.10	1.08	0.0317	-0.0204
0.06	1.05	0.0641	-0.0451
0.06	1.08	0.0660	-0.0464

It can be observed that, as for Impeller R, with the exception of the lowest flow coefficient,  $\phi = 0.06$ , the steady lift and moment decrease with increasing radial gap. The steady lift is increasing significantly with decreasing flow coefficient.

### 6.3.2. Ensemble Averaged Unsteady Vane Pressure Measurements and Spectra of Unsteady Vane Pressure Measurements

The unsteady vane pressure measurements were ensemble averaged, and will be presented as an ensemble averaged vane pressure coefficient, normalized by the dynamic pressure based on impeller tip speed,

$$\tilde{c}_{v,av}(i) = \frac{1}{N} \sum_{j=1}^N \frac{\tilde{p}_v(i,j)}{(1/2)\rho u_2^2}, \quad (6.6)$$

where  $N$  is the number of averaging periods,  $i$  the  $i$ th data point taken in any of the  $N$  averaging periods, and  $j$  the  $j$ th of the  $N$  averaging periods. During one averaging period, corresponding to one main shaft revolution (or five impeller blade passages), 1024 data points were taken. A total of 512 averaging periods was used for the ensemble averages. Furthermore, spectra of the unsteady data were obtained. In figures 6.6 and 6.7, the ensemble averaged unsteady vane pressure measurements

and the corresponding spectrum of the unsteady vane pressure measurements are presented for the medium flow coefficient,  $\phi = 0.10$ , at 3000 rpm and  $R_3/R_2=1.05$ . On the upper half of each figure, the ensemble averaged vane pressure fluctuations are shown. The position of the impeller blades is referenced to the diffuser vane leading edge. In the lower half, the magnitude of the Fourier coefficients relative to the magnitude of the largest Fourier coefficient ( $c_i/c_{i,max}$ ) for a particular test is shown versus frequency (upper horizontal scale) and frequency normalized by impeller blade passage frequency ( $f/f_b$ ) (lower horizontal scale).

The measurements at the suction side pressure tap, S2C, are examined first. It is evident that the fluctuations are periodic with impeller blade passage, and that the magnitude of the fluctuations are of the same order of magnitude as the total pressure rise across the pump. The largest pressure occurs before the impeller blade pressure side passes the diffuser vane leading edge. As the impeller blade passes the diffuser vane leading edge, the pressure drops to attain its lowest value shortly before the impeller blade suction side passes the diffuser vane. After the impeller blade has passed, the pressure rises sharply, then stays approximately constant for about the first half of the blade passage and rises on the second half of the blade passage to its maximum value, which is attained as the impeller blade reaches the diffuser vane leading edge. The spectrum of the unsteady pressure measurements at tap S2C is dominated by the impeller blade passage frequency and its higher harmonics. In fact, the second harmonic is slightly larger than the first. The fluctuations at pressure tap P2C on the vane pressure side are significantly smaller than those on the suction side. The maximum pressure value is attained after about two-thirds of the impeller blade passage. Then the pressure drops and reaches its lowest value as the impeller blade pressure side reaches the diffuser vane leading edge. While the impeller blade is passing the diffuser vane leading edge, the vane pressure is already rising again. Hence, the phase relation between maximum and minimum pressure attained at diffuser vane pressure taps S2C and P2C referenced to the position of the impeller blade relative to the diffuser vane leading edge is significantly different. The spectrum of the unsteady measurements at pressure tap

P2C is dominated by the blade passage frequency and its higher harmonics, but in contrast to the spectrum for the pressure measurements taken at S2C, the higher harmonics decay much faster, and the second harmonic is smaller than the first harmonic.

### 6.3.3. Magnitude of Ensemble Averaged Diffuser Vane Pressure Fluctuations

In the following figures, data on the magnitude of the ensemble averaged unsteady vane pressure measurements at vane mid height are presented. The fluctuations are defined as the difference between the maximum and minimum pressure value in the averaging period, which corresponds to one impeller revolution. The largest fluctuations, independent of flow coefficient or radial gap, occur at the vane leading edge and on the front half of the vane suction side. Those fluctuations are of the same order of magnitude as the total pressure rise across the pump. The fluctuations are larger on the vane suction than on the vane pressure side. On the vane pressure side, they decrease monotonically from the leading edge to the trailing edge, whereas on the vane suction side they have a relative minimum at pressure tap S1C, and they decrease from pressure tap S2C monotonically to the vane trailing edge. For the two flow coefficients investigated, the largest fluctuations occur either at the vane leading edge or at pressure tap S2C.

Figure 6.8 shows the dependence of the fluctuations on the radial gap for  $\phi = 0.10$  at  $R_3/R_2 = 1.05$  and 1.08 at 3000 rpm. The large pressure fluctuations on the front half of the suction side, at the leading edge and at the pressure tap on the pressure side closest to the leading edge decrease significantly. At the pressure taps on the rear half of the vane suction side and at the other pressure taps on the pressure side, the fluctuations do not decrease significantly.

Figure 6.9 compares the fluctuations for the two flow coefficients,  $\phi = 0.135$  and 0.10, at 3000 rpm and  $R_3/R_2 = 1.05$ . At the leading edge and at all pressure taps on the suction side, the fluctuations are larger for  $\phi = 0.135$  than for  $\phi = 0.10$ ,

although the differences with flow coefficient decrease at the pressure taps near the vane trailing edge. With the exception of pressure tap P1C, where the fluctuations are larger for  $\phi = 0.10$  than for  $\phi = 0.135$ , the magnitude of the pressure fluctuations on the vane pressure side is nearly identical for the two flow coefficients.

In figure 6.10, the magnitude of the ensemble averaged unsteady vane pressure measurements made for the maximum flow coefficient,  $\phi = 0.135$ , a radial gap of 5%, and two rotational speeds, 1200 and 3000 rpm, are shown. Normalized by the dynamic pressure based on impeller tip speed,  $(1/2)\rho u_2^2$ , the vane pressure fluctuations were found to be nearly independent of the rotational speed of the impeller.

For one pressure tap, S2C, unsteady vane pressure measurements were made over a range of flow coefficients, ranging from maximum flow coefficient,  $\phi_{max} = 0.135$ , to  $\phi = 0.06$ . The shaft speed during those tests was 1500 rpm (comparing the normalized pressure measurements for  $\phi = 0.135$  and 0.10 made at 1500 and 3000 rpm, virtually no shaft speed dependence was found). In figure 6.11, the magnitude of the fluctuations as functions of flow coefficient and radial gap, relative to the magnitude of the fluctuation for maximum flow,  $\phi = 0.135$ , at a radial gap of 5%, are presented. It can be seen that the fluctuations are largest for maximum flow and decrease with decreasing flow coefficient. Increasing the radial gap between impeller blades and diffuser vanes resulted in about a 50% decrease of the fluctuations.

Unsteady pressure measurements were also made on the vane suction side across the span of the vane at two locations downstream of the vane leading edge,  $s=0.10$  and 0.37 (at vane mid height, the pressure taps corresponding to  $s=0.10$  and 0.37 are S1C and S3C). Results will be presented for  $\phi = 0.135$  and 0.10 and a radial gap of 5% (figure 6.12). It can be seen that at all measurement locations, the fluctuations are larger for the larger flow coefficient. At  $s=0.10$ , the largest fluctuations occur at the measurement location at mid vane height, whereas the smallest fluctuations occur near the shroud. This is qualitatively similar to the results obtained for Impeller R. However, the differences in fluctuation between the different measurement locations are significantly smaller than for Impeller R. At the measurement loca-

tion farther downstream,  $s=0.37$ , the vane pressure fluctuations were found largest near the diffuser front shroud and smallest at mid vane height. In particular, the fluctuations near the shroud increased by about a factor of two from the measurement location at  $s=0.10$  to the one at  $s=0.37$ . This strong increase of the vane pressure fluctuations near the shroud was not found for Impeller R. However, the differences in the magnitude of the vane pressure fluctuations across the span of the vane at  $s=0.37$  were, as at  $s=0.10$ , found to be larger for Impeller R than for the two-dimensional impeller.

#### 6.3.4. Magnitude and Phase of Fourier Coefficients of Ensemble Averaged Vane Pressure Fluctuations

The magnitude and the phase of the Fourier coefficients corresponding to impeller blade passage frequency,  $f_b$ , twice impeller blade passage frequency,  $2f_b$ , and three times the impeller blade passage frequency,  $3f_b$ , will be presented for the medium flow coefficient,  $\phi = 0.10$ , and a radial gap of 5%. The magnitudes of the Fourier coefficients are presented in figure 6.14. Note that the vertical scale, for the magnitude of the coefficients, is not a linear but a logarithmic one. The magnitude of the first harmonic, i.e. the impeller blade passage harmonic, is approximately equal at the pressure taps P1C, P2C, S0C, S2C and S3C. The magnitude of the higher harmonics, twice and three times blade passage frequency, however, is significantly larger on the front half of the vane suction than on the vane pressure side. Hence, the pressure fluctuations on the front half of the vane suction side are larger than those on the front half of the vane pressure side because of the larger higher harmonics. In fact, the magnitude of the second harmonic at the pressure taps on the front half of the vane suction side is actually as large as the first. On the rear half of the vane suction side, the magnitude of the first harmonic is, however, significantly larger than the second harmonic. In contrast, on the rear half of the vane pressure side, the magnitude of the second harmonic is larger than the magnitude of the first harmonic. The phase angle of the blade passage harmonics is shown in

figure 6.15. The reference configuration, i.e., the geometric configuration at which the data taking process was started, is shown in figure 6.13 (Impeller R is shown in figure 6.13, but the reference configuration, i.e., the line-up of the diffuser vane leading edge and the center of the impeller blade trailing edge was the same for both impellers). It can be seen that there is a significant difference in phase, of  $\approx$  60 degrees, between the first impeller blade passage harmonic on the front half of the vane suction side and the front half of the vane pressure side.

### 6.3.5. Ensemble Averaged Lift Computations

From the vane pressure measurements described earlier, the force on the vane at mid vane height and the moment about the vane leading edge were computed. Since those measurements were obtained on different vanes, they had to be phase shifted to one reference vane for the force computations. The steady force was computed from the steady pressure distribution around the vane. Superimposing the steady and ensemble averaged unsteady pressure measurements, the ensemble averaged vane pressure distribution was obtained (it was assumed that the steady pressure value obtained by the mercury manometer measurements was identical to the time mean value about which the piezoelectric transducer measured the unsteady pressure). From the ensemble averaged pressure distribution, the ensemble averaged force and the ensemble averaged moment were computed. The steady and the ensemble averaged pressure distribution on the vane was obtained by fitting a third order periodic spline through the measured pressure values. A periodic spline fit was chosen to get continuity for the pressure and the first two pressure derivatives at the leading and trailing edge. The ensemble averaged force was computed from

$$\mathbf{F}_{av} = - \oint (\bar{p}_v + \tilde{p}_{v,av} - \bar{p}_{up})(\xi) \mathbf{n} d\xi. \quad (6.7)$$

The lift on the vane was defined as the component of the force on the vane normal to the chord joining the vane leading and trailing edge. The lift on the vane was defined as positive if the force component normal to the vane chord was in positive y direction (figure 6.5). For the two-dimensional impeller, only unsteady lift compu-

tations will be presented, since the unsteady moment about the vane leading edge, as already shown for Impeller R in Chapter 5, is with the exception of a scaling factor, nearly identical to the unsteady lift. The ensemble averaged lift is presented as an ensemble averaged lift coefficient, normalized by the dynamic pressure based on impeller tip speed,  $(1/2)\rho u_2^2$ , and the vane chord,  $c$ ,

$$\bar{c}_{L,av} = \frac{L_{av}}{(1/2)\rho u_2^2 c}. \quad (6.8)$$

In figures 6.16–6.17 data on the ensemble averaged lift and on the ratio of ensemble averaged to steady lift are presented. The position of the impeller blade is referenced to the diffuser vane leading edge. The averaging period for ensemble averaging was one shaft revolution, corresponding to five impeller blade passages; the data for the first half of shaft revolution are presented. The ensemble averaged lift for the first half of the averaging period is presented in the following figures. In figure 6.16, the ensemble averaged lift for the medium flow coefficient,  $\phi = 0.10$ , is shown for the two radial gaps of 5% and 8%. It can be seen that the differences in the lift curves from one blade passage to the next were small. Recalling that impeller blade passage and its higher harmonics were dominant in the spectra of the unsteady data, this is not surprising. Furthermore, the lift fluctuations decrease only slightly with increasing radial gap. As for Impeller R, the largest lift is attained after the suction side of the impeller blade trailing edge has passed the diffuser vane leading edge, whereas the smallest lift is attained right before the impeller blade pressure side reaches the diffuser vane leading edge. The ratio of the ensemble averaged lift to the steady lift for the medium flow coefficient,  $\phi = 0.10$ , and radial gaps of 5% and 8% is shown in figure 6.17. For both radial gaps, the ratio is about 2, decreasing only slightly with increasing radial gap.

### 6.3.6. Comparing the Vane Pressure Measurements for Impeller R and Impeller Z1

The magnitude of the ensemble averaged vane pressure fluctuations for Impeller R and for Impeller Z1 are presented in figure 6.18. The measurements were

made for comparable flow coefficients,  $\phi = 0.12$  for Impeller R and  $\phi = 0.10$  for Impeller Z1, and for comparable radial gaps between the respective impeller blade trailing edges and the instrumented diffuser vanes, 4.5% of the impeller discharge radius for Impeller R and 5.0% of the impeller discharge radius for Impeller Z1. The measurements were made at different shaft speeds, 3000 rpm for Impeller Z1 and 1800 rpm for Impeller R. This, however, should have no influence on comparing the sets of data; it has been shown that for both impellers the vane pressure fluctuations, if normalized by the dynamic pressure based on the impeller tip speed,  $(1/2)\rho u_2^2$ , are nearly independent of shaft speed. It can be seen that, with one exception of one pressure tap, the pressure fluctuations on the front half of the diffuser vane, pressure taps S0C-S4C and P1C-P4C, are of nearly identical magnitude. At pressure tap S1C, the pressure tap on the suction side closest to the vane leading edge, the fluctuations for Impeller R are about twice as large than those for Impeller Z1. On the rear half of the diffuser vane, the fluctuations are also larger for Impeller R. The magnitude of the normalized lift fluctuations resulting from the unsteady pressure distribution on the diffuser vane is  $\approx 0.2$  for both Impeller Z1 and Impeller R.

#### 6.4. Unsteady Impeller Blade Pressure Measurements Using Diffuser S

Unsteady impeller blade pressure measurements were made at three pressure taps on the impeller blades, one on the pressure side ( $R/R_2 = 0.987$ ), one on the suction side ( $R/R_2 = 0.937$ ), and one on the trailing edge ( $R/R_2 = 1.00$ ). Herein, the measurements made for Diffuser S and the two-dimensional impeller are presented. Data were taken for eight flow coefficients, ranging from  $\phi = 0.135$  to  $\phi = 0.06$  at 1500 rpm. For the pressure tap on the impeller blade pressure side, data were also taken at 2100 rpm for the same set of flow coefficients. Since the impeller was positioned eccentrically to the diffuser center, the radial gap between impeller blade trailing edge and diffuser vane leading edge varied during one impeller revolution from 5% to 8%, based on the impeller discharge radius.

#### 6.4.1. Ensemble Averaged Unsteady Blade Pressure Measurements and Spectra of Unsteady Blade Pressure Measurements

The unsteady blade pressure measurements were ensemble averaged, and will be presented as an ensemble averaged blade pressure coefficient, normalized by the dynamic pressure based on impeller tip speed,  $(1/2)\rho u_2^2$ ,

$$\tilde{c}_{b,av}(i) = \frac{1}{N} \sum_{j=1}^N \frac{\tilde{p}_b(i,j)}{(1/2)\rho u_2^2}, \quad (6.9)$$

where  $N$  is the number of averaging periods,  $i$  the  $i$ th data point taken in any of the  $N$  averaging periods, and  $j$  the  $j$ th of the  $N$  averaging periods. During one averaging period, corresponding to one main shaft revolution, 1024 data points were taken. A total of 64 averaging periods were used for the ensemble averages. Furthermore, spectra of the unsteady measurements were obtained.

In figures 6.19–6.23, ensemble averaged unsteady blade pressure measurements and the corresponding spectra of the unsteady blade pressure measurements at the three blade pressure taps are presented. In the upper part of each figure, the ensemble averaged blade pressure fluctuations are shown. The pairs of broken lines indicate the passage of the pressure side and the suction side of the impeller blade trailing edge past the diffuser vane leading edge. The one pair of solid lines indicates the passage of the pressure side and the suction side of the impeller blade trailing edge past the diffuser vane at the smallest radial distance between the instrumented impeller blade and the diffuser vanes. That smallest radial gap between the impeller blade trailing edge and the diffuser vane leading edge is 5% of the impeller blade trailing edge radius. In the lower part of each figure, the magnitude of the Fourier coefficients relative to the largest Fourier coefficient ( $c_i/c_{i,max}$ ) for a particular test is shown versus frequency (upper horizontal scale) and frequency normalized by impeller vane passage frequency ( $f/f_v$ ) (lower horizontal scale).

In figure 6.19, the measurements made at the impeller blade trailing edge are shown for a medium flow coefficient,  $\phi = 0.10$ . It can be seen that the magnitude of the fluctuations varies significantly during one impeller revolution. This is due to

the varying distance between the impeller blade trailing edge and the diffuser vanes as the impeller completes one revolution. The trailing edge pressure fluctuations are largest during the vane passage following the smallest gap between the specific instrumented impeller blade and diffuser vanes. The minimum pressure is attained after the blade trailing edge has passed the diffuser vane leading edge. The trailing edge pressure then rises sharply to its maximum value which is attained before the impeller blade trailing edge reaches the next vane leading edge. As the next vane leading edge is reached the pressure has already dropped by about half the difference between minimum and maximum pressure. For the diffuser vanes that come closest to the impeller during the impeller revolution, a small relative minimum and a small relative maximum occur just before and after the center of the impeller blade trailing edge reaches the diffuser vane leading edge. In the corresponding spectrum of the unsteady blade pressure measurements, four different discrete frequency components can be found. First, vane passage frequency and its higher harmonics,  $(f/f_v) = 1, 2, \dots$ , are the dominant frequencies. This is similar to the diffuser vane pressure measurements presented previously. Secondly, a component at shaft frequency,  $f_s = (1/z_b)f_v$ , can be seen. This component result from the varying radial gap between the impeller blades and the diffuser vanes as the impeller completes one revolution. For this particular run, the frequency component at  $f_s$  is rather small, but for other runs it was found to have a magnitude similar to the frequency component at  $f_v$ . Thirdly, frequencies at  $mf_v \pm nf_s$  ( $m, n = 1, 2$ ) can have significant magnitude. For this run, this is especially true for  $2f_v - f_s$ . These frequencies are very likely the result of frequency modulation between the vane passage frequency,  $f_v$ , and the shaft frequency,  $f_s$ ,

$$\sin(2\pi f_v t) \sin(2\pi f_s t) = 0.5(\cos((f_v - f_s)2\pi t) - \cos((f_v + f_s)2\pi t)) \quad (6.10)$$

and hence also results from the uneven radial gap between impeller blades and diffuser vanes. Frequencies at  $mf_b \pm nf_s$  ( $m, n = 1, 2$ ) with significant magnitude were not observed in the diffuser vane pressure measurements. Fourthly, a strong 60 Hz signal and some small higher harmonics can be seen. The 60 Hz is significantly

larger than for the diffuser vane pressure measurements. This may be the result of stronger pickup from the main motor, since the cables from the transducer through the slip rings came significantly closer to the motor than the cables from the transducer installed in the diffuser for the diffuser vane pressure measurements. The larger 60 Hz signal may also be due to the motor speed control, which is controlled at 60 Hz. Hence, the shaft may induce both flow oscillations around the impeller blades and impeller vibrations at 60 Hz, which may be picked up by the transducer. Since the 60 Hz signal was very sharp and sufficiently far removed from the shaft frequency and vane passage frequency, it was not expected to influence the measurements. During the ensemble averaging process, the 60 Hz signal was averaged out.

Increasing the flow coefficient from  $\phi = 0.10$  to the maximum flow coefficient,  $\phi = 0.135$ , resulted in a significant decrease of the magnitude of the pressure fluctuations at the blade trailing edge pressure tap (figure 6.20). Furthermore, the size of the second vane passage harmonic relative to the vane passage harmonic decreased strongly. In the ensemble averaged data, this is reflected by a strongly monotonic increase of the pressure from its minimum to its maximum value, and a strongly monotonic decrease from its maximum to its minimum value. No relative minima and maxima occurred.

Lowering the flow coefficient from  $\phi = 0.10$  to  $\phi = 0.06$ , in contrast, resulted in a strong increase in the second vane passage harmonic (figure 6.21). The relative minima and maxima that had already appeared for  $\phi = 0.10$  did grow in magnitude. Especially for the closest radial gap between the instrumented impeller blade and the diffuser vanes, the relative maximum attained when the center of the impeller blade trailing edge passes the diffuser vane leading edge is nearly as large as the absolute pressure maximum. Furthermore, in the spectrum of the unsteady measurements for this low flow coefficient, the magnitude of the Fourier coefficients at shaft frequency is very small; however, a distinct low frequency peak at about 34 Hz can be seen.

Figure 6.22 shows the ensemble averaged blade pressure fluctuations and the corresponding spectrum at the blade pressure side pressure tap, for the “medium”

flow coefficient,  $\phi = 0.10$ . As for the trailing edge pressure tap, it can be seen that the magnitude of the pressure fluctuation varies because of the changing radial gap between impeller blades and diffuser vanes during one impeller revolution. The maximum pressure is attained before the impeller blade reaches a diffuser vane. The pressure drops sharply from its maximum value to its minimum value, which is attained when the center of the trailing edge reaches the diffuser vane leading edge. It then increases gradually to its maximum value. In the spectrum, the same frequency components as in the spectrum for the trailing edge can be seen. The relative magnitude at  $f_s$  is larger than at the trailing edge, and the relative magnitudes at  $mf_v - nf_s$  ( $m, n = 1, 2$ ) are smaller. Since the frequency resolution for this spectrum was larger (7.5 Hz compared to 1.75 Hz for the trailing edge), the signal at 60 Hz appears broader. For the blade pressure side pressure tap, no significant variation in the relative size of the magnitudes of the vane passage harmonics occurred for the higher or the lower flow coefficients, and, similarly, no relative blade pressure minima and maxima appeared. Hence, no data for other flow coefficients are presented here.

Finally, in figure 6.23 the ensemble averaged blade pressure fluctuations and the corresponding spectrum at the blade suction side pressure tap (for the same flow coefficients as for the blade pressure side pressure tap,  $\phi = 0.10$ ) are presented. The pressure fluctuations are smaller than those at the trailing edge and at the pressure side pressure taps. In the spectra, the 60 Hz harmonics is dominant and higher harmonics can also seen. In addition to  $f_s, f_v, mf_v \pm nf_s$ , a  $3f_s$  (or  $(1/3)f_v$ ) component is found in the spectra. However, there is no significant  $2f_s$  component. For that component,  $3f_s$ , I do not have an explanation as yet. Again, no higher or lower flow coefficients are presented, for as for the pressure side pressure tap, no significant variation in the relative magnitude of the vane passage harmonics occurred.

#### 6.4.2. Magnitude of Ensemble Averaged Blade Pressure Fluctuations.

Because of the eccentric position of the impeller with respect to the diffuser center, the magnitude of the impeller blade pressure fluctuations varied with the radial distance between the particular instrumented impeller blade and the diffuser vanes, as shown in figures 6.19–6.23. In figure 6.24, the magnitude of the ensemble averaged impeller blade pressure fluctuations occurring during the passage of the nine diffuser vanes within one shaft revolution are presented. The blade pressure fluctuation for the passage of one diffuser vane is defined as the peak to peak pressure fluctuation during that passage. In figure 6.25, the magnitude of the blade pressure fluctuations (at all three impeller blade pressure taps) are presented versus “vane number,” where the vane numbered “1” is the vane to which the impeller blade attains the closest distance during one shaft revolution. Diffuser S has nine vanes, hence the vane numbers from one to nine. The shaft revolution is entirely completed if vane “1” is reached again. It can be seen that the fluctuations are decreasing significantly with increasing gap between the impeller blade and the diffuser vanes. The relative decrease is strongest at the suction side pressure tap, and smallest at the pressure side pressure tap.

For the smallest radial gap,  $R_3/R_2 = 1.05$ , that is the closest position between the impeller blade and a diffuser vane as the impeller completes one revolution, the magnitudes of the ensemble averaged blade pressure fluctuations are presented in figure 6.25. The measurements were made for a total of eight flow coefficients, ranging from maximum flow,  $\phi = 0.135$ , to  $\phi = 0.06$ .

It can be seen that the magnitudes of the pressure fluctuations range from the same order of magnitude as the total pressure rise across the pump at the trailing edge tap, to an order of magnitude smaller than the total pressure rise across the pump at the suction side pressure tap.

The largest fluctuations occur at the trailing edge. They increase significantly with flow coefficient, from  $|\tilde{c}_{b,av}| = 0.170$  for  $\phi = 0.135$  (maximum flow) to  $|\tilde{c}_{b,av}| = 0.46$  for  $\phi = 0.07$ . Comparing the normalized total pressure rise across the pump as

a function of flow coefficient (figure 6.1) to the normalized impeller blade pressure fluctuations as a function of flow coefficient, it can be observed that the magnitude of the pressure fluctuations can be as large as about 60% of the total pressure rise across the pump.

In contrast to the trailing edge pressure fluctuations, the pressure fluctuations at the pressure and suction side taps are not significantly dependent upon flow coefficient. Maxima are attained for  $\phi = 0.11$  at the pressure side tap, for  $\phi = 0.10$  at the suction side tap, and for  $\phi = 0.06$  at suction and pressure side tap. Minima are attained for maximum flow,  $\phi = 0.135$ , for both the pressure and suction side tap, and for  $\phi = 0.09$  for the pressure side tap, and for  $\phi = 0.08$  for the suction side tap. The magnitude of the fluctuations at the pressure and suction side tap, however, was found to be quite different. At the pressure side, the fluctuations were about two to three times larger than at the suction side tap. For maximum flow, the pressure side tap fluctuations were even slightly larger than those at the trailing edge. Not increasing significantly with decreasing flow coefficient, however, the fluctuations at the pressure side tap for low flow coefficients were only about half as large as those at the trailing edge.

For the impeller blade pressure side pressure tap, measurements were also made for a rotational speed of 2100 rpm, for the same set of flow coefficients as for 1500 rpm. Normalized by the dynamic pressure based on impeller tip speed,  $(1/2)\rho u_2^2$ , the blade pressure fluctuations at the pressure side pressure tap were found to be nearly independent of shaft speed (in figure 6.26, the magnitudes of the ensemble averaged fluctuations for the smallest radial gap are presented).

## 6.5. Unsteady Impeller Blade Pressure Measurements Using Different Diffusers

Unsteady impeller blade pressure measurements were also made for a second diffuser, of identical sidewall geometry as Diffuser S, but permitting variable diffuser vane configurations to investigate the effects of the number of diffuser vanes and the

diffuser vane angle on the impeller blade pressure fluctuations. Three different vane configurations employing circular arc vanes were tested. Diffuser F employed twelve vanes with a vane angle,  $\beta^*$ , of twenty degrees, Diffuser G six vanes with vane angle of 20 degrees, and Diffuser H six vanes with a vane angle of 10 degrees. Hence, the influence of the vane number on the blade pressure fluctuations was investigated by comparing the measurements for Diffuser F and Diffuser G, whereas the influence of the vane angle was investigated by comparing the measurements for Diffuser G and Diffuser H. From the performance curve presented in figure 6.1, it can be seen that Diffuser H had a rather poor head rise for all flow coefficients investigated, whereas Diffuser F had a poor head rise at large flow coefficients ( $\phi \geq 0.10$ ), but the largest head rise for low flow coefficients,  $\phi \leq 0.07$ . Diffuser G had the largest head rise for large flow coefficients, and was surpassed by Diffuser F only for lower flow coefficients. Hence Diffuser G is considered the “reference” diffuser, and the unsteady blade pressure measurements for both Diffuser F and Diffuser H will be compared to those made using Diffuser G.

Unsteady impeller blade pressure measurements were also made by Iino and Kasai (1985), who investigated impeller blade pressure fluctuations, varying both the blade and the vane angle, but kept the blade and vane number constant.

### 6.5.1. Ensemble Averaged Unsteady Blade Pressure Measurements and Spectra of Unsteady Blade Pressure Measurements

The unsteady blade pressure measurements were ensemble averaged, and will be presented as an ensemble averaged blade pressure coefficient, normalized by the dynamic pressure based on impeller tip speed,  $(1/2)\rho u_2^2$ ,

$$\tilde{c}_{b,av}(i) = \frac{1}{N} \sum_{j=1}^N \frac{\tilde{p}_b(i,j)}{(1/2)\rho u_2^2}, \quad (6.11)$$

where  $N$  is the number of averaging periods,  $i$  the  $i$ th data point taken in any of the  $N$  averaging periods, and  $j$  the  $j$ th of the  $N$  averaging periods. During one averaging period, corresponding to one main shaft revolution, 1024 data points

were taken. A total of 64 averaging periods were used for the ensemble averages. Furthermore, spectra of the unsteady measurements were obtained. In the upper half of each figure, the ensemble averaged blade pressure fluctuations are shown. The broken lines indicate the passage of the center of the impeller blade trailing edge past the diffuser vane leading edge. The one solid line indicates the passage of the diffuser vane leading edge past the center of the impeller blade trailing edge at the smallest radial distance between the instrumented impeller blade and the diffuser vanes ( $R_3/R_2 = 1.05$ ). In the lower part of each figure, the magnitude of the Fourier coefficients relative to the largest Fourier coefficient ( $c_i/c_{i,max}$ ) for a particular test is shown versus frequency (upper horizontal scale) and frequency normalized by the diffuser vane passage frequency ( $f/f_v$ ) (lower horizontal scale).

From the many data that were obtained during the testing of the three diffusers, only a few can be shown here as ensemble averaged measurements. Those were selected to point out particular differences in the pressure fluctuations using the different diffusers.

First, it has to be mentioned that, through the somewhat unfortunate choice of the shaft speed, 1500 rpm nominal (which means that runs were done in the range between 1480–1520 ranging from 1480 rpm to 1520 rpm during the set of measurements, with the shaft speed fluctuating by about  $\pm 1$  rpm during a particular measurement), the fifth harmonic of the 60 Hz signal, i.e., the 300 Hz harmonic, was “close” to the second vane passage harmonic for Diffuser G and Diffuser H at 300 Hz nominal, and to the first vane passage harmonic for Diffuser F at 300 Hz nominal. The higher harmonics of the 60 Hz signal were, however, small, so that their influence on the measurements was negligible.

The trailing edge pressure measurements using Diffuser S showed that for low flow coefficients the second vane passage harmonic was larger in magnitude than the first. A similar observation was also made for the trailing edge measurements for Diffuser G. In figure 6.27, the ensemble averaged blade pressure measurements at the trailing edge pressure tap and the spectrum of the corresponding unsteady data are presented for  $\phi = 0.06$ , using Diffuser G. As for the measurements made for

Diffuser S, peaks occur at shaft frequency,  $f_s$ , vane passage frequency and its higher harmonics,  $nf_v$ ,  $n = 1 - 5$ , the modulated frequencies,  $nf_v \pm mf_s$ ,  $n, m = 1, 2$ , and 60 Hz. The largest peak in the spectrum is at three times the vane passage frequency,  $3f_v$ . So, similar to the observations for Diffuser S, the largest peak in the spectrum does not occur at the vane passage frequency, but at one of its multiples, in this case the third. Turning now to the ensemble averaged measurements, it can be seen that the magnitude of the pressure fluctuations varies significantly during one impeller revolution. This is due to the varying distance between the impeller blade trailing edge and the diffuser vanes as the impeller completes one revolution. The trailing edge pressure fluctuations are largest during the vane passage following the smallest gap between the instrumented impeller blade and the diffuser vanes. The minimum pressure is attained right after the impeller blade trailing edge has passed the diffuser vane leading edge. As the impeller blade moves on, the pressure at the trailing edge first rises sharply to its maximum value and thereafter “oscillates” to attain two relative minima and maxima before the next vane is reached. The amplitudes between the extrema decrease until the next vane is reached and the cycle is repeated. Hence, looking at the pressure fluctuations during the passage from one vane to the next, the trailing edge pressure curve resembles a damped oscillation. The ensemble averaged pressure measurements at the blade trailing edge for Diffuser H looked similar; in the corresponding spectrum, the vane passage harmonic and the third vane passage harmonic were about equally large. For both diffusers (Diffusers G and H), the relative minima and maxima vanished gradually with increasing flow coefficient. This was found to be similar to the observations made for Diffuser S.

The diffuser employing twelve vanes showed different results for the low flow coefficients. Presented are trailing edge pressure measurements for  $\phi = 0.08$  (figure 6.28) and 0.06 (figure 6.29). The vane passage harmonic is larger than the second harmonic for both flow coefficients. Only for the lower flow coefficient,  $\phi = 0.06$ , can a (very small) relative minimum and maximum be observed during the passage of the impeller blade from one vane to the next. Furthermore, the magnitude of

the fluctuations is smaller for the diffuser employing twelve vanes (Diffuser F) than those for the one employing six vanes (Diffuser G). For the slightly larger flow coefficient,  $\phi = 0.08$ , the relative extrema vanish, and pressure increase and decrease are strongly monotonic. Hence, the vane number has obviously a significant influence not only on the magnitude of the trailing edge pressure fluctuations but also on the "shape" of the pressure fluctuations during one vane passage.

Finally, the pressure fluctuations at the pressure tap on the blade pressure side for  $\phi = 0.10$  are presented in figure 6.30 for Diffuser G and in figure 6.31 for Diffuser H. For Diffuser G the pressure fluctuations resemble a saw tooth curve with a strong decrease from the maximum pressure value which is attained just before the impeller blade reaches the diffuser vane, and a more gradual increase from the minimum value attain when or right after the impeller blade trailing edge has passed the diffuser vane. For Diffuser H, however, the minima are very wide, up to about half a vane passage. The pressure maxima are rather distinct peaks and are attained approximately at about the same time as the maxima for Diffuser G. So, it can be seen that not only the vane number, as shown in the previous set of figures for the blade trailing edge pressure fluctuations, but also the vane angle has a significant influence on the "shape" of the pressure fluctuations during one vane passage.

#### 6.5.2. Magnitude of Ensemble Averaged Blade Pressure Fluctuations

The measurements will be presented in two ways. First, the influence of the different diffusers on the pressure measurements at any of the three pressure taps is shown (in figure 6.32 for the trailing edge pressure tap, in figure 6.33 for the pressure side pressure tap, and in figure 6.34 for the suction side pressure side tap). Then, the magnitude of the pressure fluctuations at all three pressure taps for any of the three diffusers is shown to investigate how the relative magnitude of the fluctuations, i.e., the magnitude of the pressure fluctuations at the different pressure taps relative to each other, depends upon the diffuser vane configuration

(in figure 6.35 for Diffuser F, in figure 6.36 for Diffuser G, and in figure 6.37 for Diffuser H). In each figure, the magnitude of the pressure fluctuations is presented versus flow coefficient.

The largest fluctuations for all three diffusers occurred at the pressure tap at the impeller blade trailing edge, figure 6.32. As for Diffuser S, the trailing edge pressure fluctuations were of the same order of magnitude as the total pressure rise across the pump. Turning first to the influence of the number of diffuser vanes on the trailing edge pressure fluctuations, it can be seen that the pressure fluctuations increase strongly for both diffusers with decreasing flow coefficient, and that they are smaller for Diffuser F (twelve vanes) than for Diffuser G (six vanes). The pressure fluctuations are reduced between 15% for  $\phi = 0.12$  and more than 40% for  $\phi = 0.08$ . Decreasing the vane angle from 20 degrees to 10 degrees results in a significant reduction of the fluctuations of the trailing edge fluctuations for flow coefficients  $\phi \leq 0.09$ , whereas for flow coefficients  $\phi \geq 0.10$  the magnitude of the fluctuations is nearly the same for Diffuser G ( $\beta^* = 20^\circ$ ) and Diffuser H ( $\beta^* = 10^\circ$ ). It is furthermore interesting to notice that whereas for Diffuser G the trailing edge fluctuations increase strongly monotonically with decreasing flow coefficient, they stay about constant for Diffuser H in a range of "medium" flow coefficients,  $\phi = 0.10 - 0.07$ .

The pressure fluctuations at the pressure side pressure tap are presented in figure 6.33. Like the trailing edge, the fluctuations are reduced for the entire range of flow coefficients, if the diffuser vane number is increased from six (Diffuser G) to twelve (Diffuser F). The reductions are larger for the low flow coefficients ( $\approx 40\%$  for  $\phi = 0.06$ ) than for the high flow coefficients ( $\approx 20\%$  for  $\phi = 0.12$ ). Decreasing the vane angle from 20 degrees (Diffuser G) to 10 degrees (Diffuser H) resulted in larger pressure fluctuations for large flow coefficients, and smaller fluctuations for small flow coefficients. Also, the dependence of the pressure fluctuations on flow coefficient is reversed. For both diffusers with a vane angle of 20 degrees (Diffuser F and Diffuser G), the fluctuations increased with decreasing flow coefficient, whereas for the diffuser with a vane angle of 10 degrees (Diffuser H), they decreased with

the flow coefficient decreasing from  $\phi_{max} = 0.125$  to  $\phi = 0.07$ .

In figure 6.34, the pressure fluctuations at the pressure tap on the suction side are presented. Increasing the number of diffuser vanes resulted as already observed at the trailing edge tap and at the pressure side tap in a reduction of the pressure fluctuations. In contrast to the pressure side, the reduction is largest for the large flow coefficients ( $\approx 70\%$  for  $\phi = 0.12$ ), and decreases for the smaller flow coefficients ( $\approx 45\%$  for  $\phi = 0.06$ ). Decreasing the vane angle increased the pressure fluctuations for the entire range of flow coefficients with the exception of  $\phi = 0.07$  and 0.08. Again, the dependence of the pressure fluctuations on flow coefficient was qualitatively the same for Diffuser F and Diffuser G, showing increasing fluctuations with decreasing flow coefficient. For Diffuser H, however, the fluctuations attained a relative maximum for  $\phi = 0.11$ , then decreased with decreasing flow coefficient, from  $\phi = 0.11$  to  $\phi = 0.07$ , and finally increased again when the flow coefficient was lowered to  $\phi = 0.06$ .

From the last three figures, it could be seen that vane number and vane angle do have a most significant influence on the impeller blade pressure fluctuations. The increase in vane number from six to twelve at a fixed vane angle of 20 degrees resulted in a decrease of the blade pressure fluctuations at all blade pressure taps and for all flow coefficients. The reduction varied, depending upon flow coefficient and pressure tap, between 15% and 70%. Decreasing the vane angle from 20 degrees to 10 degrees for a constant number of diffuser vanes ( $z_v = 6$ ) resulted for the pressure taps on the blade pressure and on the blade suction side in an increase of the pressure fluctuations for the large flow coefficients of up to 75%, whereas for low flow coefficients the fluctuations decreased by up to 30%. For the trailing edge tap, the magnitude of the pressure fluctuations remain unchanged for large flow coefficients and decreased for low flow coefficients.

Next the magnitude of the ensemble averaged blade pressure measurements made at the three impeller blade pressure taps will be presented, in figure 6.35 for Diffuser F, in figure 6.36 for Diffuser G and in figure 6.37 for Diffuser H. As before, the magnitude of the pressure fluctuations is presented versus flow coefficient and

for the smallest radial gap between the particular instrumented impeller blade and a diffuser vane during an impeller revolution  $R_3/R_2 = 1.05$ . It can be seen that the plots for Diffuser F and Diffuser G (and also for Diffuser S (see figure 6.25)) look qualitatively similar. The pressure fluctuations are largest at the trailing edge pressure tap, with the exception of the maximum flow coefficient, for which they are slightly larger at the pressure side tap than at the trailing edge tap. The pressure fluctuations at the suction side pressure tap are significantly smaller than those at the other two pressure taps, especially for the small flow coefficients. For Diffuser H, however, the differences in the fluctuations at the three pressure taps are not as large as for the other diffusers. For maximum flow, the suction side pressure tap fluctuations are about as large as the trailing edge fluctuations, whereas for the lowest flow coefficient investigated,  $\phi = 0.06$ , the pressure fluctuations at the pressure and the suction side pressure taps are nearly equal.

So, again it can be seen that the increase in the vane number resulted in a reduction of the pressure fluctuations at all three pressure taps and for all flow coefficients. Decreasing the vane angle from 20 degrees to 10 degrees resulted in a decrease of the pressure fluctuations at the trailing edge, and at the pressure side pressure tap; however, the suction side pressure fluctuations increased and were found to be comparable to the pressure side pressure fluctuations over the whole range of flow coefficients tested.

As mentioned in the introduction, unsteady impeller blade pressure measurements in diffuser pumps were also made by Iino and Kasai (1985). The measurements were made for two two-dimensional impellers with six blades but different blade angles, 20 degrees and 30 degrees, and two radial with eleven vanes and vane angles of ten and fifteen degrees. The radial gap between impeller blades and diffuser vanes was 3% of the impeller discharge radius. The diffuser vane thickness was comparable to the diffuser vane thickness of the circular arc vanes, 0.196 inch to 0.165 inch. The impeller blade trailing edge, however, was significantly thinner,  $t_b^* = 0.046$  in comparison to  $t_b^* = 0.130$  for Impeller Z2. Of the many measurements

made by Iino and Kasai (1985), only the those closest to the impeller discharge will be mentioned here. Those were made at  $R/R_2=0.939$  on the pressure side and at  $R/R_2=0.917$  on the suction side. Therefore, only the magnitudes of the suction side pressure fluctuations are comparable to the measurements made for Impeller Z2. For four impeller/diffuser configurations tested, Iino and Kasai (1985) reported larger fluctuations on the blade pressure side than on the blade suction side. A minimum for both the pressure and suction side pressure fluctuations was observed for flow coefficients in the vicinity of the best efficiency flow coefficient. This minimum was not found, however, at the pressure tap on the blade pressure side at  $R/R_2=0.8$ . The fluctuations at the suction side pressure tap were reported to be largest for small flow coefficients,  $\phi=0.05-0.07$ , attaining (applying the normalization and definition for the magnitude of the unsteady pressure fluctuations used throughout this dissertation) a magnitude of  $\approx 0.05$  (this value can be given only approximately since Iino (1985) presents the amplitudes of the vane passage harmonics). The magnitude of the largest pressure fluctuations at the pressure tap on the blade pressure is  $\approx 0.2$ . The blade pressure fluctuations were found to be sensitive to the diffuser vane angle.

Because of the different blade and vane numbers of the impeller-diffuser configurations and the different blade and vane thicknesses employed in this investigation and in the one reported by Iino and Kasai (1985), only qualitative comparisons can be made. However, it can be seen that the unsteady pressure fluctuations, in both investigations, were of the same order of magnitude.

## 6.6. Summary

Unsteady impeller blade and diffuser vane pressure measurements have been presented. The diffuser vane pressure measurements were obtained for a nine-vaned diffuser and a five-bladed two-dimensional impeller. The magnitude of the largest vane pressure fluctuations occurring at the vane leading edge and on the front half of the vane suction side was found to be of the same order of magnitude as the

total pressure rise across the pump. The pressure fluctuations on the vane pressure side were significantly smaller than those on the vane suction side. Impeller blade pressure measurements were made at three impeller blade pressure taps located on the impeller suction and pressure side, and at the trailing edge, using four different diffusers. Independent of the specific diffuser, the largest fluctuations were found to occur at the impeller blade trailing edge. As the diffuser vane fluctuations, they were found to be of the same order of magnitude as the total pressure rise across the pump. In contrast to the pressure fluctuations on the front half of the diffuser vane which were found to decrease with decreasing flow coefficient, the impeller blade trailing edge pressure fluctuations were found to increase with decreasing flow coefficient. For most flow coefficients, the blade pressure fluctuations were found to be larger at the trailing edge tap than at the pressure side tap, and smallest at the suction side tap. Vane angle (i.e., the vane leading edge mean line angle) and vane number were found to have a significant influence on the impeller blade pressure fluctuations.

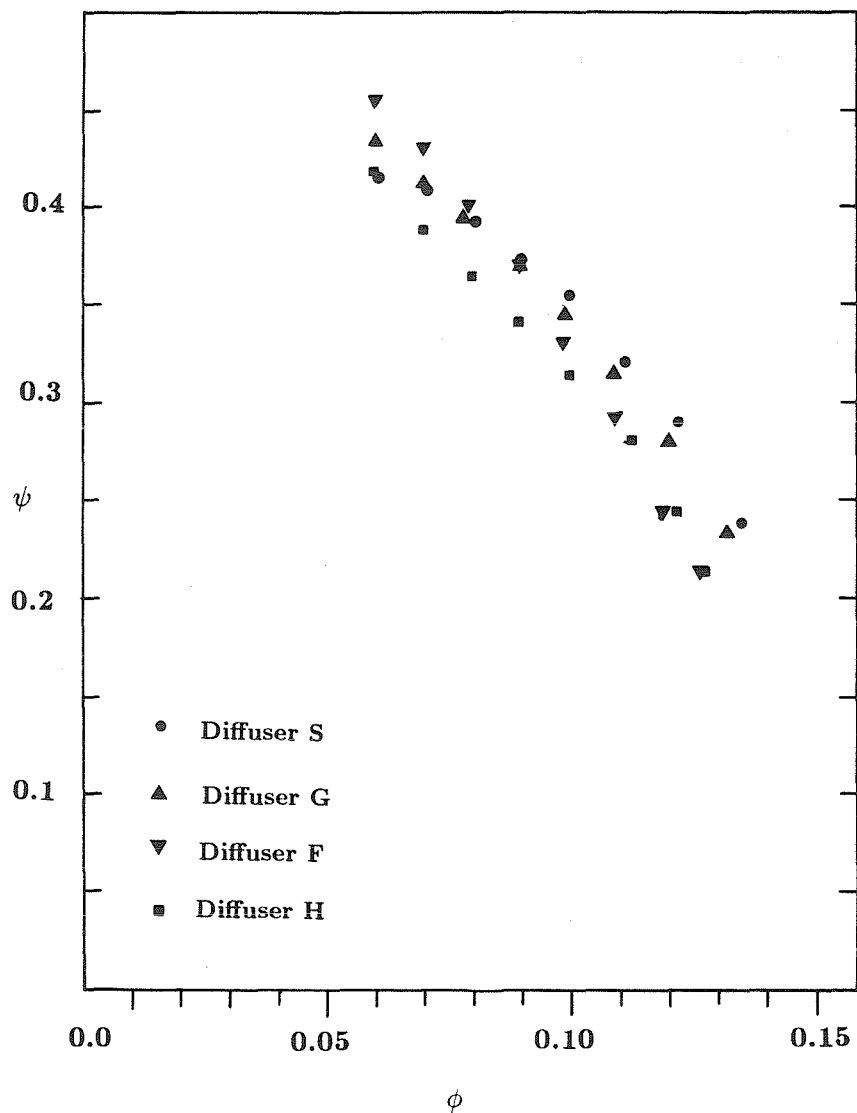


Fig. 6.1. Performance curves for Diffusers F,G,H and S.

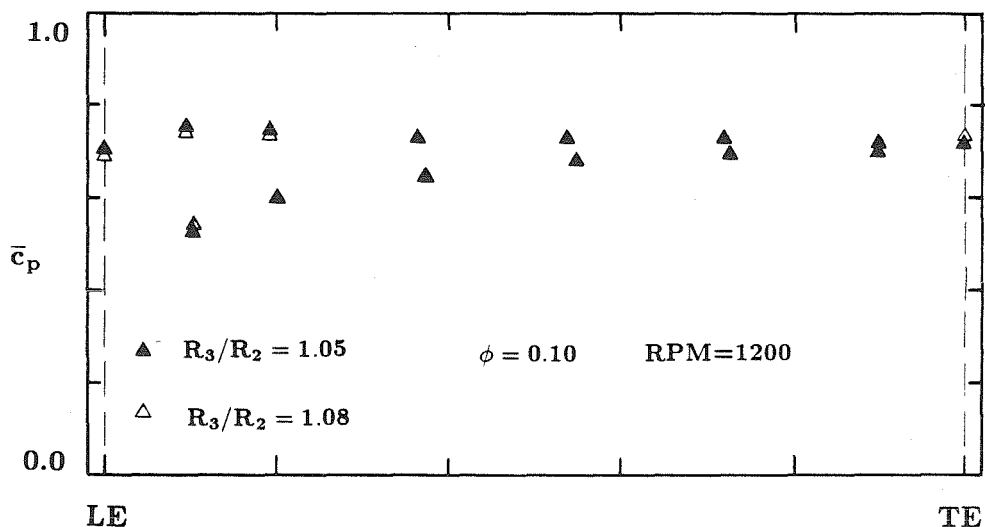


Fig. 6.2. Steady pressure measurements at mid vane height for Impeller Z1 and Diffuser S ( $\phi = 0.10$ ,  $R_3/R_2 = 1.05$  and  $1.08$ , rpm = 1200).

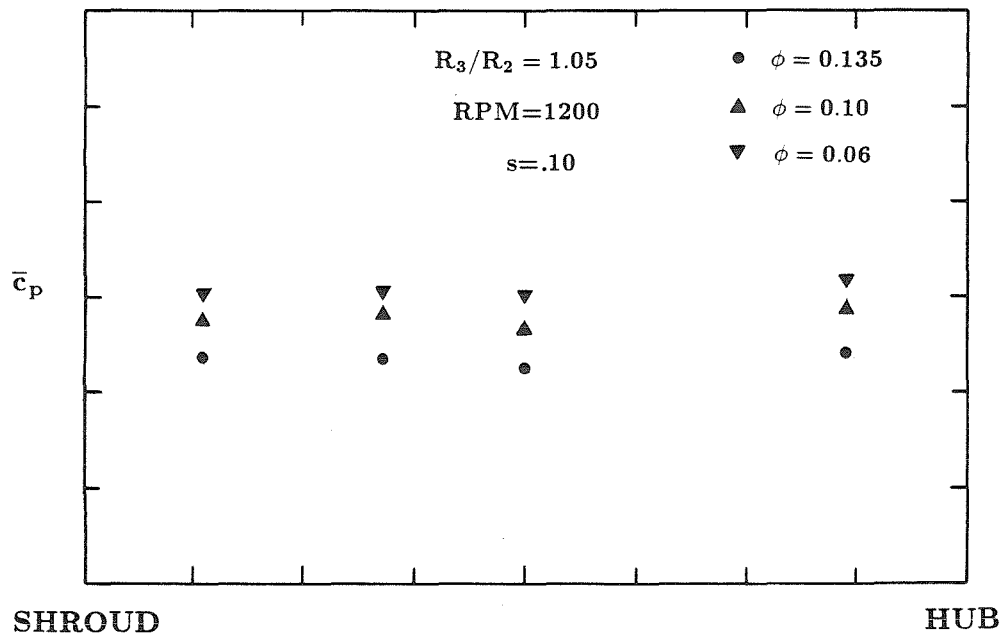


Fig. 6.3. Steady pressure measurements across the span of the vane for Impeller Z1 and Diffuser S ( $\phi = 0.10$  and  $0.135$ ,  $s = 0.10$ ,  $R_3/R_2 = 1.05$ , rpm = 1200).

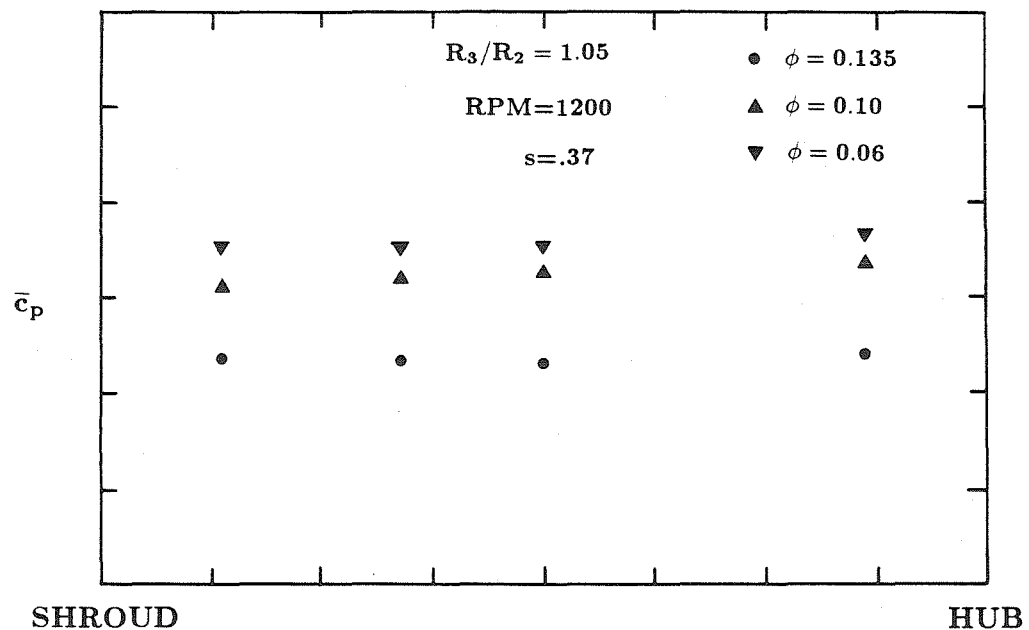


Fig. 6.4. Steady pressure measurements across the span of the vane for Impeller Z1 and Diffuser S ( $\phi = 0.10$  and  $0.135$ ,  $s = 0.37$ ,  $R_3/R_2 = 1.05$ , rpm = 1200).

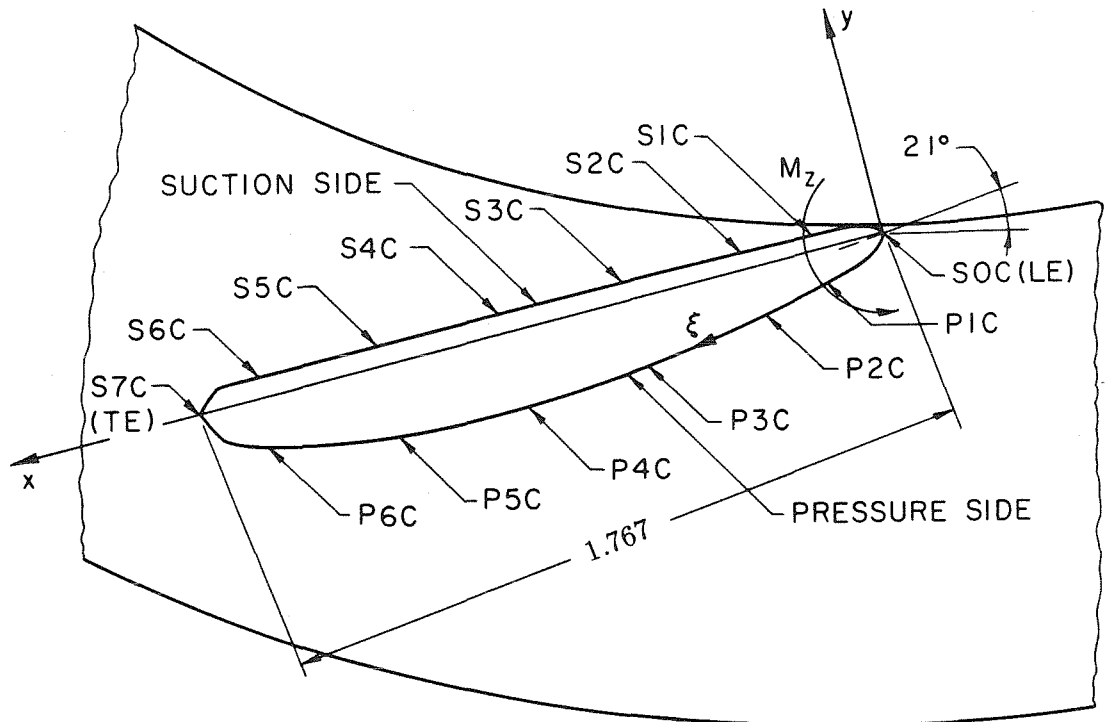


Fig. 6.5 Diffuser vane with pressure taps at mid vane height.

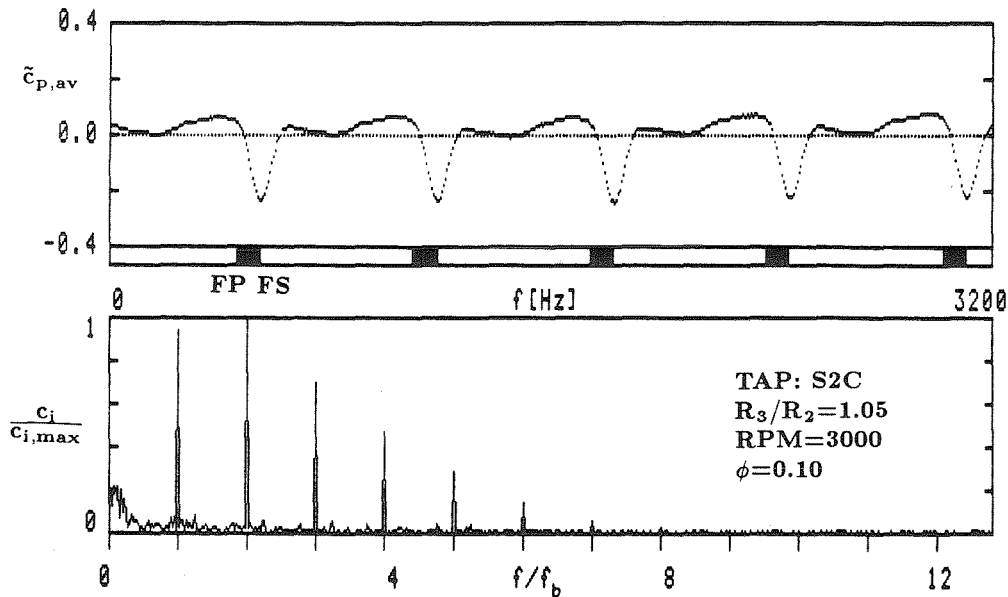


Fig. 6.6. Spectrum of unsteady vane pressure measurements and ensemble averaged unsteady vane pressure measurements at pressure tap S2C for Impeller Z1 and Diffuser S ( $\phi = 0.10$ ,  $R_3/R_2 = 1.05$ , rpm = 3000).

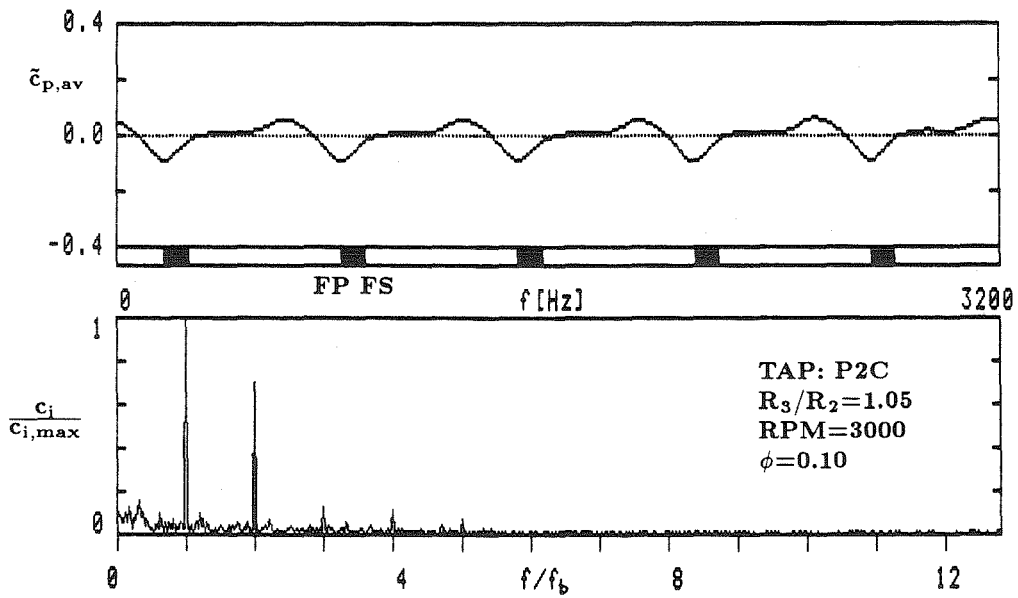


Fig. 6.7. Spectrum of unsteady vane pressure measurements and ensemble averaged unsteady vane pressure measurements at pressure tap P2C for Impeller Z1 and Diffuser S ( $\phi = 0.10$ ,  $R_3/R_2 = 1.05$ , rpm = 3000).

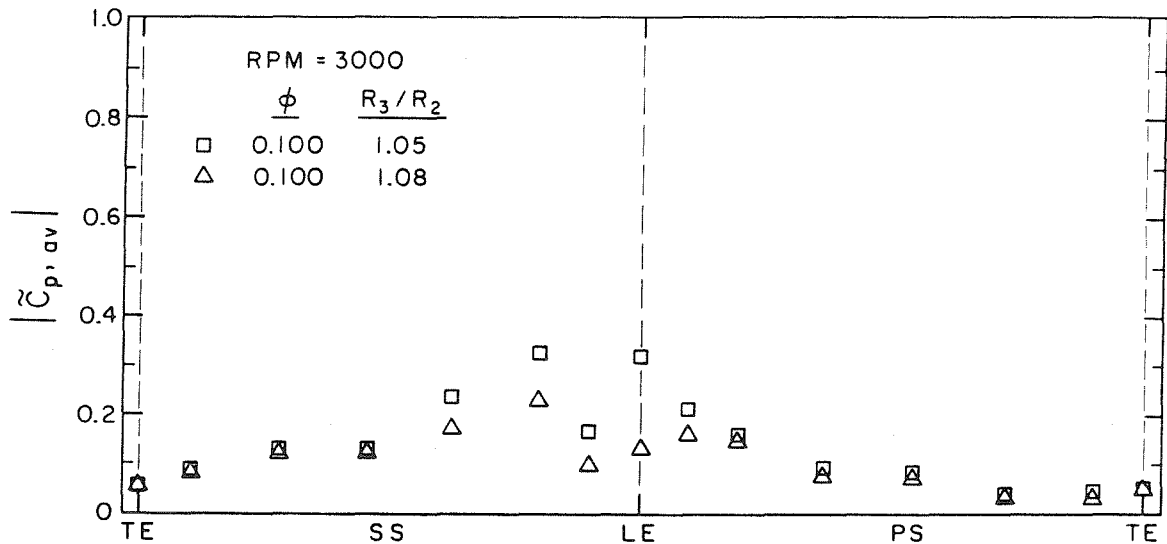


Fig. 6.8. Magnitude of ensemble averaged vane pressure fluctuations at mid vane height for Impeller Z1 and Diffuser S ( $\phi = 0.10, R_3/R_2 = 1.05$  and  $1.08$ , rpm = 3000).

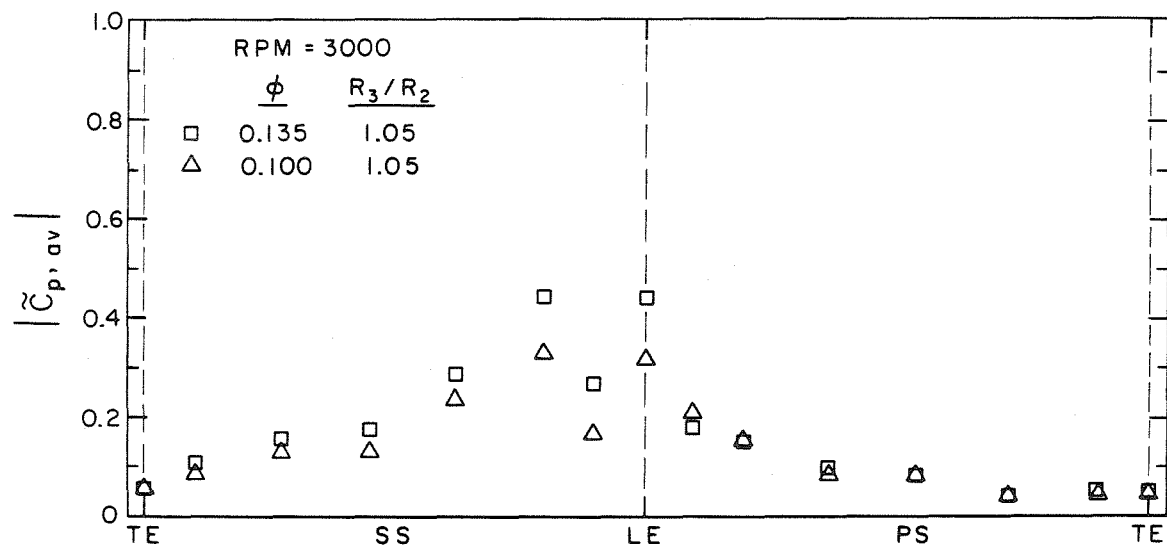


Fig. 6.9. Magnitude of ensemble averaged vane pressure fluctuations at mid vane height for Impeller Z1 and Diffuser S ( $\phi = 0.135$  and  $0.10, R_3/R_2 = 1.05$ , rpm = 3000).

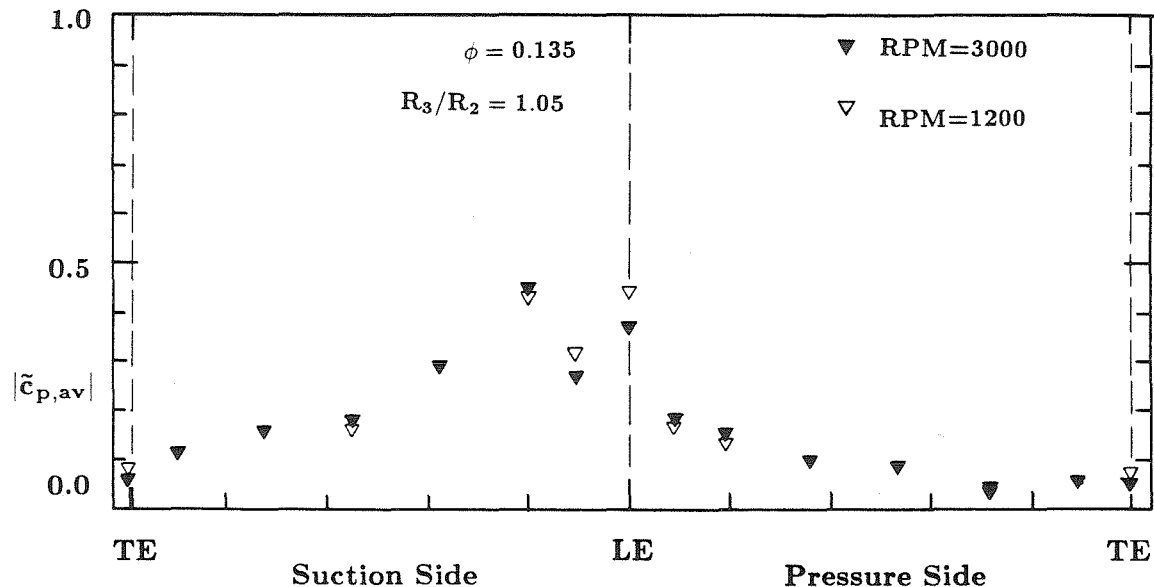


Fig. 6.10. Magnitude of ensemble averaged vane pressure fluctuations at mid vane height for Impeller Z1 and Diffuser S ( $\phi = 0.135$ ,  $R_3/R_2 = 1.05$ , rpm = 3000 and 1200).

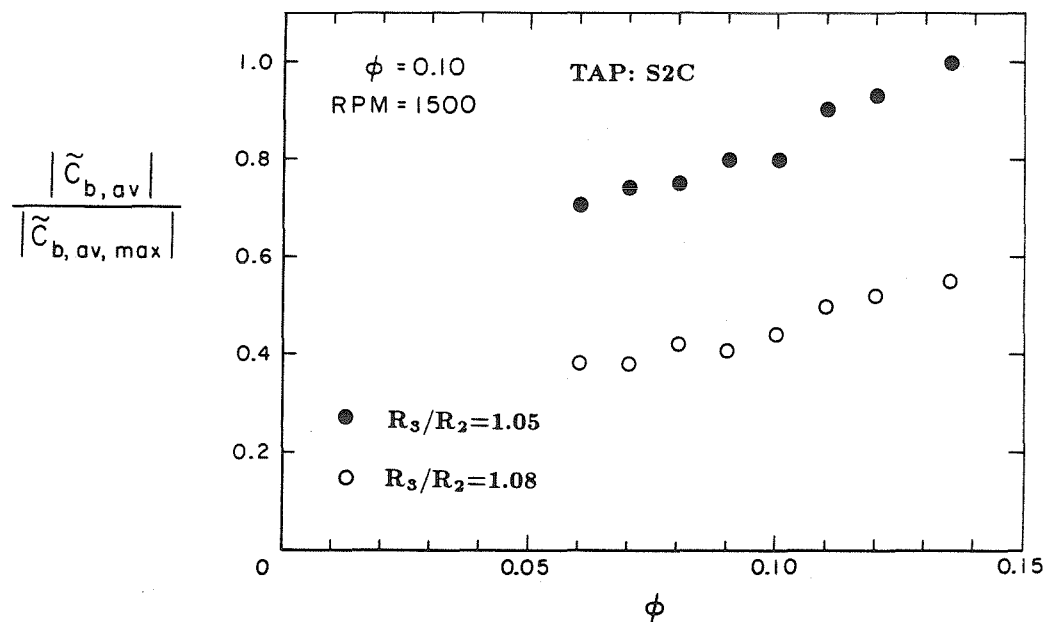


Fig. 6.11. Magnitude of ensemble averaged vane pressure fluctuations at pressure tap S2C for Impeller Z1 and Diffuser S ( $\phi = 0.06 - 0.135$ ,  $R_3/R_2 = 1.05$  and 1.08, rpm = 1500).

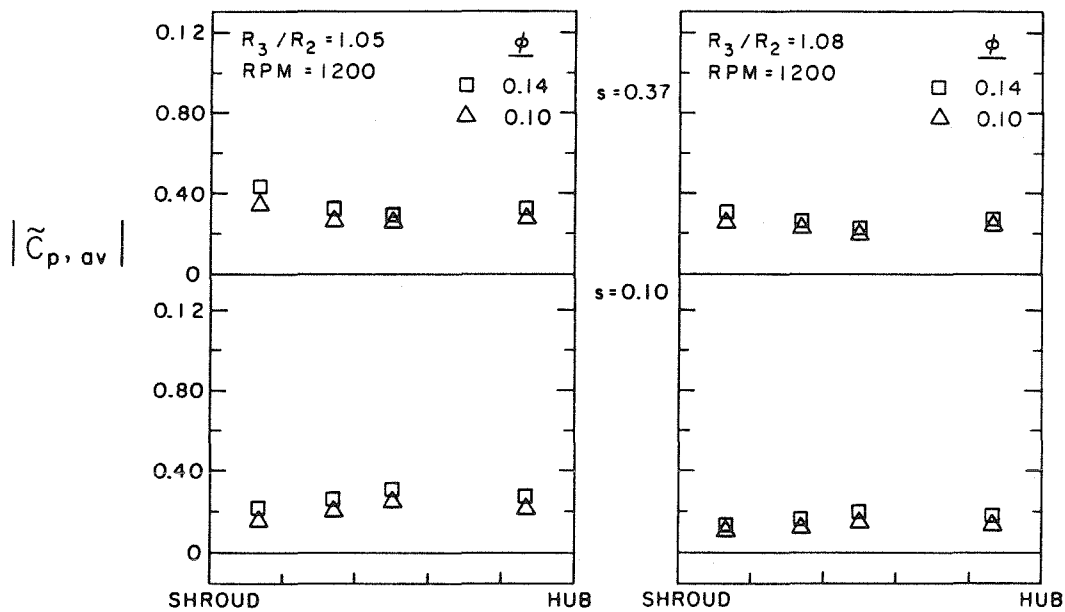


Fig. 6.12. Magnitude of ensemble averaged pressure fluctuations across the span of the vane for Impeller Z1 and Diffuser S ( $\phi = 0.135$  and  $0.10$ ,  $R_3/R_2 = 1.05$ ,  $s = 0.10$  and  $0.37$ , rpm = 1200).

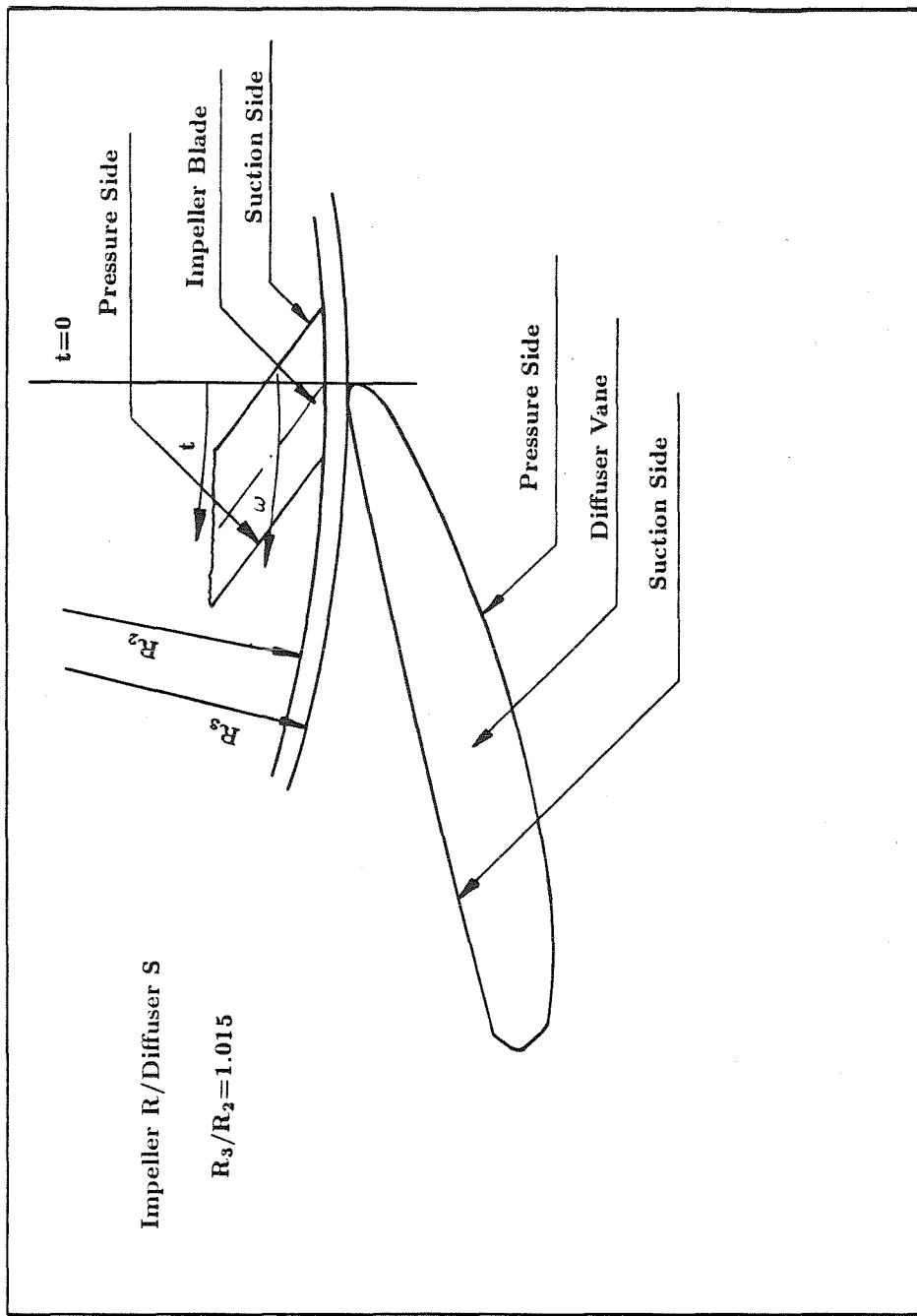


Fig. 6.13. Geometric reference configuration for phase computation.

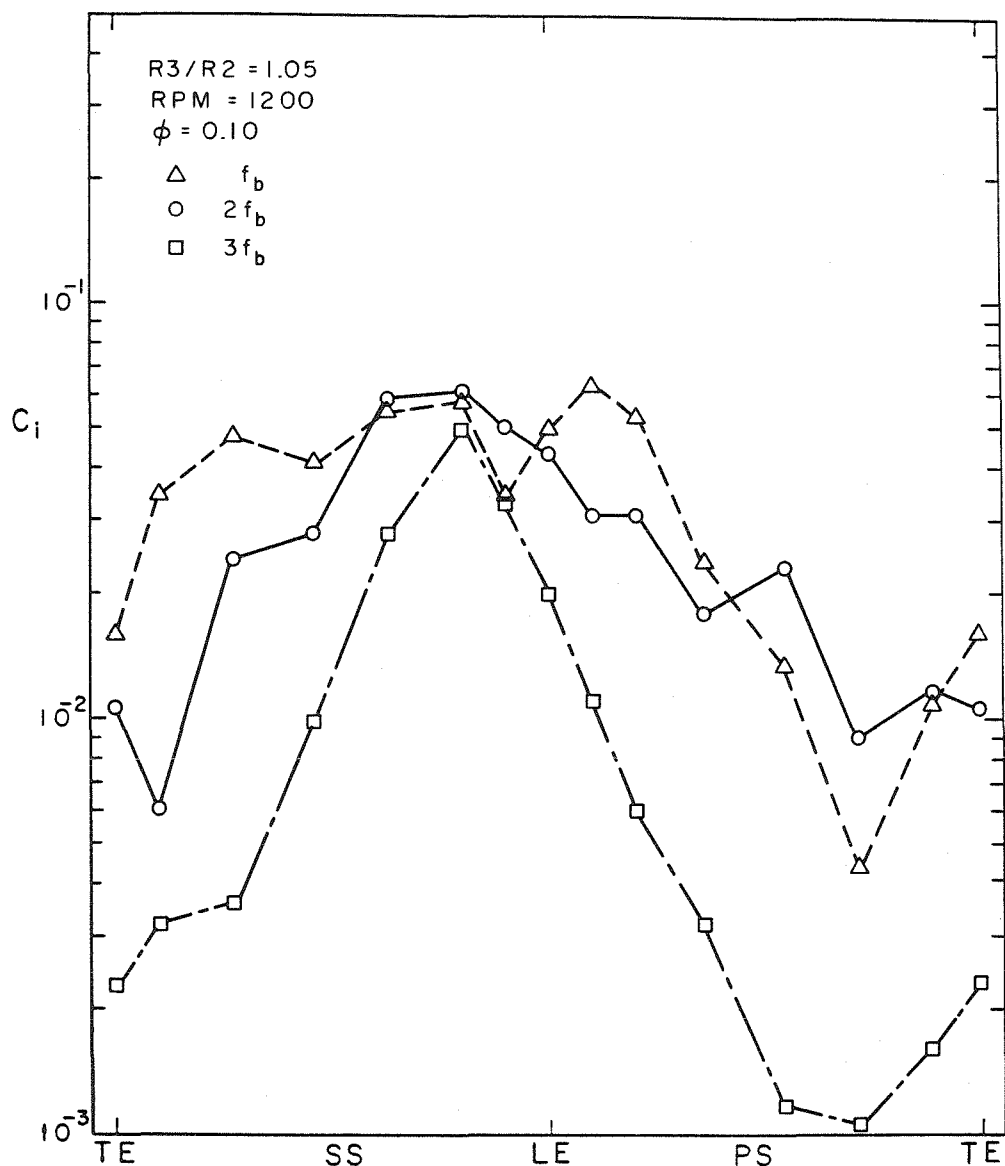


Fig. 6.14. Magnitude of Fourier coefficients of impeller blade passage harmonics for Impeller Z1 and Diffuser S ( $\phi = 0.10$ ,  $R_3/R_2 = 1.05$ , rpm = 1200).

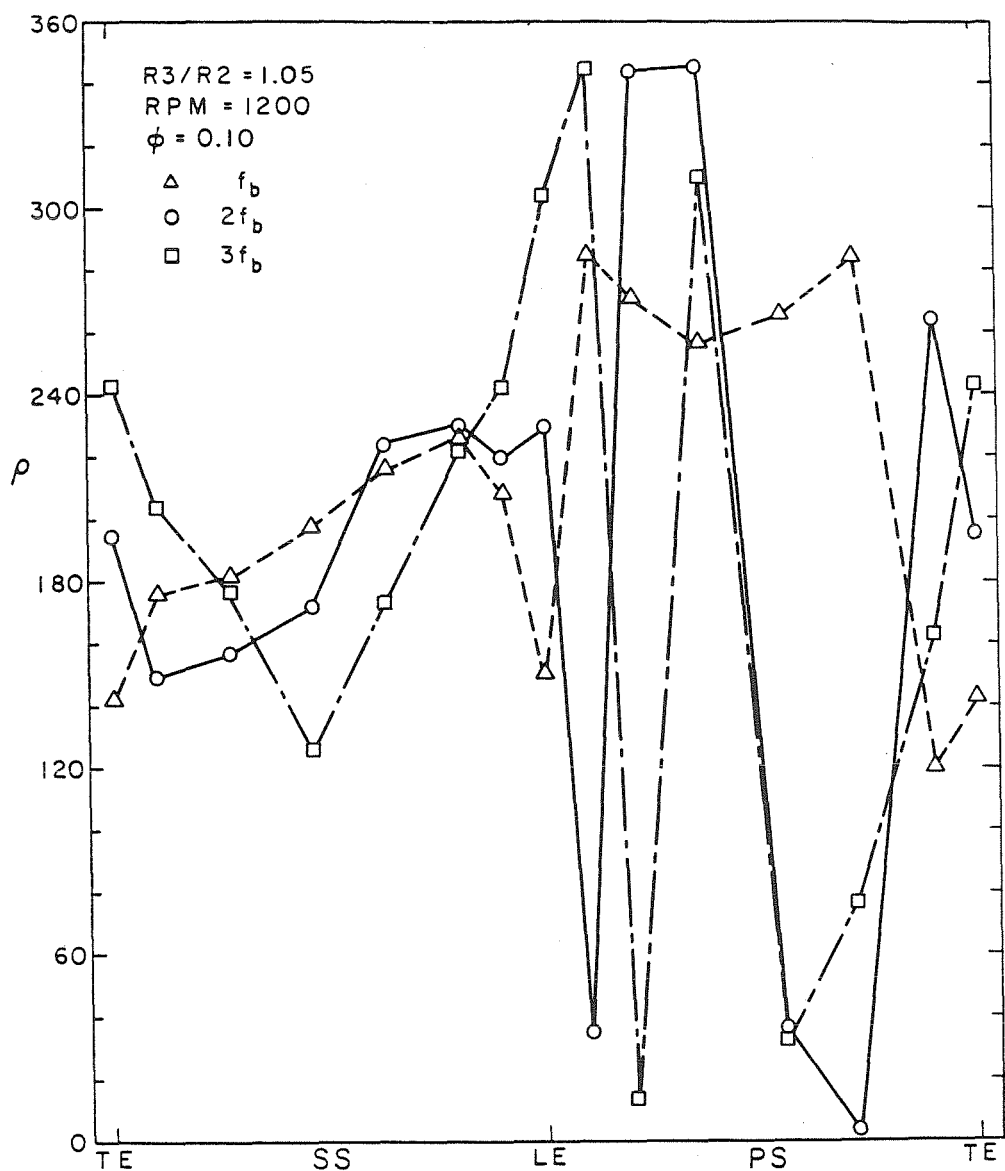


Fig. 6.15. Phase of Fourier coefficients of impeller blade passage harmonics for Impeller Z1 and Diffuser S ( $\phi = 0.10$ ,  $R_3/R_2 = 1.05$ , rpm = 1200).

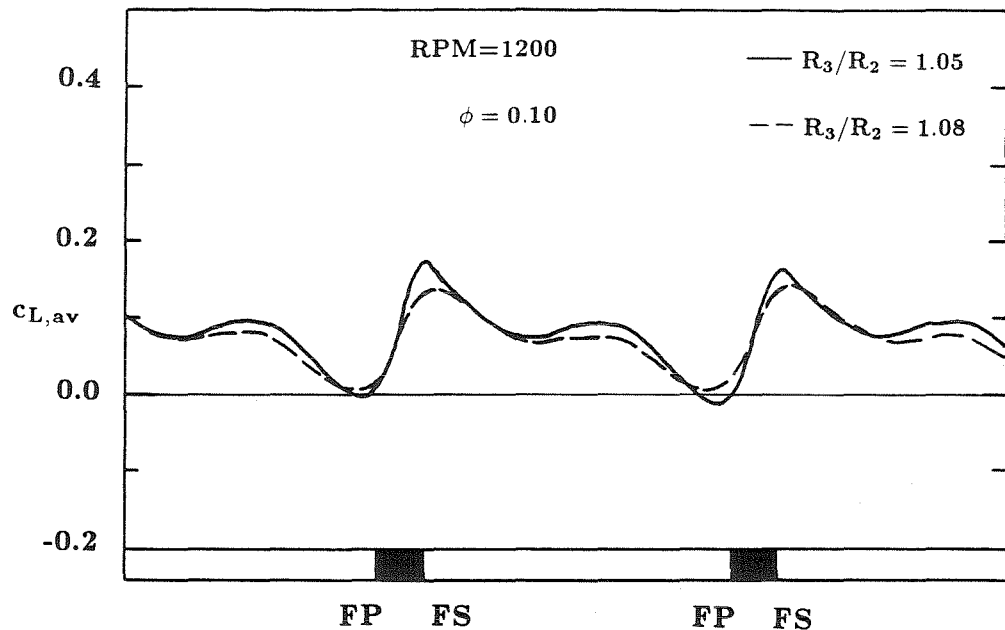


Fig. 6.16. Ensemble averaged lift on the diffuser vane at vane mid height for Impeller Z1 and Diffuser S ( $\phi = 0.10, R_3/R_2 = 1.05$  and  $1.08$ , rpm = 1200).

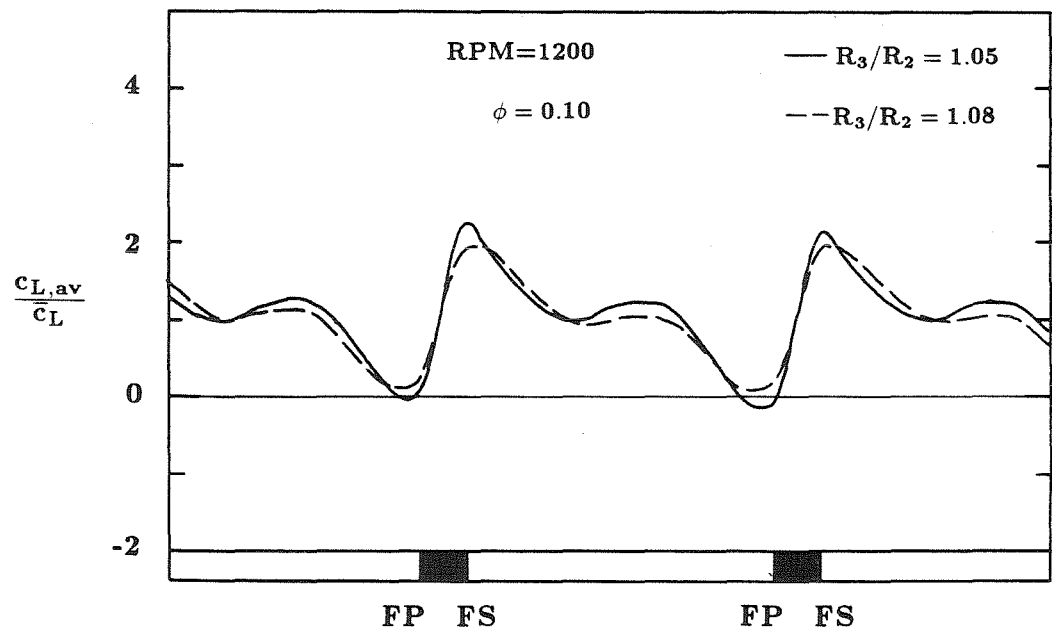


Fig. 6.17. Ratio of ensemble averaged lift to steady lift on the diffuser vane at vane mid height for Impeller Z1 and Diffuser S ( $\phi = 0.10, R_3/R_2 = 1.05$  and  $1.08$ , rpm = 1200).

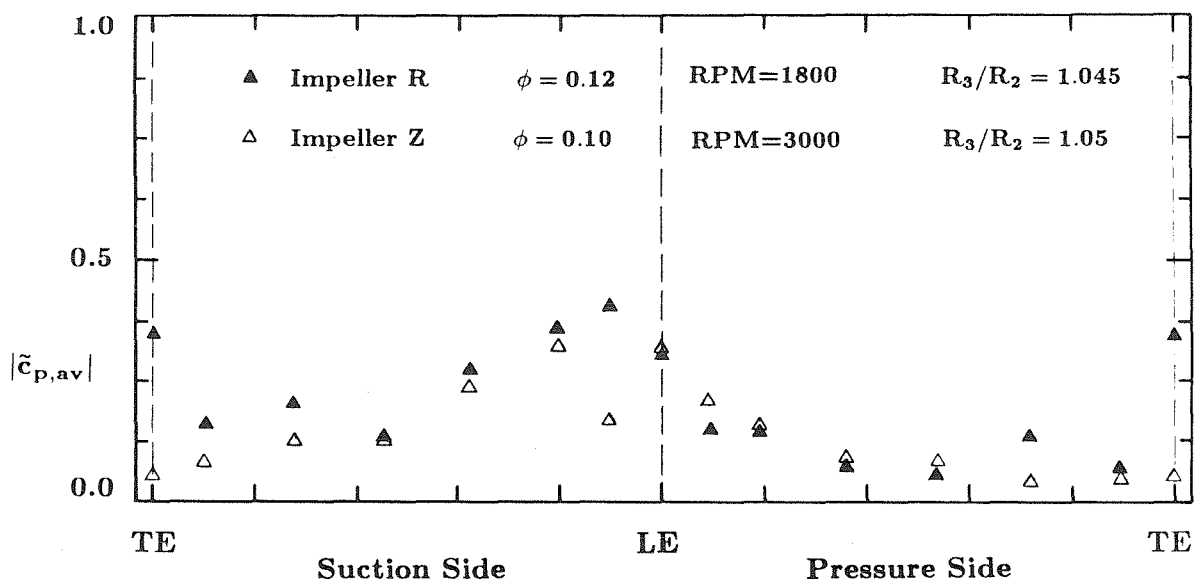


Fig. 6.18. Magnitude of ensemble averaged pressure fluctuations at mid vane height for Impeller R and Diffuser S ( $\phi = 0.12, R_3/R_2 = 1.045$ , rpm = 1800), and Impeller Z1 and Diffuser S ( $\phi = 0.10, R_3/R_2 = 1.05$ , rpm = 3000).

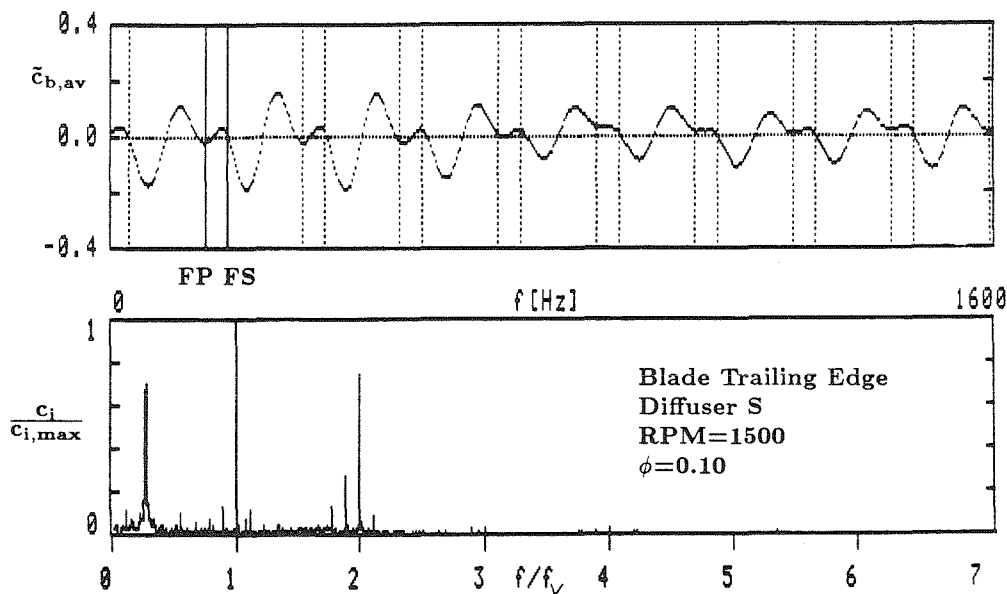


Fig. 6.19. Spectrum of unsteady blade pressure measurements and ensemble averaged unsteady blade pressure measurements at the trailing edge pressure tap for Impeller Z2 and Diffuser S ( $\phi = 0.10$ , rpm = 1500).

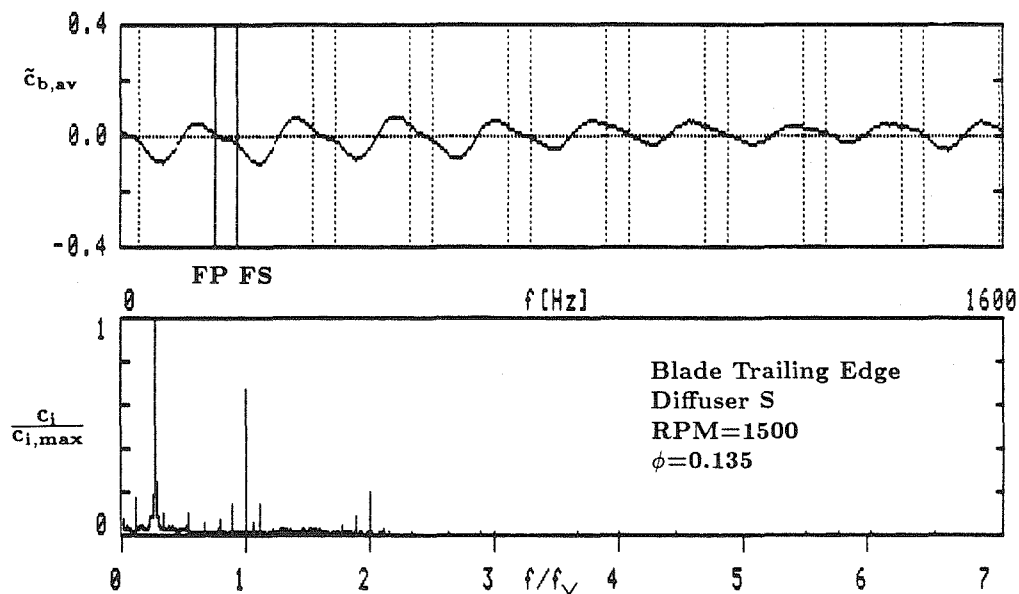


Fig. 6.20. Spectrum of unsteady blade pressure measurements and ensemble averaged unsteady blade pressure measurements at the trailing edge pressure tap for Impeller Z2 and Diffuser S ( $\phi = 0.135$ , rpm = 1500).

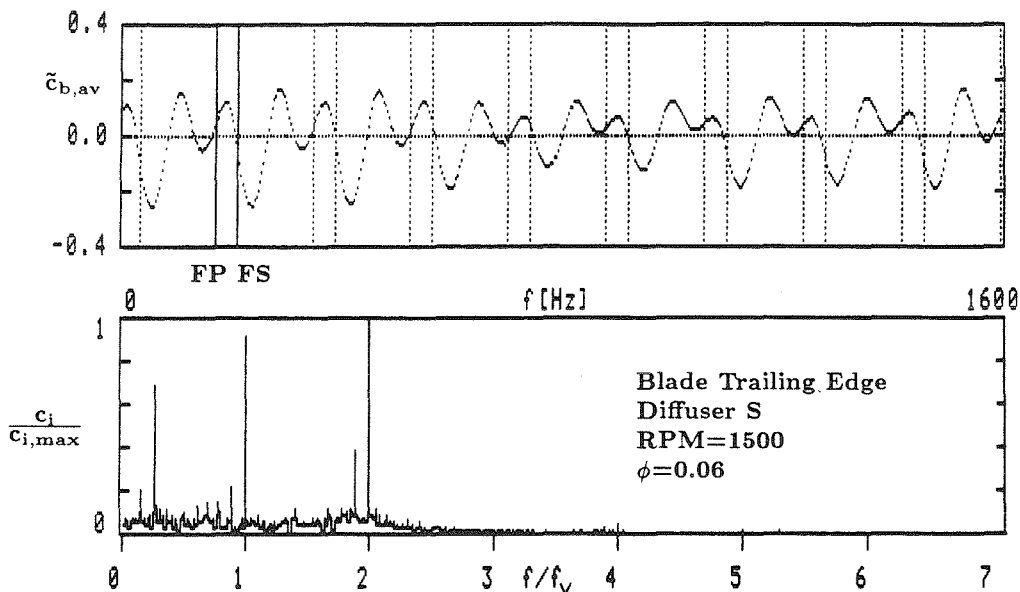


Fig. 6.21. Spectrum of unsteady blade pressure measurements and ensemble averaged unsteady blade pressure measurements at the trailing edge pressure tap for Impeller Z2 and Diffuser S ( $\phi = 0.06$ , rpm = 1500).

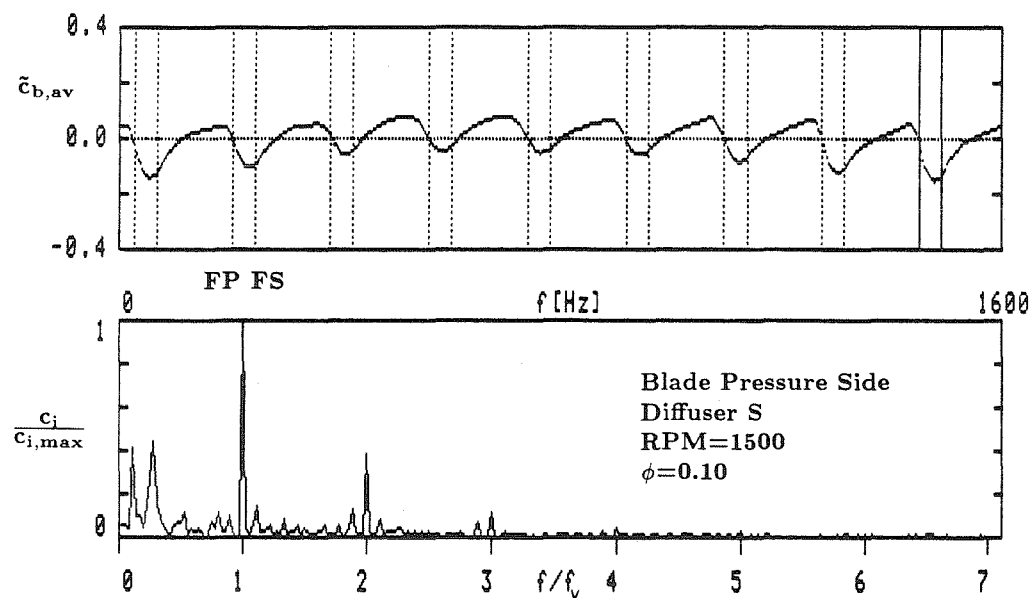


Fig. 6.22. Spectrum of unsteady blade pressure measurements and ensemble averaged unsteady blade pressure measurements at the pressure side pressure tap for Impeller Z2 and Diffuser S ( $\phi = 0.10$ , rpm = 1500).

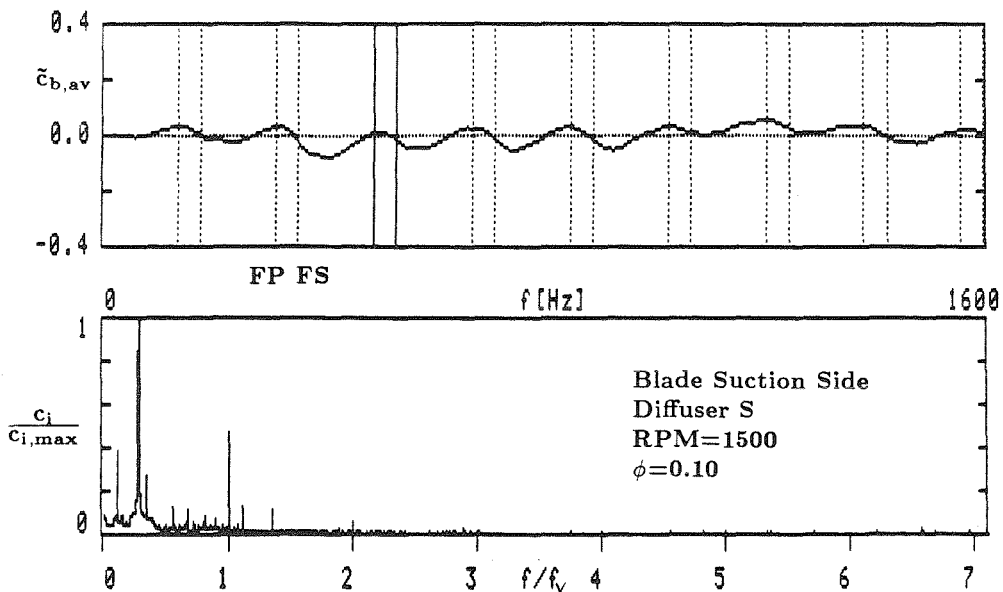


Fig. 6.23. Spectrum of unsteady blade pressure measurements and ensemble averaged unsteady blade pressure measurements at the suction side pressure tap for Impeller Z2 and Diffuser S ( $\phi = 0.10$ , rpm = 1500).

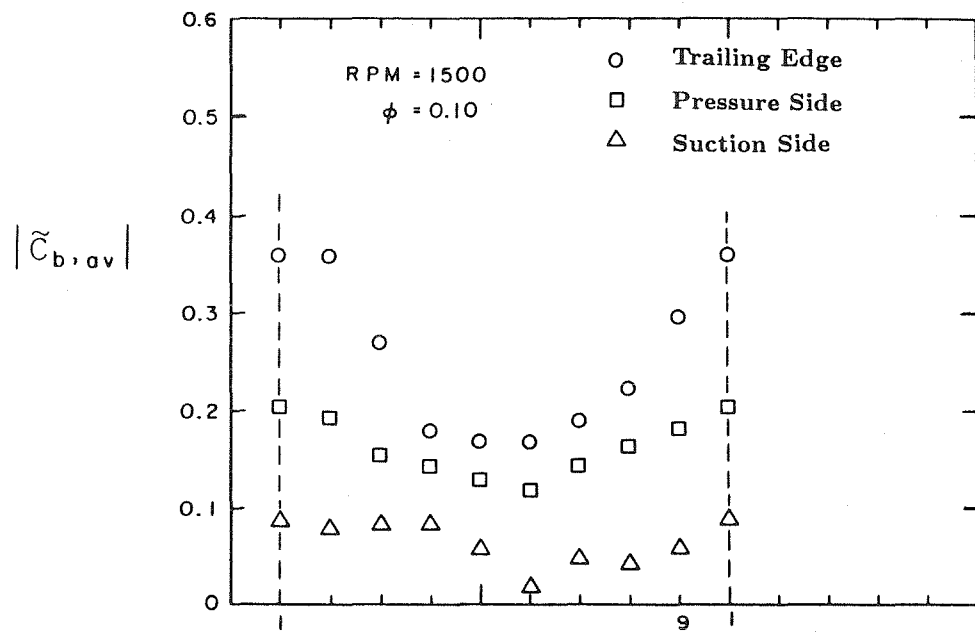


Fig. 6.24. Magnitude of ensemble averaged pressure fluctuations at the three impeller blade pressure taps during one shaft revolution for Impeller Z2 and Diffuser S ( $\phi = 0.10$ , rpm = 1500)

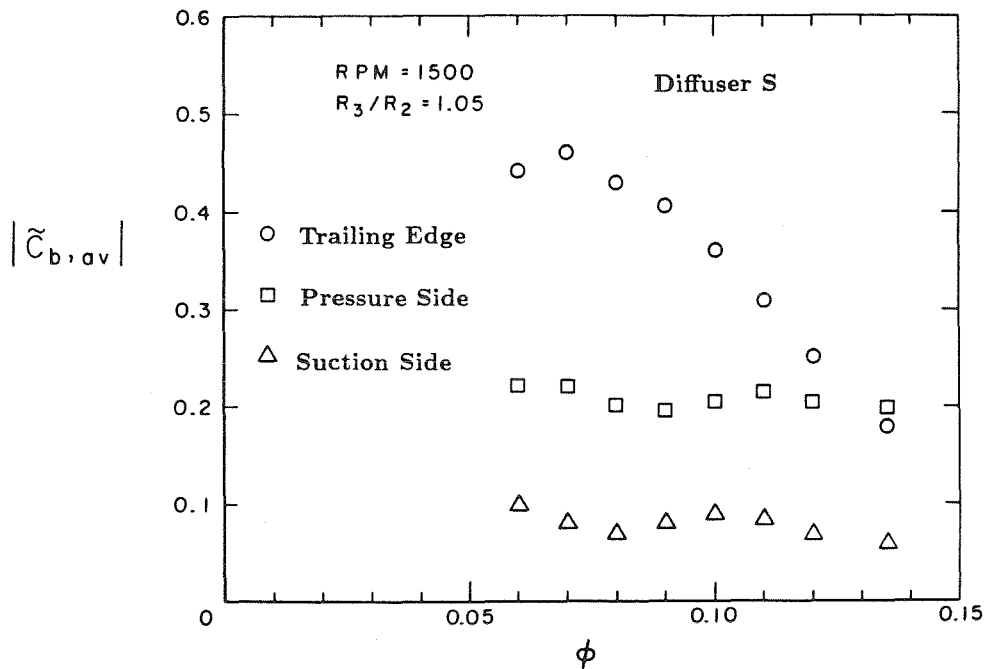


Fig. 6.25. Magnitude of ensemble averaged pressure fluctuations at the three impeller blade pressure taps for Impeller Z2 and Diffuser S ( $\phi = 0.06 - 0.135$ ,  $R_3/R_2 = 1.05$ , rpm = 1500)

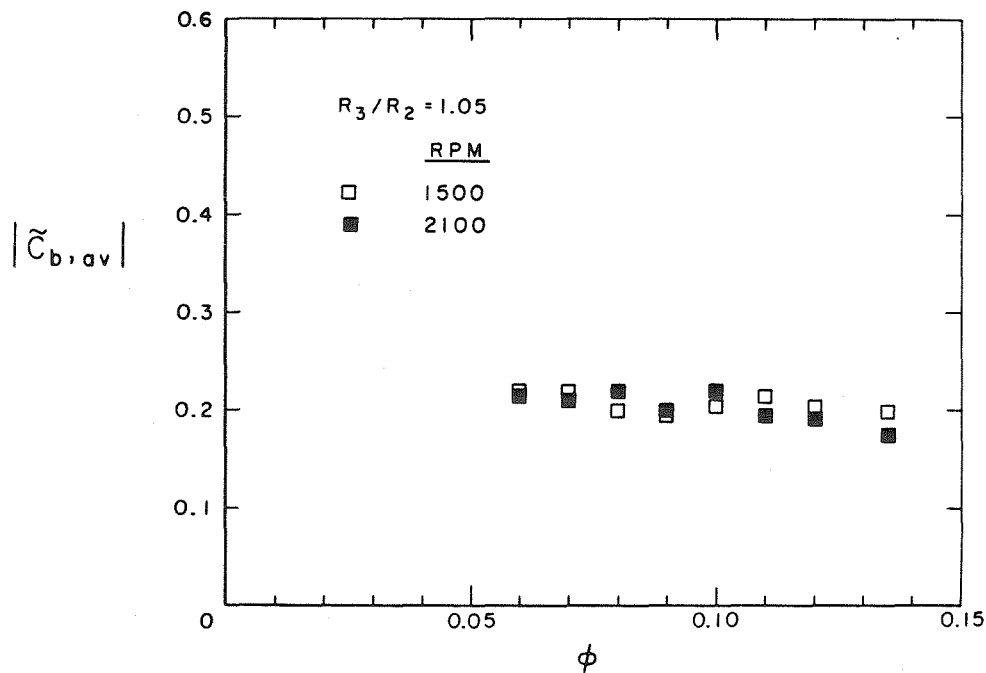


Fig. 6.26. Magnitude of ensemble averaged pressure fluctuations at the pressure tap on the blade pressure side for Impeller Z2 and Diffuser S ( $\phi = 0.06 - 0.135$ ,  $R_3/R_2 = 1.05$ , rpm = 1500 and 2100)

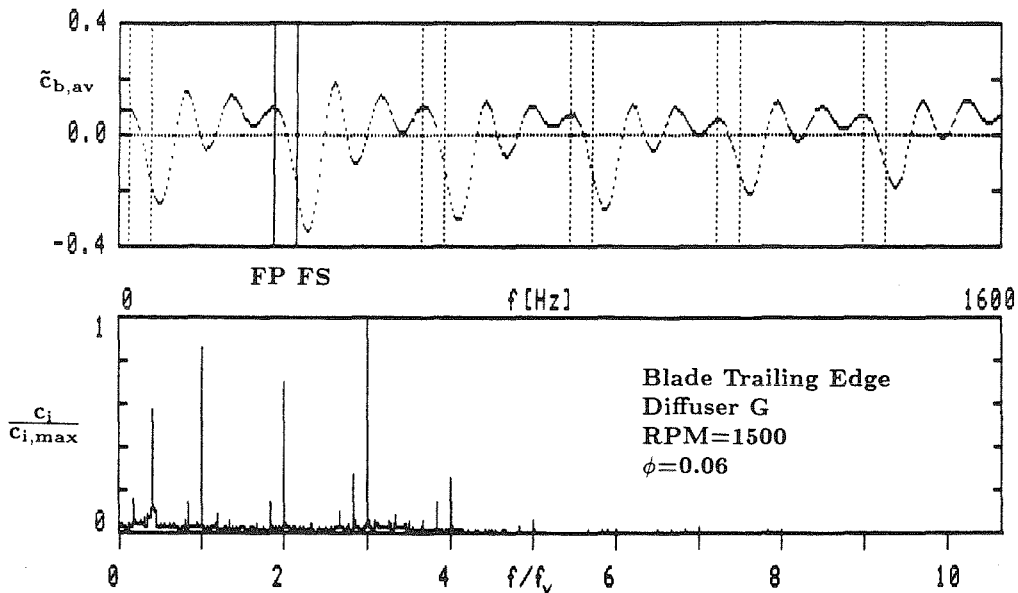


Fig. 6.27 Spectrum of unsteady blade pressure measurements and ensemble averaged unsteady blade pressure measurements at the trailing edge pressure tap for Impeller Z2 and Diffuser G ( $\phi = 0.06$ , rpm = 1500).

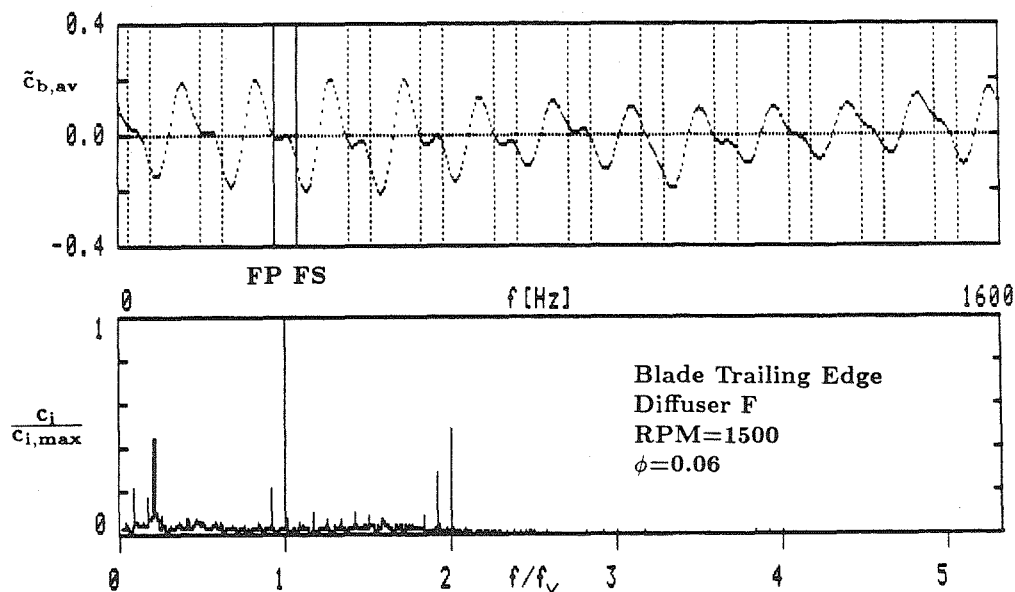


Fig. 6.28. Spectrum of unsteady blade pressure measurements and ensemble averaged unsteady blade pressure measurements at the trailing edge pressure tap for Impeller Z2 and Diffuser F ( $\phi = 0.06$ , rpm = 1500).

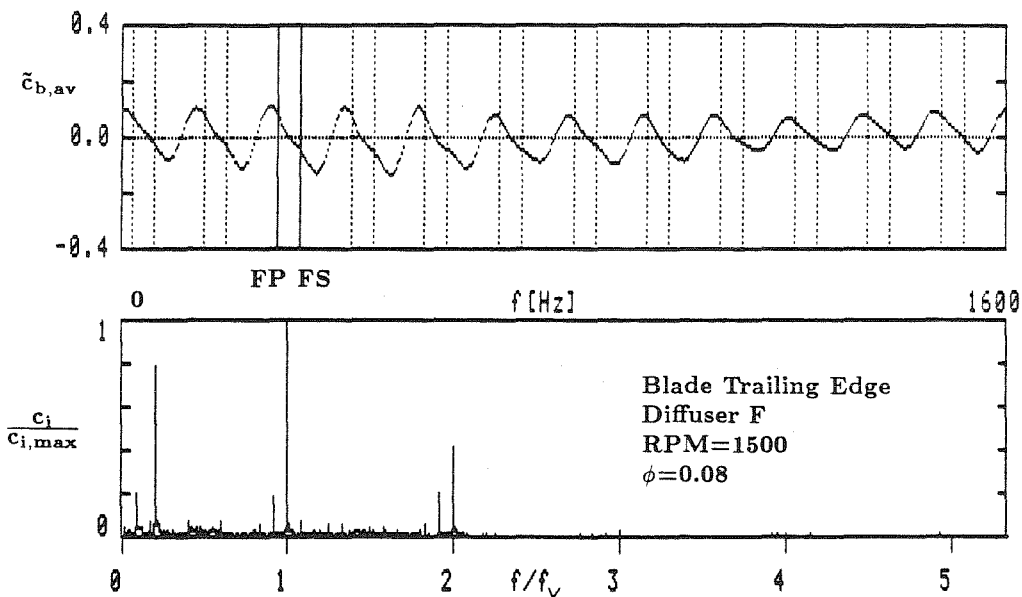


Fig. 6.29. Spectrum of unsteady blade pressure measurements and ensemble averaged unsteady blade pressure measurements at the trailing edge pressure tap for Impeller Z2 and Diffuser F ( $\phi = 0.08$ , rpm = 1500).

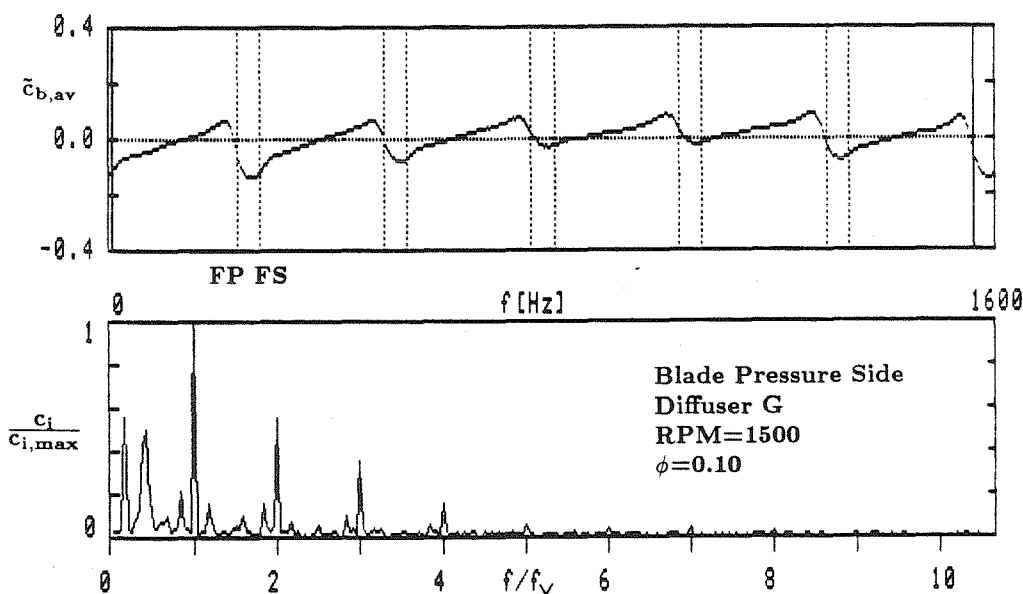


Fig. 6.30. Spectrum of unsteady blade pressure measurements and ensemble averaged unsteady blade pressure measurements at the pressure side pressure tap for Impeller Z2 and Diffuser G ( $\phi = 0.10$ , rpm = 1500).

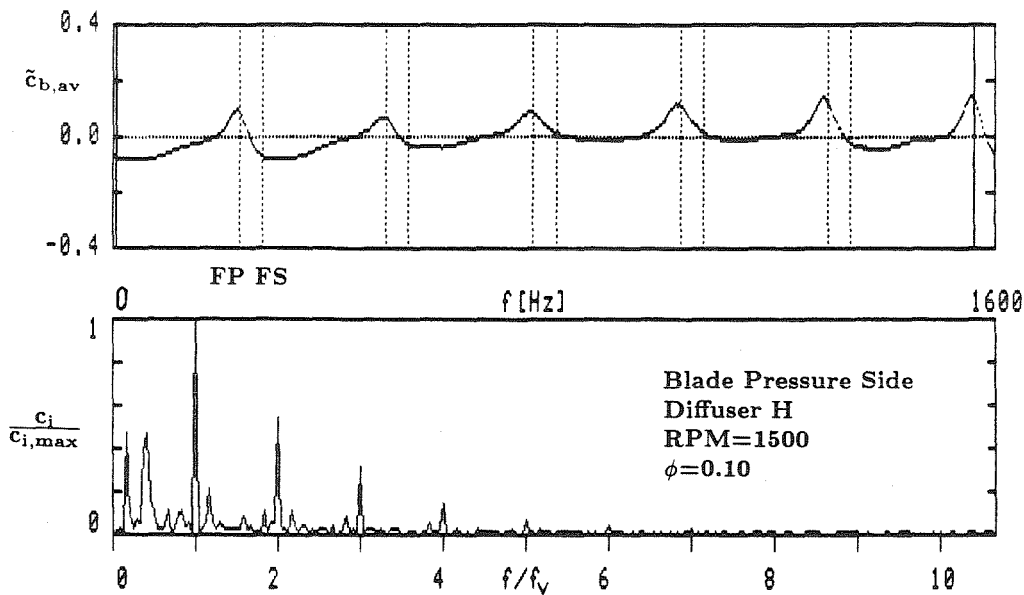


Fig. 6.31. Spectrum of unsteady blade pressure measurements and ensemble averaged unsteady blade pressure measurements at the suction side pressure tap for Impeller Z2 and Diffuser H ( $\phi = 0.10$ , rpm = 1500).

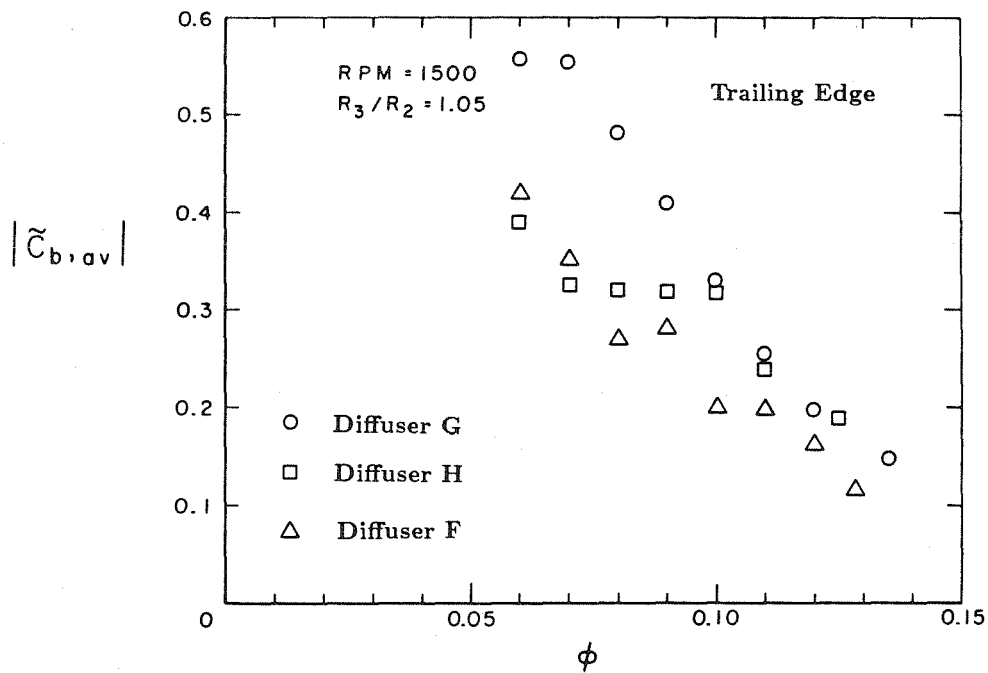


Fig. 6.32. Magnitude of ensemble averaged pressure fluctuations at the pressure tap at the impeller blade trailing edge for Impeller Z2 and Diffusers F, G and H ( $\phi = 0.06 - 0.135$ ,  $R_3/R_2 = 1.05$ , rpm = 1500).

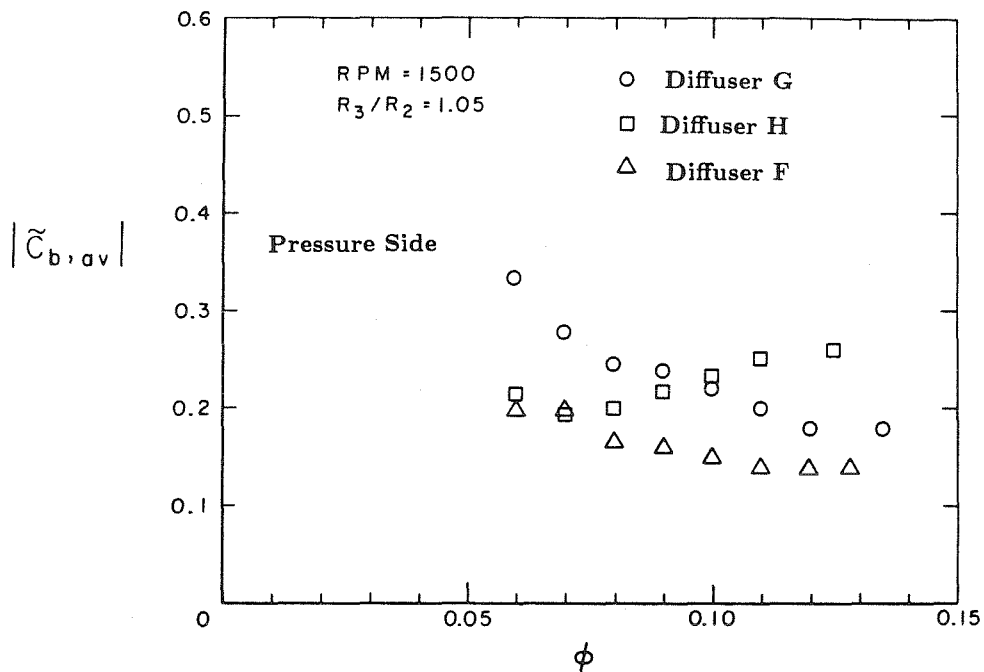


Fig. 6.33. Magnitude of ensemble averaged pressure fluctuations at the pressure tap at the impeller blade pressure side for Impeller Z2 and Diffusers F, G and H ( $\phi = 0.06 - 0.135$ ,  $R_3/R_2 = 1.5$ , rpm = 1500).

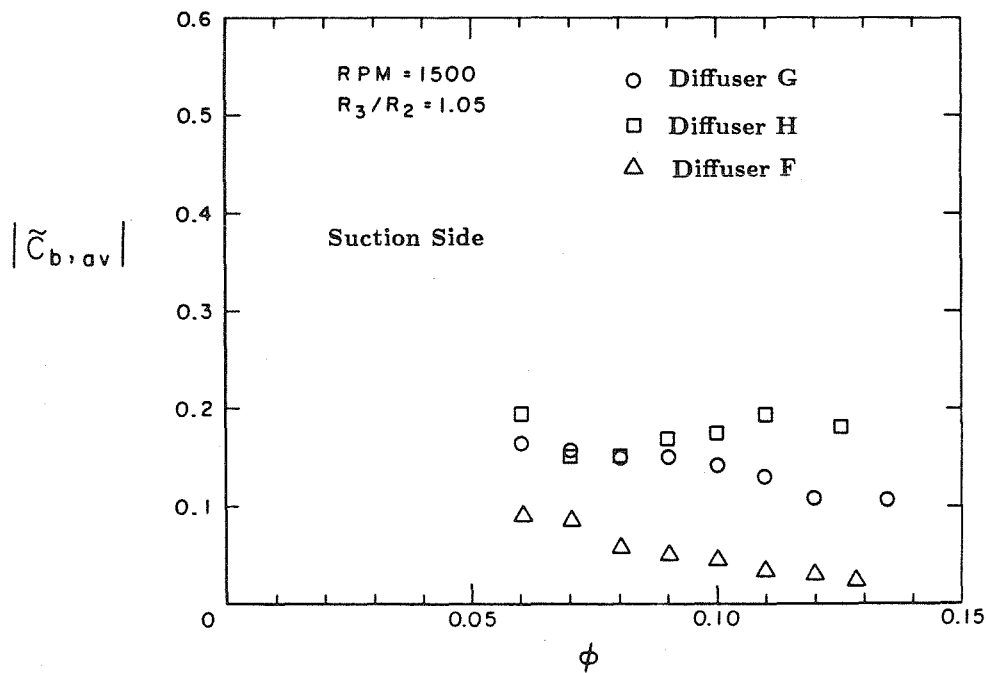


Fig. 6.34. Magnitude of ensemble averaged pressure fluctuations at the pressure tap at the impeller blade suction side for Impeller Z2 and Diffusers F, G and H ( $\phi = 0.06 - 0.135$ ,  $R_3/R_2 = 1.05$ , rpm = 1500).

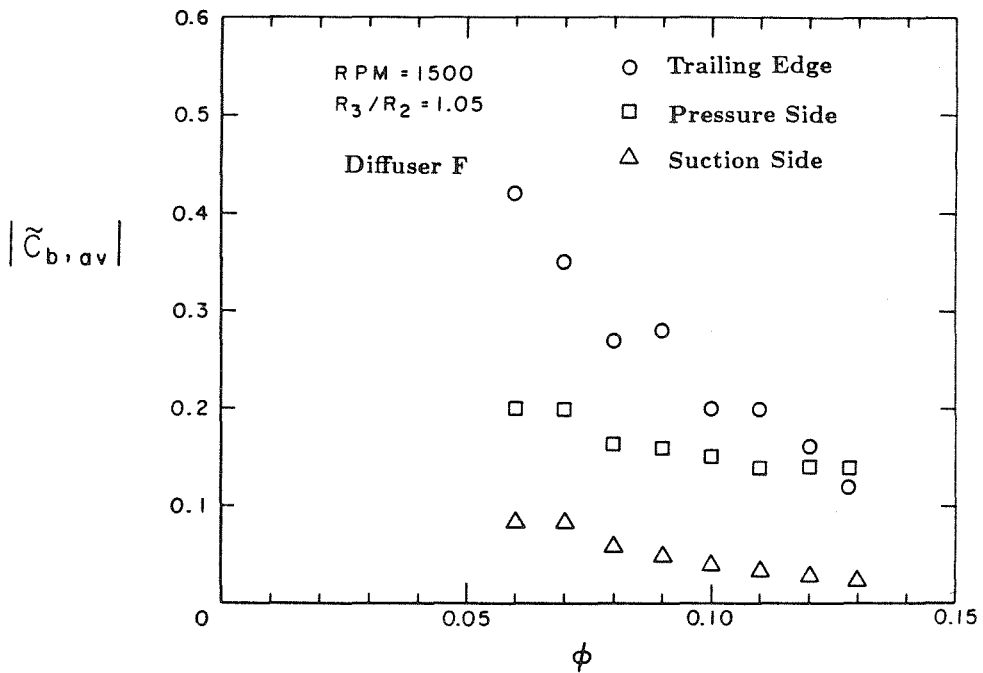


Fig. 6.35. Magnitude of ensemble averaged pressure fluctuations at the three impeller blade pressure taps for Impeller Z2 and Diffusers F ( $\phi = 0.06-0.135$ ,  $R_3/R_2 = 1.05$ , rpm = 1500).

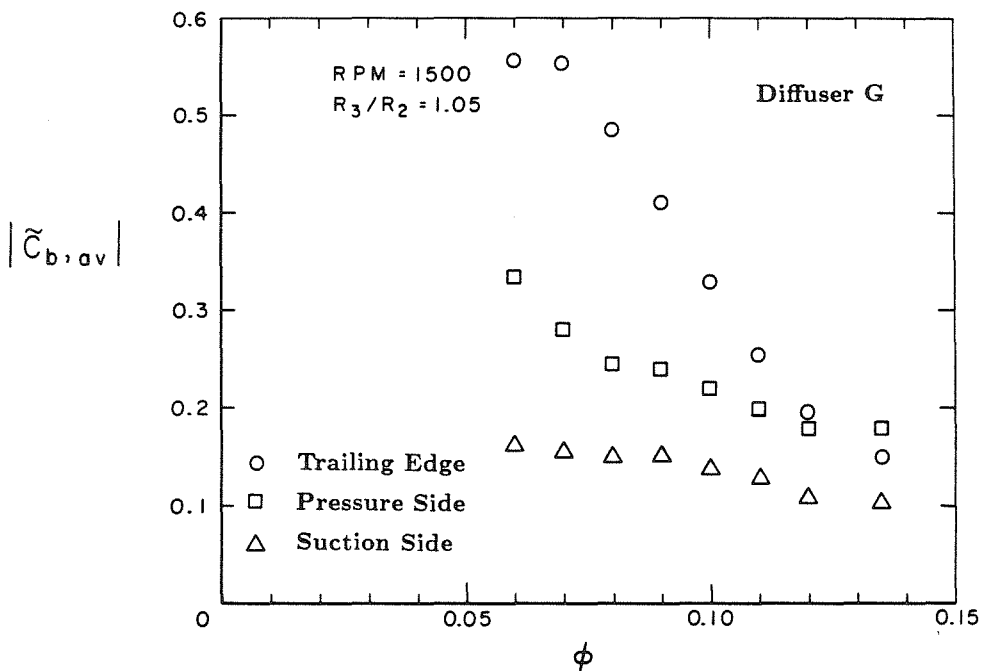
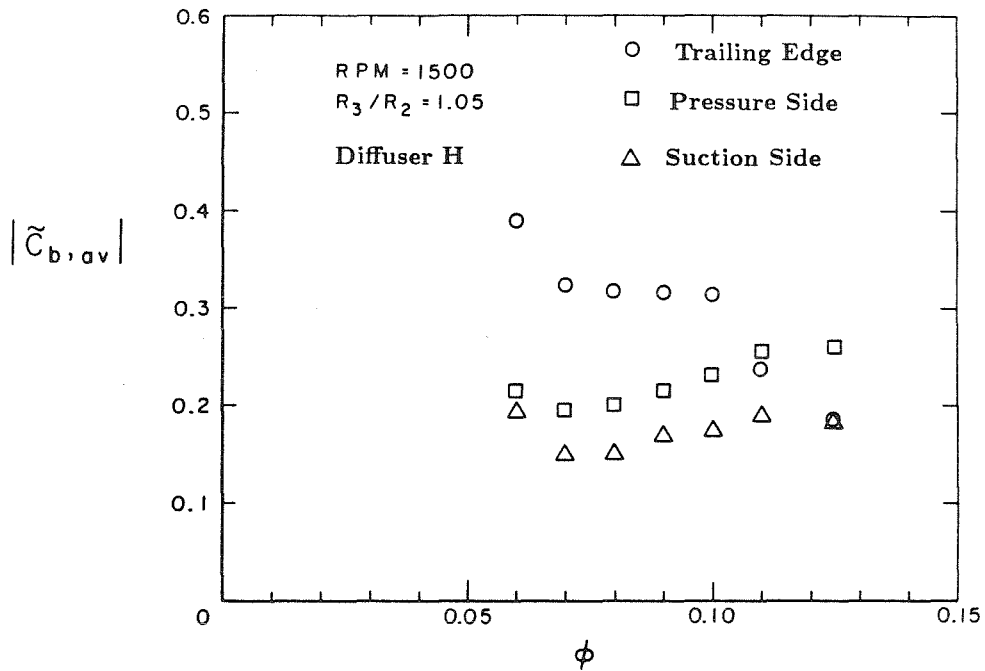


Fig. 6.36. Magnitude of ensemble averaged pressure fluctuations at the three impeller blade pressure taps for Impeller Z2 and Diffusers G ( $\phi = 0.06-0.135$ ,  $R_3/R_2 = 1.05$ , rpm = 1500).



**Fig. 6.37.** Magnitude of ensemble averaged pressure fluctuations at the three impeller blade pressure taps for Impeller Z2 and Diffusers H ( $\phi = 0.06-0.135$ ,  $R_3/R_2 = 1.05$ , rpm = 1500).

## CHAPTER 7

### 7. Conclusion

An experimental investigation of unsteady flow in radial pumps focusing on impeller blade-diffuser vane interaction was presented.

Steady and unsteady measurements of the flow discharged from two different centrifugal impellers, a two-dimensional impeller, Impeller Z1, and one half of the double suction pump impeller of the HPOTP (High Pressure Oxygen Turbopump) of the SSME (Space Shuttle Main Engine), Impeller R, into vaneless diffusers were made. The objective of these measurements was to obtain knowledge about the magnitude of the flow nonuniformities at the impeller discharge due to the wakes shed by the impeller blades and about how rapidly these nonuniformities decay with increasing radial distance from the impeller discharge. In particular, the measurements were aimed at investigating the nonuniformity of the flow in vaneless diffusers at radial distances to the impeller discharge equivalent to the radial gaps between impeller blades and diffuser vanes in diffuser pumps. These measurements were performed using a total pressure and a three-hole tube.

The unsteady total pressure measurements showed that:

- \* the total pressure fluctuations very close to the impeller discharge ( $r_3/R_2 = 1.02$ ) are as large as the total pressure rise across the pump.
- \* the total pressure fluctuations decrease strongly with increasing radial distance to the impeller discharge.
- \* for Impeller R significant total pressure nonuniformities occur from hub to shroud.

Unsteady three-hole tube measurements of the flow discharged by a two-dimensional impeller (Impeller Z1) into a vaneless diffuser were made at two ra-

dial locations,  $r_3/R_2 = 1.08$  and  $1.11$ , at the diffuser mid height. Comparing the unsteady total pressure measurements obtained by a total pressure probe at the same radial position in the vaneless diffuser, it was observed that the total pressure profiles were qualitatively similar; the magnitude of the fluctuations, however, was larger for the total pressure probe than for the three-hole tube. Hence, the three-hole tube permits qualitative unsteady measurements, but not quantitatively accurate unsteady measurements. However, even those qualitative measurements provided some valuable information on the flow.

- \* The jet wake model by Dean and Senoo (1960) was qualitatively confirmed.
- \* The impeller wakes, however, did not close as close to the impeller discharge ( $r_3/R_2 = 1.05$ ) as predicted by Dean (1960). This coincides with observations made in radial compressor research among others by Eckhard (1975, 1976). For maximum flow, the jet-wake pattern could still be distinguished at ( $r_3/R_2 = 1.11$ ).
- \* In addition to the fluctuations predicted by the jet-wake model, a significant pressure and total pressure drop, possibly resulting from the flow around the thick impeller blade trailing edge, was observed at the pressure side of the impeller blade trailing edge.
- \* Those pressure and total pressure deficits decayed slower than the jet wake flow pattern with increasing distance to the impeller discharge. The pressure and the total pressure had therefore not attained axisymmetry at  $r_3/R_2 = 1.11$ .

The unsteady measurements in the vaneless diffusers showed that large pressure, total pressure and flow angle fluctuations occurred at radial distances downstream of the impeller discharge corresponding to locations where the diffuser inlet is located in vaned diffusers. Hence, the diffuser vanes in diffuser pumps have to be expected to experience pressure fluctuations due to the impinging wakes shed by

the impeller blades.

Steady and unsteady diffuser vane pressure measurements were made very extensively for Impeller R and a vaned diffuser, Diffuser S. Sets of measurements were obtained for radial gaps of 1.5% and 4.5% of the impeller discharge radius between impeller blades and diffuser vanes. These gaps are not unreasonably small. Gaps of 4% are commonly used in high head diffuser pumps (Bolleter, 1988). The investigations for Impeller R concentrated on:

- \* Magnitude of the pressure fluctuations.
- \* Magnitude of the fluctuating lift.
- \* Difference in the pressure fluctuations caused by full and partial blades.
- \* Dependence of the magnitude of the pressure fluctuations on the radial gap between the impeller blades and the diffuser vanes.

It was found that:

- \* The largest pressure fluctuations, of the same magnitude as the total pressure rise across the pump, occurred on the vane suction side close to the leading edge.
- \* The pressure fluctuations were largest for maximum flow.
- \* The pressure fluctuations were larger on the suction than on the pressure side.
- \* Increasing the radial gap between impeller blades and diffuser vanes from 1.5% to 4.5% resulted in a significant decrease, especially of the large pressure fluctuations on the front half on the suction side.

- \* The magnitude of the low frequency components (i.e., frequency components lower than impeller blade passage frequency) in the spectra obtained from unsteady measurements made near the leading edge on the vane suction side increased with decreasing flow coefficient and with increasing radial gap.
- \* The fluctuating lift on the diffuser vane was two to three times as large as the steady lift.
- \* The magnitude of the fluctuating lift decreased with decreasing flow coefficient.
- \* Significant differences in the vane pressure fluctuations caused by full and partial impeller blades were observed for low flow coefficients.

Diffuser front shroud pressure measurements were made for the vaned and a vaneless diffuser of identical side wall geometry as the vaned diffuser. It was found that the magnitude of the front shroud pressure fluctuations increased with the presence of the diffuser vanes.

For the two-dimensional impeller, Impeller Z1, a similar program was conducted for radial gaps of 5% and 8% between impeller blades and diffuser vanes. The vane pressure measurements for Impeller Z1 led to similar findings as those for Impeller R and will not be repeated here. In fact, the magnitude of the vane pressure fluctuations and the magnitude of the lift fluctuations were found to be rather similar for Impeller Z1 for a radial gap of 5% and for Impeller R for a radial gap of 4.5%. Unsteady total pressure measurements were made for Impeller Z1 at the mid height of the vaned diffuser used for the vane pressure measurements and a vaneless diffuser of identical side wall geometry. As for the front shroud pressure measurements made for Impeller R, it was observed that the total pressure fluctuations increased with the presence of the diffuser vanes.

Unsteady impeller blade pressure measurements were made on a two-

dimensional test impeller of identical blade geometry as Impeller Z1, referred to as Impeller Z2. Those measurements were made for the vaned diffuser used for the diffuser vane pressure and a second diffuser of identical side wall geometry but permitted variable diffuser vane geometry to investigate the influence of the vane number and the influence of the vane angle on the impeller blade pressure fluctuations.

- \* The largest blade pressure fluctuations occurred, independent of the diffuser vane configuration at the impeller blade trailing edge.
- \* Those fluctuations increased significantly with decreasing flow coefficient, in contrast to the largest pressure fluctuations at the diffuser vane suction side that decreased with decreasing flow coefficient. For a low flow coefficient,  $\phi = 0.06$ , and a radial gap of 5%, the magnitude of those fluctuations reached  $\approx 60\%$  of the total pressure rise at that flow coefficient.
- \* With the exception of the maximum flow coefficient, the pressure fluctuations at the pressure side trailing edge were smaller than those at the trailing edge.
- \* The pressure fluctuations at the pressure tap on the blade suction side were for all diffuser vane configurations smaller than those at the trailing edge pressure tap and smaller than those at the pressure side pressure tap.
- \* Increasing the vane number from six to twelve resulted in a significant decrease of the blade pressure fluctuations at all blade pressure taps.
- \* Decreasing the vane angle from 20 degrees to 10 degrees (for six diffuser vanes) resulted in a decrease of the large pressure fluctuations at the blade trailing edge, and an increase of the pressure fluctuations at the suction side pressure tap (the total pressure rise across the pump was reduced for all flow coefficients investigated).

The large pressure fluctuations at the impeller blade trailing edge combined with the low steady pressure at the pressure side of the impeller blade trailing edge (measured with a three-hole tube in the stationary frame) may cause in pumps running at extremely high speeds cavitation damage at the impeller blade trailing edge, as observed for the pump impeller of the High Pressure Oxygen Turbopump of the Space Shuttle Main Engine.

The impeller blade pressure fluctuations are the result of potential interaction between the diffuser vanes and the impeller blades. From the steady vane pressure measurements for Diffuser S, a significant increase in the lift on the diffuser vanes (and hence of the circulation about a diffuser vane) was observed when the flow coefficient was reduced. Hence, the circulation about a single diffuser vane, sensed by the rotating impeller blades as a periodic fluctuation, is increasing with decreasing flow coefficient. This may cause the increase of the pressure fluctuations at the blade trailing edge with decreasing flow coefficient. Similarly, increasing the vane number from six to twelve will result in a decrease of the loading of a single diffuser vane. Hence, the circulation about a single diffuser vane, sensed by the rotating impeller blades as a periodic fluctuation is decreasing with the doubling of the vane number. Again, this may be the cause of the smaller blade pressure fluctuations measured for the twelve vaned diffuser than for the six vaned diffuser.

The large pressure fluctuations on the diffuser vane near the diffuser vane leading edge behave, as a function of flow coefficient, qualitatively like the total pressure fluctuations and the diffuser front shroud pressure fluctuations of the flow discharging into a vaneless diffuser; they are largest for the maximum flow coefficient, and decrease with decreasing flow coefficient. Similarly, the fluctuating lift on the diffuser vane decreases with decreasing flow coefficient. This may indicate that the pressure fluctuations on the diffuser vane are dominated by the viscous wake interaction, i.e., the impinging of the impeller blade wakes on the diffuser vanes. If potential flow interaction was dominant, it should be expected that the vane pres-

sure fluctuations increase with the flow coefficient decreasing from maximum flow, since the blade loading, and hence the blade circulation, is expected to increase with decreasing flow coefficient.

Therefore, it was shown that both potential flow interaction and the viscous wake interaction can cause pressure fluctuations on impeller blades and diffuser vanes that are of the same order of magnitude as the total pressure rise across the pump, if the radial gap between impeller blades and diffuser vanes is small, i.e., of the order of a few percentages of the impeller discharge radius.

Furthermore, it was shown that the fluctuating lift on the diffuser vanes can be of the same order of magnitude as the steady lift. For high speed, high performance pumps with extremely closely spaced blade rows, this should be considered in the structural vane design.

## LIST OF REFERENCES

Arndt, N., Acosta, A.J., Brennen, C.E., and Caughey, T.K., "Rotor-Stator Interaction in a Diffuser Pump," to be presented at the 33rd ASME International Gas Turbine and Aeroengine Congress, June 5-9, 1988, Amsterdam, and to appear in the ASME *Journal of Turbomachinery*.

Arndt, N., Acosta, A.J., Brennen, C.E., and Caughey, T.K., "Unsteady Diffuser Vane Pressure and Impeller Wake Measurements in a Centrifugal Pump," *Conference Proceedings 8. Conference on Fluid Machinery* Budapest, Sept. 1987.

Bolleter, U., "On Blade Passages Tones of Centrifugal Pumps," to appear in the *Journal of Vibrations*, 1988.

Braisted, D.M., "Cavitation Induced Instabilities Associated with Turbomachines," Ph.D. Thesis, Division of Engineering and Applied Science, California Institute of Technology, 1979.

Chamieh, D.S., "Forces On A Whirling Centrifugal Pump-Impeller," Ph.D. Thesis, Division of Engineering and Applied Science, California Institute of Technology, 1983.

Dean R.C., and Senoo, Y., "Rotating Wakes in Vaneless Diffusers," ASME *Journal of Basic Engineering*, Vol. 82, 1960, 563-574.

Dring, R.P., Joslyn, H.D., Hardin, L.W., and Wagner, J.H., "Turbine Rotor-Stator Interaction," ASME *Journal of Engineering for Power*, Oct. 1982, Vol. 104, 729-742.

Eckhard, D., "Instantaneous Measurements in the Jet and Wake Discharge Flow of a Centrifugal Compressor Impeller," ASME *Journal of Engineering for Power*, Vol. 97, 1975, 337-346

Eckhard, D., "Detailed Flow Investigations Within a High-Speed Centrifugal Impeller," *ASME Journal for Fluids Engineering*, Vol. 98, 1976, 390-402.

Furukawa, A., Cheng, C., Sekiya, T., and Takamatsu, Y., "Flow Analysis in Two-Dimensional Impeller of Centrifugal Pump by Surface Singularity Method Combined with Flow-Model of Three-Dimensional Boundary Layer," *Proceedings of the 2nd China-Japan Joint Conference on Hydraulic Machinery and Equipment*, October 1987.

Gallus, H.E., "High Speed Blade-Wake Interactions," *von Kármán Institute for Fluid Mechanics Lecture Series 1979-3*, Jan. 29-Feb. 2, 1979, Volume 2.

Gallus, H.E., Lambertz, J., and Wallmann, T., "Blade-Row Interaction in an Axial Flow Subsonic Compressor Stage," *ASME Journal of Engineering for Power*, Jan. 1980, Vol. 102, 169-177.

Iino, T., and Kasai, K., "An Analysis of Unsteady Flow Induced by Interaction Between a Centrifugal Impeller and a Vaned Diffuser" (in Japanese), *Transactions of the Japan Society of Engineers*, 1985, Vol. 51, No. 471, 154-159.

Iino, T., "Potential Interaction Between a Centrifugal Impeller and a Vaned Diffuser," *ASME Winter Annual Meeting* 1981, Washington D.C., Nov. 15-20, 1981.

Inoue, M., and Cumptsy, N.A., "Experimental Study of Centrifugal Impeller Discharge Flow in Vaneless and Vaned Diffusers," *ASME Journal of Engineering for Gas Turbine and Power*, Vol. 106, 1984, 455-467.

Jery, B., "Experimental Study of Unsteady Hydrodynamic Force Matrices on Whirling Centrifugal Pump-Impellers," Ph.D. Thesis, Division of Engineering and Applied Science, California Institute of Technology, 1986.

Kemp, N.H., and Sears, W.R., "The Unsteady Forces Due to Viscous Wakes in Turbomachines," *Journal of the Aeronautical Sciences*, Vol. 22, No. 1, 1955, 478-483.

Kemp, N.H., and Sears, W.R., "Aerodynamic Interference Between Moving Blade Rows," *Journal of Aeronautical Sciences*, Vol. 20, No. 9, 1953, 585-597.

Kovasznay, L.S.G., Tani, I., Kawamura, M., and Fujita, H., "Instantaneous Pressure Distribution Around a Sphere in Unsteady Flow," *ASME Journal of Fluids Engineering*, Vol. 103, 1981, 497-502.

Krain, H., "A Study on Centrifugal Impeller and Diffuser Flow," *ASME Journal of Engineering for Power*, Oct. 1981, Vol. 103, 688-967.

Krammer, P., "Computation of Unsteady Blade Forces in Turbomachines by Means of Potential Flow Theory and by Simulating Viscous Wakes," *ASME Gas Turbine Conference 1982*, ASME 82-GT-198, 1982.

Lalive, J., "Über den Wirkungsgrad von Zentrifugalpumpen," *Schweizerische Bauzeitung*, 1936, Vol. 108, 201-204.

Lefcort, M.D., "An Investigation Into Unsteady Blade Forces in Turbomachines," *ASME Journal of Engineering for Power*, Oct. 1965, Vol. XX, pp. 345-354.

Lienhart, W., "Berechnung der instationären Strömung durch gegeneinander bewegte Schaufelgitter und der Schaufelkraftschwankungen," *VDI-Forschungsheft 562*, Düsseldorf, 1974.

Matsunaga, S., Ishibashi, H., and Nishi, M., "Accurate Measurement of Non-steady Three-Dimensional Incompressible Flow by Means of a Combined Five-Hole Probe," *NONSTEADY FLUID DYNAMICS*, by D. E. Crow and J. A. Miller, ASME, New York, 1978, pp. 65-72.

Ng, S.L., "Dynamic Response of Cavitating Turbomachines," Ph.D. Thesis, Division of Engineering and Applied Science, California Institute of Technology, 1976.

Rai, M.M., "Navier-Stokes Simulations of Rotor-Stator Interaction Using Patched and Overlaid Grids," *AIAA Journal of Propulsion and Power*, Vol. 3, No. 5, Sept.-Oct. 1987, 387-396.

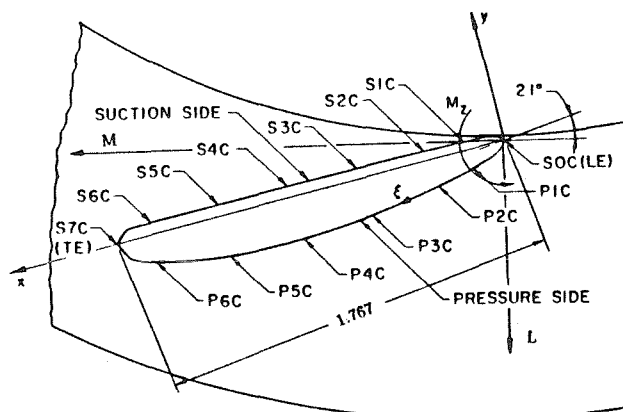
Rai, M.M., "Unsteady Three-Dimensional Navier-Stokes Simulations of Turbine Rotor-Stator Interaction," AIAA Paper 87-2058, AIAA/SAE/ASME/ASEE 23rd Joint Propulsion Conference, San Diego, Calif., June 29-July 2, 1987.

Stein, W., and Rautenberg, M., "Analysis of Measurements in Vaned Diffusers of Centrifugal Compressors," *ASME Journal of Turbomachinery*, Jan. 1988, Vol. 110, No. 1, 115-121.

## APPENDIX

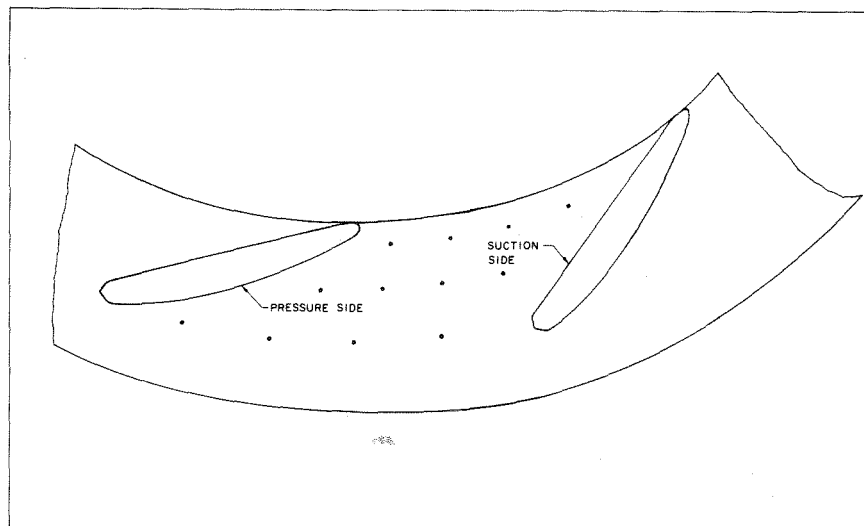
Vane coordinates for a diffuser vane of Diffuser S.

	Pressure Side		Suction Side	
	M	L	M	L
1	0.0000	0.0082	0.0000	0.0082
2	0.0080	0.0341	0.0281	-.0210
3	0.0221	0.0496	0.0485	-.0238
4	0.0436	0.0653	0.0751	-.0221
5	0.1010	0.0932	0.1365	-.0084
6	0.1586	0.1204	0.1980	0.0058
7	0.2165	0.1471	0.2594	0.0196
8	0.2746	0.1733	0.3209	0.0332
9	0.3330	0.1991	0.3824	0.0467
10	0.3917	0.2242	0.4438	0.0601
11	0.4506	0.2487	0.5051	0.0734
12	0.5098	0.2725	0.5664	0.0867
13	0.5694	0.2956	0.6276	0.1000
14	0.6293	0.3178	0.6856	0.1133
15	0.6896	0.3391	0.7496	0.1267
16	0.7503	0.3595	0.8103	0.1401
17	0.8114	0.3788	0.8710	0.1536
18	0.8729	0.3969	0.9315	0.1671
19	0.9349	0.4138	0.9916	0.1808
20	0.9973	0.4293	1.0520	0.1946
21	1.0602	0.4433	1.1121	0.2084
22	1.1236	0.4558	1.1720	0.2224
23	1.1873	0.4666	1.2319	0.2364
24	1.2515	0.4755	1.2916	0.2505
25	1.3161	0.4824	1.3513	0.2647
26	1.3810	0.4873	1.4111	0.2790
27	1.4461	0.4899	1.4709	0.2932
28	1.5115	0.4901	1.5308	0.3075
29	1.5769	0.4884	1.5909	0.3217
30	1.6452	0.4785	1.6817	0.3528
31	1.7230	0.4125	1.7230	0.4125



Coordinates of the front shroud pressure taps (Diffuser S). R is the radius from the diffuser center,  $\alpha$  the angle measured from the leading edge of the diffuser vane in the clockwise direction (leading edge coordinates: R=3.424 in,  $\alpha$  = 0°, M=0.0000 in, L=0.0082 in (see previous table)).

R	$\alpha$
3.554	15.8°
3.554	22.5°
3.554	29.2°
3.554	35.9°
3.850	24.8°
3.850	31.0°
3.850	37.2°
3.850	43.4°
4.200	32.2°
4.200	40.2°
4.200	48.2°
4.200	56.2°



Coordinates of the center of the orifice of the total pressure probe during the total pressure measurements for Impeller Z1 and Diffuser S. R is the radius from the diffuser center,  $\alpha$  the angle measured from the leading edge of the diffuser vane in the clockwise direction (leading edge coordinates: R=3.424 in,  $\alpha$  = 0°, M=0.0000 in, L=0.0082 in (see previous table)).

	R	$\alpha$
AS1	3.47	14.5°
AS2	3.47	21.0°
AS3	3.47	27.5°
AS4	3.47	34.0°